FACULTY OF SCIENCE
CHARLES UNIVERSITY
IN PRAGUE

Department of Genetics and Microbiology

PhD Thesis

Optical microscopy to study the role of cytoskeleton in cell locomotion and virus trafficking

Francesco Difato

Prague 2008

Supervisors: Jitka Forstova, Associate Professor
Lucie Kubinova, RNDr., CSc.
Dan Cojoc, Ph.D
Vincent Torre, Full Professor

Acknowledgments

I am grateful to my family that assisted with patience, and provided me necessary energies to work on my PhD thesis, especially to Mariana who was next to me during all the time. I want to thank Lucie Kubinova and all the people of the Biomathematics Department who gave me the opportunity to work in the optical microscopy lab, and helped me in the first years in Czech Republic. I want to thank my supervisor Jitka Forstova who gave me the opportunity to start a PhD study and trusted my aptitude in scientific work. I want to thanks all the people and technicians of the lab team who introduced me to biology, especially David Liebl. I want to thank Vincent Torre and Dan Cojoc who offered me the opportunity to work with a really interesting project, and their students for the important collaboration: Rajesh Shahapure, Jummy Laishram, Enrico Ferrari and Valeria Garbin. Last but not the least all my dear friends and Special thanks to MATAFRAPIMA.

This work was supported by: Grant from Howard Hughes Medical Institute, USA (75195-540501), Biotechnology programme of EC International research project (BIO-CT97-2147), Grant Agency of the Czech Republic (No. 204/03/0593 and 204/00/0271), Centre for functional organization of the cell (LC 545) and by Centre for New Antivirals and Antineoplastic (1M6138896301) from programme of Ministry of Education, Youth and Sport of the Czech Republic.

Content

1. General introduction

The optical microscopes from simple lens optical system to advanced fluorescence systems played a fundamental role in medicine and biology because it permits observation of living system in their native environment with a low level of structural and functional perturbation.

The optical microscope was the first instrument allowed cell visualization, but only in the 1665, it began to be employed in science: Robert Hooke coined the term "cellulae" or cells to define the small compartments he observed with his compound microscope in cork tissue. In his book Micrographia, Hooke reported similar structures also in wood and in other plants. Micrographia is the first book on microscopy applications: a detailed record of Hooke's observations and drawings.

Later in the 1839, the botanist Matthias Jakob Schleiden and the zoologist Theodor Schwann observed fundamental similarity between different cell types. Therefore, they suggested that all living organisms are constituted of cells, giving origin to the modern biology.

Light microscopy is one of the more utilized tools for investigation of cell organization and physiology: it is a non-invasive technique since sample preparation is non-destructive and, imaging can be performed in three dimensions by using multi-photon excitation, confocal detection or deconvolution techniques [1].

The discovery of green fluorescent proteins (GFP) which can permit to mark specific proteins by genetic manipulation[2,3], increased the interest in fluorescence microscopy. Fluorescent proteins were used to study intracellular trafficking, and to characterize protein-protein interaction[3,4].

The drawback of optical microscopy is its relatively limited spatial resolution; thus there is a need for imaging techniques that have a higher resolution to get insight the molecular biology of cells. Electron microscopy offers superb resolution but it does not allow studying living sample as in optical microscopy. Scanning probe microscopy, like atomic force microscopy (AFM), reached nanometre resolution also on living cells[5,6]. However, AFM produces a high-resolution topographical image of the sample, but it cannot image intracellular structures, and it has limitation in visualizing moving samples.

A new improvement in optical imaging systems is the advent of optical trapping techniques which provide the ability to manipulate biological particles such as virus, living cells and subcellular organelles. These techniques enable scientists to control the spatial organization of samples: perform sorting and/or induce specific interactions between sample particles, at arbitrary location and time. Optical manipulation can be calibrated to perform force spectroscopy measurement: mechanical properties of cell membranes, DNA molecule, and filamentous proteins have been quantified[7]. Moreover respect to AFM, optical tweezers is compatible with fluorescence imaging techniques. Therefore it is possible to apply localized mechanical and chemical stimuli and to follow changes in cell shape and organization[8,9].

The high sensitivity of photonic force microscopy has permitted to quantify forces in the piconewton range, relevant in cell biology. Thus force measurement represent a new point of view in biology studies: it can be applied to understand how physical forces within the cell interact to form a stable architecture[10], how cells resist physical stresses, and how a change in the cytoskeleton initiates biochemical reactions. Additionally, photonic force microscopy can help in explaining the mechanical rules that cause molecules to assemble: for example to understand how the shell of a virus, which consists of several subunits of proteins, can self assemble, starting from an apparent chaotic sequence of collisions[11]. This represents a challenging task for biophysics, because viruses represent a simple or primitive self replicating organism, since viruses have genes and evolve by natural selection. Consequently they are exploited as the simplest biological model to study essential characteristic of living organisms[12]. Viruses have been described as organisms at the edge of life due to their parasitic behaviour, and from the point of view of a microscopist, (engaged in continuous improvements in imaging systems) they also are at the edge of optical resolution (see figure below).

Fluorescence labelling already permit to visualize single virion. In addition the optical resolution limit is continuously decreasing by technological improvement. The newest microscope architecture reaches sub-diffraction resolution using stimulated emission depletion (STED) microscopy: its 70

nm lateral resolution, is demonstrated by imaging GFP-labelled viruses and the endoplasmic reticulum of a mammalian cell[13,14].
Also virus manipulation techniques have evolved in recent years. Viral gene functions studies are performed by localized genetic modification of their nucleic acid chain. Artificial viruses are constructed for the delivery of genes into cells and organisms. Viral surface capsid or envelope can be modified with different proteins to direct their invasion into specific cells and tissue[15,16].

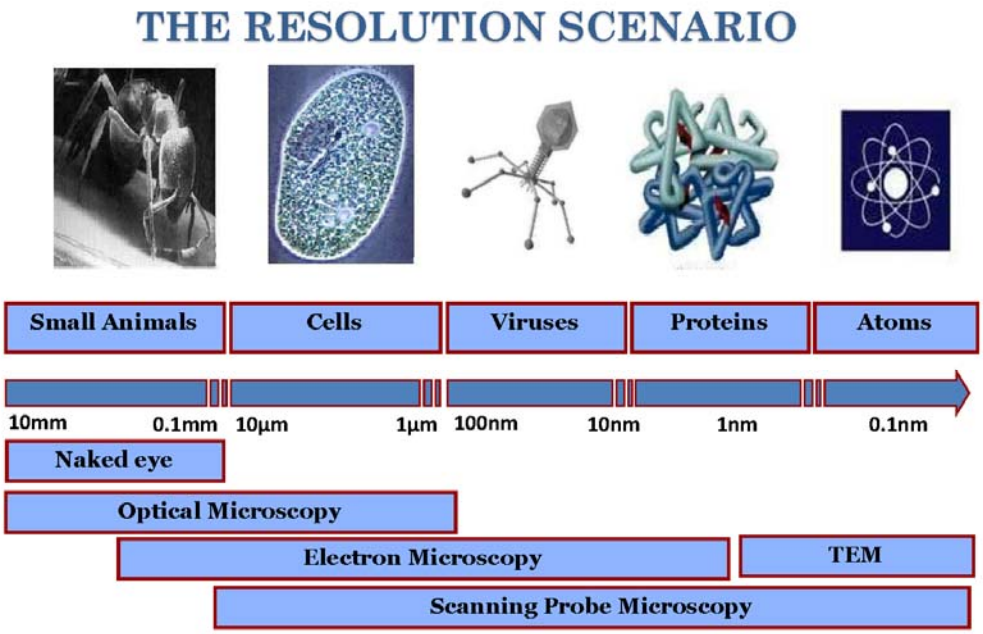

Figure from:
Valentina Caorsi, LAMBS - MicroScoBio, Department of Physics, Diaspro Lab, University of Genoa

Paolo Bianchini - LAMBS - MicroScoBiO Research Center, University of Genoa http://www.lamba.it

Virus permitted to study DNA replication, or to resolve some path of the intricate intracellular endocytic traffic. Furthermore they can represent a good tool to understand factors modulating cytoskeleton dynamics. Indeed limitations to free diffusion in the cytoplasm have forced viruses to manipulate the transport systems of their hosts and to control actin as well as microtubule cytoskeleton networks[17-19]. Thus, in combination with high resolution optical technique, viruses can help in understanding the dynamic polymerization of actin and microtubule filaments and their central role in reshaping the plasma membrane during cell migration. In this context force spectroscopy studies, consent to define the functional role of cellular process[20].

This thesis focuses on application of optical microscopy techniques to understand the roles of cytoskeleton in:

- force production during cell migration and differentiation;
- mouse Polyoma-virus trafficking towards the cell nucleus.

1.1 Optical Microscopy

1.1. 1. From Widefield to Confocal Microscopy

In this chapter, I introduce the principle of confocal microscope and I describe typical optical implementations. First we have to distinguish between widefield and scanning microscope. The widefield microscope is a system that images the entire field simultaneously, while the scanning microscope produces the image of only one point at a time. It means that in scanning microscope the optical components have not to produce the image of the entire object, but a good image of one point.
Figure 1a illustrates the key elements of the optical system of a conventional (widefield) optical microscope[21,22].

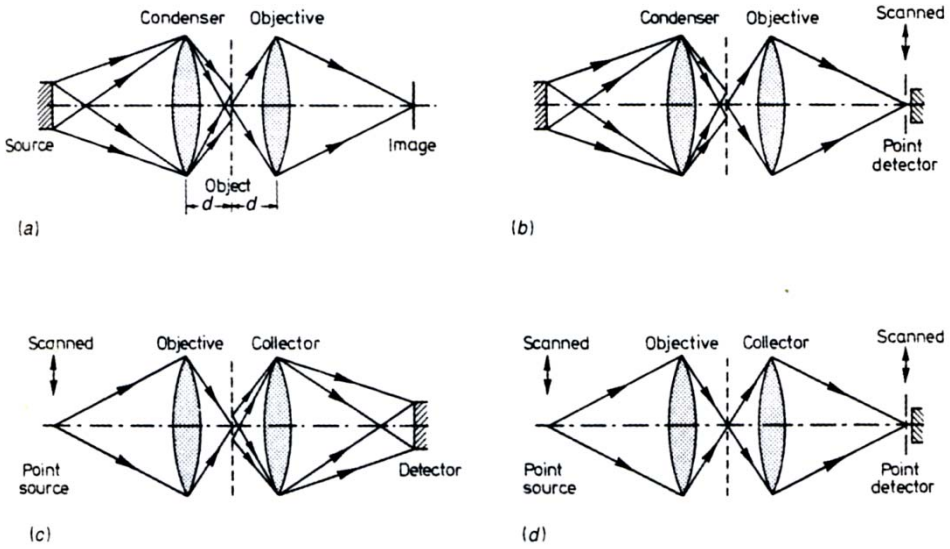

Figure 1 Architecture of various type of optical microscopes[21].

The object is illuminated from an extended source via a condenser lens. The illuminated object is then imaged by the objective lens to the image plane. In this case the resolution results primarily from the objective lens. The condenser lens plays a much less important role: its aberrations are negligible, and it serves to determine the coherence of the imaging[21]. A scanning microscope could be built by moving a point detector in the image plane or a point source as shown in figure 1b and 1c respectively, to measure the image intensity of each point object by raster scanning. In these configurations, an objective lens probes the specimen or collect the light, point by point, while the second lens is analogous to the condenser lens in conventional microscopy, because gives a negligible contribution to the resolution.
To make the second lens to contribute to the resolution, it is necessary to use a point source of light and reduce the large-area detector into a point detector by a pinhole in front of it (figure 1d). Here, light from the point source probes a very small region and the point detector ensures that only light from the same small area is detected. An image is built up by scanning the laser beam on the sample or by moving the specimen through the optical axis of the system. In such symmetric confocal configuration, both lenses play equal roles in the imaging process and the resolution is improved[21].
This improvement is explained by Lukosz's principle[23], who states that resolution can be increased at expense of the field of view. The confocal microscope was for the first time described by Minsky[24], and it can be understood easily from the figure 2 where typical configuration of a confocal microscope in reflection-mode is shown

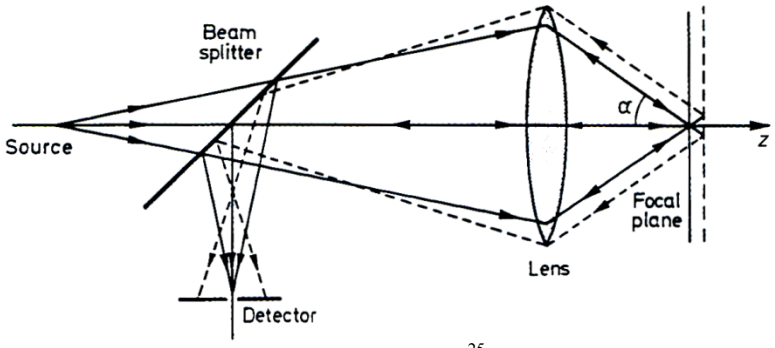

Figure 2 Confocal microscope optical sectioning[25].

The full lines show the optical path when an object lies in the focal plane of the lens and light emission reach the detector, while dashed lines show the path of rejected light from out of focus portions of the object. In this way, the system is capable of optical sectioning.
In addition to general architecture of figure 2, alternative implementations of confocal microscopes have been developed to reduce the alignment requirement of the system, as well as to increase the image acquisition speed.
The first realization of confocal microscope architecture was already satisfying requirements above mentioned and it has been constructed by Petran et al.[26] (see Figure 3).

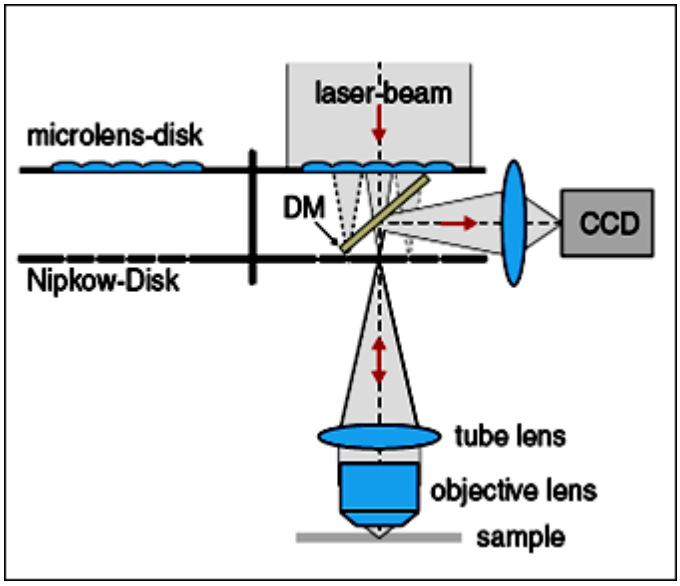

Figure 3 Optical system of tandem scanning microscope[27].

The main component of the system is a disc containing many pinholes and it works like many parallel confocal microscopes, each imaging a specific point on the object. In order to probe the entire object, the pinhole apertures are arranged in an Archimedean spirals on a rotating disc. These systems produce high quality images, without the need to use laser illumination, in real time at high speed[27].
Coming back to the conventional microscope, it also possesses many advantages as real time image capture and ease of alignment. Nevertheless, it does not produce optically sectioned images as the confocal microscope. In the confocal microscope, the signal from objects attenuates with defocus. It does not happen in a widefield microscope. However, only the zero spatial frequency component of the image does not change with defocus, but all the other spatial frequencies attenuate.

If a single spatial frequency pattern is projected onto the object, the image from the microscope will consist of a sharp image of that part of the object where the fringe pattern is in focus, together with an out of focus image of the rest of the object. To obtain an optical section, it is necessary to remove the out of focus contribution and the fringe pattern from the optical section. To do that three images are taken at three different spatial positions of the fringe pattern. The out of focus regions remain constant among these images, and the spatial shift of the fringes pattern allows to reconstruct the entire field of view by removing the fringes[25,28,29]. The image formation is different from that of the confocal microscope, but the optical sectioning strength is very similar. A schema of the system is shown in figure 5. The system is simple; it has trivial alignment and is cheap.
Another type of confocal microscope lies on the capability of a molecule to absorb simultaneously two photons[30]. In two photon excitation (TPE), the energy of two photons, for the excitation of a fluorescent molecule, can combine only if they are able to interact with the same fluorophore at the same time[31,32]. Due to the low probability of TPE process, high photon flux density is required and therefore spatial and temporal confinement of the excitation photons need to be combined. The probability that two photons are within the molecular volume, at the same time, is proportional to the squared intensity I of the source [33]; and due to the quadratic relationship between excitation and fluorescence intensity, TPE falls off as the fourth power of the distance from the focal point of the objective. This implies that regions out of the focal volume do not suffer from photobleaching or phototoxicity effects and do not contribute to the signal detected (see figure 6). Therefore, TPE is intrinsically confocal in excitation.

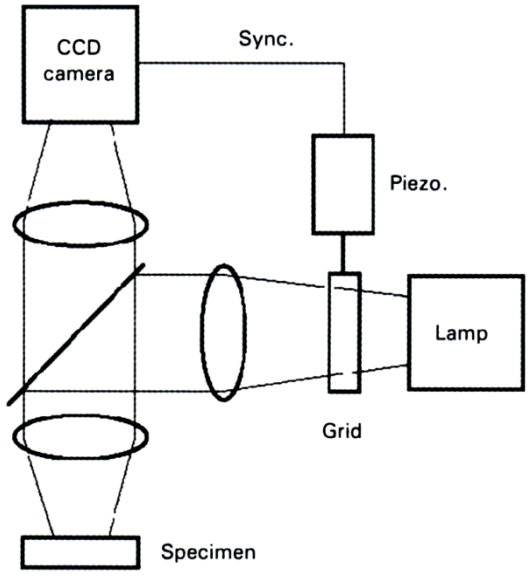

Figure 5 Optical system of the structured illumination microscope[25].

Moreover, the use of infrared instead of UV or visible light, reduces photodamage and allows deeper penetration into tissue[34].
There are two typical approaches to realize TPE microscope: one called the descanned mode, which uses the same optical pathway and mechanism as used for the one photon confocal laser scanning microscopy. The second, called the non-descanned mode, optimizes the optical pathway, collecting the emitted signal to an external large area detector without passing through the galvanometric scanning mirrors. The possibility to acquire a signal with no requirement of descanning is very useful, especially when the fluorescent intensity is very low[34,35].

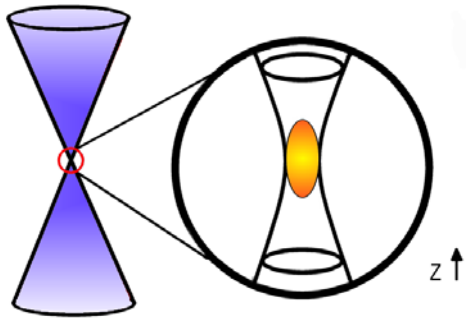

Figure 6: Fluorescence confinement in two photon excitation (in yellow) in respect to the one photon excitation (in blue)[25].

1.1.2. Resolution and aberration

The resolution, defined as the minimum distance of two point objects that provides a contrast between them, depends on the wavelength of the light (both excitation and emission light), on the numerical aperture of the objective, and on the specimen as well[36]. The last limitation means that any specimen cannot be imaged at the theoretical resolution of the instrument because samples are optically thick and inhomogeneous and a focused beam cannot maintain an ideal profile.
A useful tool for comparing the performance of the optical microscopes is the point spread function (PSF) (see figure 7). Detailed description of PSF calculation is presented by Born and Wolf[37]; briefly, if h(u, v) is the complex amplitude PSF (u and v are the normalized optical units parallel and perpendicular to the optical axis, respectively) the intensity PSF is calculated as the product of the amplitude PSF and its complex conjugate:

$$|h(u, v)|^2 = h(u, v)\, h^*(u, v) \qquad (4)$$

This equation describes the three dimensional intensity distribution of light focused by a lens, or the light from a certain point in the object that reach the detector through a collector lens. This means that equation (4) can represent the illumination and detection intensity PSF.
In a widefield laser scanning fluorescence microscope the focused beam by the objective lens is described by $h_{ill}(u, v)$ and therefore:

$$| h_{conventional}(u, v)|^2 = | h_{ill}(u, v)|^2 \qquad (5)$$

A confocal microscope uses both point illumination and detection. This means that confocal fluorescent intensity PSF is the product of the illumination and detection intensity PSF:

$$| h_{confocal}(u, v)|^2 = | h_{ill}(u, v)|^2 \, | h_{det}(u, v)|^2 \qquad (6)$$

thus the extent of its intensity distribution is reduced by a factor $1/\sqrt{2}$ compared with the conventional one.
In a two photon microscope, the fluorescent emission is proportional to the probability of simultaneous absorption of two photons, and this probability is proportional to the square of the excitation intensity. Detection is performed by using a large area detector and it is not a confocal detection. Therefore PSF of a two photon microscope is the square of the illumination intensity PSF[22,22,38]:

$$| h_{two\_photon}(u, v)|^2 = [\, | h_{ill}(u, v)|^2]^2 \qquad (7)$$

The extent of the two photon intensity PSF can be improved by addition of a pinhole in the detection path[39] and becomes:

$$| h_{two\_photon\_Confocal}(u, v)|^2 = [\, | h_{ill}(u, v)|^2]^2 \, | h_{det}(u, v)|^2 \qquad (8)$$

Measuring the extent of these PSFs it is possible to compare the resolution of different microscopes. In mathematical form confocal theoretical lateral resolution is calculated as:

$$r_{x,y} = 0.61\, \lambda_{em}/NA \qquad (9)$$

and a theoretical axial resolution as:

$$r_z = 2\, \lambda_{em} n/NA^2 \qquad (10).$$

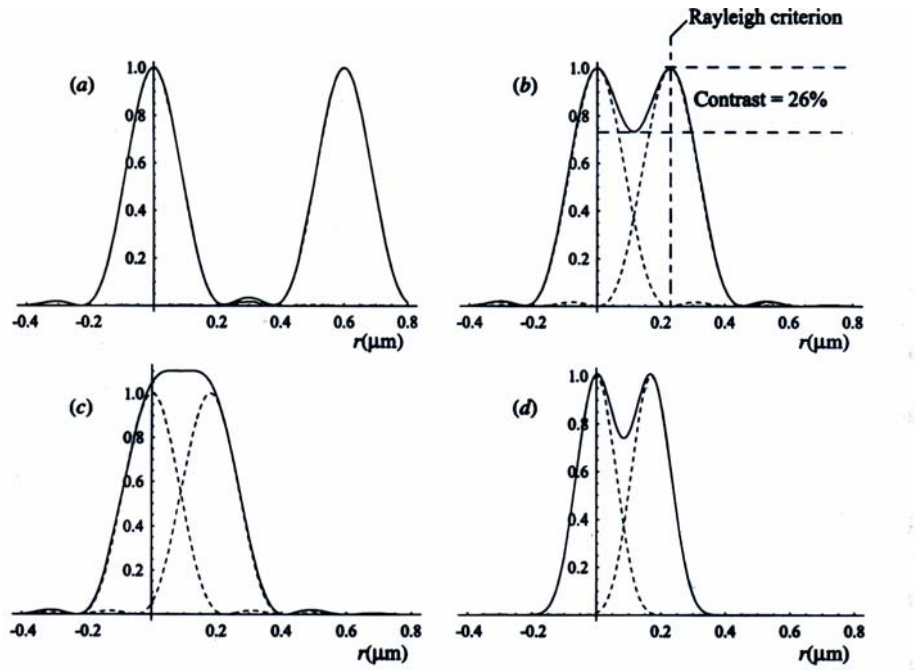

Figure 7 Intensity PSF of two point objects at different separation distance[25].

Another way to quantify the resolution is to define it by image contrast. Contrast between to point objects is described as the difference between intensity on the peak maxima and the minimum intensity between the two peaks (figure 7). The Rayleigh criterion says that 26,4% contrast is obtained when the first minimum of one Airy disc is aligned with the central maximum of the second Airy disc (see figure 7). Experimentally, this is measured as the FWHM of the 3D image of the subresolved point object (which represent the experimental PSF) in each component direction[25,40].

Analysis of the intensity PSF is important because it is a direct measure of the optical properties of the imaging system: chromatic and spherical aberrations introduced by the optical elements, and aberration resulting from focusing through a turbid sample[36,41]. These effects introduce a distortion of the focus, reduce the intensity in the focal region and thus, they reduce the fluorescent signal and the image quality. Therefore, a distorted PSF produces a reduction of the resolution. PSF distortions are ascribed to refraction and scattering of photons by different materials in the sample. Refraction takes place at interfaces: between the objective immersion medium and the sample, or between objects in the samples that have different refractive indexes.

In the first case, incorrect scaling of the image along the optical axis[36] and increase in the spherical aberrations are produced. In the second case, further refraction of the incident rays (when the objects in the sample are larger than wavelength) or scattering of the photons (when the objects are smaller then or of the same dimension as the wavelength) can appear. For particles substantially smaller than the wavelength of the incident light, the scattering has an inverse fourth power dependence on the wavelength (Rayleigh scattering). For particle of the same size, the Mie scattering theory should be used. In general, biological samples contain scatterers with a large variety of size resulting in both types of scattering. This produces wavelength dependence of the scattering less than λ^4.
In two photons excitation, near infrared light is used and therefore, there is less scattering because of the wavelength dependence. This together with use of the widefield detection (which permits to observe multiple scattered photons) improves the detection efficiency, and leads to a deeper imaging penetration in thick samples[34,39].
In ideal conditions (a single refractive index sample and no mismatch-refractive index between objective and sample) good agreement is found between the calculated and experimental FWHM of the PSF, although all measured values are slightly larger than the theoretical ones[42].

1.1.3 Deconvolution

A real image is signal carrying information about a physical object through a degraded representation of the original object. There are two sources of degradation: the process of image formation and the process of image recording (see figure 8).

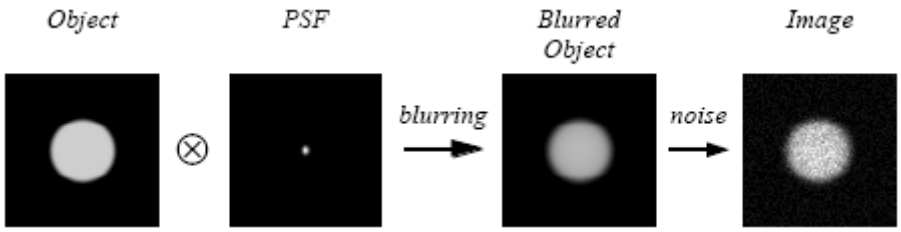

Figure 8 Image formation process in optical microscopy[43]

The degradation due to the process of image formation is denoted as blurring and it is a sort of spatial low pass filtering of the object. The degradation introduced by recording process, the so called noise, is due to measurements errors, counting errors, etc[43-47] Blurring is a deterministic process, therefore it is possible obtain an accurate mathematical model for its description (like the theoretical PSF) or a direct estimation from the measurement of the experimental PSF. On the other hand, noise is a statistical process so that the noise affecting a particular image is not known.
The optical microscope can be described by its PSF because it is a linear shift invariant imaging system. Therefore, the image formation process can be modelled by the linear convolution operator (denoted by A) associated with PSF *K(x)*:

$$A\,f(x) = \int K(x-x')\,f(x')dx' \quad (11)$$

where $f(x)$ represents the real object imaged with the optical system. Then, image recording process adds noise to the image:

$$g = A\,f + w \quad (12)$$

where f is an arbitrary object and w is the noise in the image g.

The problem of image deconvolution can now be formulated as the problem of estimating the unknown object f, given the noisy image g.
The image g contains information about the object f and therefore, it must be possible to found some estimate of f better than g itself. It is not possible to obtain a direct estimate of f by simple inverse filtering because the imaging system is band limited in the spatial frequency domain. This implies the existence of invisible objects and therefore, that solution is not unique. If the expression of the inverse filtering is written in Fourier domain, then

$$f(\omega) = f^{(0)}(\omega) + w(\omega)/K(\omega) \quad (13)$$

where $f^{(0)}(\omega)$ represents the Fourier transform of the exact solution. The solution $f(\omega)$ is the sum of the FT of the true object $f^{(0)}(\omega)$ plus a term which comes from the inversion of the noise contribution. As a consequence, in equation (13) there is division by zero outside the band of the system where $K(\omega)$ vanishes, and $f(\omega)$is completely corrupted by noise[47].
The only way to estimate $f^{(0)}$, is to look for a solution which reproduces the noisy image only approximately: the approximate solutions, found by a least square approach. If f is an approximate solution, the difference between the computed image Af and the measured image is called residual and denoted by r:

$$r = g - Af \quad (14)$$

The point now is to found a set of all approximate solutions compatible with the noisy image within a given noise level ε. This is obtained by additional information expressed in term of constrains on the solution. They are usually called a priori information and they are the basic principle on which all inversion methods rely. Any solution of constrained problem is called "constrained least-square solution".
There are many approaches to obtain a constrained least-square solution, but a general one was introduced by Tikhonov, and is termed regularization of ill-posed problems[48]. The basic idea of regularization consists of considering a family of approximate solutions depending on a positive parameter called "regularization parameter". Its main property is that, in the case of noise free data, the family converge to the exact solution of the problem when the regularization parameter tends to zero. In the case of noisy data, one can obtain an optimal approximation of the exact solution for a non-zero value of the regularization parameter.
In other words, any family $\{R_\mu\}$ of linear operators, depending on a parameter $\mu > 0$, is called a linear regularization algorithm for the solution of the ill-posed problem $A f = g$, if it satisfies these two conditions:

- for any $\mu > 0$, R_μ is a linear and continuous operator
- for any noise-free image $g^{(0)} = A f^{(0)}$

The parameter μ is the regularization parameter and the functions $f_\mu = R_\mu g$ are called regularized solutions. If we use the model for image formation, we have:

$$R_\mu g = R_\mu A f^{(0)} + R_\mu w \quad (15)$$

The first term in the second member of this equation can be called the approximation error because this is the error due to the fact that we approximate the operator A^{-1} by means of R_μ. The second term $R_\mu w$ is the error due to the noise corrupting the image and can be called the noise-propagation error since it quantifies the propagation of the noise from the image g to the regularized solution f_μ.
If we wish to reduce the approximation error, we must choose a small value of the regularization parameter but then, the noise-propagation error is very large. On the other hand, if we wish to reduce the noise-propagation error, we must choose a large value of μ but then the approximation error is too large.

The existence of a minimum of the restoration error and the related existence of an optimal value of the regularization parameter for any noisy image is a basic property of the Tikhonov regularization algorithm. It is obvious that the optimal value of the regularization parameter cannot be determined in the case of real image because $f^{(0)}$ is not known and therefore the best value of μ must be found empirically: for decreasing value of μ, the regularized solution first approaches the best approximation of the object $f^{(0)}(x)$ and then goes away. This property is called "semiconvergence".
Iterative methods can be used to regularize the solution of linear ill-posed problems, and the number of iterations plays the role of a regularization parameter[44,46,47,49,50].

1.1.4 Fluorescence techniques: FRAP, FRET

Fluorophores are often used to simply enhance the contrast and visualize specific compartments in living or fixed samples. However, a lot of information can be obtained from dynamic or permanent changes in amplitude, spectra and polarization of the fluorescent signal.
There are many fluorescence techniques that study these variations of the fluorescent emission properties in quantitative way. Here, I describe two techniques that I used to study molecule dynamics and protein interactions: Fluorescence Recovery After Photobleaching (FRAP) and Fluorescence Resonant Energy Transfer (FRET).

1.1.4.1 FRAP

Photobleaching takes place when fluorochromes loose permanently and irreversibly their ability to fluoresce. Therefore, due to photobleching, information from the sample became lost. Photobleaching is strictly related to the intensity of light excitation. When the intensity is higher, the photobleching of fluorochromes is faster. Reduction of the level of light excitation does not prevent photobleaching, it merely reduces the rate.
When a sample is acquired iteratively fluorochromes photobleach gradually. This is a problem in 3D imaging by one-photon confocal microscopy, where different optical sections of the sample are acquired iteratively, and the system is confocal in detection. This means that we excite not only the in focus plane but also regions above and below this plane, where fluorochromes loose gradually the ability to fluoresce for each acquired optical section, and the last ones appear darker. This phenomenon is eliminated when two-photon excitation is used, because the system is confocal in excitation and it means that by the laser source, we excite only the acquired section of the sample and we do not induce photobleaching in other regions of the sample. Nevertheless, photobleaching is still a problem in two-photon microscopy[31]: in live imaging, we acquire iteratively a section of a sample and so due to photobleaching, we have a limited time for observation of fluorescence emission from biological samples[38].
In any case, there are some application where, thanks to photobleaching, we can obtain information from a specimen, that otherwise, would not be avalaible. Different laser intensities in different regions of the sample are used to obtain different photobleaching rates for diverse parts of it. Thus we are able to observe the average flow of the fluorescence in the sample, which correspondes to the average flow of the fluorescent molecules. This method is the so called FRAP. In FRAP experiment, the bleach is accomplished using a short pulse of high intensity laser light, and then the recovery of the fluorescence within the bleached area over time can show the fractions of a fluorescent molecule that are mobile or immobile, or to provide an estimate of both the diffusion coefficient and the exchange rates of binding interactions that can be occurring within the bleached region[51-54].
The possibility to monitor the fluorescence recovery at arbitrary sites enables an alternative approach called Fluorescent Loss In Photobleaching (FLIP)[53]. While a site is photobleached, the rest of the sample or another specific site in it, is monitored to record the dynamic of fluorescent

intensity. If there is exchange of fluorescent molecule between these two compartments, there will be loss of fluorescence at the monitored site. The rate at which fluorescence is lost at the monitoring site is the measure of the exchange rate between the two sites. If the molecules are immobile or if a structural barrier exists between the regions of interest, no exchange will occur[4].
The confocal laser scanning microscope enables to bleach arbitrary patterns in the sample and therefore, another photobleaching strategy is possible: inverse-FRAP (IFRAP)[25]. In IFRAP, all regions of the cell, except the region of interest, are bleached and then loss of the fluorescence from the region of interest is monitored. This approach simplifies the analysis of the data. For example if binding reaction occurs in the non-bleached area, it reveals the "off rate" binding without contribution from the "on rate", because only the loss of the fluorescent molecule at the binding site is monitored.
The same type of experiments and analyses is now possible to obtain by a less invasive technique then IFRAP, which uses a special form of the fluorescent protein, the Photo-Activable Green Fluorescent Protein (PAGFP). By a short pulse of light, it is possible to switch on the PAGFP molecules at the desired place of the sample at arbitrary time, and then to follow the dynamic of the activated fluorescent molecules[55].
In many cases, it is of interest to simply demonstrate that a specific protein moves and turn over on a specific site, or that it is nearly immobile, or that there is a combination of the two aspects. In other cases, it is of interest to obtain a quantitative parameter to distinguish between different states of the molecule, e. g. to compare different motilities of the same molecule in the sample. In the latter case, a precise definition of the dimensions of the bleached area, and the choose of a correct mathematical model for fitting the data are critical for quantitative analysis of a photobleaching experiment[3,4].

1.1.4.2 FRET

FRET microscopy relies on the ability to capture fluorescent signals derived from the interactions of labelled molecules in living or fixed cells[56]. FRET is a distance dependent physical process by which energy is transferred non-radioactively from an excited fluorophore (the donor) to another fluorophore (the acceptor) by means of intermolecular long-range dipole–dipole coupling. Therefore with FRET microscopic imaging, not only colocalization of the labelled probes within the focal volume can be seen, but molecular associations at close distances can be verified. Its efficiency is dependent on the inverse sixth power of intermolecular separation[56] making it a technique for investigating biological phenomena that produce changes in molecular proximity at angstrom resolution (10–100 Å)[57].
FRET imaging methods have been important in determining the functional compartmentalization of living cells and for tracing the movement of proteins, or viruses inside cells[58,59].
Several FRET microscopy techniques exist, each with advantages and disadvantages. Widefield microscopy is the simplest and most widely used technique. However, it suffers from the generation of out of focus signals. Laser scanning confocal and two photons FRET microscopy reject out of focus information and allow localizing in three dimensions associations occurring inside the cell.
Two photon microscope provides very similar spatial resolution with respect to one photon confocal microscope, but the pulsed laser source gives the possibility to apply time-resolved fluorescence microscopy. Time-resolved fluorescence emission spectroscopy is a powerful tool for the study of living cells in both space and time, because fluorescence measurements in the time-domain possess much more information about the rates and kinetics of intermolecular processes than wavelength spectroscopy alone. For example, fluorescence lifetime is a method for computing FRET efficiency with less contaminations or artifacts in obtained data[60,61]. The presence of acceptor molecules within the local environment of the donor reduce the fluorescence lifetime of the donor. By measuring the donor lifetime in the presence or absence of acceptor, it is possible to calculate the distance between the donor and acceptor labeled proteins.

Another easer method to compute FRET is based on the change in fluorescence intensity. Calculation of FRET efficiency using the classical steady state fluorescence imaging microscopy requires a method of contamination removing from the FRET signal. The spectral overlap between the two fluorophore is required, but it is cause for two types of data contaminations: one due to the overlap of the emission spectra of donor and acceptor (donor cross-talk), the second one comes from the part of the acceptor absorption spectrum which is excited by the donor wavelength (acceptor bleed-through). There are a number of methods minimizing or correcting the contaminations[61-64].
I used the method "acceptor photobleaching" on fixed samples, following the principles established in the literature[64-66], by acquiring two image of the cell separately, with the acceptor and donor lasers before and after photobleaching process. The laser for acceptor excitation was allowed to scan continuously until the acceptor was bleached. FRET efficiency was then quantified by the donor emission increase due to the acceptor bleaching that could not be more involved in FRET.
At state of art, FRET is a difficult technique to apply, but permits to explore the sample well below the optical resolution limit. Therefore, FRET is not only studied to obtain information about molecular interactions, but also to reach 3D imaging at resolution of nm scale, for example in combination with probe microscopy techniques[67].

1.1.5 Optical Tweezers: Optical manipulation and Force Spectroscopy

Experiments on light radiation pressure were performed by Arthur Ashkin in the early 70s[68,69]. He observed that objects in the sample dish were attracted towards the centre of a focused laser beam, and pushed in the direction of propagation. This experimental observation contributed to the idea to use two counter propagating beams to equilibrate their contrasting radiation pressure and to trap an object. Later, in 1986, Ashkin used a single laser beam focused by a high NA objective, to equilibrate the reflected and refracted photons effect at probe interface, to perform optical trapping. This system was called single beam gradient force optical trap[70] and it represented the latest architecture generation. In any case the first configuration, also if require difficult alignment of the two laser beams, is still used because it offer the possibility to trap object more in deep in the sample dish, it can be constructed with low NA objectives, and it can trap objects with high refractive index, where the scattering force have major contribution respect to the gradient force. In the following years, Ashkin pioneered the biological application of optical tweezers by trapping Tobacco mosaic virus, single Escherichia coli bacteria[71], and by manipulating particles within the cytoplasm of cells[72].
The success of light manipulation technique lies on the fact that it is a "contact-free" tool. This mean that it is extremely soft in comparison with mechanical manipulators[73]. Further laser tweezers are highly compatible with optical microscopy techniques[74,75].
Many laboratories now are improving their optical setup to obtain multitrapping spots in the sample and increase the manipulation skill. Two kind of approach are practically used. One is based on acoustic optical device which are able to fast steer the laser beam in the sample, so that trapped probes don't feel the scanning of the laser to time share the light power[76]. Another lies on diffractive optical elements that reshape the Gaussian beam of the laser in an arbitrary shape to obtain the desired trapping configuration on the sample[77]. The first approach permit to change the number and position of spot at high speed, but trapping spot are created only in planar arrangement. The second method need higher computational skill, but permit to obtain a three dimensional system of trapping spots, or more complex shape of the trapping spot: Bessel beam is "non-diffracting" and it propagates without much spreading trough obstacle, Laguerre-Gauss beam can transfer its angular orbital momentum on trapped particles or it can trap low refractive index probe as bubbles[78], anisotropic beam shape create a potential which influence molecular dipole diffusion and distribution and it could influence cell growth[79]. Recently this technique based on diffractive

optical elements was transferred to solid support to trap particle without the need of a microscope objective[80].

However, optical tweezers applications can induce photodamage, which arise from the exposure of the trapped sample to high intensity of light. To overcome this problem it is possible to decrease the intensity reaching the sample, if a better trapping efficiency of the system is reached. For example by adaptive optics methods it is possible to recover non ideal behaviour of the objective lens to obtain ideal light confinement in space of photons and thus unblurred focus spot[81]. Another way to decrease phototoxicity it is to use a laser source in the wavelengths window for which the absorption of the biological matter is low. The typical wavelength used for biological applications is in the infrared range were it was shown, by viability tests both on bacteria and eukaryotic cells, that damage per exposure time is reduced[8,82]. Because the best wavelength range for trapping is the same used in two photon excitation, some groups tried to use femto-second pulsed laser source to obtain trapping, ablation and fluorescence excitation with only one beam[83]. Optical tweezers has been also used in combination with a UV laser to form optical scissors[84] or as part of confocal systems[74,85].

Light manipulators started to be used as force transducers in 1989, after Block[86], made the first calibrated measurement of the compliance of bacterial flagella, using the tweezers to force rotate bacteria (it was tethered to a microscope cover-glass by their flagellum). Subsequently many scientist experimentally demonstrated[87-89] that for small displacements from the equilibrium position within the trap, particle experiences a restoring force which obeys Hooke's law, $F = -Kx$, where K is the calibrated stiffness of the spring and x is the detected displacement from the equilibrium position. To calibrate the stiffness many method are available[9] but the faster and more precise is based on Brownian motion analysis of the trapped probe[90]. To employ such method it is necessary to resolve the Brownian motion of the probe, thus high temporal and spatial resolution is required. The use of the back focal plain interferometry[91,92] allows to measure the position of a trapped object with nm spatial resolution at millisecond time resolution and thus to measure the motion of the trapped bead with the necessary accuracy. As Brownian motion became measurable, its constrained form was used to study the local properties of the media as temperature[93], or to resolve nanostructure as in AFM[94].

Also mathematical models of optical system and Brownian motion improved, and this allows performing quantitative analysis of experimental data. Low pass filtering effect of the detector[88,89], shape of trapping potential and condenser NA influence on the instrument sensitivity were modelled or measured[89,95,96]. Trapped probe Brownian motion considering hydrodynamic effect on medium viscosity were also formulated[97,98]. Such studies represented an important contribution to obtain system calibration with high accuracy and reach the sensitivity of tens of femto Newton force[99].

Thanks to its potential to trap nano particles, optical tweezers became a well-established technique for single-molecule studies: Bustamante was the first person that used such technique to manipulate single molecule of DNA[100]. After this seminal paper followed many works on single molecule biophysical characterization[7]. In other force spectroscopy measurements membrane elasticity was quantified by tether extraction of membrane-embedded beads [101] and piconewton tension was applied to the phospholipids bi-layer to stimulate receptor membrane trafficking [102,103].

Optical tweezers can also be used to track membrane proteins with no need of fluorescent marker at unravelled resolution[104]. For example receptor tracking permitted to distinguish difference in membrane fluidity in living and dead cell[105]. Application of optical tweezers as particle tracker is now moving toward the intracellular space and this represent a first step toward the stiffness calibration and force measurement in subcellular compartments[106].

1.2. The role of cytoskeleton in cell locomotion

1.2 Cytoskeleton

Cells need to organize their internal space and interact with their environment: they evaluate the extracellular matrix properties to move from place to place, and they have to organize their internal compartmentalization.
A theoretical model, known as tensegrity, explains such spatial organization as a network of cable and membranes stabilized by substrate anchors, which create mechanical stability of the living system[107]. The network filaments, the cytoskeleton, represent connections to distribute tensile forces through the cytoplasm to nucleus as a signalling pathway[108]. Transmembrane receptor, as integrins, function as mechanoreceptors and provide a preferred path to transfer mechanical forces across cell surface[109,110]. During motion cell organize integrins distribution in cluster at special complex called focal adhesion[111]. Forces transmitted to the cytoskeleton from these sites produce stress in associated cytoskeletal molecule which can be converted in gene expression, protein recruitment at local sites and dynamic cytoskeleton architecture modulation[110,112-114]. Thus cell shape and stability is the effect of a mechanical force balance between cytoskeleton traction forces and extracellular substrate local rigidity[108,114-116].
The cytoskeleton behaviour is based on three types of protein molecules, which assemble to form three main types of filaments. The different mechanical properties and dynamics of this filaments, provide the principle for understanding how the cytoskeleton works[117,118]. **i)** Intermediate filaments are the most rigid component, responsible for the maintenance of the overall cell shape. **ii)** Microtubules form a polarized network allowing organelle and protein movement throughout the cell. They maintain cell shape and they support motor proteins to generate the force required for cell movement or intracellular transport. **iii)** The actin cytoskeleton is thought to provide protrusive forces[119]. Regulation of assembly processes modulate dynamically the mechanical properties of such network locally and globally to balance compression and tension force, to extend cell protrusions such as lamellipodia and filopodia, or to propel intracellular vesicle or pathogens through the cytoplasm[117,120].

1.2.1 Locomotion

The motion of animal cells over a substrate has been described as the succession of protrusion, attachment, and retraction[121,122] (see figure 10).
Protrusion is the first step, followed by adhesion of the protrusion to the substrate and traction supported from tail deadhesion and retraction[123]. During exploratory motion, cell extend lamellipodia and filopodia[123-126]. The lamellipodium is a flat extension structure at the periphery of spreading cells usually extruded in the direction of a strong signal such as a chemo-attractant which induces cell migration. Filopodia are actin-rich thin structures seen generally as extensions of the lamellipodium[127]. The role of filopodia is that of a sensor of the local environment[128]After their random motion they form adhesive contacts[111] and work as robust scaffold for the lamellipodial protrusion[128]. For example, in some cells, filopodia are essential for navigation: in neurons, when filopodia are suppressed, the nerve growth cones can advance but cannot navigate[122].

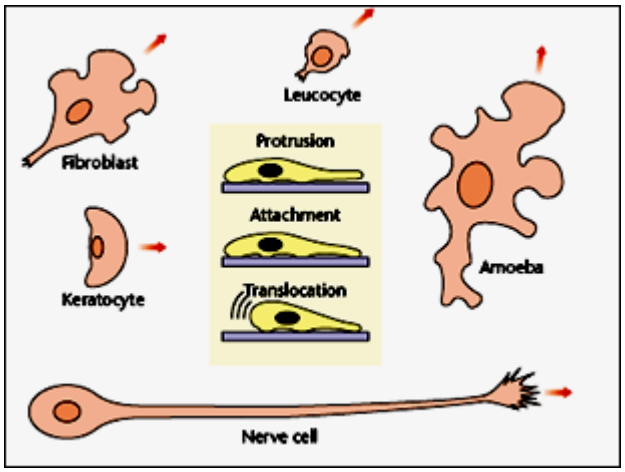

Figure 10 Adherent cells crawl along surfaces by extending protrusions (pseudopods) in the direction of motion. These protrusions attach to the substrate, and then the cell draws its body forward. In many cases this forward movement is driven by internal contractions, followed by release of the rearmost attachments. Different cell types show a variety of mechanisms. Shown are several examples of extensively studied motile cell types. Keratocytes move rapidly while maintaining a constant half-moon shape. Amoeba proteus is a traditional model for amoeboid movement; the mechanism of protrusion formation is quite different from that in most tissue cells. Crawling fibroblasts and leucocytes differ in their degree of attachment to the substrate, and in their typical velocities. Fibroblasts move slowly while applying forces to the extracellular matrix much larger than those required for movement, while leucocytes are weakly attached to the substrate and move more rapidly. Nerve cells do not translocate their bodies, but they extend long processes by means of growth cones at the tips that behave very much like motile cells (figure from ENCYCLOPEDIA OF LIFE SCIENCES / & 2001 Nature Publishing Group / www.els.net).

1.2.3 Membrane resistance

For cells moving through tissues, the resistive force is coming from the surrounding extracellular matrix. For cells in vitro, the major force against extension arises from tension in the plasma membrane which modulates the shape of extruding process. The membrane deform passively in response to cytoskeleton reorganization and its mechanical properties contribute to the cell movement[129].

It has been shown, using giant vesicles like a model, that polymerization of dendritic actin networks on the membrane induces phase separation of initially homogenous vesicles[130]. It seems, therefore, that dynamic membrane-actin network bounds can control when and where membrane domains form and thus modulate local physical properties of the membrane. Physical change, such as decrease in the membrane resistance, could favourite distortion of the phospholipids bi-layer and the local extension process during cell motility.

Important factor in membrane resistance is the number of membrane–cytoskeleton adhesion component. It was shown that the force needed to extract a membrane tether can be modified by alterations of the cytoskeleton[121,122,129,131,132]. It was also demonstrated that mechanical stimuli, which induce membrane tension change, can regulate membrane traffic through exocytosis and endocytosis[103]. These results are in agreement with observation of normal behaviour of the cell, for example: during endocytosis, clathrin displace the membrane-associated cytoskeleton to decrease membrane tension and to cause membrane engulfment[102,131,133,134].

In the case of membrane protrusion, it is required displacement of the normal cytoskeletal components to create a gap for the insertion of new monomers at the filament tips [101,129,131,135].

Apparent membrane tension can be measured from the force exerted on membrane tethers and it is on the order of tens of pN[101,136,137](see Figure 11).

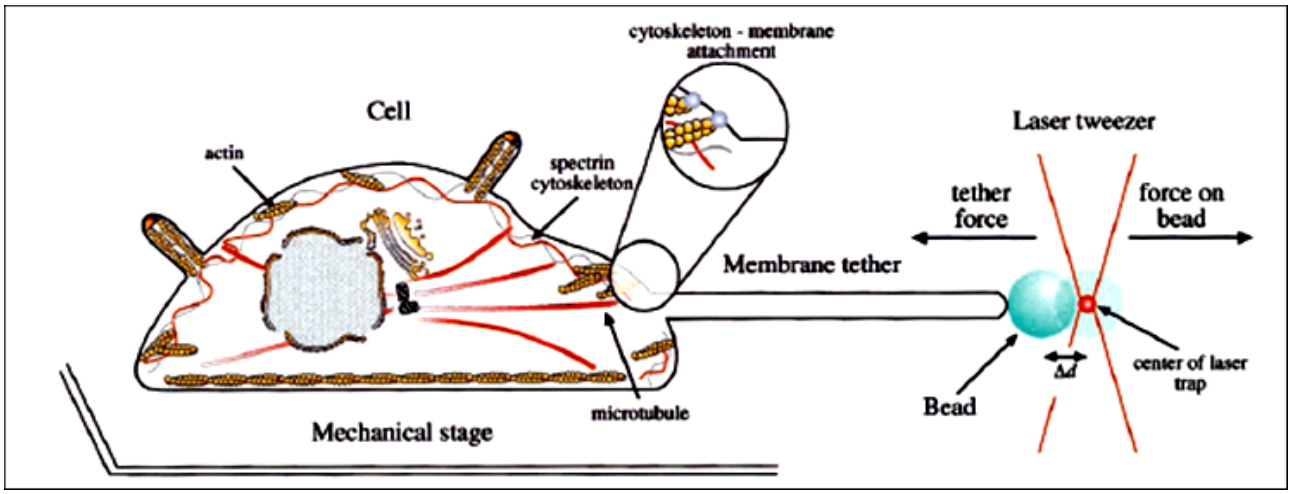

Figure 11 Use of laser tweezers to probe plasma membrane tension. . Attached to the bead is a thin membrane tether that remains associated with the plasma membrane but is free of the cytoskeleton. The in-plane membrane tension, bending stiffness of the membrane and cytoskeleton attachment pulls the bead toward the cell and contributes to the tether force. The tether force is calculated by measuring the displacement of the bead from the center of the laser. An apparent membrane tension can be calculated from the tether force[136].

When tethers are extracted from cells[101,129], the force on the tether increases linearly with the velocity of extraction, which indicates that the viscous resistance in this process is linear. An analysis of the tether-formation process is important because it allows calculating the bending rigidity of membranes, the apparent surface tension, and therefore to obtain a theoretical model of the force produced or the energy dissipated during motion.

1.2.4 Filaments assembly and force production

In cellular extension, two zones can be distinguished: actin rich regions, which are filled by a dense network of filamentous actin and rarely contain any microtubules; and microtubule-rich regions with a dense microtubule network (see Figure 12). The relative extension of these actin rich and microtubule rich regions varies with cell types and is correlated with the shape of the protrusion[119,138,139].
Actin is a globular protein that polymerizes into a linear, two-stranded and right-handed doubles helix which twists around itself every 37 nm[140]. Two types of proteins control actin dynamics independently: actin depolymerising factor (ADF) and capping proteins. ADF accelerates pointed end depolymerisation, to establish higher concentration of monomeric ATP-actin which supports faster barbed-end growth. Capping proteins are required for regulate motility of cells by blocking a fraction of the barbed ends, and to sustain faster growth of few non capped filaments. In conclusion, ADF and capping proteins cooperate to enhance tread milling and to promote actin-based motility.
Maintenance of a steady number of growing filaments requires the generation of barbed ends. The cellular factor that generates new filaments and branches in the actin network[127,141] is the Arp2/3 (see Figure 13) complex[124,125]. Cellular activators of the Arp2/3 complex are members of the Wiskott-Aldrich syndrome protein (WASP) family. Pathways, involving receptor tyrosine kinases, guanosine-5'-triphosphate (GTP) binding proteins (G proteins), or the small GTPases Cdc42 and Rac, target WASP to the sites of signalling, producing recruitment of the Arp2/3 complex.

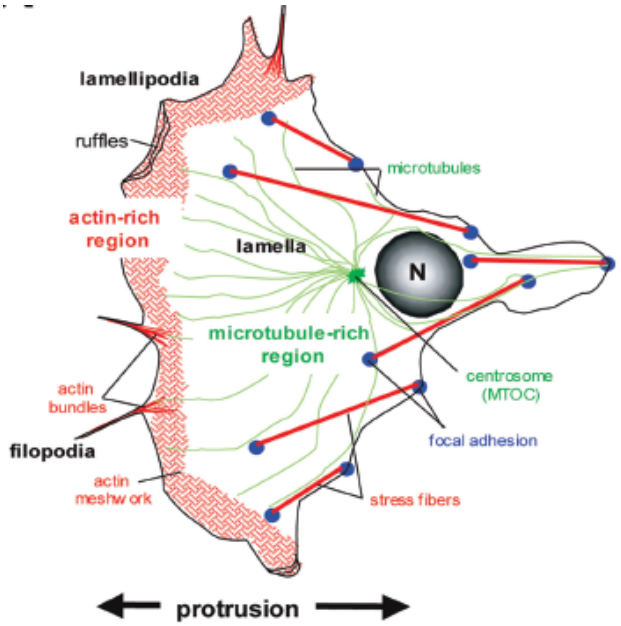

Figure 12 Schematic representation of filopodia and lamellipodia[119].

By this mechanism, actin polymerization is stimulated locally and it is modulated by the input of several signals, at the leading edge[124,142].
Activation of Arp2/3 mediated polymerization generate the dense criss-cross arrangement of actin filaments observed by electron microscopy in lamellipodia[143,143].

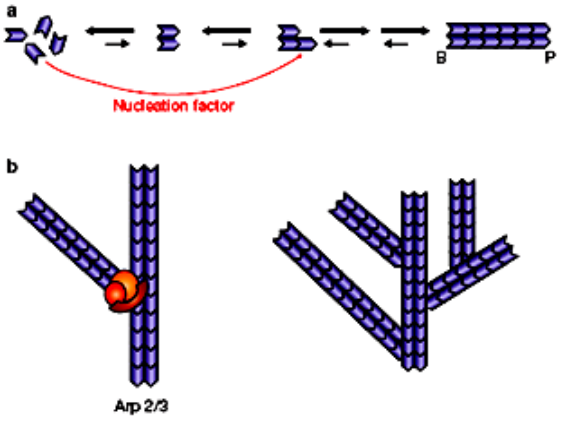

Figure 13. Actin filament polymerization. (a) During actin filament assembly from monomers, the dimerization and trimerization steps are unfavorable, whereas subsequent monomer additions are much more favorable. Nucleation factors overcome these unfavorable dimerization and/or trimerization steps. (b) The Arp2/3 complex (multi-colored) nucleates a new filament from the side of an existing filament, causing filament branching at a 70° angle. The Arp2/3 complex remains at the branch point between the pointed end of the new filament and the side of the existing filament. Repeated branching results in the assembly of a dendritic network[144].

Filopodia, in contrast, are composed of bundles of parallel actin filaments, whose generation depend on the presence of lamellipodial actin meshworks[145]. Faix and Rottner [146] proposed hypothesis for filopodia protrusion, called "the convergent elongation model." In this model, collisions and clustering of filament barbed end, in the lamellipodia actin meshwork, lead to the formation of filopodial precursors; called Λ-precursors (see Figure 14). Actin filaments, in the Λ-precursors, are subsequently reorganized by bundling at their vertices and protected against capping to persistently elongate[147].
Microtubules, the other important cytoskeletal element in cell motion, are long filamentous protein structures that alternate between periods of elongation and shortening in a process termed dynamic

instability. The average time a microtubule spends in an elongation phase, known as the catastrophe time, is regulated by the biochemical machinery of the cell[140].

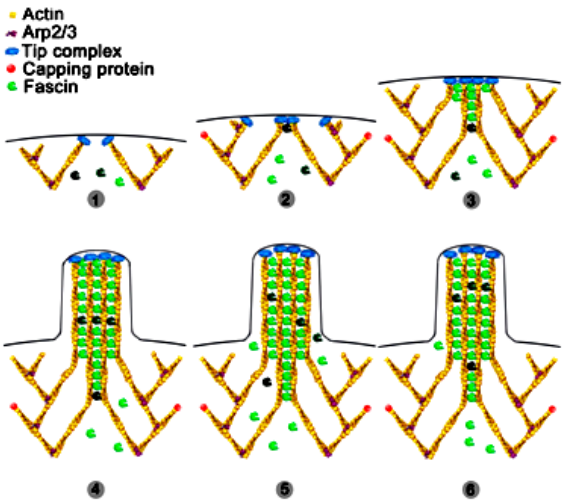

Figure 14. Model of filopodia formation. (1) Uncapped actin filaments elongate and form Λ-precursors. (2) Fascin becomes recruited to the tip complex. (3) Elongation of filaments is closely followed by fascin recruitment and cross-linking, which allows the bundling process to keep up with elongation and guarantees efficient pushing. (4) Filopodia is formed. (5 and 6) Fascin molecules undergo fast dissociation/ association from the shaft of filopodia, ensuring its concentration is high enough, which is necessary for coordination of actin elongation and bundling at the filopodia tips[147].

Comparison of catastrophe times for microtubules growing freely or in front an obstacle leads to conclusion that force reduces the catastrophe time by limiting the rate of tubulin addition[148-151]. Like actin, microtubule architecture is polarized during cell migration and correlation between actin and microtubule organization suggests that the two polymers are linked through intermediate proteins or signalling molecules to produce cell motion[119].
Because actin filaments are rather fragile, mechanical properties of a single actin fibre is difficult to measure. Microtubules are much stiffer, and force generation by this polymer has been measured by observing how a single microtubule buckles when polymerizing against a wall. This experiment demonstrated that a microtubule growing at the plus end develops a force of a few piconewton and that polymerization velocity decreases exponentially as a function of the load force[139,152].
In any case, if individual filaments are modelled as a rod, they result too flexible to resist compressive forces, and to overcome membrane resistance to produce cell's protrusion.
Flexural rigidity (YI) is one of the parameters used to quantify filament deformation[139,152]. The mechanical principle is analogous to Hooke's law for a spring and represents the deforming force required under the assumption that the filament is a homogenous thin rod. Knowing the values of flexural rigidity[152] it can be calculated that the force exerted by a beam of length L bent by z is equal: $F_{bending} = 3\ Y\ I\ \ z / L^3$. A filament of length 3 um composed by a microtubule if bent by 2-3 µm will exert a force with a modulus equal to: 9.5 piconewton. An actin filament in the same conditions will produce a force of 0.4 femtonewton. A bundle of 100 actin filaments will exert a force of 0.04 piconewton.
If the filament is exerting a force because it buckles against an obstacle, the buckling force has a modulus equal to $F_{buckling} = \pi^2\ Y\ I / L^2$ which provides a larger force. For a microtubule is about 2 piconewton and for an actin filament is 6 femtonewton.
Although actin filament is less stiff then microtubule, it represents an essential component in locomotion. The forces generated by elongation of a few parallel-growing actin filaments against a rigid barrier, mimicking the geometry of filopodial protrusion, has been measured[150,153], and it was shown that growth of approximately eight actin parallel-growing filaments can be stalled by

relatively small applied load forces on the order of 1 piconewton. These results suggest that force generation by small actin bundles is limited and therefore living cells must use actin-associated factors to generate substantial force to overcame membrane resistance[150,153]and to produce stable protrusions at the leading edge of the cell during locomotion (see figure 12).
Force production by microtubules is more complex than that of actin because microtubules consist of about 13 protofilaments, which do not polymerize independently. Thus, the force generated by the protofilaments is not simply the sum of the individual protofilament forces. The reason is that at any instant, protofilaments that are too close to the load cannot polymerize because the gaps between their tips and the load are insufficient to allow intercalation of a tubulin dimer, but they can permit the growth of other protofilaments by supporting a large portion of the load[154,155].

1.2.5 Potrusion models

Filopodial and lamellipodial protrusions rely on different mechanisms: filament tread milling and array tread milling, respectively[142,156]. In any case, mathematical models, to explain molecular processes of motion, can be applied to filopodia or lamellipodia with no exception, because they are based on the very same molecular motor: the actin polymerization motor.

Termodynamic model

In 1982, Hill & Kirshner[157] used thermodynamic theory to explain that protein polymerization accompanied by free energy release ($\Delta G<0$) is theoretically capable of generating a force. The ability of actin networks to displace a load depends on the fact that monomer addition is thermodynamically favourable even in the presence of a force. Theoretical expression gives a simple relationship between force and velocity based only on actin concentration and reaction rates. The thermodynamic approach doesn't explain the molecular mechanism, and tells only what force could be generated in the case of very slow polymerization rates when the system is close to equilibrium, which is not the case in a living cell[155,158].

Brownian Ratchet model

Peskin et al. (1993) suggested a Brownian ratchet mechanism[159].
When a growing filament tip encounter an object the growth should simply cease because there is no room between the tip and the object for a monomer. In a Brownian ratchet, the role of monomer binding reaction is to prevent backward fluctuations of the load, rather than to apply a mechanical force directly to it. This means, that the load is driven by its own Brownian fluctuations, and the chemistry provides the energy to rectify its diffusive motion. More precisely, the force is generated by thermal fluctuations of the load, and the binding free energy is used to rectify its thermal displacements. The role of ATP hydrolysis is to control the rate and location of polymerization, and not force production[154,155].

Elastic Ratchet model

Mogilner and Oster (1996) suggested an ''elastic Brownian ratchet''[158].
If the polymer is not rigid, its own thermal undulations can create a gap between its tip and the load. If the gap is large enough, a monomer can intercalate into the gap and bind onto the tip of the growing polymer. This increases the fibre's length so that, when the tip contacts the load, the polymer is bent and the resulting elastic force pushes on the load. In this model, both filament and load are fluctuating, and the combined effect can be sufficient to allow intercalation of monomers and consequent force generation.

Gel model

Oster GF. proposed the gel model[160].
The propulsive force for cell spreading derives from the swelling pressure of the cytogel within the lamellipodia. The actin cytoskeleton comprises an osmotically swollen polyelectrolyte gel and it is always in a state of elastic tension. At equilibrium, the elastic tension in the gel filaments counterbalances the osmotic pressure of the gel counter ions. In motile cells, the actin gel adjacent to the leading edge membrane could be partially severed, for example, by the action of proteins like gelsolin. This weakens elasticity of the gel and the local osmotic pressure expands the gel boundary to a new equilibrium. Subsequently, the gel solidifies again to stabilize the protrusion[155].

Autocatalytic model

Pantaloni noted that in vitro polymerization kinetics are well described by autocatalytic models[124,124,125,141].
To explain the autocatalytic model, it is assumed an obstacle of finite size and that new filament are generated inside a narrow branching region, at the obstacle. Therefore the formation rate of new branches is proportional to the number of actin filaments in the branching region. The network growth velocity is independent of the applied force, and its density is proportional to the applied force[126,161]: when the force on the obstacle is increased, the obstacle will temporarily slow down the growth, allowing the creation of new filaments, until the filament density is that required to compensate the additional obstacle force, and the velocity returns to its steady-state value.
Filament branching is assumed to occur only in the thin region at the obstacle because there, filament uncapping can be induced by obstacle and occur more rapidly[162,163] producing higher filament density at the leading edge. Experimental observations of the network around lamellipodia indicate that density of actin filaments decays over a distance of microns away from the obstacle[118,156].

In conclusion, the force–velocity relation characterizes the ability for a moving object to sustain its velocity while a load is applied. Various force–velocity relations have been predicted for the different theoretical models of actin-based propulsion mentioned above, but only a direct measurement of the force generated by actin polymerization during motion can permit to discern between them[164-167].

1.2.6 Anchoring and retraction

Cell migration involves spatial-temporal organization of adhesion sites to the extracellular matrix (ECM). Cells adhesion to the extracellular matrix is mediated via transmembrane integrin molecules which are associated via their cytoplasmic domains with a complex of proteins including vinculin, talin, paxillin, tensin, and many others[168,169].
Filopodia and lamellipodia size, shape and site of formation depend on the stiffness of the ECM tested by exertion of force on the substratum[115]. Experiments show that solid substrates induce formation of large focal contacts more efficiently than flexible substrates of the same chemical composition[170].
Polymerization is involved in matrix probing by producing cell extensions where integrins clustering occur[111], while formation of adhesion sites results from rearward forces applied on the extracellular matrix. Molecular motor contraction generate actin filament reflow and produce tension on cell adhesion sites as “periodic contractions”[116], which couple protrusion with stabilization of the cell contact area. It is possible that force at localized integrin contacts sites are transported radially by actin rearward flow and they trigger signals for the accumulation of talin, paxillin, and vinculin to stabilize integrins-actin cytoskeleton interaction[110]. Stiffer regions induce

stronger contractile response[109,115,115,116] and vinculin colocalization can recruit the Arp2/3 complex which induce filament branching and stimulate actin polymerization.
Deadhesion at rear of the cell can be regulated by microtubules. In fact, microtubule growth induces disruption of focal adhesions, whereas depolymerisation of microtubules leads to a general increase in cell contractility and to the formation of stress fibres and focal adhesions. Therefore microtubules play an essential role in focal adhesion turnover.
These opposing cytoskeletal elements provides the cell with a sensitive modulated adhesion system[168,171] fundamental in motility process.

1.3 Trafficking of intracellular pathogens

1.3.1 Virus and cytoscheleton

The actin and microtubule cytoskeleton play important roles in the life cycle of every virus. Viruses use the actin and microtubule transport systems and their motors during, endocytosis, nuclear targeting, replication, transport of subviral particles, assembly, exocytosis for cell to cell spread[12,143]. Various intracellular transports are based on controlled actin polymerization or on myosins which translocate along actin filaments.

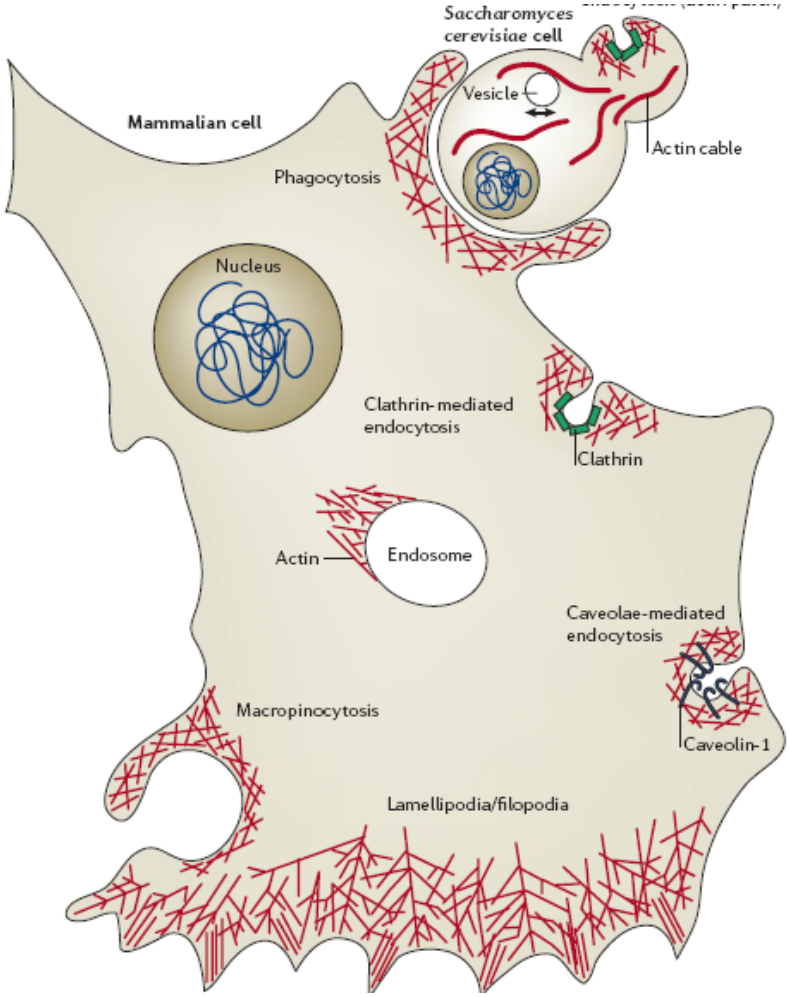

Figure 15 Actin-polymerization-driven processes in eukaryotic cells[20].

For long distances, other transport systems are implied: dyneins and kinesins walk one direction of the polarized microtubule filament, and cellular cargoes use specific motors to reach different regions of a cell[140].
Viruses use both ways and travel either inside cellular vesicles or organelles, or as cytosolic viral complexes[172]. Motion on microtubules depends on intact filaments and therefore microtubules serve as tracks for motor-driven transport. Otherwise, actin induce cargo movements by polymerization and depolymerisation events at filament ends[173].
Many laboratories are studying drugs which affect the cytoskeleton, to decrease pathogens infection efficiency: in case of Herpes simplex virus type 1 and Adenovirus type 2 infection, depolymerisation of the microtubules by drugs (nocodazol) abolishes intracellular virus transport but does not affect virus entry into the cytosol[174]; Measles virus and Sendai virus were observed to

require microtubules for efficient replication, while replication of Parainfluenza virus type 3 requires actin filaments[175].
Several retroviruses move along filopodia towards the cell body before being internalized at the filopodium base[176]. During this movement, the virus is probably bound to its receptor which in turn is coupled to an actin filament inside the filopodium. This filament may be pulled towards the base of the filopodium by myosin II, as in actin reflow observed during cell motility, to test the rigidity of ECM.
The virus entry process meets two obstacles: the plasma membrane and the actin cortex[12]. In uninfected cells, endocytosis and exocytosis are accompanied by local actin dynamics[177,178]. During infection, viruses can interfere with cellular signalling pathways to induce actin rearrangements. Thus actin cortex is not a barrier but participates as a scaffold for virus entry, and then it can also contribute actively to their transport[172].
For example, Simian virus 40 (SV40) causes depolymerisation of actin stress fibres and recruitment of actin patches or tails to caveolae containing SV40 virions[179], while Murine polyomavirus, which belong to the same virus family, induce actin cortex depolymerisation and then it is transported along microtubules as cytosolic cargo[172,180,181].
After viral assembly has been completed, viruses leave the cell either one-by-one by exocytosis or budding from the plasma membrane or after cell lysis by disruption of the plasma membrane. The latter approach is mainly used by non-enveloped viruses, but probably occurs for all viruses after cell death[172]. Another approach used by virus to spread in tissue is to increase contact between cells. For example Respiratory-Syncytial virus spreads in cell monolayer culture by two principal independent mechanisms: by budding to neighbouring cells, or through the fusion of infected cells to adjacent uninfected cells to create a syncytium. In this context it has been observed that actin inhibitors completely prevented syncytium formation[182].
Other studies have demonstrated that vaccinia virus infection stimulates cell migration, changes in cell adhesion, and a loss of contact inhibition[183]. Vaccinia virus induces the formation of long microtubule- filled projections that represent a path to contact neighbouring cells and enhance the spread of infection. Vaccinia is not the only virus to induce long cellular projections, for example also Herpes virus and Pseudorabies virus induces the formation of membrane protrusions to increased cell surface contacts[184,185].
Therefore stimulation of cell migration and modulation of cytoskeleton architecture by virus, offers an additional mechanism to study cytoskeleton role and organization during intracellular transport and cell locomotion.

1.3.2 Actin based intracellular transport

Intracellular transport of various cargos is essential for proper cell function. In intracellular transport two aspects have to be analyzed: one it is how cargo use the network and the second is how the cell change the structure of the networks to assist cargo motion.
Pathogens are able to recruit molecular motors to move along filaments and/or induce cytoskeleton rearrangement to reach their final destination. Microorganisms, such as Listeria monocytogenes, Shigella flexneri, Rickettsia, use actin to propel themselves through an infected host cell. Cellular components, such as vasodilatator-stimulated phosphoprotein (VASP), Neural-WASP protein and the multiprotein Arp2/3 complex have been suggested to be involved in bacterial actin-based motility (see figure 16)[186 187,188].
Also viruses use actin based transport. For example Vaccinia virions mimics signalling pathways, involved in actin polymerization at cellular plasma membrane, nucleating formation of actin tails which propel enveloped virus particles through the cell at velocities of several micrometers per minute[173].
Each of the pathogens listed above expresses a different surface protein that either directly or indirectly activates the Arp2/3 complex, which restrict filament growth to the sites where force

must be produced[124,126,189,189], and leads to the formation of branched actin networks like those observed in lamellipodial protrusions of cells.
This common aspect suggested that pathogens may serve as simplified model systems for study eukaryotic cell motility. In vitro monitoring of their movement in cell extracts converted a complex cell biology problem into a biochemically tractable problem, and opened the way to design a minimal motility medium for study the biochemical mechanism of actin dynamics control[190,191].
Loisel[120] demonstrated that, in addition to actin monomers and ATP, some other proteins in cytoplasmic extracts are essential for bacterial propulsion and that no myosin is required for their propulsion. The medium should contain Arp2/3 complex which multiplies barbed ends by interacting with the specific activator on pathogen surface; ADF, and capping proteins which produce the tread milling of actin filaments.
The concentrations of all components that yield optimum motility are similar to the in vivo concentrations, except for capping proteins which are one order of magnitude more abundant in vivo, suggesting that their function might be regulated[124,125,141].
Furthermore, the protein on the surface of Listeria ActA was purified and coated onto polystyrene beads[192-195]. Therefore pathogen movement could be mimicked by functionalized polystyrene beads when placed in the reconstituted motility medium, and permitted to introduce another controlled variable in the experimental model.

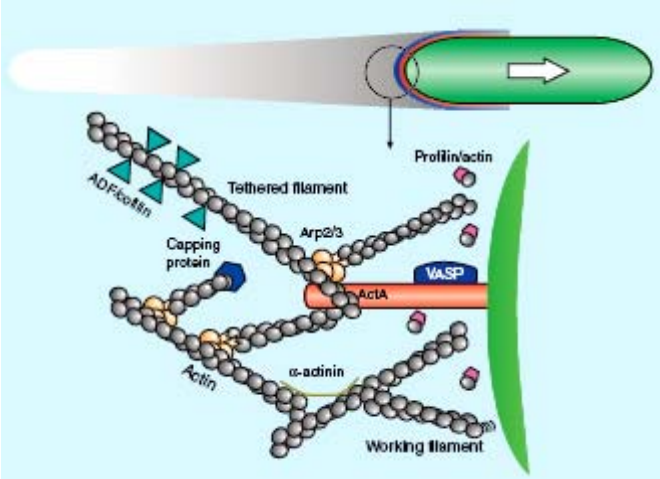

Figure 16 How actin polymerization pushes *Listeria*[155]. Actin polymerizes at the bacterial surface and disassembles distally causing tail to thin and narrow far from the bacterium

Bead movement could be tracked with high accuracy by video microscopy, and bead velocity could be studied as a function of factors as bead diameter and surface density of ActA[192,193] (see figure 17).
These systems have been used to characterize the process of actin comet formation, to measure the elastic properties of actin gels growing from a surface, and to explore the dynamic regime of actin-based propulsion[196].

1.3.3 Propulsion models

A series of theoretical models have been proposed to explain some observed features of bacterial and bead motion. Progress requires deeper knowledge of the structure and function of motile machinery components bound to membrane, and high resolution trajectory analysis of a cargo in a chemically controlled motility assay[123,124,197].
Kuo and McGrath observed that Listeria appeared to advance in discrete steps of 5.5 nm, similar to the size of an actin monomer[187]. These steps could suggest some molecular mechanism at the interface between filaments and pathogen surface. The molecular ratchet motor proposed by

Laurent[198] said that frequent attachment and detachment of VASP on a cargo surface allowed it to slide along a growing filament, driven by the free energy of monomer addition.
Another theoretical model comes from the thought that biological processes rectify Brownian motion. Theoretical Brownian ratchet models relied on the polymerization-biased diffusion of Listeria[123,197,199], and it predicted that the velocity of bacterium should depend on its diffusion coefficient, and thereby on its size.
One of the most important recent discoveries about the actin propulsion is the proof that the actin tail is attached to the surface of the pathogens[188]. Noireaux[200] used an optical trap to measure the force required to separate the bacterial cell from the actin tail, which turned out to be greater than 10 piconewton. Finally, Cameron[193] used electron microscopy to observe that actin filaments of the branching network are transiently attached to the surface of the bead. This leads to more widely accepted model - the elastic tethered ratchet model[158] in which attached fibres are in tension and resist the forward motion of the bacterium/bead, while dissociated fibres are in compression, and generate the force of propulsion.

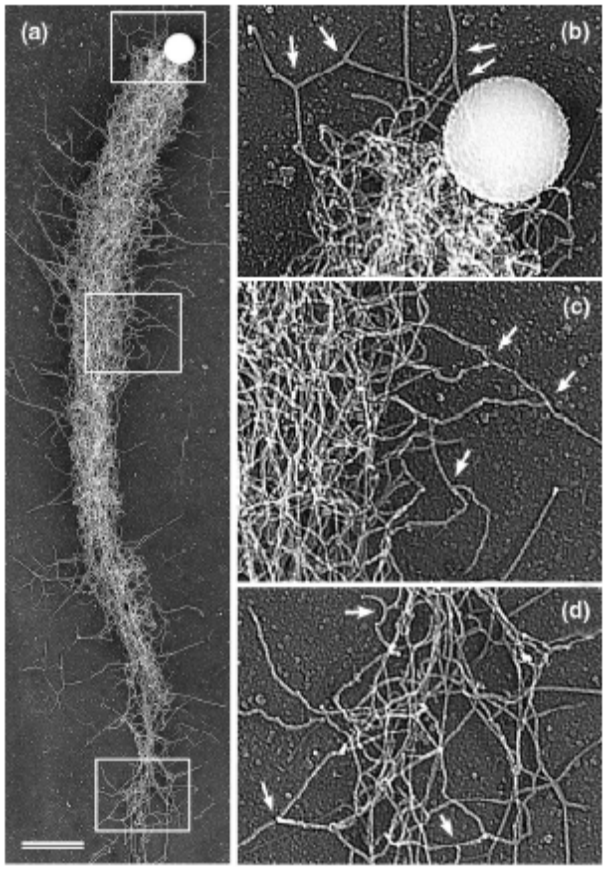

Figure 17 Comet tails assembled by ActA-coated beads. a) An overview shows the very dense array of twisted actin filaments in the tail. (b-d) Enlargements of the boxed regions show Y-junctions (arrows). The scale bars represent 1 μm[193].

It has been shown that, Acta coated beads move with rates of 10–100 nm/s, and that there is a correlation between the size and the velocity of the beads: smaller beads move slower[192,193]. These result are in disagreement with the expected size dependent behaviour of the Brownian ratchet model, and it can be explained as follows: compressed filaments lose contact with the bead's surface in two ways: first, because they become capped and stop to grow, and second, because most of the filaments are not aligned in the direction of movement, so they grow and loose contact with bead surface before they are capped. Therefore, the ratio of the numbers of compressed and

attached filaments decreases in proportion to bead radius and thus smaller beads move more slowly than larger beads[155,158].
Gerbal[196,201] et al, proposed another model where Listeria movement was due to asymmetric build up of elastic stresses in the actin network. The addition of actin monomers at the bacterium surface push the existing actin network outwards, stretching it elastically. This build up of stress is continuously relaxed by movement of the bacterium forward[167,202-204].
Rigid bacteria and beads are resistant to deformation and elastic stresses in the actin gel are hard to visualize, therefore they are not very good experimental systems for characterizing the forces arising in cytoskeleton. In contrast, deformable lipid vesicles provide direct visualization of the actin forces distribution on a moving load by the changes in vesicle shape[202,204]. A vesicle deforms from a spherical shape to an elongated shape. This shape occurs because some actin filaments are tethered to the vesicle surface and exert a tensile stress, whereas others are free to polymerize and produce a compression force. The tensile force at the tail of the vesicle reaches a critical value beyond which the bonds between actin and the membrane rupture, and the vesicle membrane moves to its equilibrium shape. This behaviour is reminiscent of the stepping motion of beads or Listeria, and the stress generated in the deformable membrane can help to model deformation produced in the actin gel of Gerbal's model[164-166].
Indirect approaches have been developed to measure the maximum force developed during actin based motility. For example increasing viscosity of the medium by several orders of magnitude slowed only slightly bead movement [199], suggesting that the propulsive force is much larger than 50 piconewton. Also McGrath used to increase the medium viscosity to affect the Listeria velocity and he obtained a lower bound of 200 piconewton for stalling force [188]
Experiments with micromanipulation of a micropipette, suggested that the propelling force of actin polymerization is on the order of nanonewton. Under fast-pulling of the actin tail at a constant micropipette velocity, the comet remained attached to the bead at a maximum force of about 3 nN. After the comet was detached, a new comet started to grow and push the bead, with identical properties (the same speed, geometric characteristics, and density). In pushing experiment, a force of 4.3 nanonewton was not sufficient to stop the growth of the actin comet[167].
Recently atomic force microscopy (AFM) measurements have succeeded in stalling actin network growth and revealed that two or more stable growth velocities can exist at a single load value. These results demonstrate that a single Force-Velocity relationship does not describe completely the behaviour of the system which depends on loading history and not only on the instantaneous load[161].
Another experiment described the effort to stop motion of Listeria with an optical trap. It was shown that the trap could temporarily stop its motion, and then the bacterium escapes due to an increase in the force supplied by the tail, like in an autocatalytic model[196,201]. Autocatalytic model is also sustained from measurements with fluorescent actin[205], where it has been shown that the fluorescence intensity in actin tail, increases during the stationary period of the bacteria motion, suggesting that the actin density is building up to overcome the opposing forces

In conclusion all theoretical and experimental results present agreement and discrepancy. This can be due to the fact that the process underlying pathogen motility is the same but measurement methods applied has some resolution limits: they had low spatial or time or force resolution. Therefore experimental measurements couldn't help to develop a theoretical model taking into account all important variable in actin based motility process. Present experiments obtained only a lower bound of the force to stall movement of propelled cargo or resolve the trajectory of moving cargoes and they couldn't obtain an experimental Force-Velocity relationship which could explain the molecular behaviour of motility.

2. Experimental Results and Discussion

2.1. Experimental PSF and Stereological method:

1. **Improvement in volume estimation from confocal sections after image deconvolution.** **F. Difato,** F. Mazzone, S. Scaglione, M. Fato, F. Beltrame, L. Kubínová, J. Janácek, P. Ramoino, G. Vicidomini, A. Diaspro: Microsc Res Tech. 2004 Jun 1;64 (2):151-5 15352086

2. **Confocal stereology and image analysis: methods for estimating geometrical characteristics of cells and tissues from three-dimensional confocal images.** L. Kubínová, J. Janácek, P. Karen, B. Radochová, **F. Difato,** I. Krekule Physiol Res. 2004; 53 Suppl 1 :S47-55 15119935

2.1.1. Aims and results

Aims:

- To measure experimental PSF with 64nm diameter microsphere.
- To apply deconvolution to recover aberration and ameliorate image contrast.
- To apply a quantitative method for estimation of the information recovery obtained by deconvolution process.
- To apply deconvolution to obtain a better 3D reconstruction of the sample.

Results:

- We measured experimental PSF with 64 nm diameter microspheres, which are a better Dirac pulse approximation then previously larger diameter beads used.
- After image deconvolution, both qualitative and quantitative image aspects have been substantially improved to obtain a better 3D reconstruction of the sample.
- We have used some representative samples for which a priori information about shape and dimensions are available to test the effectiveness of the reconstruction process.
- We applied Volume calculation on test samples, which represent solid measure because it takes into accounts the dimensions of the sample in all spatial directions, where the optical system have different properties.
- Before deconvolution processing in each experiment we obtained an overestimation of the volume due to blurring effects and presence of out-of-focus light.
- We have shown, with microsphere test, that only with perfect match condition of refractive index between lens and sample, we could recover the overall systematic error introduced by the system optics.
- When there was a refractive index mismatch, we could have a good restoration of the image but couldn't recover the bead volume and diameter theoretical values.
- We applied the same measurements on erythrocytes, after deconvolution and obtained better estimation of the cell volume than that obtained from the acquired image.
- It has been shown how confocal microscopy can be used as a powerful tool to analyse morphometric parameters of biological samples, taking advantage of the optical sectioning capability of confocal fluorescence microscope.

2.1.2. Discussion

Confocal microscopy is a linear shift invariant system; therefore it can be represented by its response to a Dirac pulse. Because a Dirac pulse in imaging systems can be represented by a subresolved object, transfer function of the system can be obtained through an image of a sub-resolved object, as a microsphere with diameter smaller than the optical resolution of the system. The optical system, in this case, is not able to resolve the shape of the object but the detector is sensible to the intensity of the fluorescence emission and provide a blurred image of it. Many works reported use of 100 nm diameter bead, but we used 64 nm diameter microspheres (which was further below the optical resolution) and therefore better approximate the Dirac pulse. Thus, we reduce systematic errors during measurement of the PSF. Smaller diameter bead means a worse signal to noise ratio in measurement of PSF. This can be an important issue in the deconvolution algorithm where noise in the PSF image can be interpreted as aberration of the optical system and creates artefacts in the processed image. To improve the signal noise ratio, we had to acquire images of more beads and average them.
Then we used the experimental PSF to deconvolve image of artificial and biological sample.

The artificial sample (a bead of well resolved dimension) represented a good test to evaluate the quality of the experimental PSF and the efficiency of image processing, because

- they have known shape and dimension
- they represent homogeneous material and therefore only one kind of refraction takes place as they produce only one interface of mismatch refractive index at the surface (a true biological sample is a complex assembly of many structures which gives more complex refraction and scattering)

Through analysis of the acquired and deconvolved image it was possible to quantitatively compare the results with the datasheet of the sample. We decided to apply volume measurement because it represents a solid measure that takes into account the dimensions of samples in all spatial directions. Such analysis represented first quantitative measurement of the information recovery through deconvolution process. This was achieved by measurement of morphological parameters in the image of the sample before and after processing. We compared the results in two conditions of refractive index match between the objective and the sample media. In case of match condition between sample and objective media, we obtained almost the theoretical value of the radius of the beads and this was a measurement of the goodness of the experimental PSF. In case of no-perfect match condition, typical for measurements of a biological sample with a high NA oil immersion objective, we reported worse restoration of the image quantified by the overestimate of the radius of the bead. This case of mismatch of refractive index is a simple representation of the situation encountered with a biological sample, as a cell where the light have to pass different compartments with different optical properties (i.e. media, membrane, cytoplasm, nucleus). Then, we repeated measurements with erythrocytes and we reported that deconvolution process gave us better quality images in which the sample characteristics are only partially recovered.

In any case, deconvolution gave the possibility to remove noise from the image with no loss of resolution as it usually happens through a simple low pass filtering of the data. This produces a better contrast of the image and easier analysis of data represented in it. Moreover, after deconvolution, a better 3D rendering of the sample can be obtained.

Deconvolution processing of the images is yet waiting for a method to obtain an exact estimate of the regularization parameter which will permit to obtain the best estimate of the sample and to have data from the images that are not corrupted by noise. Such quantification of information recovery could help to found experimentally a good value of the regularization parameter. In any case, deconvolution ameliorates the contrast of the image and therefore the experimental resolution of the system.

2.1.3. **Publications**

Improvement in Volume Estimation From Confocal Sections After Image Deconvolution

F. DIFATO,[1,4] F. MAZZONE,[1] S. SCAGLIONE,[2] M. FATO,[2] F. BELTRAME,[2] L. KUBÍNOVÁ,[4] J. JANÁČEK,[4] P. RAMOINO,[3] G. VICIDOMINI,[1] AND A. DIASPRO[1]*
[1]*INFM, LAMBS-DIFI, University of Genoa, 16146, Genoa, Italy*
[2]*BIOLAB-DIST, University of Genoa, 16145, Genoa, Italy*
[3]*LAMBS-DIPTERIS, University of Genoa, 16145, Genoa, Italy*
[4]*Department of Biomathematics, Inst. of Physiology, Academy of Sciences of Czech Republic, Prague CZ-14220, Czech Republic*

KEY WORDS confocal microscopy; volume estimation; image deconvolution; point spread function; three-dimensional microscopy

ABSTRACT The confocal microscope can image a specimen in its natural environment forming a 3D image of the whole structure by scanning it and collecting light through a small aperture (pinhole), allowing in vivo and in vitro observations. So far, the confocal fluorescence microscope (CFM) is considered a true volume imager because of the role of the pinhole that rejects information coming from out-of-focus planes. Unfortunately, intrinsic imaging properties of the optical scheme presently employed yield a corrupted image that can hamper quantitative analysis of successive image planes. By a post-image collection restoration, it is possible to obtain an estimate, with respect to a given optimization criterium, of the true object, utilizing the impulse response of system or Point Spread Function (PSF). The PSF can be measured or predicted so as to have a mathematical and physical model of the image-formation process. Further modelling and recording noise as an additive Gaussian process has used the regularized Iterative Constrained Tykhonov Miller (ICTM) restoration algorithm for solving the inverse problem. This algorithm finds the best estimate iteratively searching among the possible positive solutions; in the Fourier domain, such an approach is relatively fast and elegant. In order to compare the effective improvement in the quantitative image information analysis, we measured the volume of reference objects before and after image restoration, using the isotropic Fakir method. *Microsc. Res. Tech. 64:151–155, 2004.*

INTRODUCTION

Morphometrical measurements of structural components of organs, tissue, or cells are the principal goal for quantitative analysis in many biological research studies, especially when the relationships between function and structure are analysed (Kubínová, 1998). Stereological methods are precise tools for the quantitative evaluation of the structure of three-dimensional (3D) objects (Castleman, 1996). It is possible to achieve a 3D reconstruction of thick specimen by using confocal laser scanning microscope (CLSM). The CLSM enables one to obtain perfectly registered stacks of parallel optical sections from thick specimens (Diaspro, 2002). Due to the large number of fluorescent probes for the fluorescence technique, their specificity and optimum resolution capability, digital images obtained represent suitable 3D data for quantitative measurements.

Sampling distances of serial optical sections are physically limited by the resolution of the objective. According to the Nyquist principle, sampling at twice the theoretical resolution we can avoid the aliasing artefact (Castleman, 1996). Within the simplified optical model of a linear and space invariant system, let h(x,y,z) be the impulse response for such a system also referred to as the PSF of the microscope, f(x,y,z) the true distribution of fluorescent intensity within the specimen, n(x,y,z) a general additive noise distortion, and o(x,y,z) the observed image; we can model the image formation in a confocal fluorescence microscope as (Bertero and Boccacci, 1998; van der Voort and Strasters, 1995):

$$o(x, y, z) = f(x, y, z)*h(x, y, z) + n(x, y, z) \qquad (1)$$

where "*" is the convolution operator.

Non-ideal behaviours of the system contribute to reduce the contrast and, therefore, the resolution of microscope images (Hell and Stelzer, 1995; Hell et al., 1993; Pawley, 1995). Indeed, we can observe that experimental PSF profiles deviate from the theoretical ones. The experimental PSF needs to be calculated under the same experimental conditions of sample acquisition (because it depends on: wavelength excitation and emission, objective lens, and specific optical path).

We show further that the deconvolution process with appropriate PSF can be used to correct the different wavelength components of a multi-wavelength image and recover the architectural systematic errors. We have observed synthetic fluorescent beads of a 2-μm nominal radius immersed in two different media: an oil immersion objective medium to avoid refractive index

*Correspondence to: Alberto Diaspro, Department of Physics, University of Genoa, Via Dodecaneso 33, 16146 Genova, Italy. E-mail: diaspro@fisica.unige.it
Received 15 April 2004; accepted in revised form 15 April 2004
DOI 10.1002/jemt.20063
Published online in Wiley InterScience (www.interscience.wiley.com).

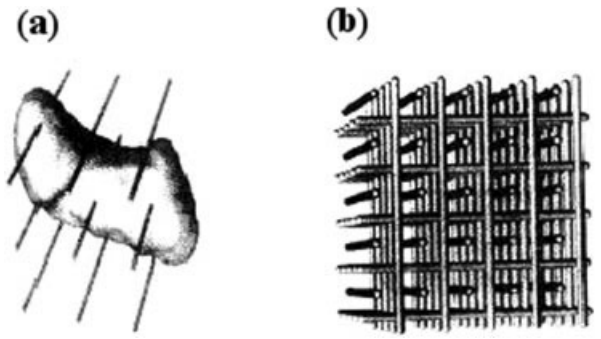

Fig. 1. **a:** Fakir probe piercing a 3D object. **b:** Orthogonal triplet of shifted Fakir probes. The estimation of surface and volume depend on the grid constant μ: the shortest grid constant gives a better estimate.

TABLE 1. Experimental test sample in oil

Microspheres in oil: (sample number)	Volume after acquisition (μm^3)	Volume after deconvolution (μm^3)
1	48.66	30.66
2	54.37	30.80
3	48.97	32.09
4	50.10	32.11
5	55.04	34.69
6	45.03	32.88
7	62.36	38.65
8	49.62	32.34
9	45.04	31.58
10	56.70	31.89
11	46.15	31.68
12	49.38	35.64
13	50.63	30.60
14	46.27	30.51
15	43.59	33.87
16	40.50	30.50
17	52.43	35.61
18	57.27	36.58
19	50.13	32.98
20	47.93	30.71
Mean value	50.13	32.80
Nominal value	33.49	
Mean radius	2.28 (μm)	1.99 (μm)
Nominal radius	2.00 (μm)	

mismatch that may cause other distortion effects (Diaspro et al., 2002) and a water immersion medium for simulating the typical immersion media of biological specimens.

We repeated this experiment with a true biological specimen, the human erythrocytes. The volume of the erythrocytes is known in scientific literature by using methods other than microscopy (Bunyaratvej and Bunyaratvej, 1992). Volumes were computed using the isotropic Fakir method (Kubínová and Janáček, 2001) that yields robust measures and data were compared on acquired data sets before and after deconvolution. We used, as a second biological test, the sperm head of eledone cirrhosa, which is a reference biological sample for studying the spatial arrangement of linear helical structures. This helical specimen is considered similar to chromatin-DNA, an important biostructure governing cell functions (Maxwell, 1974). (We wanted show how it is possible after deconvolution to distinguish shape and changes in helical structures.)

TABLE 2. Experimental test sample in water

Microspheres in water (sample number)	Volume after acquisition (μm^3)	Volume after deconvolution (μm^3)
1	51.89	46.06
2	67.35	51.74
3	53.41	51.01
4	48.38	46.24
5	45.76	39.89
6	53.14	47.98
7	55.60	50.00
8	51.05	47.41
9	58.67	52.22
10	56.62	54.47
Mean value	53.44	46.98
Nominal value	33.49	
Mean radius	2.34 (μm)	2.26 (μm)
Nominal radius	2.00 (μm)	

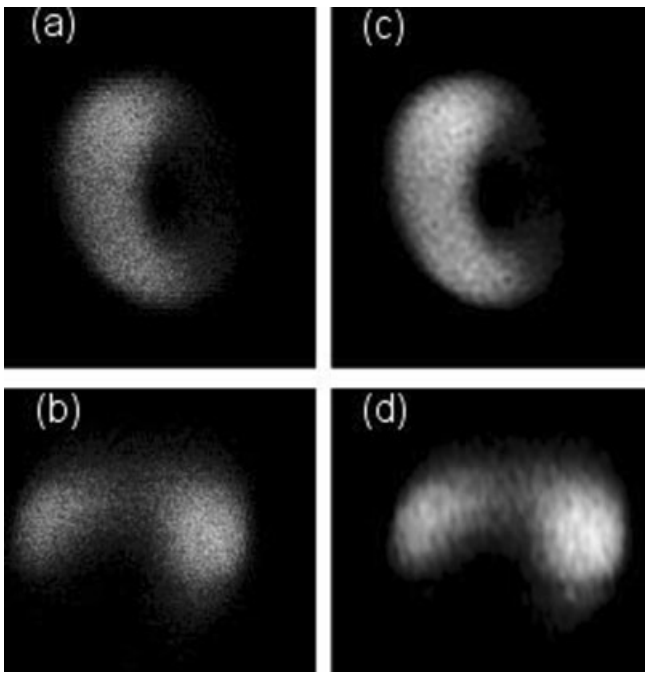

Fig. 2. Human erythrocyte, in paraffin, imaged using a 40× 1.3 N.A. oil immersion objective. **a,b:** Original x-y plane, x-z plane. **c,d:** Restored x-y plane, x-z plane. Field of view: 15.1 × 15.1 (μm) in the x-y plane; 15.1 × 6 (μm) in the x-z plane.

MATERIALS AND METHODS

Confocal Microscopy

The whole system is based on a Leica DIAPLAN microscope equipped with an intermediate tube for laser scanning, an x/y mirror scanner, and a detector unit operating with two independent acquisition channels allowing confocal reflection and/or fluorescence microscopy. The acquisition system can also be switched to wide-field mode for transmission, fluorescence, or phase contrast microscopy. The laser source is an Argon-krypton gas laser. Confocal fluorescence images were taken using a 40×/1.3N.A. oil immersion objective and a 100×/1.4N.A. oil immersion objective. Different collections of optical slices (16–64 images) were acquired in confocal mode: 512 × 512 × 8-bit or 256 × 256 × 8-bit image format was used. An electronic zoom was employed with a magnification ranging from 1 to 8.

TABLE 3. Erythrocyte data set

Erythrocytes (sample number)	Volume after acquisition (μm^3)	Volume after deconvolution (μm^3)
1	125.54	97.89
2	128.38	109.28
3	118.74	105.08
4	135.32	114.87
5	142.34	119.91
6	136.32	117.93
7	144.65	122.05
8	86.06	82.19
9	124.95	99.16
10	138.28	118.09
Mean value	128.06	118.09
Nominal range value	82–99	

We acquired the experimental PSF of the system in three different immersion media: oil (n = 1.52), glycerol (n = 1.48), and distilled water (n = 1.33) (Diaspro et al., 2000). The images were sampled at 100-nm steps along the z-axis and at 59-nm steps in the *xy* plane (according to the Nyquist principle), with a 20-μm pinhole aperture size (1 Airy disk unit).

Samples

PSF Measurements. We acquired Latex subresolved beads (Ø = 64 nm) loaded with Yellow-Green dye and Latex subresolved beads (Ø = 100 nm) loaded with orange-red dye (Polyscience, Warrington, PA), with a 20-μm pinhole aperture size. A drop of dilute samples of bead suspensions was put on a coverslip of nominal thickness 0.17 mm and air dried in a dust clean chamber. Then a drop of the immersion media was deposited on the dried sample.

We acquired the PSFs in three different conditions:

- beads in oil (488 nm excitation/520 nm emission with a 40×/N.A. 1.3 oil immersion objective);
- beads in water (488 nm excitation/520 nm emission with a 40×/N.A. 1.3 oil immersion objective);
- beads in glycerol (568 nm excitaion/580 nm emission in glycerol with a 100×/N.A. 1.4 oil immersion objective).

Microsphere. We used Latex microspheres loaded with Yellow-Green (Polyscience), whose diameters was 2 μm. A drop of a water-diluted sample was put on a glass coverslip of 0.17-mm nominal thickness and air dried in a dust clean chamber. Drops of different substances, i.e., oil n = 1.52 and water n = 1.33, were deposited on the dried sample in order to test different refractive-index mismatch conditions.

Biological Samples

1. Human erythrocytes: from placenta tissue, fixed in paraffin. Only in this case, we observed the autofluorescence signal from specimen without any fluorescent dye.
2. Sperm head of eledone cirrhosa: a lyophilised sample of impure sperm heads of E. Cirrhosa (Mollusca, Cephalopoda, Octopoda) was resuspended in 0.15 M NaCl with 0.5% Triton X-100.

In order to break the large amount of sperm tails, the sample was homogenized and sedimented by centrifugation for 10 minutes at 2,000 rpm. The pellet was washed in 0.1 M phosphate buffer (PB), pH 7.4, and diluted in a small amount of PB then air dried directly on glass slides treated with poly-L-lysine (1 mg/ml). Sample were fixed in ethanol-acetic acid (3:1) for 20 minutes at 4°C, washed, and labelled with propidium iodide (2 μg/ml in PB containing 20 mM $MgCl_2$, pH 7.4) for 40 minutes at 4°C. After a short washing with PB, the specimens were mounted in glycerol.

Image-Restoration Method

In a simplified hypothesis of a linear and space-invariant imager, we have a model to solve the inverse problem of deconvolution. The Tykhonov-Miller approach finds the solution searching in a set of feasible solutions that minimize a mean square error criterion between the acquired image and an estimate of it. Being "f" such an estimate and "o" the acquired image we can write a first functional as:

$$\Phi(f') = \|o - h*f'\| <= \varepsilon \tag{2}$$

where h is the point spread function of the system and ε is an estimate of the noise (Bertero and Boccacci, 1998). Since this inverse problem is an ill-posed one, we need a regularization on the solution by a penalty function to get a stable and meaningful estimate.

We choose a limit on the total amount of energy in the estimate "f":

$$\Psi(f') = \|f'\| <= E \tag{3}$$

where E is that limit. Combining equation [2] and [3], we obtain the regularized Tykhonov–Miller functional:

$$\Phi(f') = \|o - h*f'\| + \alpha\|f'\| \tag{4}$$

where α is the regularization parameter and it expresses a ratio between the fidelity of the data and a smoothing function necessary to avoid noise amplification at high frequencies. We found the solution of [3] by an iterative approach that allowed us to include in the algorithm a positivity constraint at each iteration.

In a real image, we can miss an estimate of the noise power and the energy limit for the signal. We need an alternative method to find the regularization parameter that does not need any a priori knowledge of the image. We calculated a posteriori the regularization parameter by a general cross-validation (GCV) function (Bertero and Boccacci, 1998) that produced similar values to the theoretical ones, when synthetic data were available (Bertero and Boccacci, 1998; van der Voort and Strasters, 1995).

Stereological Method: The Fakir Method

In evaluating geometrical parameters of biological samples, many approaches require randomisation of direction of the thick slice of the optical sections. Nevertheless, in practice, it may be essential to take sections in a particular fixed direction. For example, it is not easy to orientate cells in a suspension or a cell culture at random, and it can be easier to determine

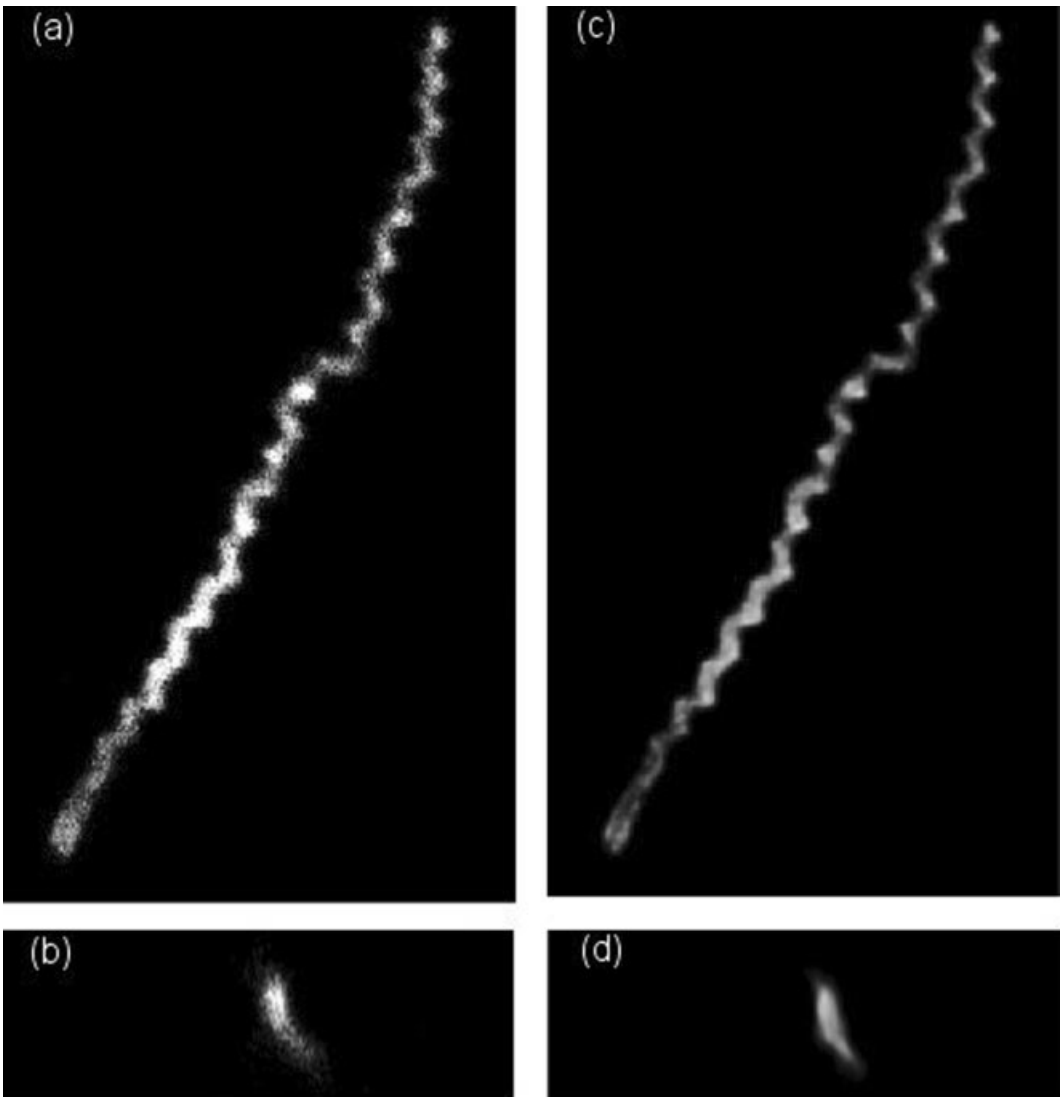

Fig. 3. Eledone cirrhosa sperm head labelled with propidium iodide acquired using a 100× 1.4 N.A. oil immersion objective. **a,b:** Original x-y plane, x-z plane. **c,d:** Restored x-y plane, x-z plane. Field of view: 13.6 × 24.2 (μm) in the x-y plane; 13.6 × 4.4 (μm) in the x-z plane.

the mutual localization of different tissues in sections with a specific direction. Consequently the Fakir method, without assumptions on thick-slice orientation, enables us to estimate such important parameters as volume, surface area, and length (Fig. 1). The main idea here is to use virtual, randomly oriented spatial grids of points, lines, or planes that can be generated by a computer and visualized together with the structure under study. Thus, both test grid and microscopic structure are "focused through" by browsing through the stack of optical sections, and so interactions between the grid and structure can be evaluated (Maxwell, 1974).

RESULTS

We have used some representative samples for which a priori information about shape and dimensions are available so we can test the effectiveness of the reconstruction process that we applied. We acquired images of the samples at Nyquist rate, assigned by theoretical resolution, and also took into account all the spatial frequencies collected by the system. Since it is known that the theoretical resolution of a system is always better than the experimental resolution, we chose the theoretical resolution as the reference for the Nyquist rate. Moreover, we selected a minimum oversampling that assured us of avoiding the aliasing phenomenon.

Volume calculation is a solid measure because it takes into account the dimensions of sample in all spatial directions, which usually have different properties. We observed synthetic green fluorescent beads of a 2 ± 0.02 μm nominal radius yielding a volume of $33.49 \pm 3.4*10^{-4}$ μm^3; therefore, we have a priori information with a tolerance of 0.0001%. The volume of the erythrocytes is known in scientific literature by using different non-microscopic methods. Erythrocytes

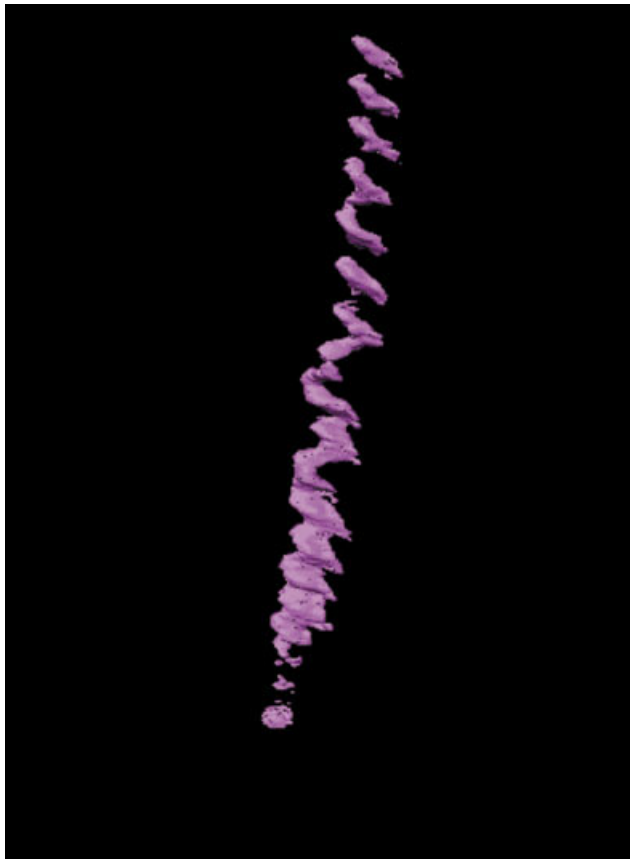

Fig. 4. 3D rendering of Eledone cirrhosa sperm head labelled with propidium iodide acquired using a 100× 1.4 N.A. oil immersion objective, after deconvolution. Field of view: 22.6 × 27.4 (μm). [Color figure can be viewed in the online issue, which is available at www.interscience.wiley.com]

have been measured with a range of volumes of 82 to 98 μm^3 (Bunyaratvej and Bunyaratvej, 1992).

Before deconvolution processing in each experiment, we obtained an overestimation of the volume due to blurring effects and presence of out-of-focus light; for fluorescent beads in oil immersion-medium, we calculated the radius of the specimen in the acquired image as 2.28 ± 0.66 μm^3 and after deconvolution as 1.99 ± 0.49 μm^3 and image restoration. This radius is almost the theoretical value of the radius in Table 1; for fluorescent beads in water immersion-medium, we obtained a poorer estimate of the bead radius before (2.348 ± 0.70 μm^3) and after (2.260 ± 0.58 μm^3) image restoration (Table 2).

In the case of erythrocytes (Fig. 2), after deconvolution we obtained a better estimate of cell volume (105 ± 5.0 μm^3) than the uncorrected volume from the acquired image (128.06 ± 6.34 μm^3) (Table 3). We also demonstrated how it is possible to study the structural differences in the organisation of helical structures (handedness, pitch, and radius) only after image restoration. From single 2D images (Fig. 3), it was not possible to find a section where sperm heads had clear handedness or any accessible geometrical parameters. Therefore, we show a 3D visualisation of the stacks of optical slices of the sperm heads in Figure 4.

DISCUSSION

In this report, it has been shown how confocal microscopy can be used as a powerful tool to analyse morphometrical parameters of biological samples, taking advantage of the optical sectioning capability of confocal fluorescence microscope. Knowledge of the 3D structure can be related to different functional states of the organism and pathology states (Kubínová, 1998).

After image deconvolution, both qualitative and quantitative image aspects have been substantially improved. Therefore, we suggest that analysis of specimens only take place after the deconvolution process. We have shown with a microspheres test that only with perfect match condition of refractive index between lens and sample could we recover the overall systematic error introduced by the system optics. When there is a refractive index mismatch, we had a good restoration of the image but we couldn't reach the bead volume and diameter theoretical values. This particular problem is due to non-linear distortion (Bertero and Boccacci, 1998; Castleman, 1996; Diaspro, 2002; van der Voort and Strasters, 1995) that we get with beads in water and that cannot be corrected in a simplified image formation model.

REFERENCES

Bertero M, Boccacci P. 1998. Introduction to inverse problems in imaging. Philadelphia: Institute of Physics Publishing.

Bunyaratvej A, Bunyaratvej P. 1992. Measurements of cell volume and hemoglobin concentration of erythrocytes from hereditary ovalocytosis and hereditary spherocytosis. J Med Assoc Thai 75(Suppl 1):248–252.

Castleman K. 1996. Digital image processing. Englewood Cliffs, NJ: Prentice Hall.

Diaspro A, editor. 2002. Confocal and two-photon microscopy: foundations, applications and advances. New York: Wiley-Liss.

Diaspro A, Annunziata S, Robello M. 2000. Single-pinhole confocal imaging of sub-resolution sparse objects using experimental point spread function and image restoration. Microsc Res Tech 51:464–468.

Diaspro A, Federici F, Robello M. 2002. Influence of refractive-index mismatch in high-resolution three-dimensional confocal microscopy. Appl Opt OT 41:685–690.

Hell SW, Stelzer EHK. 1995. Lens aberrations in confocal fluorescence microscopy. In: Handbook of biological confocal microscopy. Pawley JB, ed. Plenum Press, New York and London, pp. 347-353.

Hell S, Reiner G, Cremer C, Stelzer EHK. 1993. Aberrations in confocal fluorescence microscopy induced by mismatches in refractive index. J Microsc 16:391–405.

Kubínová L. 1998. Advantages of stereological methods in biomedicine. IEEE Eng Med Biol 17:110–115.

Kubínová L, Janáček J. 2001. Confocal microscopy and stereology: estimating volume, number, surface area and length by virtual test probes applied to three-dimensional images. Microsc Res Tech 53: 425–435.

Maxwell WL. 1974. Spermiogenesis of Eledone cirrhosa Lamarck (Cephalopoda, Octopoda). Proc R Soc Lond B186:181–190.

Pawley JB, editor. 1995. Handbook of biological confocal microscopy. New York: Plenum Press.

van der Voort HTM, Strasters KC. 1995. J Microsc 178:161.

Physiol. Res. 53 (*Suppl. 1*): S47-S55, 2004

Confocal Stereology and Image Analysis: Methods for Estimating Geometrical Characteristics of Cells and Tissues from Three-Dimensional Confocal Images

L. KUBÍNOVÁ, J. JANÁČEK, P. KAREN, B. RADOCHOVÁ, F. DIFATO, I. KREKULE

Department of Biomathematics, Institute of Physiology, Academy of Sciences of the Czech Republic, Prague, Czech Republic

Received December 15, 2003
Accepted March 1, 2004

Summary

A short review of confocal stereology and three-dimensional image analysis is presented, pointing out the achievements accomplished in this field by the Department of Biomathematics (Institute of Physiology, Prague). One of the methods of confocal stereology, the fakir method for surface area estimation, developed by this laboratory, is described. Methods for automatic measurement of geometrical characteristics of microscopical structures, based on 3-D image processing or surface triangulation, are discussed and compared with interactive stereological methods. Three-dimensional reconstruction programs and software implementation of stereological and digital methods as well as their practical applications are presented. The future trends are discussed.

Key words

Confocal microscopy • Image analysis • Stereology • Three-dimensional reconstructions

Introduction

The present paper reviews achievements accomplished by this laboratory in the field of confocal stereology and three-dimensional (3-D) image analysis of confocal data during several past years. We have focused on development and software implementation of methods for measuring geometrical parameters of structural components of organs, tissues, cells or cell compartments. Such measurements are the main prerequisite for quantitative analysis in a number of studies in biological research, especially when the relationships between function and structure are analyzed. Taking into account that the information on the spatial organization of microscopical structures is also very useful to get a complex idea about such relationships, we have also been engaged in studies of 3-D arrangement of microscopical structures by relevant measurements and 3-D reconstructions. We have found confocal microscopy to be an invaluable tool in 3-D analysis of microscopical structures.

Confocal microscopy

Confocal microscopy is a special type of optical microscopy that enables to obtain perfectly registered

stacks of thin serial optical sections (having thickness from approx. 350 nm) within thick specimens (Fig. 1a). Digital images of such stacks represent suitable data for quantitative measurements as well as for computer 3-D reconstructions that can be made without having to solve the tedious problem of alignment of images of successive sections (Pawley 1995). The principle of a confocal microscope was patented by Marvin Minsky in 1957, but confocal microscopy became a useful and efficient tool not earlier than almost 30 years later, after the confocal microscope with a laser light source was introduced (confocal laser scanning microscope, CLSM, Åslund *et al.* 1983). The first commercially available system was Bio-Rad MRC-500 in 1986.

Recently, two-photon microscopy representing a new type of laser scanning microscopy providing images of thin optical sections has emerged (Denk *et al.* 1990), which is reported to be able to focus even deeper into the thick specimen (up to several hundred micrometers, see Svoboda *et al.* 1997).

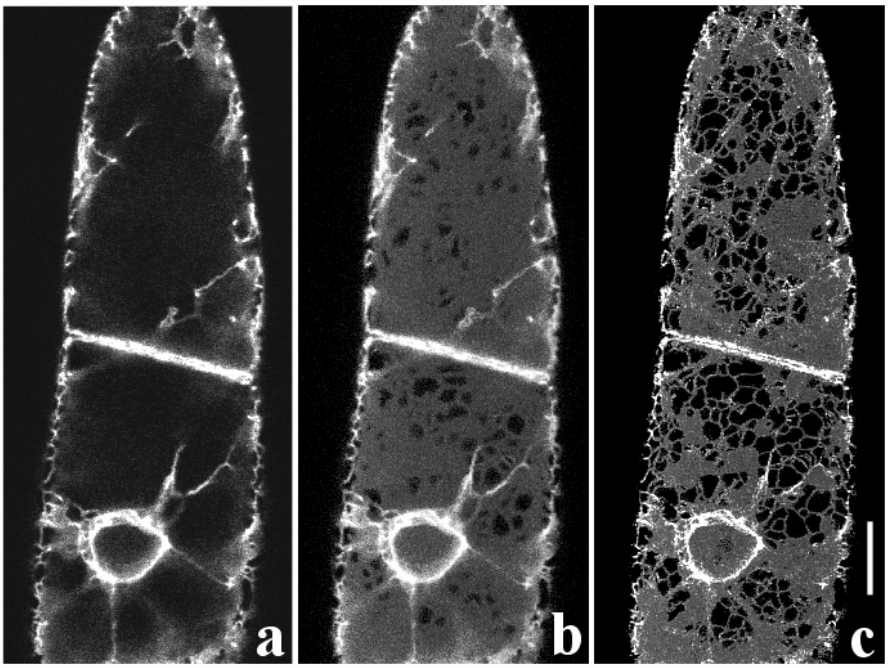

Fig. 1. Endoplasmic reticulum of *Nicotiana tabacum* BY-2 cell line transformed by a DNA construct with GFP sequence captured by a confocal microscope. a) A single confocal optical section. b) Maximum intensity projection of 42 confocal sections 0.2 µm apart. c) Maximum intensity projection of the same confocal series after applying a deconvolution algorithm. Scale = 10 µm.

Confocal stereology

Confocal stereology represents a contemporary approach to evaluation of structures by using the combination of stereological methods and confocal microscopy.

Stereological methods are precise tools for the quantitative evaluation of the structure of three-dimensional objects (Weibel 1979, Howard and Reed 1998). The term of stereology as a new scientific discipline was coined in 1961, motivated by the need of investigators in material and life sciences to establish a rigorous theoretical basis for the solution of problems encountered in morphometry. Stereological methods are based mainly on observations made on 2-D sections or 3-D subsamples of tissue, applying test probes of different dimensions, i.e. zero-dimensional (0-D, i.e. points), 1-D (i.e. lines) or 2-D (i.e. planes) and counting the interactions of the probes with the structures under study. For example, the number of test points falling into the given structure or number of intersection points of test lines with the structure surface is counted.

The first application of confocal microscopy for stereological measurements was presented by Howard *et al.* (1985) in their concept of unbiased sampling brick. They used a special type of a confocal microscope – tandem scanning reflected light microscope (Petráň *et al.* 1968) for counting osteocyte lacunae. Yet, though mentioned by several authors (Gundersen 1986, Rigaut 1989), the unique features of confocal microscopy advantageous for stereological measurements of not only number but also other parameters such as surface area, have not been fully recognized earlier than during the last decade (Rigaut *et al.* 1992, Howard and Sandau 1992). Here, especially the possibility of a confocal microscope to capture series of optical sections within a thick

specimen and thus providing 3-D image data is exploited. This laboratory was among the first to develop implementations of different stereological methods using confocal microscopy including the development of new methods (Kubínová *et al.* 1995, 1996, Kubínová and Janáček 1998). Confocal microscopy proved to be especially useful in application of methods based on spatial estimators evaluating small 3-D samples of structure under study (Howard and Sandau 1992, Kubínová and Janáček 1998, Kubínová *et al*. 1999, Kubínová and Janáček 2001, Kubínová *et al.* 2002). A 3-D sample of examined tissue can be analyzed if a rectangle within a field of view of a microscope is focused through. By using a special software, it is possible to generate different virtual test probes with arbitrary pre-defined (e.g. random) position and orientation within the stack of sections and apply them directly to this 3-D image data. Such approach is used in estimation of surface area by a fakir method developed by this laboratory (Kubínová and Janáček 1998) and in length estimation by global spatial sampling (Larsen *et al.* 1998) where special planar "slicer" probes are used (Kubínová and Janáček 2001, Kubínová *et al*. 2001). Another examples of spatial probes are the spatial point grid used for efficient volume estimation (Cruz-Orive 1997, Kubínová and Janáček 2001) and the optical disector (Gundersen 1986) or unbiased sampling brick (Howard *et al*. 1985) used for counting or sampling particles (e.g. cells). We will describe in more detail fakir method, developed by this laboratory, that can be used for surface area estimation if series of confocal sections within a thick physical slice are available. Unlike classical stereological methods applied to thin physical sections, this method does not require randomizing the orientation of the section, hence the slice can be cut in arbitrary direction.

Fakir method

The surface area of, e.g. cell, S(cell), can be estimated using fakir probes. The fakir probe (named by Cruz-Orive 1993) is a systematic probe consisting of parallel test lines (resembling nails of a fakir bed piercing the surface, see Fig. 2). When estimating, e.g. the cell surface area, the intersections between the cell surface and the fakir probe are counted. We can imagine the cell is pierced through by the nails of the fakir bed and we are counting how many times the nails went into or out of the cell. The cell surface area *S(cell)* can be estimated by the following formula:

$$estS(cell) = 2 \cdot u^2 \cdot I \qquad (1)$$

where u is the distance between neighboring parallel lines of the probe, I is the number of intersections between the fakir probe and the cell surface.

A high efficiency of the measurement can be achieved if we use a cubic spatial grid consisting of three mutually perpendicular fakir probes, halfway shifted with respect to each other (Fig. 2). In such case the average over the three fakir probes is considered in the surface area estimation:

$$estS(cell) = \frac{2}{3} \cdot u^2 \cdot (I_1 + I_2 + I_3) \qquad (2)$$

where u is the distance between neighboring parallel lines of the grid and I_j (j=1,2,3) is the number of intersections between the j-th fakir probe and the cell surface.

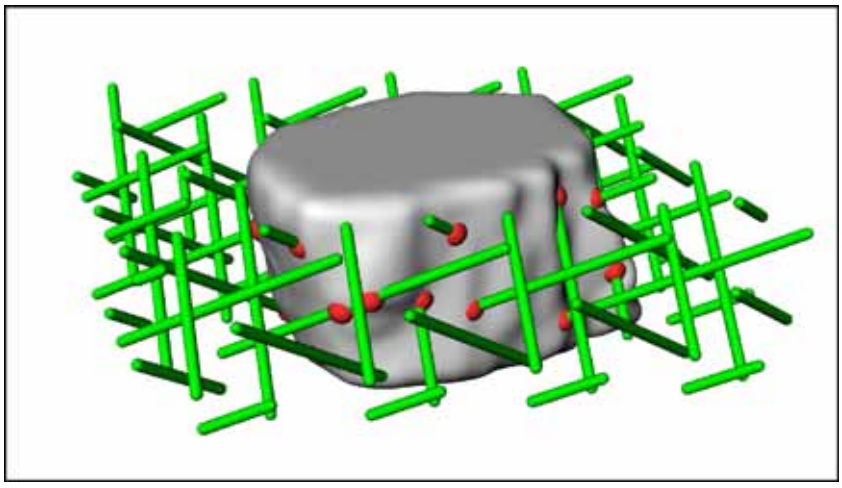

Fig. 2. A spatial grid consisting of three mutually perpendicular fakir probes, halfway shifted with respect to each other, applied to the measurement of the surface area of the side walls of a 3-D object (i.e. thick slice of a muscle fiber). The number of intersections (red) of the fakir probes (green) and object walls is proportional to the object surface area. For the sake of clarity, intersections are represented by "balls" and test lines by "pipes" here.

The measurement can be easily performed using our interactive FAKIR program (Kubínová and Janáček 2001; http://www.biomed.cas.cz/fgu/fakir/3dtools.htm for free download) or FAKIR module running in *Ellipse* (ViDiTo, Slovakia) environment. This software generates an isotropic set of virtual fakir probes and so it is not necessary to randomize the direction of the stack of sections.

Variance and efficiency of fakir method

In practical application of stereological methods, the question of efficiency is important, as it is always desirable to get sufficiently precise results with the least workload. Therefore, still more and more attention is being paid to the study of variances of stereological estimators. The variances of the estimators based on the Cavalieri principle, spatial grid of points and disector principle have been studied using Matheron's theory of regionalized variables (Matheron 1965) – see e.g. Gundersen and Jensen (1987), Cruz-Orive (1989, 1993, 1999), Kiêu *et al*. (1998) and Gundersen *et al*. (1999). For the estimators based on measuring intersections of the object with isotropic uniform random grids, such as the fakir method, their variance can be split into the component due to the grid orientation and to the residual component due to the grid position (Hahn and Sandau 1989). The first component depends on the mutual orientation of the fakir probes applied and on the shape of the object under study, namely the anisotropy of the surface, which can be expressed by the rose of directions of normals to the surface. The second, residual component of variance is dependent mainly on the grid density and arrangement, e.g. on the mutual shift of the fakir probes. The first component of variance is clearly the highest for totally anisotropic object, which rose of directions is represented by a single vector, i.e. for the flat surface in 3D. It can be proved that in this special, 'worst' case the coefficient of variance of surface area estimate by applying a single fakir probe is 57.74 % while by three orthogonal fakir probes (Fig. 2) it is only 10.16 % (Mattfeldt *et al.* 1985, Janáček 1999). For less anisotropic surfaces the first component of variance is decreasing, e.g. for the triple grid estimator of the surface area of ellipsoid with diameter ratios of 1:4:4 the coefficient of variance was calculated to be 4.90 % while for ellipsoid with diameter ratios of 1:1.6:1.6 it is already very close to zero (Hahn and Sandau 1989). The second, residual component of variance reflects the arrangement of the spatial grid applied. We have shown that the spatial grid consisting of three mutually perpendicular fakir probes, halfway shifted with respect to each other (Fig. 2), is much more efficient than non-shifted orthogonal triplet of fakir probes (Janáček 1999), requiring only about one half of the number of intersections for the same residual variance.

Methods based on 3-D image processing

Automatic measurements of geometrical characteristics of 3-D objects can be applied directly to their binary images obtained by automatic segmentation of the grayscale images captured by a confocal microscope. Automatic segmentation is a procedure of processing the source digital grayscale image (defined as a data structure of numerical values in the spatial grid of image elements called pixels in 2D or voxels in 3D) resulting in a binary image, in which the foreground elements belong to the objects under study (Serra 1982). The validity of the results of such automatic measurement, i.e. their unbiasedness and precision, depends on how precisely the model describes the object under study. Appropriate spatial resolution and high image quality are necessary for geometrical measurements. High quality contrast images enable segmentation by simply thresholding the image values while image inhomogeneities due to uneven staining or heterogeneous acquisition conditions require more advanced techniques of segmentation based on region and edge detection techniques. The images distorted by noise must be pre-processed by filtration. A 3-D image may contain more complete spatial information on the object under study, e.g. separate 2-D sections do not contain information on gradients in the axial direction (i.e. perpendicular to the image plane). Further, topological properties, such as the continuity of objects, cannot be judged from a single section. Finally, the 3-D image processing, using more spatial information, can be more effective and robust than the 2-D processing of individual slices. Basic algorithms of 3-D image processing can be derived from those used in 2-D image processing in a straightforward way (Meyer 1992).

We have developed several 3-D image analysis algorithms for software implementation of automatic methods for measuring geometrical characteristics of 3-D structures captured by a confocal microscope (Kubínová *et al*. 1999, 2002): voxel-counting method for volume estimation and digital Crofton methods for surface area and length estimation.

Methods based on surface triangulation

Triangulated surfaces are currently used to model 3-D objects in computer graphics. Such surfaces can be obtained from the 3-D grayscale digital images by isosurface detection using the marching cube algorithm (Lorensen and Cline 1987) or by detecting the object contours in subsequent horizontal slices first and then connecting the contours by triangulated stripes (Oliva *et al*. 1996). The contours can be detected interactively or by (semi-) automatic tracking of the object boundaries in the slices (Baba 1991). Geometrical characteristics of the models delimited by the triangulated surfaces can be used as estimates of the characteristics of the objects under study (Guilak 1994). We have implemented methods based on surface triangulation for measuring volume, surface area, and length (Kubínová *et al.* 2002).

Three-dimensional reconstructions

The stacks of confocal images can have only a limited size, which means that confocal microscopy can be used in a straightforward manner to reconstruct only small structures like single cells or small pieces of tissue. It is often desirable to reconstruct larger tissue volumes with sufficient detail, so that the structure arrangement and organization can be revealed, e.g. arrangement of capillaries in different organs or tumors. From this reason we have developed a special GLUEMRC and LINKMRC software for composing stacks of confocal images (neighboring in lateral or axial direction) together into one large stack using algorithms for alignment of 3-D images (Karen *et al*. 2003, for free download contact karen@biomed.cas.cz). The surface renderings of microscopical structure under study can then be made. For this purpose, the structure contours in individual optical sections are obtained by image segmentation algorithms or, if the automatic segmentation is not feasible, the contours are outlined manually. Finally, the structure surface is rendered, after applying image processing algorithms like smoothing by 3-D Gaussian filtration. For example, see our 3-D reconstruction of human placental villi with their capillary bed in Figure 3.

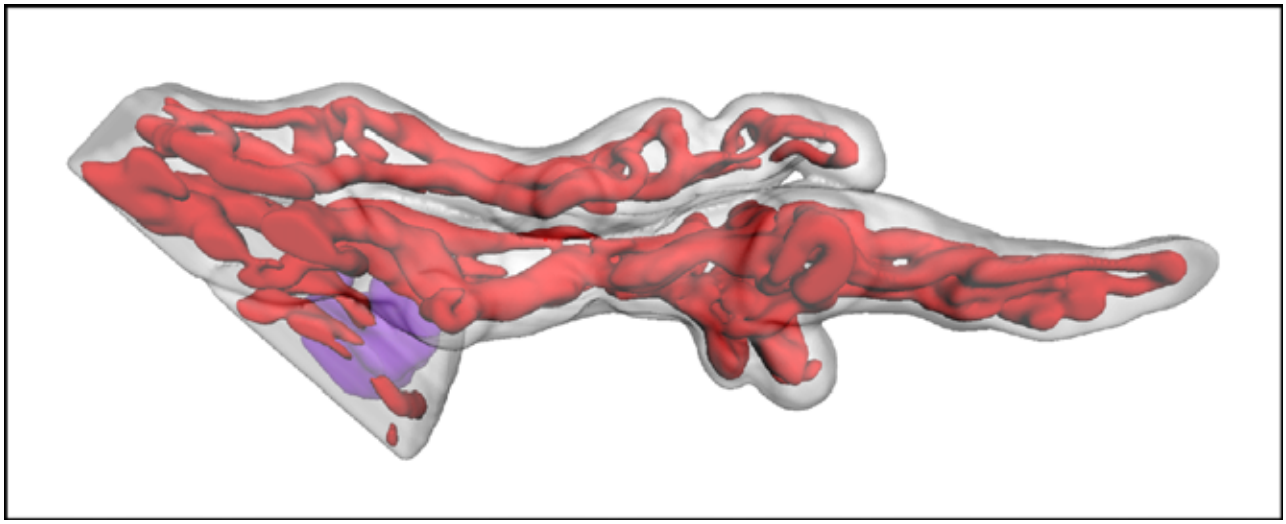

Fig. 3. 3-D reconstruction of human placental villi and their capillary bed. The confocal stack used for reconstruction had dimensions of 325x300x74 μm^3.

Software implementation of methods

The first programs for implementation of above methods that were developed by this laboratory were independent programs written in TurboPascal 6 for IBM PC under the MS DOS operating system (some of them still available as a freeware via the Internet at http://www.biomed.cas.cz/fgu/fakir/3dtools.htm). Other, mainly 3-D image processing algorithms, automatic methods and 3-D reconstructions, have been implemented as special modules of originally IRIS Explorer (SGI, USA, UNIX operating system, later NAG, UK, Windows NT operating system) visualization environment (for free download of our modules contact janacek@biomed.cas.cz). Following the further hardware and software development we have gradually turned to

building a system of mutually compatible modules, written in C++, running under *Ellipse* (ViDiTo, Slovakia) software image analysis environment. So far, a number of such modules have been developed, e.g. for implementation of fakir, slicer (global spatial sampling), disector, spatial point grid methods, contour delineation, and surface rendering algorithms for 3-D reconstructions.

Comparison of methods

We have compared many of the above mentioned stereological and image analysis techniques from the point of view of their applicability, efficiency and precision (Kubínová *et al.* 1999, 2002). It should be stressed that there is no absolutely universal method which would be optimal for all types of structure. In general, the automatic methods are faster than interactive stereological methods but require automatic segmentation of analyzed objects from the images or at least a high contrast between the object and the background. They also require careful testing and adjusting to the given type of microscopic structures. For surface area estimation, the fakir method appears to be the most universal of all tested methods and so it might be recommended for testing the applicability of other, less time-consuming methods. The method using spatial grid of points is very good for interactive volume estimation. If the object segmentation is feasible, the voxel-counting method is suitable for the volume measurement. Methods for volume estimation usually give precise results and they are not sensitive to voxel size and degree of smoothing. The triangulation method applied to grayscale images appears to be suitable for measuring the volume and surface area of isotropic as well as anisotropic objects, provided a high contrast between the object and the background is achieved. Digital methods for surface area estimation, especially triangulation method are more sensitive to image processing. Therefore, it is necessary to be cautious with noisy images, taking into account that noise increases the surface area measured. It can be reduced by smoothing, but a suitable degree of smoothing should be found and carefully tested.

Application of methods

The methods of confocal stereology and 3-D image analysis can be applied for evaluation of a large variety of structural components of organs, tissues, cells or cell compartments. This laboratory contributed to successful application of such methods in different fields of biological research, e.g. embryology and histology. The number of capillary connections in terminal villi of human diabetic placenta was proved to be higher than in normal placenta (Jirkovská *et al.* 1998, 2002). The length of capillaries going along fibers of a rat muscle per fiber length was found to be larger in soleus muscle than in extensor digitorum longus muscle while the capillary length per fiber surface area was not different in both muscle types (Kubínová *et al.* 2001). The number of satellite cells per fiber length and per the number of all myonuclei was lower in old human vastus lateralis muscles than in the young ones (Sajko *et al.* 2002, 2004). Other applications of our methods comprise diverse scientific fields, such as plant anatomy (Albrechtová *et al*. 2001) or radiobiology (Kubínová *et al.* 2003).

Practical considerations

Whether interactive stereological or automatic image analysis techniques are applied, it is always necessary to follow proper sampling, i.e. the fields of view chosen for evaluation must be selected in a representative, unbiased manner. Usually, systematic sampling is a good and efficient way to select the sections and sampling frames for analysis (Gundersen and Jensen 1987). It is also necessary to define precisely conditions and aims of the study. The above methods as any other technique lead to reliable results only if the reference space and structures under study can be unambiguously identified. Further, it is necessary to take into account possible bias due to technical processing of the tissues under study, especially deformation caused by the tissue shrinkage during fixation, embedding and cutting of material (Dorph-Petersen *et al.* 2001). Such deformations should be minimized by developing suitable processing techniques. The possible deformations should be measured and controlled in different steps of technical processing. This requires to calibrate the microtome or vibratome used for cutting the tissue and to measure lateral and axial deformations – a confocal microscope enabling to measure axial and lateral distances in different steps of tissue processing can be a very useful tool for such evaluation.

Confocal microscopy, like any other technique, has some drawbacks. Sometimes it can be difficult to find a suitable fluorescence staining of structures to be examined. It should be noted that in histological specimens a non-specific staining like eosin can often be

used (Jirkovská *et al*. 1998) while the cell surface can be visualized by immunofluorescence techniques when antibodies are bound to integral membrane proteins of cellular plasma membranes and labeled by a common fluorescent dye. Another drawback consists in the axial resolution (though higher than in a conventional optical microscope) being lower than the lateral resolution. The shape of the point spread function of a confocal microscope is elongated in the direction of z-axis (Shaw 1994) which causes defocusing that can possibly result in an overestimation of the surface area and volume of the examined objects. This can be eliminated by applying special deconvolution algorithms to perform 3-D deblurring of the images before the measurements (Fig. 1). In two-photon excitation fluorescence microscopy, the axial resolution is higher than in confocal microscopy (Denk *et al.* 1990, Nakamura 1999, Diaspro 2002) and it is also possible to penetrate more deeply into the specimen with decreased bleaching of fluorescence dyes. However, possible deblurring of 3-D images should be considered even here. Aberrations, especially the axial displacement due to the unmatched refractive indices (Sheppard and Török 1997), should also be taken into account in the measurements of microscopical structures.

Glimpse into the future

It was demonstrated how useful confocal microscopy in connection with stereology and 3-D image analysis can be for estimating different geometrical parameters of microscopical structure and for its three-dimensional visualization. In comparison with a conventional optical microscopy, confocal and especially two-photon microscopy offers not only higher resolution and examination of thicker specimens but also a better possibility to analyze living, fresh or more easily prepared specimens.

In the years to come, further development of confocal stereology and its applications can be anticipated with the spreading of usage of confocal microscopy and the ever increasing demands for objective measurements of different types of biological structures. This laboratory will follow this trend exploiting confocal and two-photon microscopy available. One of our topics will be the development of methods of spatial statistics for measuring second-order properties of biological structures, analyzed by a confocal microscope, characterizing their arrangement and mutual relationships. We have already developed and implemented methods of spatial statistics for evaluation of clustering of one type of marker or colocalization of two types of markers in electron micrographs of immunostained ultrastructures of the cell nucleus (Philimonenko *et al.* 2000). Another direction in the evaluation of 3-D structure arrangement is the study of its orientation and texture, e.g. of fibrous structures like capillaries, microtubules or endoplasmic reticulum (Fig. 1). Here, stereological as well as image analysis methods can be useful. In our opinion, the future development in quantitative evaluation and 3-D visualization of structures will proceed in the direction of combination of stereological and digital, image analysis based methods, applying both interactive and automatic methods. This laboratory, being engaged in all types of these techniques, is prepared to search for efficient combination of techniques leading to a complex evaluation of the 3-D microscopical structures under study.

Acknowledgements

We wish to thank Dr. K. Schwarzerová (Department of Plant Physiology, Faculty of Science, Charles University, Prague) for preparing the specimen of tobacco cells shown in Figure 1 and Dr. M. Jirkovská (Institute of Histology and Embryology, First Medical Faculty, Charles University, Prague) for providing us with placenta specimen shown in Figure 3.

The study was supported by the Grant Agency of the Czech Republic (Grants 304/01/0257, 310/02/1410), by the Academy of Sciences of the Czech Republic (Grants KJB6011309, KJB6039302 and Grant AVOZ 5011922), by the Ministry of Science and Technology of Slovenia and the Ministry of Education, Youth and Sports of the Czech Republic (KONTAKT grant No. 001/2001).

References

ALBRECHTOVÁ J, JANÁČEK J, TOMORI Z, KUBÍNOVÁ L: Unbiased estimation of anatomical characteristics of Norway spruce needle from thick transverse sections using confocal microscopy. *Abstracts of the 8th European Congress for Stereology and Image Analysis,* Bordeaux, 2001, pp 140-141.

ÅSLUND N, CARLSSON K, LILJEBORG A, MAJLOF L: PHOIBOS, a microscope scanner designed for micro-fluorometric applications, using laser induced fluorescence. *Proceedings of the Third Scandinavian Conference on Image Analysis, Studentliteratur,* Lund, 1983, p 338.

BABA N: Computer aided three-dimensional reconstruction from serial section images. In: *Image Analysis in Biology*. HÄDER DP (ed), CRC Press, Boca Raton, Ann Arbor, London, 1991, pp 251-270.

CRUZ-ORIVE, LM: On the precision of systematic sampling: a review of Matheron's transitive methods. *J Microsc* **153**: 315-333, 1989.

CRUZ-ORIVE LM: Systematic sampling in stereology. *Bull Int Statistic Inst* **55**: 451-468, 1993.

CRUZ-ORIVE LM: Stereology of single objects. *J Microsc* **186**: 93-107, 1997.

CRUZ-ORIVE LM: Precision of Cavalieri sections and slices with local errors. *J Microsc* **193**: 182-198, 1999.

DENK W, STRICKLER JH, WEBB WW: Two-photon laser scanning fluorescence microscopy. *Science* **248**: 73-76, 1990.

DIASPRO A (ed): *Confocal and Two-photon Microscopy*, Wiley-Liss, New York, 2002.

DORPH-PETERSEN KA, NYENGAARD JR, GUNDERSEN HJG: Tissue shrinkage and unbiased stereological estimation of particle number and size. *J Microsc* **204**: 232-246, 2001.

GUILAK F: Volume and surface area measurement of viable chondrocytes in situ using geometric modelling of serial confocal sections. *J Microsc* **173**: 245-256, 1994.

GUNDERSEN HJG: Stereology of arbitrary particles. A review of unbiased number and size estimators and the presentation of some new ones, in memory of William R. Thompson. *J Microsc* **143**: 3-45, 1986.

GUNDERSEN HJG, JENSEN EB: The efficiency of systematic sampling in stereology and its prediction. *J Microsc* **147**: 229-263, 1987.

GUNDERSEN HJG, JENSEN EBV, KIÊU K, NIELSEN J: The efficiency of systematic sampling in stereology – reconsidered. *J Microsc* **193**: 199-211, 1999.

HAHN U, SANDAU K: Precision of surface area estimation using spatial grids. *Acta Stereol* **8**: 425-430, 1989.

HOWARD CV, REED MG: *Unbiased Stereology: Three-Dimensional Measurement in Microscopy. Microscopy Handbooks. Vol. 41*, Springer-Verlag, New York, 1998.

HOWARD CV, SANDAU K: Measuring the surface area of a cell by the method of the spatial grid with a CSLM – a demonstration. *J Microsc* **165**: 183-188, 1992.

HOWARD CV, REID S, BADDELEY A, BOYDE A: Unbiased estimation of particle density in the tandem scanning reflected light microscope. *J Microsc* **138**: 203-212, 1985.

JANÁČEK J: Errors of spatial grids estimators of volume and surface area. *Acta Stereol* **18**: 389-396, 1999.

JIRKOVSKÁ M, KUBÍNOVÁ L, KREKULE I, HACH P: Spatial arrangement of fetal placental capillaries in terminal villi: a study using confocal microscopy. *Anat Embryol* **197**: 263-272, 1998.

JIRKOVSKÁ M, KUBÍNOVÁ L, JANÁČEK J, MORAVCOVÁ M, KREJČÍ V, KAREN P: Topological properties and spatial organization of villous capillaries in normal and diabetic placentas. *J Vasc Res* **39**: 268-278, 2002.

KAREN P, JIRKOVSKÁ M, TOMORI Z, DEMJÉNOVÁ E, JANÁČEK J, KUBÍNOVÁ L: Three-dimensional computer reconstruction of large tissue volumes based on composing series of high-resolution confocal images by GlueMRC and LinkMRC software. *Microsc Res Tech* **62**: 415-422, 2003.

KIÊU K, XIONG W, TRUBUIL A: Precision of systematic counts. *Rapport Technique 1998-1, Unité de Biométrie, INRA-Versailles*, 1998.

KUBÍNOVÁ L, JANÁČEK J: Estimating surface area by the isotropic fakir method from thick slices cut in an arbitrary direction. *J Microsc* **191**: 201-211, 1998.

KUBÍNOVÁ L, JANÁČEK J: Confocal microscopy and stereology: Estimating volume, number, surface area and length by virtual test probes applied to three-dimensional images. *Microsc Res Tech* **53**: 425-435, 2001.

KUBÍNOVÁ L, KAREN P, INDRA M, JIRKOVSKÁ M, PALOVSKÝ R, KREKULE I: The role of stereology, confocal microscopy and 3-D reconstructions in morphometrical analysis of 3-D biological structures. *Biomed Tech* **40**: 196-197, 1995.

KUBÍNOVÁ L, JIRKOVSKÁ M, HACH P: Stereology and confocal microscopy: Application to the study of placental terminal villus. *Acta Stereol* **15**: 153-158, 1996.

KUBÍNOVÁ L, JANÁČEK J, GUILAK F, OPATRNÝ Z: Comparison of several digital and stereological methods for estimating surface area and volume of cells studied by confocal microscopy. *Cytometry* **36**: 85-95, 1999.

KUBÍNOVÁ L, JANÁČEK J, RIBARIČ S, ČEBAŠEK V, ERŽEN I: Three-dimensional study of the capillary supply of skeletal muscle fibers using confocal microscopy. *J Musc Res Cell Motil* **22**: 217-227, 2001.

KUBÍNOVÁ L, JANÁČEK J, KREKULE I: Stereological methods for estimating geometrical parameters of microscopical structure studied by three-dimensional microscopical techniques. In: *Confocal and Two-photon Microscopy*. DIASPRO A (ed), Wiley-Liss, New York, 2002, pp 299-332.

KUBÍNOVÁ L, MAO XW, JANÁČEK J, ARCHAMBEAU JO: Stereology techniques in radiation biology. *Radiat Res* **160**: 110-119, 2003.

LARSEN JO, GUNDERSEN HJG, NIELSEN J: Global spatial sampling with isotropic virtual planes: estimators of length density and total length in thick, arbitrarily orientated sections. *J Microsc* **191**: 238-248, 1998.

LORENSEN WE, CLINE HE: Marching cubes: a high resolution 3D surface construction algorithm. *Comp Graph* **21**:163-169, 1987.

MATHERON G: *Les Variables Régionalisées et leur Estimation*, Masson, Paris, 1965.

MATTFELDT T, MÖBIUS HJ, MALL G: Orthogonal triplet probes; an efficient method for unbiased estimation of length and surface of objects with unknown orientation in space. *J Microsc* **139**: 279-289, 1985.

MEYER F: Mathematical morphology: from two dimensions to three dimensions. *J Microsc* **165**: 5-28, 1992.

NAKAMURA O: Fundamental of two-photon microscopy. *Microsc Res Tech* **47**: 165-171, 1999.

OLIVA JM, PERRIN M, COQUILLART S: 3D reconstruction of complex polyhedral shapes from contours using a simplified generalized Voronoi diagram. In: *Eurographics 96*. ROSSIGNAC J, SILLION F (eds), Blackwell Publishers, 1996, pp 397-408.

PAWLEY J (ed): *Handbook of Biological Confocal Microscopy*. Plenum Press, New York, 1995.

PETRÁŇ M, HADRAVSKÝ M, EGGER D, GALAMBOS R: Tandem-scanning reflected-light microscope. *J Opt Soc Am* **58**: 661-664, 1968.

PHILIMONENKO AA, JANÁČEK J, HOZÁK P: Statistical evaluation of colocalization patterns in immunogold labeling experiments. *J Struct Biol* **132**: 201-210, 2000.

RIGAUT JP: Image analysis in histology – hope, disillusion, and hope again. *Acta Stereol* **8**: 3-12, 1989.

RIGAUT JP, CARVAJAL-GONZALES S, VASSY J: 3-D image cytometry. In: *Visualization in Biomedical Microscopies*. KRIETE A (ed), VCH, Weinheim, New York, 1992.

SAJKO Š, KUBÍNOVÁ L, KREFT M, DAHMANE R, WERNIG A, ERŽEN I: Improving methodological strategies for satellite cells counting in human muscle during aging. *Image Anal Stereol* **21**: 7-12, 2002.

SAJKO Š, KUBÍNOVÁ L, CVETKO E, KREFT M, WERNIG A, ERŽEN I: Frequency of M-cadherin stained satellite cells declines in human muscles during aging. *J Cytochem Histochem* **52**: 179-185, 2004.

SERRA J: *Image Analysis and Mathematical Morphology*. Academic Press, London, 1982.

SHAW P: Deconvolution in 3-D optical microscopy. *Histochem J* **26**: 687-94, 1994.

SHEPPARD CJR, TÖRÖK P: Effects of specimen refractive index on confocal imaging. *J Microsc* **185**: 366-374, 1997.

SVOBODA K, DENK W, KLEINFELD D, TANK DW: In vivo dendritic calcium dynamics in neocortical pyramidal neurons. *Nature* **385**: 161-165, 1997.

WEIBEL ER: *Stereological Methods, Vol. 1: Practical Methods for Biological Morphometry*, Academic Press, London, 1979.

Reprint requests

Dr. Lucie Kubínová, Department of Biomathematics, Institute of Physiology, Academy of Sciences of the Czech Republic, Vídeňská 1083, 14220 Prague, Czech Republic, E-mail: kubinova@biomed.cas.cz

2.2 Tissue imaging in mouse experimental melanoma.

1. **Imaging of mouse experimental melanoma in vivo and ex vivo by combination of confocal and nonlinear microscopy.** O. Chernyavskiy, L. Vannucci, P. Bianchini, **F. Difato**, M. Sajeh and L. Kubínová (Submitted to Microsc Res Tech)

2.2.1. Aims and results

Aims:

- To investigate possibilities of combination of one and two photon microscopy for examination of the experimental melanoma tissue in vivo
- To monitor tumor tissues, and their modifications after hyperthermia treatment

Results:

- We exploited potential of combination of the one- and two- photon microscopy techniques in the evaluation of morphology of cancer tissue
- Our approach proved to be suitable for documenting changes in tumor structure due to the effect of microwave hyperthermia treatment.

2.2.2. Discussion

Dimensions of a cell in culture (e.g. a fibroblast growing on a coverslip) are in the order of tens of microns in the plane of the dish, which can be well resolved through the optical resolution of about 200 nm. In the optical axis of the microscope, the cell reaches dimension of tens of microns near the nucleus to tens nanometers in cell periphery, near the plasma membrane. The optical resolution in this axis is about 500 nm and therefore it is not always sufficient to observe the biological process of interest.
The optical resolution of a confocal microscope is sufficient in the case of tissue imaging. The capability to acquire images of thin optical sections from different depths to reconstruct the three dimensional architecture of the tissue is achieved at a resolution that permits visualization of sub-cellular details. Thus, non-invasive *in vivo* imaging of the upper layers of different organs, such as cornea or skin could be applied.
The major problem of tissue imaging by confocal microscopy appeared to be how to mark different cells or compartments or proteins in the overall specimen. This was resolved thanks to discovery of fluorescent proteins that could be fused with specific proteins in the complete organism. This does not represent a solution in the clinical use perspectives of confocal microscopy. The low invasivity of optical systems can be an important tool for medicine. Therefore, there is a growing interest to find appropriate techniques to visualize structures and properties of living tissues.
We applied various imaging modes that brought different and often complementary information on histology of tissues studied. We applied confocal reflectance microscopy in combination with second harmonic generation (SHG) and two-photon autofluorescence imaging for the examination of experimental melanoma tissues *in vivo*, in mice under general anesthesia, and *ex vivo* on freshly harvested specimens. We were able to study the collagen fiber network in relation to different tissues, and to identify invasive tumor cells.
The 1PE reflectance mode proved to be well applicable to unstained fresh tissues, allowing clear visualization of different layers both in the control skin flap and in the melanoma capsule. In 1PE reflectance imaging, we checked all available excitation wavelengths, finding out that, due to the difference in their scattering behavior, they yielded different images, revealing various details in the examined tissues.
The SHG imaging microscopy proved to be suitable for detecting collagen fibers without any staining, considering the high specificity of SHG imaging microscopy for detection of fibrillar collagen.
Further information was gained by simultaneous detection of the 2PE autofluorescence. The 2PE autofluorescence was especially useful in detecting melanoma cells with a high content of melanin granules, not always clearly visualized by the reflectance imaging. This enabled their identification

in the fibrous network of the inner layers of the melanoma capsule, which would be important for possible clinical application in detecting melanoma invading front. The autoflourescence signal could also be acquired by one photon excitation. However, in our experiment, there was lower deep penetration in the tissue due to higher scattering of the visible light. Therefore, we had to use higher average power to reach the same contrast, at expense of higher invasivity. Furthermore, by two- photon excitation, it is possible to excite different fluorochromes with only one laser with no need of assumption in the tissue content.
Our approach proved to be suitable for describing the tumor structure and documenting changes due to the effect of microwave hyperthermia treatment, such as modification of the collagen fiber network. This approach represents further documentation of possible exploitation of confocal microscopy in diagnosis and prevention protocols in medicine.

2.2.3. Publications

Imaging of mouse experimental melanoma in vivo and *ex vivo* by combination of confocal and nonlinear microscopy

Oleksandr Chernyavskiy,[1] Luca Vannucci,[2] Paolo Bianchini,[1,3] Francesco Difato,[1,4] Mustafa Sajeh,[2] and Lucie Kubínová[1,*]

[1] *Department of Biomathematics, Institute of Physiology, Academy of Sciences of the Czech Republic, v.v.i., Vídeňská 1083, 14220 Prague 4, Czech Republic* [2] *Department of Immunology, Institute of Microbiology, Academy of Sciences of the Czech Republic, v.v.i., Vídeňská 1083, 14220 Prague 4, Czech Republic*

[3] *LAMBS, Department of Physics, University of Genoa, Via Dodecaneso 33, 16146 Genoa, Italy* [4] *Department of Neuroscience and Brain Technologies, The Italian Institute of Technology, Via Morego 30, 16163 Genoa, Italy*

[*] *Corresponding author: kubinova@biomed.cas.cz*

Abstract: We investigated possibilities of confocal reflectance and fluorescence microscopy in combination with SHG and two-photon autofluorescence imaging for the examination of experimental melanoma tissues *in vivo,* in mice under general anesthesia, and *ex vivo* on freshly harvested specimens. Our approach facilitated the examination of interrelationships between functional and morphological aspects based on optical properties of the tissues. It proved to be suitable for describing the tumor structure and documenting changes due to the effect of microwave hyperthermia treatment, such as modification of the collagen fiber network together with the other tissues. The results showed that the proposed approach could be suitable for a direct evaluation of clinical interventions.

OCIS codes: (170.3880) Medical and biological imaging; (190.4160) Multiharmonic generation; (170.1790) Confocal microscopy; (190.4180) Multiphoton processes

References and links

1. B. R. Masters and A. A. Thaer, "Real-time scanning slit confocal microscopy of the *in vivo* human cornea," Appl. Opt. **33**, 695-701 (1994).
2. M. Rajadhyaksha, M. Grossman, D. Esterowitz, R. H. Webb, and R. R. Anderson: "*In vivo* confocal scanning laser microscopy of human skin: Melanin provides strong contrast," J. Invest. Dermatol. **104**, 946-952 (1995).
3. K. Kőnig, "Multiphoton microscopy in life sciences," J. Microsc. **200**, 83-104 (2000).
4. M. J. Koehler, K. König, P. Elsner, R. Bückle, and M. Kaatz, "*In vivo* assessment of human skin aging by multiphoton laser scanning tomography," Opt. Lett. **31**, 2879-2881 (2006).
5. M. Rajadhyaksha, S. González, J. M. Zavislan, R. R. Anderson, and R. H. Webb: "*In vivo* confocal scanning laser microscopy of human skin II: Advances in instrumentation and comparison with histology," J. Invest. Dermatol. **113**, 293-303 (1999).
6. K. J. Busam, C. Charles, G. Lee, and A. C. Halpern, "Morphologic features of melanocytes, pigmented keratinocytes, and melanophages by *in vivo* confocal scanning laser microscopy," Mod. Pathol. **14**, 862-868 (2001).
7. M. Huzaira, F. Rius, M. Rajadhyaksha, R. R. Anderson, and S. González, "Topographic variations in normal skin, as viewed by *in vivo* reflectance confocal microscopy," J. Invest. Dermatol. **116**, 846-852 (2001).
8. G. Pellacani, A. M. Cesinaro, C. Longo, C. Grana, and S. Seidenari, "Microscopic *in vivo* description of cellular architecture of dermoscopic pigment network in nevi and melanomas," Arch. Dermatol. **141**, 147-54 (2005).
9. A. L. Branzan, M. Landthaler, and R. M. Szeimies, "*In vivo* confocal scanning laser microscopy in dermatology," Lasers Med. Sci. **22**, 73-82 (2007).

10. Y. Li, S. Gonzalez, T. H. Terwey, J. Wolchok, Y. Li, I. Aranda, R. Toledo-Crow, and A. C. Halpern, "Dual mode reflectance and fluorescence confocal laser scanning microscopy for *in vivo* imaging melanoma progression in murine skin," J. Invest. Dermatol. **125**, 798 –804 (2005).
11. P. Anikijenko, L. T. Vo, E. R. Murr, J. Carrasco, W. J. McLaren, Q. Chen, S. G. Thomas, P. M. Delaney, and R. G. King, "*In vivo* detection of small subsurface melanomas in athymic mice using noninvasive fiber optic confocal imaging," J. Invest. Dermatol. **117**, 1442-1448 (2001).
12. C. Suihko, L. D. Swindle, S. G. Thomas, and J. Serup, "Fluorescence fibre-optic confocal microscopy of skin *in vivo*: microscope and fluorophores," Skin Res. Technol. **11**, 254–267 (2005).
13. W. Denk, J. H. Strickler, and W. W. Webb, "Two-photon laser scanning fluorescence microscopy," Science **248**, 73-76 (1990).
14. A. Diaspro (ed), *Confocal and two-photon microscopy : foundations, applications, and advances* (Wiley-Liss, New York, 2002).
15. A. Diaspro, G. Chirico, and M. Collini, "Two-photon fluorescence excitation and related techniques in biological microscopy," Q. Rev. Biophys. **38**, 97-166 (2005).
16. J. M. Vroom, K. J. D. Grauw, H. C. Gerritsen, D. J. Bradshaw, P. D. Marsh, G. K. Watson, J. J. Birmingham, and C. Allison, "Depth penetration and detection of pH gradients in biofilms by two-photon excitation microscopy," Appl. Environ. Microbiol. **65**, 3502-3511 (1999).
17. P. So, H. Kim, and I. Kochevar, "Two-Photon deep tissue *ex vivo* imaging of mouse dermal and subcutaneous structures," Opt. Express **3**, 339-350 (1998).
18. K. Schenke-Layland, I. Riemann, O. Damour, U. A. Stock, and K. König, "Two-photon microscopes and *in vivo* multiphoton tomographs — Powerful diagnostic tools for tissue engineering and drug delivery," Adv. Drug Deliv. Rev. **58**, 878–896 (2006).
19. C. Sheppard, J. Gannaway, R. Kompfner, and D. Walsh, "The scanning harmonic optical microscope," IEEE J. Quant. El. **13**, 912-912 (1977).
20. P. J. Campagnola, A. C. Millard, M. Terasaki, P. E. Hoppe, C. J. Malone and W. A. Mohler, "Three-dimensional high-resolution second-harmonic generation imaging of endogenous structural proteins in biological tissues," Biophys. J. **82**, 493-508 (2002).
21. A. Zoumi, A. Yeh and B. J. Tromberg, "Imaging cells and extracellular matrix *in vivo* by using second harmonic generation and two-photon excited fluorescence," Proc. Natl. Acad. Sci. USA **99**, 11014-11019 (2002).
22. R. M. Williams, W. R. Zipfel and W. W. Webb, "Interpreting second-harmonic generation images of collagen fibrils," Biophys. J. **88**, 1377-1386 (2005).
23. Erikson A, Örtegren J, Hompland T, **de** Lange Davies C, Lindgren M: "Quantification of the second-order nonlinear susceptibility of collagen I using a laser scanning microscope. Journal of Biomedical Optics 12(04), 044002 , 2007.
24. J. Chen, S. Zhuo, T. Luo, X. Jiang, and J. Zhao, "Spectral characteristics of autofluorescence and second harmonic generation from *ex vivo* human skin induced by femtosecond laser and visible lasers," Scanning **28**, 319-326 (2006).
25. A. Zoumi, X. Lu, G. S. Kassab, and B. J. Tromberg, "Imaging coronary artery microstructure using second-harmonic and two-photon fluorescence microscopy," Biophys. J. **87,** 2778-2786, (2004).
26. E. Brown, T. McKee, E. diTomaso, A. Pluen, B. Seed, Y. Boucher, and R. K. Jain, "Dynamic imaging of collagen and its modulation in tumors *in vivo* using second-harmonic generation," Nat. Med. **9**, 796-800 (2003).
27. P. P. Provenzano, K. W. Eliceiri, J. M. Campbell, D. R. Inman, J. G. White, and P.J. Keely, "Collagen reorganization at the tumor-stromal interface facilitates local invasion," BMC Med. **4**, 38 (2006). http://www.biomedcentral.com/1741-7015/4/38
28. E. C. Rothstein, M. Nauman, S. Chesnick, and R. S. Balaban, "Multi-photon excitation microscopy in intact animals," J. Microsc. **222**, 58-64 (2006).
29. A.-M. Pena, A. Fabre, D. Débarre, J. Marchal-Somme, B. Crestani, J.-L. Martin, E. Beaurepaire and M.-C. Schanne-Klein, "Three-dimensional investigation and scoring of extracellular matrix remodeling during lung fibrosis using multiphoton microscopy," Microsc. Res. Tech. **70**,162-170 (2007).
30. M. Strupler, A.-M. Pena, M. Hernest, P.-L. Tharaux, J.-L. Martin, E. Beaurepaire, and M.-C. Schanne-Klein, "Second harmonic imaging and scoring of collagen in fibrotic tissues, " Opt. Express **15**, 4054-4065 (2007).
31. W.-L. Chen, Y. Sun, W. Lo, H.-Y. Tan, and C.-Y. Dong, "Combination of multiphoton and reflective confocal imaging of cornea," Microsc. Res. Tech. **71**, 83-85 (2008).
32. P. Wust, B. Hildebrandt, G. Sreenivasa, B. Rau, J. Gellermann, H. Riess, R. Felix, and P. M. Schlag, "Hyperthermia in combined treatment of cancer," Lancet Oncol. **3**, 487-497 (2002).
33. S. Zhuo, J. Chen, T. Luo, and D. Zou, "Multimode nonlinear optical imaging of the dermis in *ex vivo* human skin based on the combination of multichannel mode and Lambda mode," Opt. Express **14**, 7810-7820 (2006).
34. D. R. Larson, W. R. Zipfel, R. M. Williams, S. W. Clark, M. P. Bruchez, F. W. Wise, and W. W. Web, "Water-soluble quantum dots for multiphoton fluorescence imaging *in vivo*," Science **300**, 1434-1436 (2003).

35. M. J. C. Hendrix, R. E. B. Seftor, E. A. Seftor, L. M. Gruman, L. M. L. Lee, B. J. Nickoloff, L. Miele, D. D. Sheriff, and G. C. Schatteman, "Transendothelial function of human metastatic melanoma cells: role of the microenvironment in cell-fate determination," Cancer Res. **62**, 665-668 (2002).
36. T. B. Huff and J.-X. Cheng, "*In vivo* coherent anti-Stokes Raman scattering imaging of sciatic nerve tissue," J. Microsc. **225**, 175-182 (2007).
37. X. Han, R. M. Burke, M. L. Zettel, P. Tang, and E. B. Brown, "Second harmonic properties of tumor collagen: determining the structural relationship between reactive stroma and healthy stroma," Opt. Express **16**, 1846-1859 (2008).

1. Introduction

Microscopy techniques based on confocal principle and multiphoton excitation play a growing role in studies of biological tissues *in vivo*. This is due to their capability to acquire images of thin optical sections from different depths of living or fresh tissues. Non-invasive *in vivo* imaging of the upper layers of different organs, such as cornea [1] or skin [2-4], at a resolution that permits visualization of cellular details is thus possible. Due to its easy accessibility, human and animal skin is especially suitable for application of this type of imaging.

For the visualization of different skin layers, one-photon excitation (1PE) in reflectance was applied most frequently. In 1PE reflectance confocal microscopy the detected signal has the same wavelength as the excitation light, unlike 1PE fluorescence confocal microscopy based on the excitation of exogenous or endogenous fluorophores and detection of corresponding fluorescence signal. The 1PE reflectance microscopy, often using near infrared (IR) excitation wavelength, proved to be useful especially in investigations of human normal skin, skin lesions, melanoma and other skin cancers [2,5-9]. Its implementation to murine skin was demonstrated by Li et al. [10], who used combination of 1PE reflectance and fluorescence microscopy for the examination of normal skin and experimental GFP-expressing cutaneous melanoma in the mouse ear. Other authors used 1PE fluorescence microscopy for the visualization of murine dermal microvasculature in normal skin and experimental melanoma after intravenous administration of FITC-dextran [11], or for the examination of human skin morphology after the topical administration of fluorescein sodium and other fluorochromes to the skin [12].

Microscopy using two-photon excitation (2PE) enables the observation of unstained intact tissues based on endogenous sources of nonlinear signals [13-15]. It is generally accepted that 2PE microscopy has the advantage of a higher penetration depth than 1PE confocal microscopy. It was shown that the imaging penetration depth in 2PE microscopy can be four times higher than in 1PE confocal microscopy [16]. This advantage is due to the use of less-scattering, near IR excitation light. The 2PE microscopy enabled to visualize different layers of mouse dermal and subcutaneous structures in a mouse ear [17] or human skin down to a depth of 200 μm [3,18], exploiting solely autofluorescence of tissues.

Although 2PE fluorescence microscopy is the primary imaging technique for thick tissue imaging, second harmonic generation (SHG) imaging microscopy can be also used to visualize certain types of biological specimens. The SHG imaging microscopy was one of the earliest forms of biological nonlinear microscopy, proposed and demonstrated by Sheppard et al. [19]. The SHG occurs when an intense laser beam passes through and interacts with a highly polarizable material with noncentrosymmetric molecular organization. The generated second harmonic signal has twice the frequency (i.e. half of the wavelength) of the light entering the material. It was demonstrated that strong second harmonic signal can be generated by fibrillar collagen and myosin fibers, as well as by dipolar protein, such as microtubule arrays [20-22]. Similar to 2PE fluorescence, SHG has a quadratic dependence on the laser light intensity, thus, it also has an intrinsic optical sectioning capability. In contrast, SHG does not involve an excited state, it is energy conserving, and preserves the coherence of the laser light. In imaging of fresh skin, SHG is used mainly for detection of fibrillar collagen [20,23]. The 2PE fluorescence and SHG microscopy can be easily implemented simultaneously, while providing complementary information on tissue structure due to

different contrast mechanisms. Recently, the combination of these two imaging modalities has been proved to be useful in examination of skin [20,24,27] and other tissues [21,25-30]. On the other hand, the combination of imaging modalities based on 1PE and 2PE is still used very rarely [24,31], although it could bring a complex information on appearance and arrangement of fresh tissues.

Implementing the above microscopy techniques into the *in vivo* as well as *ex vivo* experimental cancer examination could be well exploited in clinical applications, mainly skin pathologies. However, in studies of experimental melanoma in mouse or rat only 1PE based techniques [10,11] and SHG imaging [23] separately were applied. Our idea was that the combination of 1PE and 2PE microscopy could shed more light on relationships between different types of tissues, thus being of a significant diagnostic value in cancer research. The above microscopy techniques could be especially useful in studies of changes in tissue morphology after different clinical interventions, such as a hyperthermia (HT) treatment. The use of heat-induced damage as an anticancer treatment was demonstrated as a therapeutic tool for enhancing the curative effect of other anticancer treatments (chemotherapy, radiation therapy) [32]. However, a better evaluation of the efficacy of HT application during the course of treatments is still needed. To our knowledge, the HT effect on cancer morphology has not been studied by this approach yet.

The aim of the present study was to investigate possibilities of the combination of the one- and two- photon microscopy techniques for defined imaging of the experimental melanoma tissue *in vivo* in totally anesthetized animals, and *ex vivo* on freshly harvested specimens without using staining procedures. We focused on suitable definition of tumor tissue structures and on the study of the effect of hyperthermia treatment on these structures. We also compared experimental melanoma and normal subcutaneous tissue from the same animal by confocal and nonlinear microscopy techniques, using (i) 1PE fluorescence, (ii) 1PE reflectance, (iii) SHG imaging, and (iv) 2PE autofluorescence. We tested different spectral conditions and other settings of image acquisition, as well as combinations of the above imaging modalities to fully exploit the potential of these techniques in the evaluation of treated and untreated cancer tissue morphology.

2. Materials and methods

2.1 Experimental conditions and sample preparation

Experimental tumors were produced in C57BL/6 mice by subcutaneous inoculation of syngeneic B16F10 melanoma cells (106 cells/mouse). An easily accessible neoplasm down the skin (Fig. 1) was thus developed. It was let to grow into up to 15-20 mm in diameter to permit establishment of vascular and stroma structures. Tumors were studied either directly in the living animal under general anesthesia (ketamine-xylamine, IP), or freshly harvested, after sacrificing the animal. The access to the tumor surface in the living animal was obtained by dissecting the overlaying skin in a large flap. The subcutaneous part of the flap far from the site of neoplasm development was used as a normal tissue control. In some cases, the still anesthetized animals received intracardial injection of 0.1 ml FITC-dextran 150 kD (Sigma, Germany), dilution 1:50, to quickly reveal the tumor vascular net. Otherwise no staining was applied. The animals were sacrificed by cervical dislocation after they were studied.

We also examined mouse subcutaneous tumors after microwave-induced hyperthermia, both *in vivo* and *ex-vivo*, to evaluate the possibility to detect qualitative changes of the tissues produced by the procedure. Hyperthermia treatment was applied for 25 minutes with intratumor temperature maintained at 44°C.

All experiments were approved by the Ethical Committee of the Institute of Microbiology, according to the Animal Protection Act of the Academy of Sciences of the Czech Republic and the European Convention for the Care and Use of Laboratory Animals.

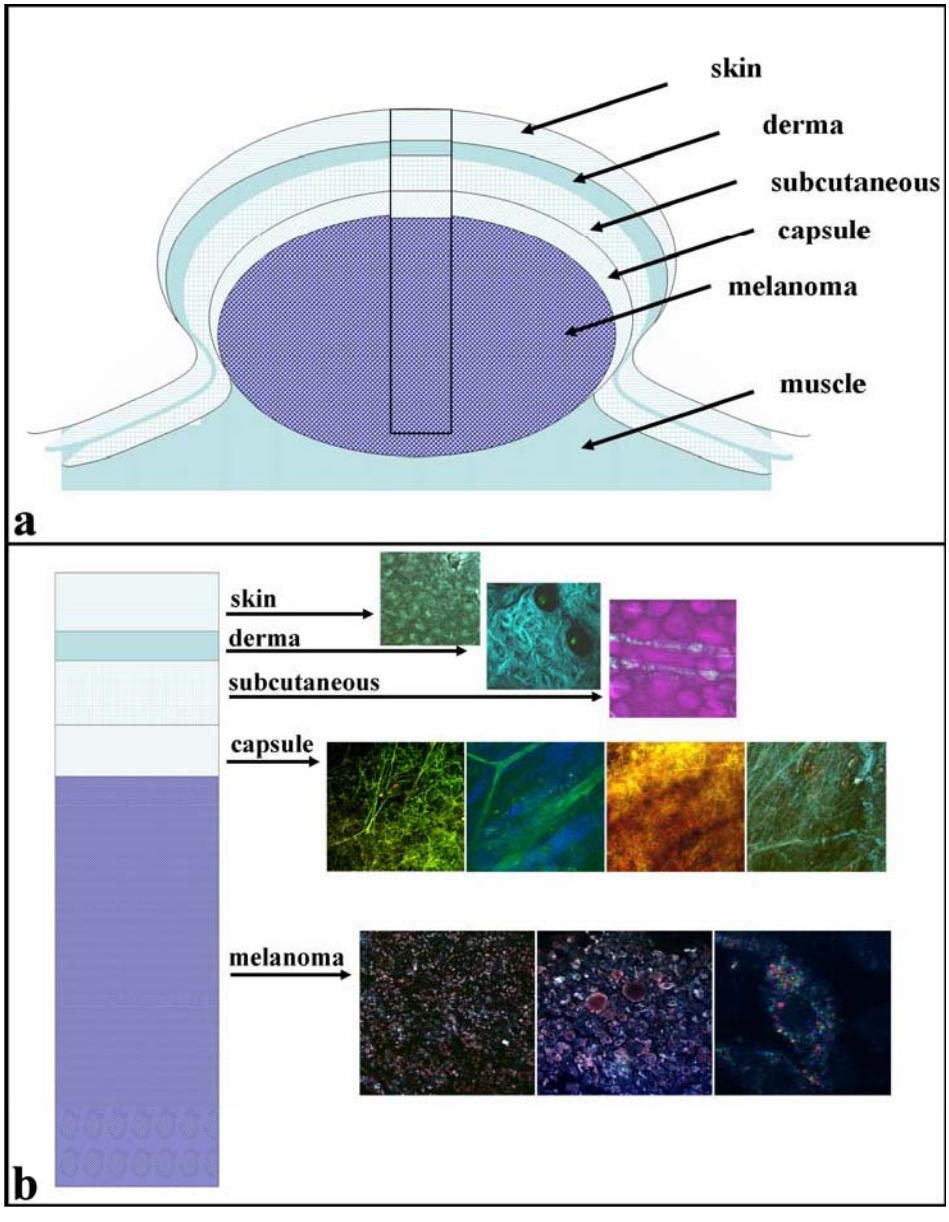

Fig. 1. Experimental subcutaneous melanoma in relation with the surrounding tissues. A cross section of melanoma is shown in (a). The frame indicates the parts of tissues studied in the progressive depth by variously combined microscopy methods. The framed section is zoomed in (b) where the localization of the samples from the skin surface to the central part of melanoma is indicated. The proportions of tissue layers are only indicative.

2.2 Image acquisition

For all our observations we used a Leica SP2 AOBS MP confocal laser scanning microscope based on Leica DM IRE2 inverted microscope and equipped with an argon laser (458 nm/5 mW, 476 nm/5 mW, 488 nm/20 mW, 514 nm/20 mW), green (543 nm/1.2 mW) or red (633 nm/10 mW) HeNe lasers for one-photon excitation. For two-photon excitation, it was coupled to a mode-locked Ti:Sapphire Chameleon Ultra laser (Coherent Inc., Santa Clara, CA, USA), tunable from 690 nm to 1040 nm. We applied objectives with different magnification, depending on the required resolution.

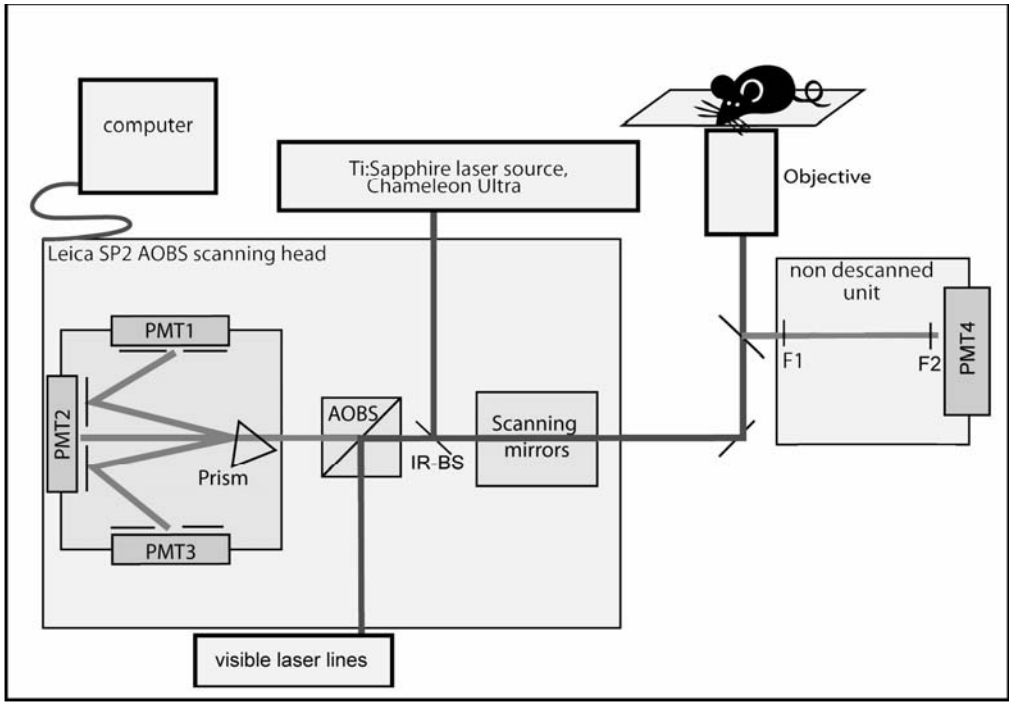

Fig. 2. Schematic view of the experimental setup. Confocal laser scanning microscope Leica SP2 AOBS was coupled with IR pulsed laser Chameleon Ultra for two-photon excitation. In the presented setup, the living mouse, under general anesthesia, lays on a cover slip glass placed on the stage of the inverted microscope, with the tumor exposed by dissecting and removing a skin flap. Four different photomultipliers (PMTs) were used for detection in different image modes: 1. For imaging of FITC-dextran fluorescence signal 1PE excitation by 488 nm line of Ar laser was used, with emitted light collected through the confocal scanning head by PMT1. 2. Reflectance mode was provided by simultaneous sample illumination with up to three different laser lines (488 nm, 514 nm and 633 nm) and recording three channels, i.e. 478-498 nm (PMT1), 504-524 nm (PMT2), and 623-643 nm (PMT3), respectively, with AOBS set to maximum detection of reflected light. 3. For SHG imaging, we used descanned or non-descanned mode. In a non-descanned mode, the light was collected directly behind the objective by PMT4 after passing through E700SP short pass filter (F1) followed by a 430DF15 band pass filter (F2), providing SHG signal when IR laser wavelength of 860 nm was used. In a descanned mode, SHG was recorded through the confocal scanning head in the detection range 420-440 nm (PMT1) while excited with 860 nm of IR pulsed laser. 4. 2PE autofluorescence was recorded in a descanned mode through the confocal scanning head in the appropriate detection range (PMT3) while excited with 860 nm of IR pulsed laser.

The experimental setup of image acquisition is shown in Fig. 2. The previously exposed tumor was directly placed on the cover slip glass, and maintained humid by drops of the same liquid used for the microscope objective. Thus, the damage by drying was avoided, more homogeneous adhesion to the glass was achieved, and possible optical aberrations were reduced. A similar procedure was applied for imaging the subcutaneous side of the skin flap, which was used as a control, and for the fresh samples. This procedure was not followed for the tumors invading the skin when their superficial layers became directly accessible for the examination. As indicated in Fig. 2 and Table 1, the microscopic images were acquired in the following four imaging modes:

2.2a Imaging of fluorescence signal using one-photon excitation

We examined the vasculature in the experimental melanoma capsule in living mouse with vessels stained by intracardially injected FITC-dextran. We used FITC-dextran 150 kD because its large molecular weight was impeding the diffusion of the molecules from the vessels into the surrounding tissues. The wavelength of 488 nm was used for excitation and the wavelength range from 500 nm to 560 nm or 600 nm for detection.

2.2b One-photon imaging in reflectance mode

For visualization of reflection from all tissues under study, we applied one, two, or all three from excitation wavelengths of 488 nm, 514 nm and 633 nm. The reflected signal was detected in up to three corresponding channels, using detection wavelength range of 478-498 nm, 504-524 nm, or 623-643 nm, respectively. Each of the three different excitation wavelengths applied in reflection mode was valuable and brought specific information due to its specific scattering behavior.

2.2c Second harmonic generation imaging

For investigation of structures generating SHG signal, especially fibers containing fibrillar collagen, we used two-photon excitation at the wavelength of 860 nm, which implied expected detection of SHG signal at the wavelength of 430 nm. We recorded the back-scattering of SHG either in a descanned (D), or non-descanned (ND) mode (Fig. 2). In D mode the SHG signal was detected by an internal detector located in the scanning head, using the detection wavelength range set to 420-440 nm. In ND configuration, which is supposed to improve the signal-to-noise ratio (SNR) in the acquired images, the external detector was applied, placed behind a 700 nm short pass filter for removal of reflected light of wavelengths over 700 nm, thus preventing detector damage by reflected IR light of high power, followed by a 430 nm band pass filter with a bandwidth of 15 nm. To confirm the detection of SHG signal, we checked if the signal disappeared when the excitation wavelength was changed to 800 nm, and then re-appeared after setting up a band pass filter for 400 nm.

2.2d Two-photon imaging of autofluorescence

The autofluorescence of non-stained cells and tissues was detected also by 2PE microscopy. Two-photon fluorescence signal was collected by internal detector, using the excitation wavelength of 860 nm, to enable simultaneous acquisition of SHG signal. For detection we applied different wavelength ranges, usually optimized using lambda scans to get as strong autofluorescence signal of the tissues as possible.

Table 1. Microscopy imaging techniques used for examination of mouse normal skin and experimental melanoma.

Type of excitation	Excitation wavelength	Detection wavelength range(s)	Type of detected signal	Figure(s) where the technique was used
1-photon	488 nm	500 – 560 nm 500 – 600 nm	Fluorescence	6,11
1-photon	488 nm 514 nm 633 nm	478 – 498 nm 504 – 524 nm 623 – 643 nm	Reflection	3,4,5,6,7, 0,12 5,7,8,10 3,4,5,7,8, 0,12
2-photon	860 nm	430 nm 420 – 440	SHG non-descanned	5,9,10 4,10,11

We checked different settings of image acquisition, as well as different combinations of the above imaging modes, to achieve the most detailed and informative images of treated and untreated cancers, as well as of control tissues (Figs. 3-11). Appropriate pseudocolors were assigned to the images acquired by different modes and in different channels. The corresponding images were usually merged into one image, which was applied after the proper image alignment in case of combination of 1PE and 2PE imaging. In some cases

further information on arrangement of tissues was obtained from three-dimensional (3D) reconstructions, based on series of optical sections of the specimen. For 3D visualization we applied maximum intensity projection of these series using Leica LCS software (Fig. 5h,i), volume rendering by Volume plug-in module (Fig. 6a), or browsing through the 3D stack in xy, xz, and yz directions by OrthoSlice plug-in module (Fig. 6b,c), both modules being developed in Ellipse software environment (ViDiTo, Košice, Slovakia).

3. Results

The experimental mouse melanoma develops after the inoculation of cells in the subcutaneous of syngeneic animals. Characteristically, it forms spheroidal tumors surrounded by a connective capsule furnishing the vascular support to the growing tumor mass. In its evolution it can infiltrate the overlaying skin and invade the muscle at its base. The described structures are schematically illustrated in Fig. 1. The melanoma consistence is soft because the cellular component predominates over the connective stroma. The observations were conducted in continuity from the surface down to the maximal depth permitted by each method. The evaluation of inner parts of the melanoma was possible only ex vivo, on fresh samples prepared after dissection and splitting off the tumor mass. Observations were performed on the tumor section at a distance of 200-500 μm from the melanoma surface.

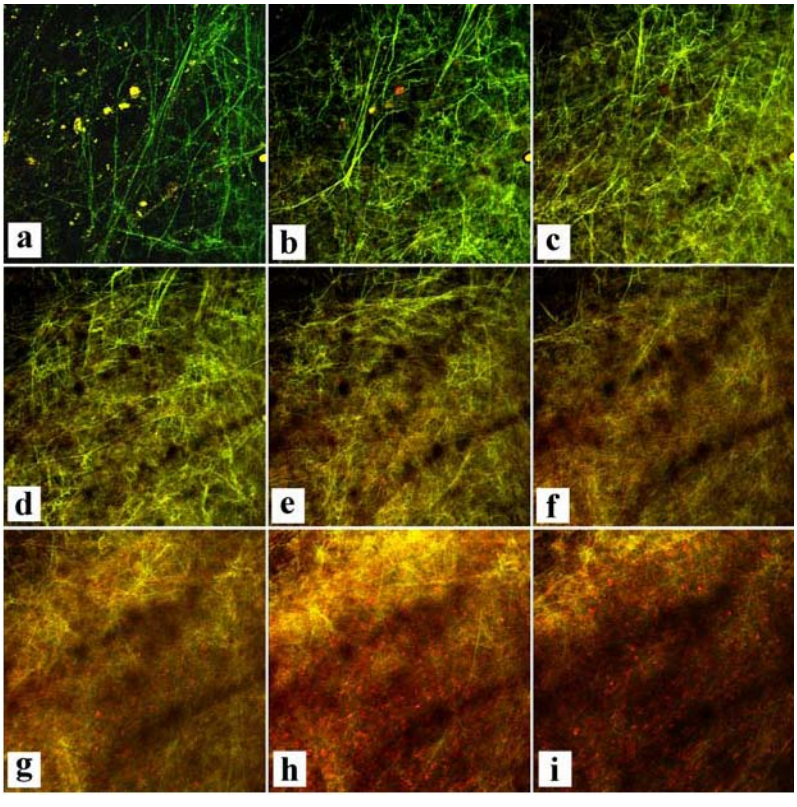

Fig. 3. Experimental melanoma capsule. The series of optical images (within a depth of 72 μm) shows the melanoma capsule in its complexity, from its surface up to its progressive mixing with the tumor cellular mass. In the superficial layer of the capsule, composed by a delicate net of fibers, we can see some cells derived from the removed subcutaneous tissue (a,b) differing in their characteristic features from the melanoma cells (h,i). When progressing into deeper layers, the capsule becomes thicker and vessels appear, visualized as dark voids in the structure (negative stripes clearly seen in e-i). The melanoma cells can be seen in deepest layers (g-i).The series was obtained by 1PE reflectance imaging. Merged images of 9 serial optical sections, 9 μm apart, from two channels (green channel: excitation 488 nm, detection 478-498 nm; red channel: excitation 633 nm, detection 623-643 nm). Water immersion objective HC PL APO CS 20x objective was used. Image size: 750 μm x 750 μm.

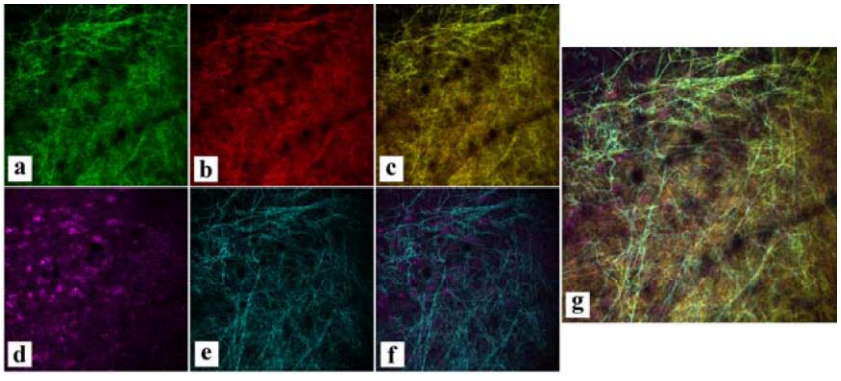

Fig. 4. Superficial layer of experimental melanoma capsule visualized by 1PE reflectance, 2PE autofluorescence, and SHG imaging. The field corresponds to Fig. 3e. (a) 1PE reflectance imaging in green channel (excitation 488 nm, detection 478-498 nm). (b) 1PE reflectance imaging in red channel (excitation 633 nm, detection 623-643 nm). (c) Merged image of images (a) and (b). (d) Melanoma cells are detected by 2PE autofluorescence in magenta channel (excitation 860 nm and detection 475-600 nm). (e) Collagen fibers are visualized by SHG imaging in cyan channel (descanned 2PE excitation at 860nm and detection 420-440 nm). (f) Merged image of images (d) and (e). (g) Combination of all imaging modalities (merged image from green, red, magenta, and cyan channels). Water immersion objective HC PL APO CS 20x was used. Image size: 727 μm x 727 μm.

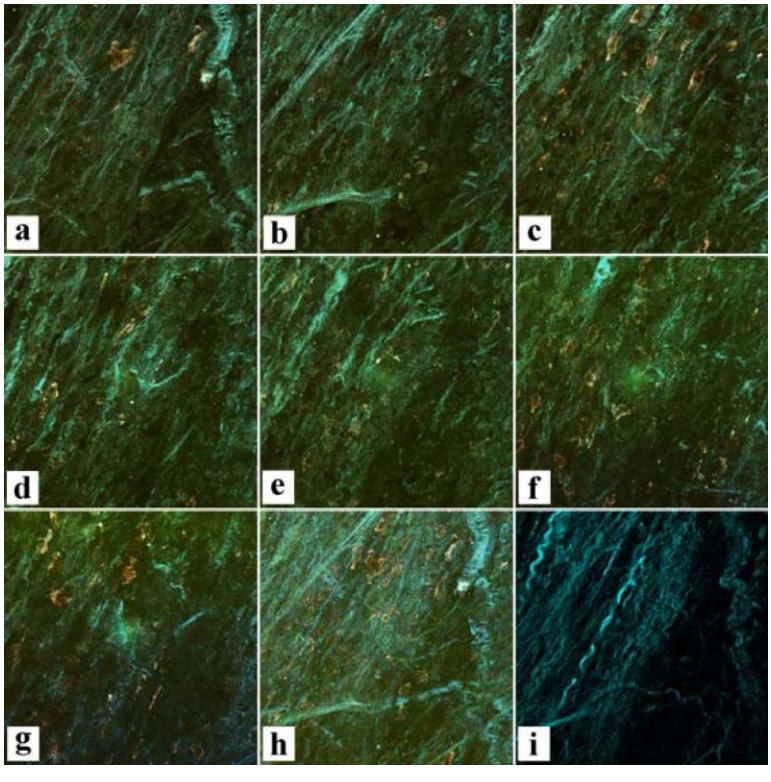

Fig. 5. Inner layers of the experimental melanoma capsule within the depth of 42 μm. The dense part of the melanoma capsule is formed by a network of tiny vessels, fibers are organized into convoluted stripes (a,e,h), and collagen fibres of various thickness follow a regularly parallel orientation (i). The brown melanoma cells infiltrating the capsule are clearly detected. (a-g) Images of serial optical sections 6 μm apart, beginning near the capsule surface, acquired by 1PE reflectance imaging (merged images from three channels - blue channel: excitation 488 nm, detection 478-498 nm; green channel: excitation 514 nm, detection 504-524 nm; red channel: excitation 633 nm, detection 623-643 nm). (h) Maximum intensity projection of serial sections shown in (a-g). (i) Maximum projection of serial images acquired by non-descanned SHG imaging within the same depth (cyan channel: 2PE at 860 nm and detection 430 nm). Water immersion objective HCX PL APO CS 63x was used. Image size: 238 μm x 238 μm.

We confirmed that the stroma components (collagen and elastin fibers, vessels) could be observed by the various 1PE and 2PE microscopy approaches applied to fresh tissue. They enabled to visualize the structure of the peri-tumoral capsule without the need of previous staining. The capsule demonstrated a complex network of fibers that became particularly dense in its internal part, as clearly evidenced by 1PE reflectance serial optical sections (Fig. 3c-f). As detected by SHG imaging, collagen represents an important component of these fibrous structures (Figs. 4 and 5). In this context, vessels can be recognized either as voids in the tumor capsule structure ("negative" imaging, see Figs. 3 and 4) or evidenced by the injection of a fluorescent marker into the blood circulation (Figs. 6 and 11d). Both the superficial and inner layers of the capsule revealed a composition of fine fibers, in part constituted by fibrillar collagen, as visualized by SHG imaging. This delicate fibrillar net on one side connected the capsule to the dense dermal layer, and on the other side progressed with rarefaction into the superficial layers of the melanoma. The progressive increase of the tumor cell component was clearly visible in the inner part of the capsule, as it was well evidenced by 1 PE red channel (633 nm) reflectance, revealing cells incorporated in the stroma network (Figs. 3g-i and 5). Melanoma cells were also visualized using 2PE eliciting autofluorescence of their melanin content (Fig. 4d).

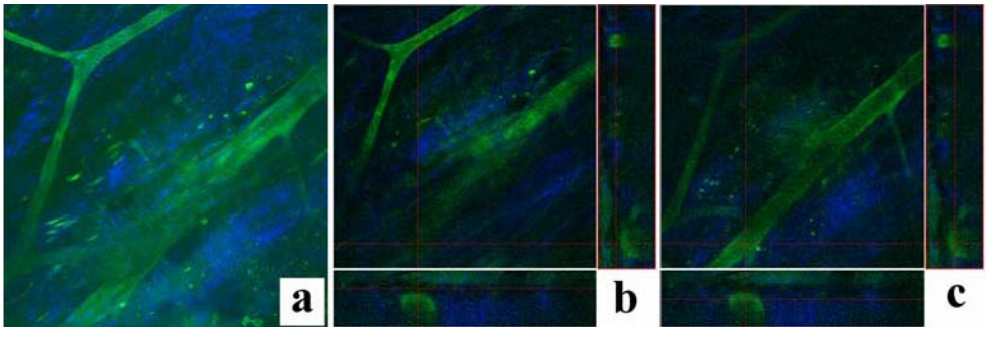

Fig. 6. Vascular network in the melanoma capsule. 3D visualization of experimental melanoma capsule in living mouse with vessels stained by intracardially injected FITC-dextran using 1PE reflectance and 1PE fluorescence imaging. The depth of the stack of optical sections was 162 μm, the field of view was 750 μm x 750 μm. Blue channel: 1PE reflectance (excitation 488 nm, detection 478-498 nm); green channel: 1PE fluorescence (excitation 488 nm, detection 505-560 nm). (a) 3D volume rendering showing the vessels in green. (b,c) Orthogonal views showing sections in xy, xz, and yz directions with their positions within the stack given by the red lines. Note transverse sections of vessels, clearly seen in xy and yz views. Water immersion objective HC PL APO CS 20x objective was used.

The visualization of the inner part of the tumor was possible after sectioning a fresh sample, placing the excised tumor on a cover glass, and then applying 1PE imaging in reflectance mode at different magnifications. By this way, the individual cells and their content (melanin granules) could be clearly distinguished. The nucleus appeared as a void surrounded by granules ("negative" imaging, see Figs. 7 and 8d). The image depiction was particularly defined, considering the absence of any previous staining.

The evaluation of changes in the images after microwave-induced hyperthermia of the tumor demonstrated changes in the architecture and organization in both the tumor capsule and tumor mass. SHG imaging revealed that the harmonic and delicate net of capsular fibers visible in untreated tumor conditions acquired a simplified arrangement in less harmonic, thicker, and less organized bands (Fig. 9b,e). The 1PE red channel reflectance, applied to the same optical field, showed the disappearance of cells and confirmed the disorganization of the original connective network (Fig. 9a,d). At the tumor mass level, different changes caused by the direct and indirect heat effect induced modification of the reflectance capacity of the tissue components. The loss of structured image with homogeneous tissue distribution was evidenced in the area closer to the microwave delivery (Fig. 8c), while in the zones farther

from the microwave application site but heated by passive heat transmission, cells were still visible, although forming aggregates and loosing their previously well-defined appearance (Fig. 8b). In zoomed 1PE reflectance images (Fig. 8d-f) these differences were more clearly demonstrated, with the evidence of a shadowing effect in the indirectly heated tissue, probably caused by the presence of fluid (reactive edema) within the tumor structures (Fig. 8e). In this case, the study of fresh samples brought relevant information on specific morpho-functional changes produced by the applied HT treatment (i.e. tissue coagulation, inflammatory reaction, differences between direct and indirect heating) with practical outcome for the evaluation of treatment effectiveness.

The set of images collected from normal and untreated tissues in the control skin flap confirmed the validity of the approach to obtain *in vivo* information about the structure of the observed tissue. Both skin layers and subcutaneous tissue were investigated. It was shown that 1PE reflectance, 2PE autofluorescence, and SHG imaging, was capable to evidence the respective structural aspects, such as types of cells and connective tissues, as shown in Figures 10 and 11.

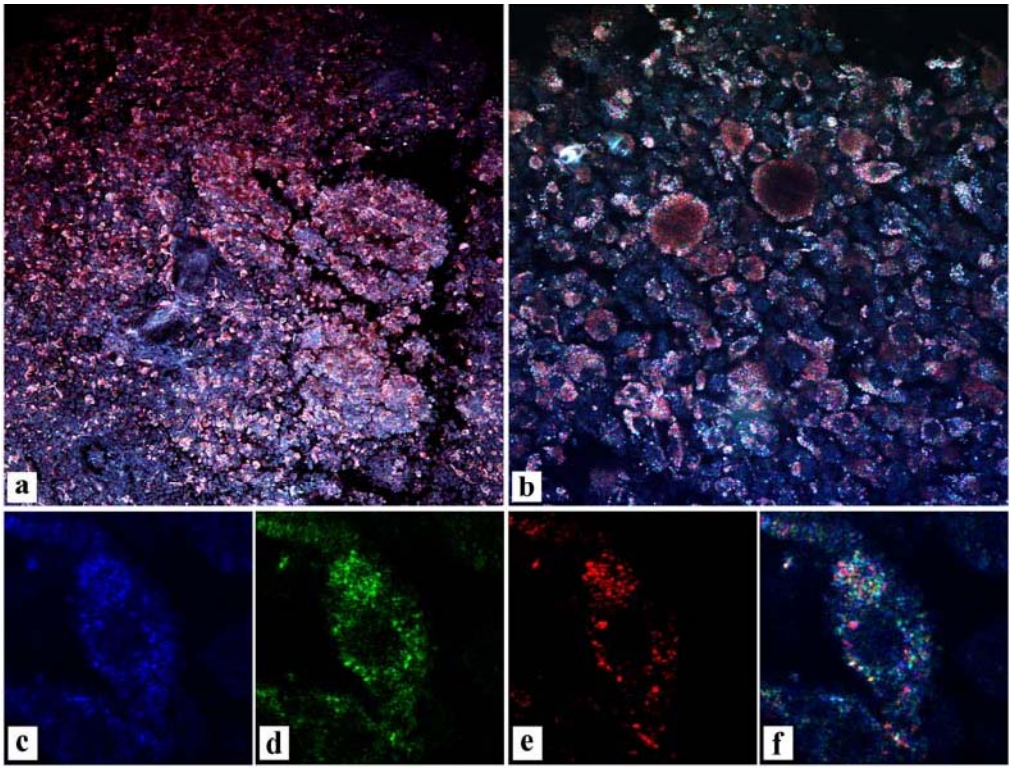

Fig. 7. Section of the experimental melanoma. Tumor tissue and cells from excised experimental melanoma were visualized by 1PE reflectance imaging. Blue channel: excitation 488 nm, detection 478-498 nm; green channel: excitation 514 nm, detection 504-524 nm; red channel: excitation 633 nm, detection 623-643 nm. (a) Tumor tissue, captured by 20x objective, merged image from all three channels. The individual cells are distinguishable and are packed together with a scarce stroma component. Image size was 750 μm x 750 μm. (b) Detail of tumor tissue with cell structure (granular cytoplasm and nucleus) clearly visible, objective 100x, merged image from all three channels. Image size was 150 μm x 150 μm. (c-f) One melanoma cell in detail, acquired using 100x objective with zoom 6.8x, images from individual channels (c-e) and merged image from all three channels (f). Image size was 22 μm x 22 μm.

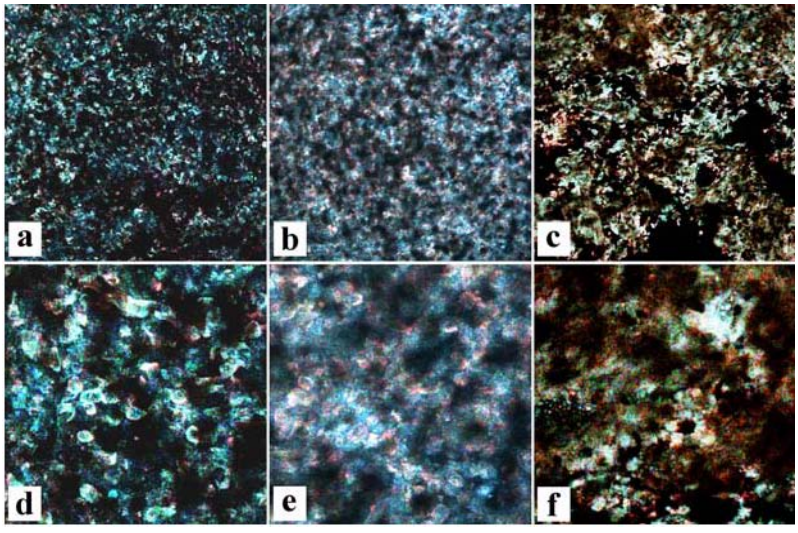

Fig. 8. Melanoma after administration of microwave-induced hyperthermia. Tumor tissue from the excised experimental melanomas was visualized by 1PE reflectance imaging. In untreated melanoma (a,d) cells are distinguishable and form a quite homogeneous tissue. After application of hyperthermia (b,e) the tissue appears less homogeneous, with clamping of cells anf reduction of the previous detailed definition due to intercellular edemas that modify the optical characteristic of the tissue (e). In the site of direct delivery of microwaves (c,f) a more intense alteration of the tissue structure is produced, with the cellular aspect disappearing, accompanied by the increased inhomogeneity of the imaged tissue. An increase of black areas indicates a less homogeneous adhesion of the section to the coverslip glass suggesting a less plastic tissue (coagulative necrosis). Merged images from three channels (blue channel: excitation 488 nm, detection 478-498 nm; green channel: excitation 514 nm, detection 504-524 nm; red channel: excitation 633 nm, detection 623-643 nm). Water immersion objective HC PL APO CS 20x was used. Image size was 750 μm x 750 μm in (a-c) and 233 μm x 233 μm in (d-f) .

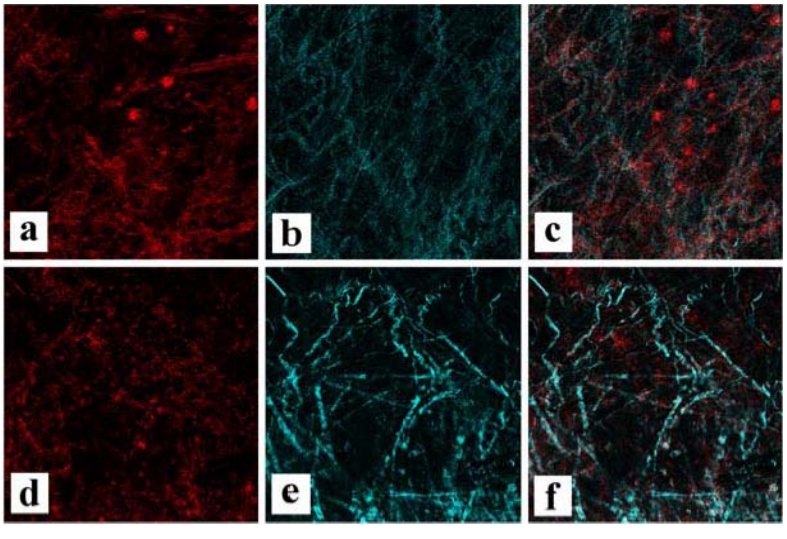

Fig. 9. Effects of microwave-induced hyperthermia on collagen. Intermediate layer of experimental melanoma capsule before (a-c) and 5 hours after hyperthermia treatment (d-f) visualized by 1PE reflectance imaging in red channel (a,d) (excitation 633 nm, detection 623-643 nm), SHG imaging (b,e) in cyan channel (non-descanned 2PE at 860nm and detection 430nm), and by their combination (c,f) (merged images from red and cyan channels). The structure of the untreated melanoma capsule (a-c) consists of a net of subtle fibers with some infiltrated melanoma cells. The SHG highlights a constitution of very thin, regularly organized collagen fibers. After the HT treatment (d-f), the melanoma tissue is denser and infiltrating cells are no more visible; the collagen structure becomes brighter and more distinct and gets less regularly organized than in the untreated tissue. Fibers are more evident and thicker than in normal conditions. Water immersion objective HC PL APO CS 20x and 2.5x zoom were used. Image size: 304 μm x 304 μm.

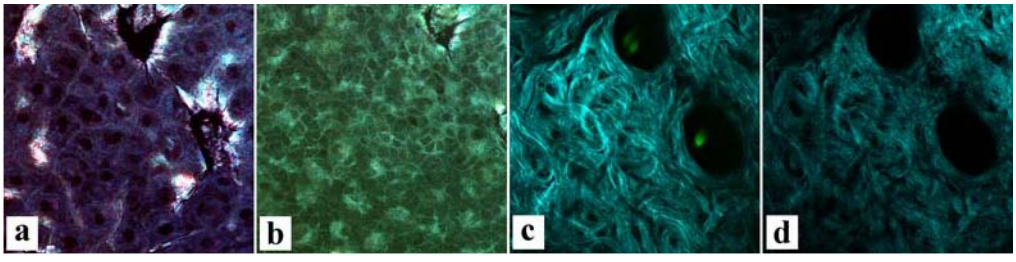

Fig. 10. Skin layers in control tissue. Different layers in a control skin flap were observed *in vivo*. A granular layer of epidermis (a) with granular cells and a layer of spinous cells (b) were detected by 1PE reflectance imaging (merged images from three channels - blue channel: excitation 488 nm, detection 478-498 nm; green channel: excitation 514 nm, detection 504-524 nm; red channel: excitation 633 nm, detection 623-643 nm). Collagen fibres of derma (cyan) and hairs (green) were detected by SHG and 2PE autofluorescence (c) in a merged image from two channels, i.e. cyan channel (non-descanned SHG imaging using 2PE at 860 nm and detection 430 nm) and green channel (2PE fluorescence with excitation at 860 nm and detection 497-652 nm). The same field as in (c) acquired by descanned SHG imaging is shown in (d) (2PE at 860 nm and detection 420-440 nm). Note a weaker signal and more noise than in (c). Water immersion objective HCX PL APO CS 63x was used. Image size: 238 µm x 238 µm.

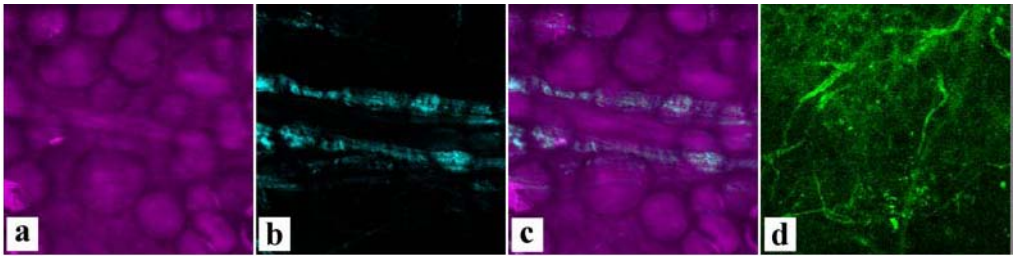

Fig. 11. Subcutaneous tissue in the control skin flap. Vessel walls in adipose tissue were visualized using 2PE imaging (a-c). Adipocytes were detected by 2PE autofluorescence in magenta channel (a) (2PE at 860 nm and detection 517-850 nm). Vessel walls were detected by descanned SHG imaging in cyan channel (b) (2PE at 860 nm and detection 420-440 nm). Merged image of (a) and (b) is shown in (c). 20x objective and 3.13x zoom were used. Image size in (a-c): 240µm x 240 µm. In the normal subcutaneous after FITC-dextran injection (d) the stained vessels are clearly visible. Adipocytes can be seen as dark regions in a brighter autofluorescence background. 1PE fluorescence (excitation 488 nm, detection 500-600 nm) imaging using 10x objective with 1.82x zoom was applied. Image size in (d): 825 µm x 825 µm.

4. Discussion

In the present study, the various imaging modes brought different, and often complementary information on the histology of tissues under study. The 1PE reflectance mode proved to be well applicable to unstained fresh tissues, allowing clear visualization of different layers both in the control skin flap (Fig. 10) and in the melanoma capsule (Figs. 3 and 5). This is in accordance with observations made by other authors [2,5-9] in their studies of human skin using 1PE reflectance microscopy. We were able to find valuable differences after the hyperthermia administration in comparison with untreated tissues (Figs. 8 and 9) by this technique. The SHG imaging microscopy proved to be very suitable for detecting collagen fibers in our fresh tissue samples without any staining, considering the high specificity of SHG imaging microscopy for detection of fibrillar collagen (i.e. collagen type I), as demonstrated by several authors [21,26,30].

The application of 1PE reflectance imaging, providing non-specific detection of fibrous structures (Fig. 4a-c), when combined with SHG imaging (Fig. 4e) revealed more details in the structure of the examined tissues. Further information was gained when, moreover, the 2PE autofluorescence (Fig. 4d) was detected simultaneously. The 2PE autofluorescence was especially useful in detecting melanoma cells with a high content of melanin granules, not always clearly visualized by the reflectance imaging. This enabled their identification in the fibrous network of the inner layers of the melanoma capsule, which would be important for

possible clinical application in detecting melanoma invading front. To our knowledge, this combination of confocal and nonlinear optical imaging has not been yet applied for study of either fresh skin or skin tumors. Recently, a similar approach has been used for observation of cornea in excised bovine eyes [31].

On the other hand, nowadays, the combination of 2PE autofluorescence and SHG imaging microscopy is frequently used for non-invasive examination of different unstained tissues, including skin [20,33], mammary tissues and tumors [27], aortic walls [25], normal and fibrotic pulmonary tissue [29], fibrotic kidney [30], and skeletal muscle [28]. We used the nonlinear optical imaging mainly for evidencing melanoma cell relationships with the connective structures composing the layers of the melanoma capsule, as shown in Fig. 4. Moreover, this technique can bring interesting results in examination of vessels with dimensions exceeding 10 μm in diameter, as illustrated in Fig. 11a-c, where vessel walls were detected by SHG imaging, while the surrounding adipocytes showed strong 2PE autofluorescence. A similar observation was made by Larson et al. [34], who combined the visualization of adipocytes by 2PE autofluorescence with 2PE fluorescence microscopy for *in vivo* detection of capillaries, which were stained by quantum dots. Other authors used intravenous administration of FITC-dextran and Texas Red-dextran [11] or perfusion with FITC-labeled *Ulex europaeus* agglutinin [35]. We found that the vessels in experimental melanoma capsule can be well visualized after intracardial injection of FITC-dextran with a high molecular weight (150 kD) in untreated tissues (Figs. 6 and 11d), while after HT the dye quickly extravasated into the surrounding tissues due to the increased permeability of vessels after heating. In untreated melanoma capsule we were able to obtain approximately 150 μm thick stacks of optical sections, yielding clear 3D visualization of vessels *in vivo*, as shown in Fig. 6.

The images presented in this study were acquired after accurate settings of the different imaging modes (Fig. 2), guided also by the progressive confidence with the experienced various combinations. The optimized setting accomplished the aim to get the best images as possible according to their information content as well as quality, expressed by a high contrast and high SNR.

In 1PE fluorescence imaging we took into account the spectral characteristics of the applied staining, i.e. FITC, and we adjusted the acquisition to get a stack of confocal microscopic images encompassing the largest volume as possible, while keeping the resolution high enough for the examination of vessel network. This was achieved by using a 20x water immersion planapochromat objective with a working distance of 250 μm and a numerical aperture of 0.7, yielding sufficient resolution while offering a relatively large field of view.

In 1PE reflectance imaging we checked all available excitation wavelengths, finding out that, due to the difference in their scattering behavior, they yield different images, revealing various details in the examined tissues. Our final choice of excitation wavelengths was 488 nm, 514 nm and 633 nm, taking into account that: 1. The argon laser has a higher power (20 mW) at the 488 nm and 514 nm lines than at the other lines 2. The argon laser is more powerful than the green HeNe laser. Thus, we obtained a stronger signal, resulting in a higher SNR in acquired images, than the signal we would have achieved by using the other excitation wavelengths. We took care to set the AOBS for maximum detection of reflected light during the 1PE reflectance acquisition. The combination and subsequent merging of the three channels usually yielded the most informative images, especially when suitable pseudocolors were assigned to each channel (i.e. blue, green and red for, respectively, 488 nm, 514 nm, and 633 nm excitation), see Figures 5, 7, 8, 10a,b. While focusing deeper into the tissue, we observed that the reflected images corresponding to blue or green channel were fading away faster than those in the red channel, as clearly illustrated in Fig. 3. This is due to the lower scattering of “red” photons which have lower energy than the “blue” and “green” ones.

In SHG imaging we considered the backward mode with the SHG signal collected via a detector (PMT4 in Fig. 2) placed behind the objective, and the forward mode using the transmission detector behind the condenser. We decided to apply the backward SHG imaging,

taking into account its suitability for the detection of strong signals in the depth of thick specimens, as it was necessary in our tests. Moreover, a good detection of fibrillar collagen in this mode was reported [31,36,37].

In principle, a simultaneous image acquisition of SHG signal and 2PE autofluorescence is possible both via the scanning head of the confocal microscope, i.e. in the descanned (D) mode, and by the external detectors in the non-descanned (ND) mode (Fig. 2). In D mode for both SHG and 2PE fluorescence imaging, it is sufficient to set up two detection bands in two detection channels (e.g. PMT1 for SHG and PMT2 for 2PE autofluorescence). The simultaneous collection of both types of signals in ND mode was possible but we would have to introduce more optical elements into the beam path, which would decrease the detected light intensity. Therefore, in our final setup (Fig. 2), we decided to use only two filters, i.e. E700SP low-pass filter (F1), preventing detector damage by high-intensity IR light reflected from the sample, and 430DF15 band pass filter (F2) allowing the detection of SHG narrow peak. The SNR of acquired images by SHG imaging proved to be higher in this configuration compared to SHG detection in D mode (compare Fig. 10e,d). In this setting it was impossible to record any signal other than SHG in ND mode, therefore we had to collect the 2PE fluorescence signal via the scanning head. However, the intensity of 2PE autofluorescence signal was usually high enough if we applied suitable detection wavelength ranges, which we usually optimized using lambda scans. The flexible setting of the detection ranges and the possibility of lambda scans, exploiting the AOBS placed in the scanning head, makes the D mode advantageous if the detected signal is not too weak. Therefore, sometimes it was useful to apply both SHG and 2PE fluorescence imaging in D mode.

The presented approach using 1PE and 2PE based microscopy techniques proved to be suitable for examination of important structure details in *in vivo* or freshly harvested tissue, which was unstained or, in the case of studies of vessels, stained *in vivo*. These results bring possibility of an almost non-invasive observation of living tissues together with 3D imaging of relatively thick tissue layers. However, a possible damage of the observed tissues caused by laser application should be taken into account, especially when the pulsed high-energy laser for 2PE is used. Prolonged observation of the same optical field in the sample may result in overheating and subsequent deterioration of the specimen. This possible damage should be considered during the microscopic examination of living tissues, especially in the clinical use perspective Thus, the settings of the image acquisition have to be carefully chosen also from the point of view of the delivered energy and the time the laser beam remains focused to one spot in the specimen. For example, slow scanning combined with multiple line averaging and high number of pixels in the image should be avoided.

5. Conclusion

In the present study we focused on examination of the experimental mouse melanoma, representing a simple model of cancer, with possibilities of translational results to the human patients. This experimental approach is advantageous for cancer studies as it enables to quickly obtain easily accessible tumors suitable for evaluation of therapeutic approaches. Here we showed the possibilities of imaging fresh tissue of experimental cancers by simultaneous application of confocal and nonlinear optical microscopy techniques in several acquisition modes. Such integrate approach was applied for *in vivo* examination of experimental melanoma for the first time. It enabled to study the collagen fiber network in relation to other tissues, and to identify invasive tumor cells. It also facilitated the examination of interrelationships between functional and morphological aspects based on optical properties of the tissues, as documented by the changes observed between the tumor and control tissue, as well as changes due to delivery of microwave hyperthermia treatment.

Acknowledgments

The presented study was supported by the Academy of Sciences of the Czech Republic (grant IAA500200510, Institutional Research Concepts No.AV0Z50200510, AV0Z50110509), and Ministry of Education, Youth and Sports of the Czech Republic (research program LC06063).

2.3 Polyoma Virus infection pathway and FRET technique

1. **Mouse Polyomavirus Enters Early Endosomes, Requires Their Acidic pH for Productive Infection, and Meets Transferrin Cargo in Rab11-Positive Endosomes.**
   D. Liebl, **F. Difato**, L. Horníková, P. Mannová, J. Stokrová, J. Forstová
   J Virol. 2006 May ;80 (9):4610-22 16611921

2. **Dynamics of cytoplasmic trafficking of mouse polyomavirus revealed by time-lapse live imaging confocal fluorescence microscopy.**
   F. Difato, D. Liebl, V. Zila, L. Klimova, L. Hornikova and J. Forstová (In preparation for submission to Journal Virology)

2.3.1. Aims and results

Aims:

- To apply FRET to go beyond the optical resolution limit of the system.
- To apply live imaging for studies mouse Polyoma virus (mPyV) intracellular trafficking.
- To identify the endocytic pathway used by mPyV
- To define the role of cytoskeleton in productive virus trafficking

Results:

- Twenty minutes post adsorption, virions appeared in early endosomes.
- FRET assay was exploited to identify perinuclear endosomes targeted by the virus. Positive FRET between VP1 structural protein of mPyV virions and transferrin (the cargo characteristic for recycling endosomes) or between VP1 and Rab11 GTPase, revealed that these compartments are recycling endosomes.
- Co-localization studies of mPyV with the early endosome antigen (EEA1), caveolin-1, transferrin and RAB11 GTPase revealed intersection of different endocytic pathways in common endosome compartments.
- Live imaging of virion trafficking permitted to follow infectious paths of a single virions.
- We quantify trajectory properties of more than 200 mPyV virions. Trajectories of virion movements measured by single particle tracking appeared to be much more complex than previously recognized.
- Trafficking of virions revealed three modes of transport rates, reflecting characteristic dynamics of motor-driven transport with saltatory bi-directional movements and velocity peaks of 1,5 μm/sec. Their trajectories were composed of pausing and switching direction during the long-range motion from the cell surface to the nuclear periphery.
- mPyVs were captured in caveolin domains both, at the cell surface and in the nuclear periphery. However, virions not colocalising with caveolin 1 during their trafficking were also observed.
- mPyV was found to exploit for its trafficking both actin and microtubules.
- mPyV infection was accompanied with transient disorganization of actin stress fibres.
- We observed that actin polymerization machinery became recruited by endocytic vesicles and used for their propulsion through the cytoplasm. Dynamic actin assemblies, reminding actin comets, moved virion loaded vesicles in short range distance.
- At high multiplicity of infection, actin was found also to be organized into ring shaped structures around endosomes. Such vesicle became static.
- Transient dissasembly of microfilaments by cytochalasin or latrunculin enhanced the efficiency of mouse polyomavirus infection.
- Intact microtubules were found to be essential for productive infection as treatment of cells with nocodazol strongly inhibited infection.

2.3.2. Discussion

The major structural protein of Polyomavirus, VP1, was found to have properties of capsid self-assembly and binding of DNA in a sequence independent manner. Consequently, there has been growing interest in application of Polyoma virus capsid-like particles (VLPs) in gene therapy as vehicles for gene delivery into cells. However, the efficiency of DNA delivery into the cell nucleus by chimeric capsids was much lower than that by virions. To understand the reason for such low

efficiency of polyoma VLP infection, researchers started to study polyomavirus trafficking pathway in cells.
Previous works based on electron microscopy studies and fluorescence microscopy of fixed cells gave information on the colocalization of mPyV virions at fixed time post infection, but could not give information on the dynamic behaviour of mPyV. Moreover, in fixed samples it is difficult to distinguish artefact due to the invasive experimental protocol from real data.
Immunofluorescence assay already showed colocalization of virions with transferrin and Rab 11. However, due the low optical resolution and the huge accumulation of different endocytic compartments in perinuclear area it was not be sure that transferrin and mPyV appeared in the same compartments. Therefore, it was necessary to confirm this data at higher resolution technique. We applied FRET assay which permits to study colocalization in the nanometre range. FRET assay resolved the different location of transferrin and RAB11 GTPase on recycling endosome. The first is present inside of endosome while the second is present only on the outer surface of the endosome. The different localization of the proteins due to the membrane of the endosome (about 5nm thick) gives two different average values of FRET. Therefore by FRET we were able to resolve colocalization of proteins at resolution below the diffractive optical limit of the system, and it was provided strong support for the presence of mPyV VP1 and transferrin within the same compartment.
We further examined the effect of the elevation of endosomal pH on mPyV infection. Infection of SV40 (known to enter cells via caveolae and to continue through caveosomes into ER) was found to be not affected by increased endosomal pH. We have shown that treatment of cells with Bafilomycin A or NH4Cl prevented mPyV productive infection when cells were exposed to the drugs during the initial steps of infection. At later times post infection, since the virus was detected in the perinuclear space, infection became pH insensitive.

We applied confocal live imaging on cells expressing GFP-tagged caveolin-1 or g-actin or α-tubulin infected with fluorophore labeled virions. This method permitted us to follow infection pathway of a single virions. The problem with studies of productive trafficking of mPyV is the low infection efficiency. Only few virions are successful while the majority of entering virions never deliver their genomes into the cell nucleus. Therefore it is really important to have the possibility to follow single virion movement because it permits to detect different pathways of the minor subpopulation of viral particles that can be masked by stronger colocalisation of the majority of particles which can represent the non infective path. In fact, we observe that mPyV exploit more than one way to reach perinuclear space. However, the mechanism of delivery of mPyV genomes into the cell nucleus remains unclear.
Observations of interactions of mPyV with caveolin-1 domains in living cells expressing EGFP-fused caveolin-1 revealed that some mPyV particles enter cells through caveolin-1-rich domains, while others bypass them. Nevertheless, no colocalization of clathrin with mPyV was observed in different types of cells, including Jurkat cells that do not express caveolin. Later post infection, the signal of mPyV can be seen in large caveolin-1-rich compartments in the perinuclear space. This may suggest that mouse polyomavirus enters the compartments called caveosomes.
Dynamic virus-cytoskeleton interactions revealed direct evidence for cytoskeleton-driven trafficking in host cells. The movement along microtubules is absolutely essential for the productive infection as nocodazol which disassebles tubulin cytoskeleton, inhibits mPyV infection.
The role of actin is not so clear. When actin microfilament assembly and dynamics were destabilized by the presence of cytochalasin or latrunculin, the number of infected cells decreased in a dose-dependent manner, but not more then to 50% of the control infectivity. However, when drugs were washed out (15 h. p.i.) and microfilaments were left to recover their native organization, the efficiency of infection in drug pretreated cells increased two times in comparison to that achieved in untreated cells. Therefore, we conclude that actin microfilament rearrangement may have a double role in mPyV virion entry and transport: apparently, two-dimensional cortical actin meshwork can play a role of steric barrier for free

movement of endocytosed vesicles into the cell interior, but actin propelled vesicle, could be important for short range vesicle movement to microtubule tracks.
At later time post infection, at high multiplicities of infection (MOI), we showed numerous actin rings per infected cell. These structures appeared to be rather static and reflect the actin filaments reorganized into actin ring-shaped assemblies around endocytic/exocytic vesicles. An enormous load of vesicles is clearly visible in transmission light. Whether this observation represents signal-induced enhancement in the rate of endocytosis triggered by virus binding, is not clear yet. We hypothesize that a massive virus uptake consumes large area of membrane sheet, which fails to be recycled back at the same rate, and therefore, the cell regulation machinery may promote a signal to pause endocytosis until the membrane recovery.

2.3.3. Publications

JOURNAL OF VIROLOGY, May 2006, p. 4610–4622 Vol. 80, No. 9
0022-538X/06/$08.00+0 doi:10.1128/JVI.80.9.4610–4622.2006

Mouse Polyomavirus Enters Early Endosomes, Requires Their Acidic pH for Productive Infection, and Meets Transferrin Cargo in Rab11-Positive Endosomes

David Liebl,[1] Francesco Difato,[1] Lenka Horníková,[1] Petra Mannová,[1]† Jitka Štokrová,[1,2] and Jitka Forstová[1]*

Department of Genetics and Microbiology, Faculty of Science, Charles University, Prague, Czech Republic,[1] and Institute of Molecular Genetics, Academy of Sciences of the Czech Republic, Prague, Czech Republic[2]

Received 25 October 2005/Accepted 8 February 2006

Mouse polyomavirus (PyV) virions enter cells by internalization into smooth monopinocytic vesicles, which fuse under the cell membrane with larger endosomes. Caveolin-1 was detected on monopinocytic vesicles carrying PyV particles in mouse fibroblasts and epithelial cells (33). Here, we show that PyV can be efficiently internalized by Jurkat cells, which do not express caveolin-1 and lack caveolae, and that overexpression of a caveolin-1 dominant-negative mutant in mouse epithelial cells does not prevent their productive infection. Strong colocalization of VP1 with early endosome antigen 1 (EEA1) and of EEA1 with caveolin-1 in mouse fibroblasts and epithelial cells suggests that the monopinocytic vesicles carrying the virus (and vesicles containing caveolin-1) fuse with EEA1-positive early endosomes. In contrast to SV40, PyV infection is dependent on the acidic pH of endosomes. Bafilomycin A1 abolished PyV infection, and an increase in endosomal pH by NH_4Cl markedly reduced its efficiency when drugs were applied during virion transport towards the cell nucleus. The block of acidification resulted in the retention of a fraction of virions in early endosomes. To monitor further trafficking of PyV, we used fluorescent resonance energy transfer (FRET) to determine mutual localization of PyV VP1 with transferrin and Rab11 GTPase at a 2- to 10-nm resolution. Positive FRET between PyV VP1 and transferrin cargo and between PyV VP1 and Rab11 suggests that during later times postinfection (1.5 to 3 h), the virus meets up with transferrin in the Rab11-positive recycling endosome. These results point to a convergence of the virus and the cargo internalized by different pathways in common transitional compartments.

Adsorption of mouse polyomavirus (PyV) on the host cell surface is mediated by the interaction of its major structural protein, VP1, with sialic acid. Recently, anionic glycosphingolipids GD1a and GT1b, which are heavily glycosylated gangliosides carrying sialic acid residues, were identified as specific receptors for PyV (37). Integrin $\alpha4\beta1$ (also sialyated) has been implicated as a possible coreceptor in mouse cells (9). For simian virus 40 (SV40), another member of the *Polyomaviridae*, the major histocompatibility complex class I molecule was described as a receptor (8). However, it was later shown that the major histocompatibility complex class I molecule is not endocytosed together with the virus (2). Tsai et al. (37) previously demonstrated that ganglioside GM1 can serve as a functional receptor for SV40. This virus enters cells via caveola invaginations that fuse with larger peripheral organelles (called caveosomes) enriched by caveolin-1. In the steps that followed, SV40 was detected in tubular, caveolin-free membrane vesicles that move along microtubules and deliver virions to the smooth endoplasmic reticulum (ER) (29). The import of SV40 into the ER was found to be brefeldin A sensitive and thus mediated by the ER-Golgi-intermediate compartment represented by COPI-coated vesicles (25, 32). The endocytic pathway exploited by PyV is not completely understood and exhibits both similarities to and differences from that of SV40. PyV is internalized into smooth, monopinocytic vesicles, which fuse with larger peripheral endosomes, often found to contain caveolin-1 (33). However, expression of a dominant-negative mutant of dynamin-1 GTPase required for the formation of caveolae (but also of clathrin-coated vesicles) did not affect polyomavirus infection in some cell types, suggesting that caveolin-1 might not be necessary for PyV uptake (13).

In our previous studies, we observed only rare colocalization of PyV with Rab5 GTPase, which is involved in the regulation of early endosome fusion. At later times postinfection (p.i.), a subpopulation of the virus was found in the perinuclear area of 3T6 fibroblasts colocalizing with Rab11 GTPase and with transferrin, markers of recycling endosomes (20). The movement of the internalized virus is accompanied by transient disorganization of actin stress fibers (15, 33), and the importance of the microtubule cytoskeleton for virus trafficking has also been demonstrated previously (15, 18, 33). At later times after adsorption (approximately 3 h), the signal of PyV, similarly to SV40, was detected in ER cisternae, where it colocalized with ER-resident protein BiP/GRP78 (endoplasmic lumenal chaperone involved in the export of abnormal proteins from the ER to the cytosol) (10). Unlike SV40, PyV infection of 3T6 fibroblasts was not substantially inhibited by brefeldin A, suggesting that PyV does not exploit COPI vesicles em-

* Corresponding author. Mailing address: Department of Genetics and Microbiology, Charles University in Prague, Viničná 5, 128 44 Prague 2, Czech Republic. Phone: 420-2-21 951730. Fax: 420-2-21 951729. E-mail: jitkaf@natur.cuni.cz.

† Present address: Public Health Sciences Division, Fred Hutchinson Cancer Research Center, Seattle, WA 98109.

ployed in retrograde transport from the Golgi apparatus to the ER. Moreover, an alternative retrograde transport from the Golgi apparatus to the ER, used by other intracellular pathogens (e.g., Shiga toxin), also seems not to be utilized by PyV, as no significant colocalization of PyV and Rab6 GTPase (coordinating that retrograde pathway) has been detected. Because PyV bypasses late endosomes that are positive for Rab7 GTPase, it is apparent that the virus can escape degradation in lysosomes (20).

In this study, we applied selected inhibitors and confocal and electron microscopy approaches to further trace the endocytic route used by PyV to establish productive infection.

MATERIALS AND METHODS

Cell line cultivation and virus. Swiss albino mouse cells (NIH 3T6) and normal murine mammary gland (NMuMG) epithelial cells were grown at 37°C in a 5% CO_2–air humidified incubator using Dulbecco's modified Eagle's medium (DMEM; Sigma) supplemented with 4 mM L-glutamine and 10% fetal calf serum (FCS). The culture medium of cells expressing green fluorescent protein (GFP) fusion proteins was further supplemented with 0.5 mg/ml G418 (Sigma). Jurkat cells (human leukemic T-lymphoblast cells, clone E6-1, TIB 152; kindly provided by V. Hoňejší, IMG AS CR, Prague, Czech Republic) were cultivated in RPMI medium (Sigma) supplemented with 4 mM L-glutamine and 10% FCS. For virus infections, mouse polyomavirus (strain A3) was used at the indicated multiplicities of infection (MOIs).

GFP constructs and cell lines. A plasmid DNA construct expressing GFP-tagged caveolin-1 was a gift from Andre Le Bivic (IBDM, Marseille, France). Caveolin-1–GFP was produced by the fusion of GFP to the C terminus of caveolin-1 in the pEGFP-C2 cloning vector (Clontech). pCINeo/IRES-GFP/cav-1 DN (bicistronic expression vector for dominant-negative caveolin-1 [deletion of amino acids 1 to 81]) was a gift of Jan Eggermont (Katholieke Universiteit, Leuven, Belgium) (36). Constructs expressing GFP-fused mutant Eps15 (DIIIΔ2, DIII, and EΔ95/295) cloned into pEGFP-C2 were gifts from Alexandre Benmerah (URA-CNRS, Paris Cedex, France) and were described elsewhere previously (5, 6). For the assay for evaluating the efficiency of PyV infection, vector γEGFP-N1 (Clontech) was used as a positive control. Vectors for expression of GFP-fused wild-type Rab5 and a dominant-negative mutant of Rab5 S34N were kindly provided by P. D. Stahl (Washington University School of Medicine) (19). All GFP constructs were transfected to mouse 3T6 fibroblasts or NMuMG cell lines by electroporation. Briefly, exponentially grown cells (1 day after the passage) were trypsinized, and the homogenized cell suspension (1×10^7 cells) was pelleted. Cells were resuspended in 1 ml OPTIMEM-I medium (Gibco) with 10 to 20 μg DNA. Two hundred microliters of the suspension was electroporated using a Gene Pulser apparatus (Bio-Rad) set at 960 μF, 1,000 Ω, and 300 V with a pulse length of 60 to 70 ms. Transfected cells were diluted 1:20 into fresh complete DMEM and grown for 48 h. Stable cell lines expressing GFP-tagged proteins were established by subcloning and maintaining cells upon G418 (Sigma) selection antibiotic in DMEM supplemented with 10% fetal calf serum (Gibco).

Virus. Mouse polyomavirus (A2 strain) was isolated from infected whole mouse embryo primary culture cells according to the standard protocol and purified to homogeneity by CsCl and sucrose gradient ultracentrifugation. The quality of preparation was confirmed by Coomassie blue-stained sodium dodecyl sulfate-acrylamide gel electrophoresis and electron microscopy (EM) (negative staining). The amount of virus particles was estimated by hemagglutination and by protein concentration analysis. For microscopy of living cells, virions were labeled with the red fluorescent marker Alexa-594 coupled with an amine-reactive probe (carboxylic acid succinimidyl ester [purchased from Molecular Probes]) according to the following labeling procedure: purified virus was dialyzed in 0.1 M carbonate buffer (pH 8.3), and 1 mg of the virus with 0.1 mg of the fluorescent reagent was incubated for 1 h at room temperature and then incubated overnight at 4°C. The separation of the conjugate from unreacted labeling reagent was made by extensive dialysis and subsequent purification of the virus on a 10 to 40% sucrose gradient. The virus was aliquoted and stored at −20°C before use. The optimal degree of labeling (ratio of virus to fluorescent marker) was assessed and improved to ensure that natural virus infectiveness was not affected. Briefly, Alexa-594-prestained virus was used to infect cells, and after fixation, coimmunolabeling with anti-VP1 antibody was performed, followed by green Alexa-488 secondary antibody staining. Colocalization of red and green signals proved that all viral particles were conjugated with red Alexa-594 dye, while the VP1 immunoepitope remained available for anti-VP1 antibody binding.

Virus tracking. For live microscopy, cells expressing enhanced GFP-caveolin were grown on 40-mm glass coverslips in phenol red-free DMEM. The cell cycle was synchronized by starving cultured cells in DMEM supplemented with 0.5% serum for 24 h before infection. Coverslips were mounted in an open metal chamber system maintained at 37°C and overlaid with fresh medium. To avoid rapid temperature changes and microtubule depolymerization at 4°C, all procedures were performed at 37°C with prewarmed media and solutions. Virus was diluted with serum-free culture medium and added to cells at an MOI of 100 to 1,000 particles/cell. Unbound virus was gently washed away after 30 min, and complete culture medium was added. Internalization of the virus by the host cells and cytoplasmic transport were monitored at the indicated times postinfection by time lapse live imaging using confocal microscopy. We used a Leica TCS SP2 AOBS confocal microscope operating with an argon laser (458, 476, 488, 496, and 514 nm; 10 mW) and with an HeNe laser (543 and 594 nm; 1 mW). Cells were examined with a 1.2-numerical-aperture water immersion objective (×60). According to the specific signal-to-noise ratio and GFP level of expression, we applied different sampling frequencies (ΔT = 1 to 6 s). Sequential scanning between channels was used to separate fluorescence emission from different fluorochromes and to completely eliminate bleed-through channels. Leica confocal software was used for live microscopy. Video sequences and images were processed by Image J (NIH, Bethesda, MD) and Adobe Photoshop 7.0 (Adobe Systems, San Jose, CA), respectively.

Relevance of caveolin for virus entry. Jurkat cells were infected with either PyV or SV40 (MOI of 3×10^3 virus particles per cell) or incubated with cholera toxin B subunit (CTb) (fluorescein isothiocyanate labeled and diluted to a final concentration of 0.5 μg/ml; Sigma) for 90 min at 37°C and then washed with RPMI-FCS and incubated another 2 h (PyV or SV40) or 1 h (CTb) before fixation. Cells were immunostained for PyV VP1, SV40 VP1, clathrin light-chain subunit, EEA1 marker of early endosomes, or α-tubulin. DNA was stained with DAPI (4′,6′-diamidino-2-phenylindole). For EM, PyV-infected cells were fixed with 3% glutaraldehyde in 0.1 M cacodylate buffer, pH 7.4, at the appropriate time p.i., postfixed with 1% osmium tetroxide, dehydrated in graded ethanol solutions, and embedded in epoxy resin AGAR 100 (Gröpl, Tuln, Austria) as described previously (33). Ultrastructural analysis was performed on ultrathin sections stained with uranyl acetate and lead citrate. The samples were examined with a JEOL JEM 1200EX electron microscope.

Role of endosomal pH in PyV infection. The cell cycle of 3T6 or NMuMG cells was synchronized by starvation (24-h incubation in DMEM supplemented with 0.5% FCS). Cells were then treated with bafilomycin A1 (0.5 μM) or ammonium chloride (NH_4Cl) (1 mM or 5 mM) for a total interval of 4 h, starting 2 h prior virus addition, immediately after adsorption, 2 h postadsorption, or 4 h postadsorption. Virus adsorption to cells was performed within a 30-min interval on ice. Nonadsorbed virus was washed out, DMEM (warmed to 37°C) with 10% FCS (with or without a drug) was added, and cells were then incubated at 37°C in a 5% CO_2–air humidified incubator. In the case of drug treatment in the interval of −2 to +2 h postinfection, the adsorption of the virus was performed in the presence of drugs, but the time of adsorption was not included in the 4-h interval. At the end of drug treatment, the cells were washed, incubated for 24 h with freshly added complete DMEM, fixed, and immunostained with antibody against PyV early large T (LT) antigen. Numbers of infected cells were scored by immunofluorescence microscopy.

Immunofluorescence staining. At the indicated times postinfection (MOI of 10^2 to 10^3 virus particles per cell), cells grown on coverslips were washed three times with phosphate-buffered saline (PBS), fixed with 3% paraformaldehyde in PBS (30 min), and permeabilized with 0.5% Triton X-100 in PBS (10 min). After washing in PBS, cells were incubated with 0.25% bovine serum albumin and 0.25% porcine skin gelatin in PBS. Immunostaining with primary and secondary antibodies was carried out for 1 h and 30 min, respectively, with extensive washing with PBS after each incubation. The following primary antibodies were used: monoclonal rat anti-PyV LT (kindly provided by B. E. Griffin, Imperial College of Science, Technology, and Medicine at St. Mary's, London, United Kingdom), polyclonal rabbit anti-PyV VP1 (prepared in our laboratory), rabbit anti-SV40 VP1 (kindly provided by H. Kasamatsu, University of California—Los Angeles), mouse anti-α-tubulin (Exbio), mouse anti-transferrin antibody (Exbio), goat anti-EEA1 (Santa Cruz), mouse Con-1 antibody against clathrin light-chain subunit (24), rabbit polyclonal anti-caveolin-1 (Santa Cruz), rabbit anti-Rab11 (Zymed), and rabbit anti-GFP (Abcam). The following secondary antibodies were used: chicken anti-rabbit, goat anti-rabbit, donkey anti-rat, donkey anti-goat, and donkey anti-mouse conjugated with Alexa Fluor-488; goat anti-mouse conjugated with Alexa Fluor-546; and chicken anti-rabbit conjugated with Alexa Fluor-647 (all purchased from Molecular Probes). For fluorescent reso-

nance energy transfer (FRET) analysis, Cy3-conjugated anti-mouse and Cy5-conjugated anti-rabbit secondary antibodies (purchased from Sigma) were used.

Colocalization assessment of confocal dual-color images. The following two requirements had to be satisfied to consider a given position as colocalization: (i) fluorescent signal-emitting molecules labeled with different fluorochromes should occupy the same pixel in the image, and (ii) the intensity of each component of the image should be within a certain range (in other words, the fluorochrome pairs with very different signal intensities should not be considered as colocalizing). To accommodate these conditions, we studied colocalization on the scatter plots of the signal intensities detected by two separate channels. In these plots, dimmer pixels are located close to the origin, brighter pixels are situated further out, and pure (red and green) pixels are clustered close to the axis. If colocalizing pixels are present, they are displayed (depending on the degree of colocalization) closer to the middle of the plot. We selected a field in the scatter plot that represents pixels in the image where colocalization in both channels occurs. We defined it as a region with its origin in the diagonal of the plot (maximum colocalization) and at coordinates that define the upper limit for the background intensity in the image. In this way, we could mark pixels that colocalize without taking into account pixels with a low intensity value, where the background intensity has high influence and pixels near the axis of the plot, which can represent bleed-through channels and false colocalization. In conclusion, in this mode, we considered pixels as colocalizing only when they were near the diagonal of the plot, and data pairs with very different signal intensities only in the case that both intensities were indeed high.

FRET by acceptor photobleaching method. 3T6 cells grown on coverslips were incubated with PyV (MOI of 10^2 to 10^3 virus particles per cell) or with both PyV and transferrin (1 ng per 10^5 cells) for 30 min on ice before a shift back to 37°C. Cells were fixed for 1.5 or 3 h after the shift and immunostained with anti-VP1- and anti-transferrin- or anti-Rab11-specific antibodies followed by secondary antibodies conjugated with Cy3 and Cy5, respectively. FRET efficiency (E_f) was calculated using the following formula: $E_f = (D_{post} - D_{pre}) \times 100/D_{post}$, where D_{post} and D_{pre} are the fluorescence intensities of the donor molecule after and before bleaching of the acceptor, respectively (4). This formula yields the increase in Cy3 fluorescence following Cy5 bleaching normalized by Cy3 fluorescence after the bleaching. We used a Leica SP2 AOBS confocal microscope operating with an HeNe laser tuned to lines at 543 nm (1.2 mW) to excite the Cy3 dye and at 633 nm (10 mW) to excite the Cy5 dye. Cells were examined with a ×63 1.4-numerical-aperture oil immersion objective.

RESULTS

PyV utilizes caveolin-1-rich domains for internalization and trafficking. Our previous electron microscopic analysis of polyomavirus entry revealed ultramorphological similarities between PyV and SV40 uptake. We observed that PyV is not associated with clathrin-coated pits at the cell surface and that virion-loaded endocytic vesicles are devoid of the typical clathrin coat (33). In agreement with those previous findings, we now demonstrate that PyV does not colocalize with Con-1 (marker of clathrin-coated pits) at 20 min p.i. (Fig. 1A). The time of fixation and screening was chosen on the basis of a kinetic study of PyV internalization by cells (not shown).

We further tested the effects of epidermal growth factor receptor pathway substrate receptor clone 15 (Eps15) mutants that inhibit clathrin endocytosis. For this purpose, we prepared cell lines expressing the GFP-fused dominant-negative mutants DIII and EΔ95/295 (5, 6), respectively, which compete for binding of the AP-2 clathrin adaptor with endogenous Eps15. The efficiency of infection in these cell lines was compared with that in control, nontransfected cells; cells expressing GFP alone (pEGFP-N1); or cells transfected with the control Eps15 mutant DIIIΔ2 (not binding AP-2 α-adapting subunit and therefore not affecting the efficiency of clathrin endocytosis). The inhibition of clathrin endocytosis in the mutant cell lines was verified by the analysis of transferrin uptake (not shown). As expected, overexpression of GFP-fused dominant-negative mutant Eps15-DIII or Eps15-EΔ95/295 did not reduce the efficiency of PyV infection (Fig. 1B). Moreover, the efficiency of infection was slightly enhanced in comparison with that assessed in all three control cell lines. A much more significant increase (approximately 100%) in the efficiency of PyV infection was observed in cells overexpressing the wild-type caveolin-1–GFP fusion protein (Fig. 1B).

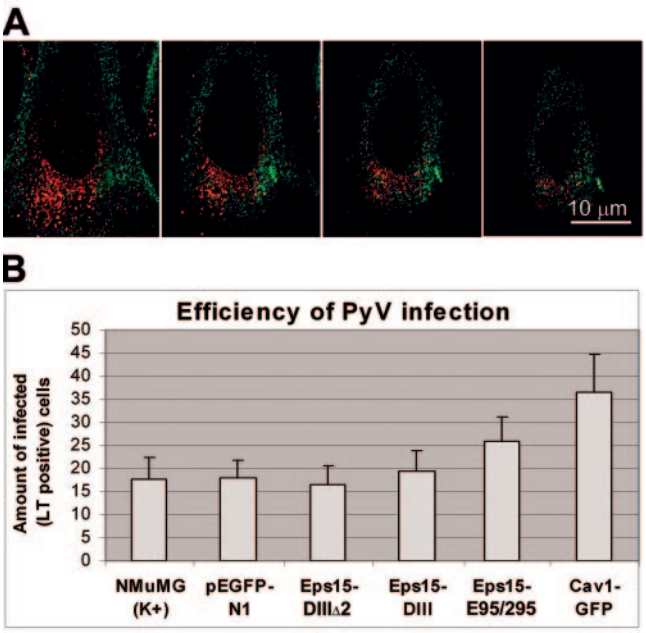

FIG. 1. Polyomavirus entry and efficiency of infection are clathrin independent. (A) Virions do not colocalize with the clathrin marker. 3T6 cells were infected with PyV (MOI of 10^2 PFU/cell) and fixed 20 min p.i. Immunofluorescence staining of VP1 (green) and the clathrin light-chain subunit (red) was performed. Four merged confocal sections of an infected cell are shown. (B) Efficiency of PyV infection in host NMuMG cells is not reduced by overexpression of dominant-negative Eps15 mutants. Cell lines expressing Eps15 mutants strongly inhibiting clathrin endocytosis (Eps15-DIII and Eps15-EΔ95/295, respectively) are compared with control cells (NMuMG K^+, nontransfected cells; pEGFP-N1, cells expressing GFP alone; Eps15-DIIIΔ2, cells transfected with a control mutant not interfering with clathrin endocytosis; Cav1-GFP, cells overexpressing caveolin-1–GFP). Infected cells were detected by the antibody against PyV large T antigen. Data represent the average values of 30 optical fields of infected cells from each of three independent experiments.

To visualize a direct involvement of caveolin-1-positive membrane domains in living cells, we established a cell line of mouse epithelial cells expressing GFP-tagged caveolin-1. Live imaging of these cells showed that when caveolin was overexpressed, it still retained its ability to segregate into the surface membrane domains and was also present in intracellular mobile vesicles, pausing at the perinuclear area. Time lapse series have proven that the formation of caveolar invaginations and membrane fission and fusion events were not affected in this cell line (Fig. 2a). We also show here that caveolin-GFP membrane domains are highly dynamic.

When GFP-caveolin cells were infected with fluorescently labeled virus, we observed its movements in directions parallel to the cell surface at the peripheral (apical) cell confocal section. Virions were seen to bypass immobile plasma membrane-anchored caveolar domains (Fig. 2b). However, at least a fraction

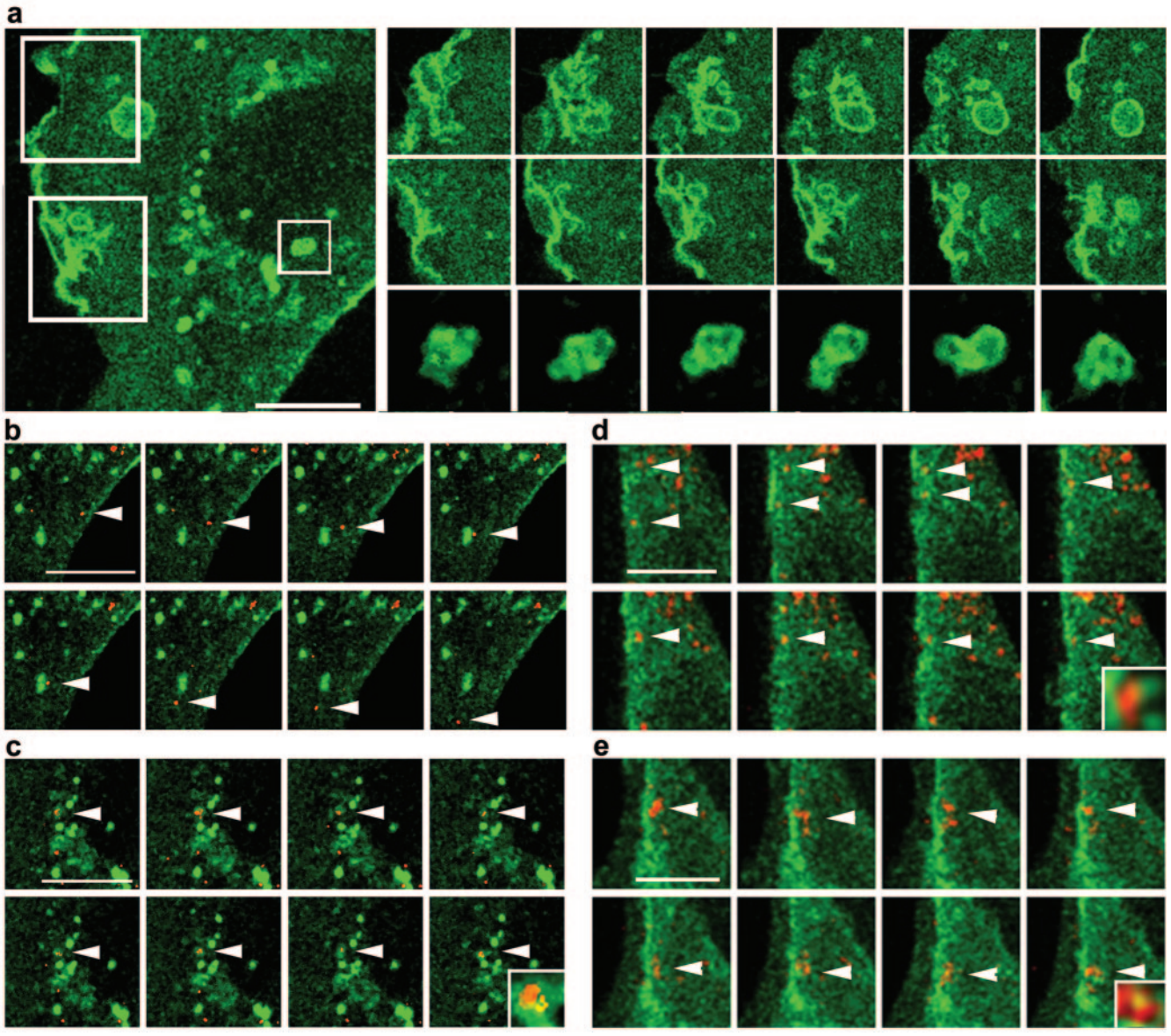

FIG. 2. Virus tracking in living NMuMG epithelial cells expressing GFP-fused caveolin-1. (a) Caveolar endocytosis, fission and fusion events, and internal vesicle membrane dynamics are shown not to be affected in a stable cell line. (b) Detail of an infected cell (in a surface confocal section) with a virion bypassing a caveolin-rich domain. (c) In-depth confocal section with a virion(s) captured in a caveolin-rich vesicle at the nuclear periphery. (d and e) Uptake of virions through caveolin membrane domains at the cell surface. Mouse NMuMG epithelial cells expressing GFP-tagged caveolin-1 were infected with Alexa 594-prestained virus (MOI of 10^3 virus particles per cell) and scanned in an open, medium-containing chamber with a ΔT of 6 s. Selected frames are shown in detail (see CavA1, CavA2, caveosome, and CavB-CavE movies at http://www.natur.cuni.cz/molbio/virology/suppl.html). Bars, 5 μm (a to c) and 2 μm (d and e).

of endocytosed virions was internalized through caveolin-rich domains (Fig. 2d and e), and a virion(s) captured in the immobile caveolin-1-positive membrane compartment at the nuclear periphery was also observed (Fig. 2c). These observations are in agreement with our hypothesis that mouse PyV can follow alternative trafficking pathways in the host cell.

Caveolin is not necessary for PyV internalization. The evidence for the exploitation of caveolae and/or cavicles (vesicles derived from caveolae) for mouse PyV entry and trafficking is still controversial. Previously, Gilbert and Benjamin (13) did not detect a connection between caveola-mediated endocytosis and polyomavirus uptake in 3T3 fibroblasts and in BMK cells (baby kidney cells). However, later, they showed that when rat glioma C6 cells (which are deficient for complex gangliosides and thus poorly susceptible to PyV infection) were supplemented with GD1a ganglioside, they became infected with PyV with a much higher efficiency. Moreover, the virus entry pathway in these cells was dependent on functional caveola endocytosis (14).

In our previous experiments using different cell lines or different infection conditions, the extent of PyV and caveolin colocalization varied. To address the relevance of caveolae for

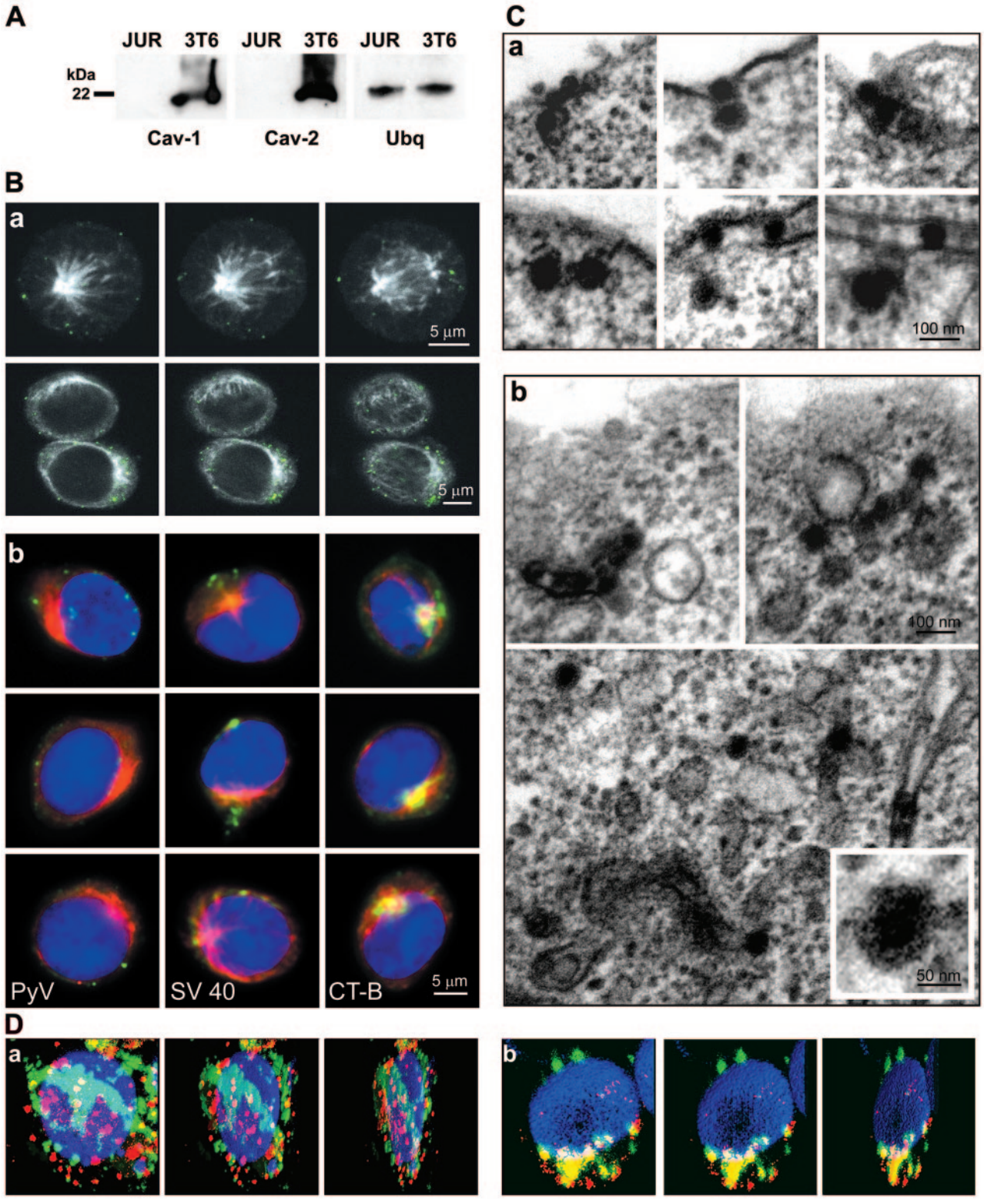

FIG. 3. Virions of PyV enter Jurkat cells. (A) Jurkat cells lack caveola essential protein. Westen blot of Jurkat (JUR) and 3T6 (control) cell lysates immunostained with anti-caveolin-1, anti-caveolin-2, and ubiquitin (Ubq) (loading control) is shown. (B) (a) Uptake of PyV by Jurkat cells. Cells were infected with PyV (MOI of 3×10^3 PFU/cell) and fixed 3 h p.i. Immunofluorescence staining of VP1 (green) and tubulin (white) was performed. Three sequential merged confocal sections from different cells are shown. (b) PyV VP1, SV40 VP1, and cholera toxin B fragment (CT-B) enter Jurkat cells. Jurkat cells were infected with either PyV or SV40 (MOI of 3×10^3 virus PFU/cell) or incubated with the cholera toxin B subunit (fluorescein isothiocyanate labeled). Cells were immunostained for PyV VP1 (green) or SV40 VP1 (green) and α-tubulin (red). DNA was stained with DAPI. Merged images are shown. (C) Electron microscopy of Jurkat cells. (a) At early times after infection (1 h p.i.), virions are

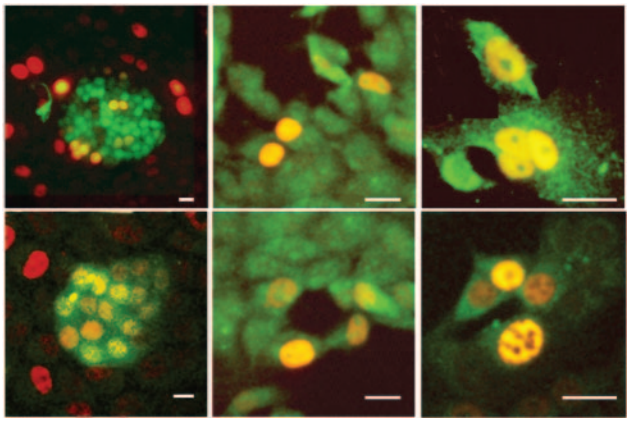

FIG. 4. Expression of a dominant-negative mutant of caveolin-1 does not prevent productive PyV infection. NMuMG cells were transfected by pCINeo/IRES-GFP/cav-1 DN (bicistronic expression vector for dominant-negative caveolin-1), and 10 days later, cells were infected with PyV. Cells were fixed and immunostained for PyV LT antigen (red) 24 h p.i. Transfected cells are shown in green. Bars, 20 μm.

PyV internalization and trafficking, we monitored the uptake of PyV by Jurkat cells, which do not express caveolin-1 and lack functional caveolae. The absence of caveolin-1 in Jurkat cells was confirmed by Western blot analysis of cell lysates using anti-caveolin-1 and anti-caveolin-2 antibodies (Fig. 3A). As shown on confocal sections of Jurkat cells labeled for tubulin and VP1, PyV virions entered cells, and their signal was found spread in the cytoplasm (Fig. 3B). Electron microscopy of ultrathin cell sections showed that the internalizing invaginations and monopinocytic vesicles were morphologically similar to those found in caveolin-positive fibroblasts or epithelial cell lines (Fig. 3C). In agreement with observations by EM, immunofluorescent staining of Jurkat cells for PyV VP1 and Con-1 (clathrin light-chain subunit) did not detect substantial colocalization of PyV with clathrin (Fig. 3D, panel a). CTb and SV40 (both with binding affinity to ganglioside GM1 as a receptor) were internalized by Jurkat cells, but in contrast to PyV, their signal was found concentrated in the perinuclear area colocalizing with microtubule-organizing center (MTOC) at the same time postinfection (Fig. 3B, panel b). Our experiments demonstrate that PyV, SV40, and cholera toxin, all exploiting caveolar endocytosis to enter cells and join their own specific trafficking route, can also be internalized by cells lacking caveolin through an alternative (clathrin coat-independent and caveolin-independent) endocytic pathway.

Transient expression of a dominant-negative mutant of caveolin-1 in NMuMG cells did not prevent infection by PyV (Fig. 4). The ratio of infected cells to uninfected cells was not significantly diminished for green (caveolin-1 mutant-expressing) cells in comparison with nontransfected control cells.

PyV enters early endosomes. To further investigate the character of compartments through which virions are transported during postendocytic steps, we monitored mutual colocalization of EEA1 (early endosome antigen), PyV, and caveolin-1 in 3T6 and NMuMG cells. While previous experiments performed with Rab5 GTPase (20) showed only rare colocalization with the major PyV capsid protein, VP1, we now observed a high extent of colocalization of EEA1 and VP1 beneath the cell membrane 30 min p.i. (Fig. 5A, panel a). Because a high proportion of entering PyV virions colocalized with GFP–caveolin-1 (Fig. 5A, panel b), we were interested in whether both EEA1 and caveolin-1 overlap, being components of the same early endosome. Figure 5A, panel c, shows a high proportion of colocalization of both signals. Thus, we conclude that after internalization of mouse PyV through membrane raft domains rich in caveolin-1, monopinocytic vesicles fuse with early endosomes (defined by the presence of EEA1) into a common endocytic compartment. Figure 5B demonstrates not only that the presence of EEA1 and caveolin-1 on the same compartments is the result of fusions induced by virus invasion but also that the compartments possessing both caveolin-1 and EEA1 markers occur in noninfected 3T6 fibroblasts. In enlarged details of the merged picture, small endosomes as well as large caveolin-1-positive compartments with distinct patches of EEA1-positive domains (similar to those observed previously by Pelkmans et al. in HeLa cells) (28) can be seen.

PyV infection is dependent upon acidic pH of endosomes. In order to determine whether a transient presence of PyV in the acidic endosomes is necessary for productive infection, we examined the effects of ammonium chloride and bafilomycin A1. NH_4Cl penetrates into endosomes and increases endosomal pH, whereas bafilomycin A1 (a specific inhibitor of vacuolar H^+ ATPase) prevents acidification of endosomes. Bafilomycin A1 (at a concentration as low as 0.5 μM) completely abolished PyV infection of 3T6 and NMuMG cells when applied 2 h prior to infection and left in medium for an additional 2 h after the addition of the virus (Fig. 6). Treatment by NH_4Cl (at a concentration of 1 mM) inhibited infection of 3T6 and NMuMG cells by approximately 85% and 65%, respectively, compared to untreated controls. Virus infectivity diminished with increasing NH_4Cl concentrations. The inhibition effect of an elevated endosomal pH was also obvious when NH_4Cl or bafilomycin A1 was added to cells immediately after adsorption of the virus. However, no effect on the efficiency of PyV infection was observed when cells were exposed to the agent 2 h (and later) after virus adsorption, at the time when the virus left early endosomal compartments and was transported further to the nuclear periphery.

Furthermore, we tried to determine the particular step in which virus trafficking is affected when acidification of endosomes is blocked. Substantial colocalization of virus and EEA1 was observed in both treated and nontreated cells 20 min postinfection

internalized into membrane vesicles. (b) At later times postinfection (3 h p.i.), vesicles fuse into multivirion compartments (lower panels). (D) (a) PyV (red) does not colocalize with clathrin (green). (b) PyV(red) colocalizes with the EEA1 marker of early endosomes (green). Jurkat cells, 30 min p.i. PyV was labeled with Alexa Fluor 594, clathrin and EEA1 are shown in green (mouse Con-1 and goat anti-EEA1 followed by goat anti-mouse and donkey anti-goat Alexa-488), and DAPI is shown in blue. Shown is a three-dimensional rendering from 25 confocal sections with tilt angles of 0°, 40°, and 80° (from left to right).

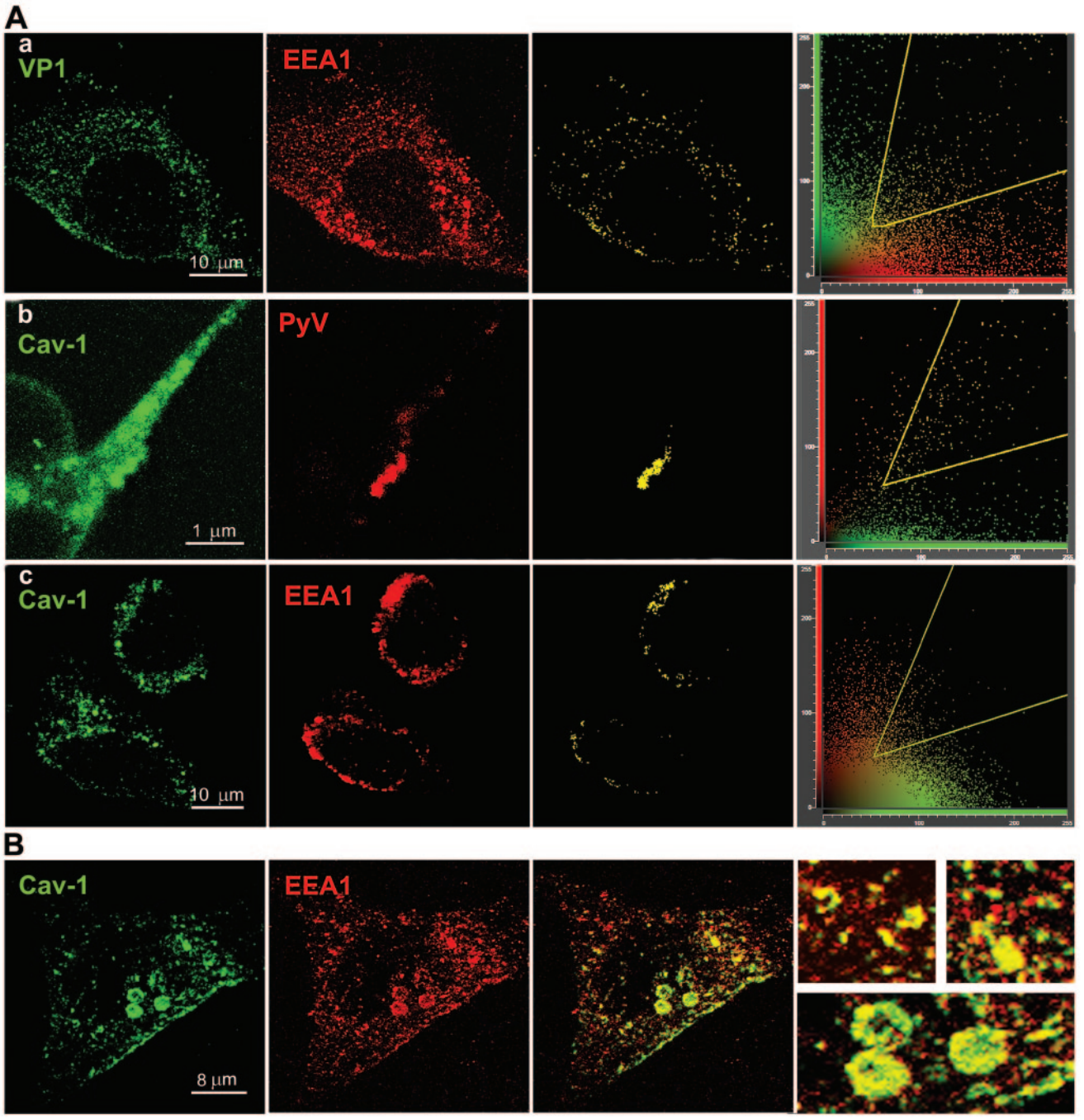

FIG. 5. (A) Endocytic markers Cav-1 and EEA1 colocalize with VP1 of incoming PyV virions. Shown are selected confocal sections of immunostained NMuMG cells infected and fixed 30 min p.i. (a) Distribution of VP1 (green) and EEA1 (red); (b) distribution of caveolin-1 (green) and VP1 (red); (c) distribution of caveolin-1 (green) and EEA1 (red). The third image of each panel represents colocalization signals (yellow) corresponding to those selected by scatter plot in the fourth image. (B) Caveolin-1 and EEA1 occur in common endocytic compartments in uninfected NMuMG cells. Shown is a selected confocal section of NMuMG cells immunostained for caveolin-1 (green) and EEA1 (red). Enlarged details of the third, merged image are presented in the fourth panel.

by confocal microscopy (Fig. 7A). However, 4 h postinfection, when the virus exited early endosomes in control, untreated cells, a substantial colocalization of VP1 and EEA1 was still observed in cells treated with bafilomycin A1 or NH_4Cl (Fig. 7B).

These data indicate that the acidic milieu of endosomes is necessary for productive PyV infection of the host cells. When pH is increased (or acidification is blocked), the virus is still able to enter early endosomal compartments, but its exit and further trafficking are suppressed. Accordingly, overexpression of the dominant-negative mutant of Rab5 (Rab5S34N) reduced PyV infection markedly, while overexpression of wild-type Rab5 had no inhibition effect (not shown).

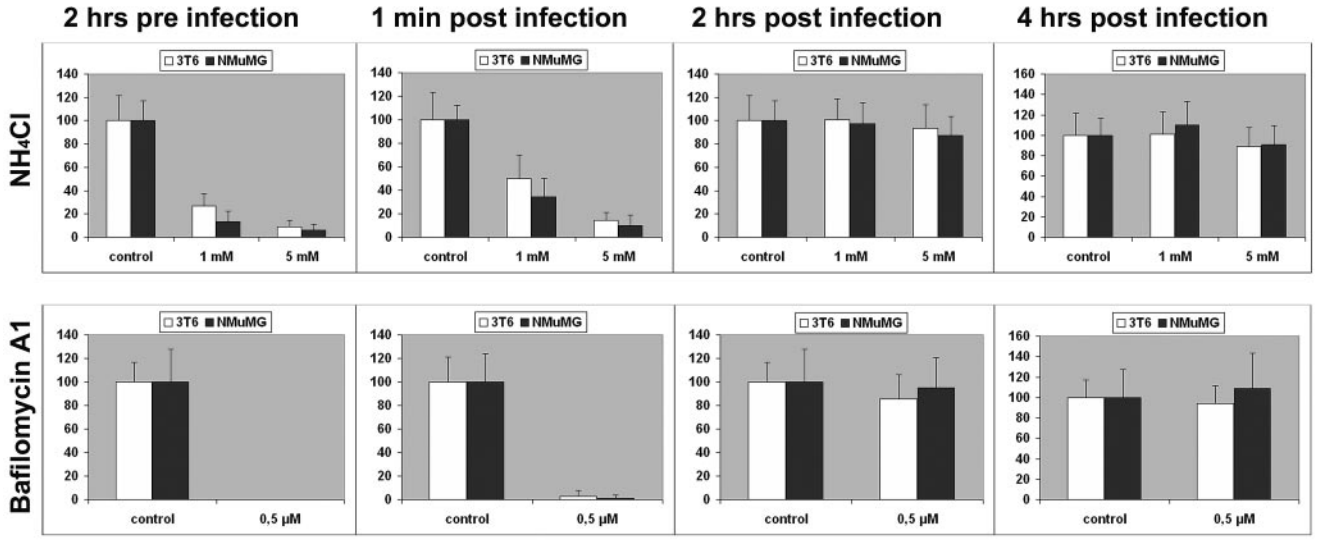

FIG. 6. Treatment of cells with NH_4Cl and bafilomycin A1 affects PyV infection. 3T6 and NMuMG cells were treated starting 2 h prior to infection, immediately (1 min) after infection, 2 h postinfection, and 4 h postinfection, and the drug was left in the medium for a 4-h interval. Cells were fixed 24 h p.i. and stained for PyV LT antigen. Positive cells were scored by immunofluorescence microscopy. Control cells were infected with PyV in the absence of the drug (mock). The values in the graphs refer to the percentages of infected cells relative to the control (mock) and represent the average values of at least 30 optical fields of cells from each of two (NMuMG) or three (3T6) independent experiments.

PyV and transferrin meet in Rab11-positive endosomes. As we have shown previously (20), PyV VP1 colocalizes with both transferrin and Rab11 GTPase between 1 and 3 h postadsorption. At the same time, partial colocalization of PyV VP1 with the BiP/GRP78 marker of the ER was demonstrated.

Various endosomal compartments, including caveosomes and recycling endosomes, accumulate in the perinuclear space near the MTOC (22, 27). The resolution of a confocal microscope (≥200 nm) is not sufficient to distinguish whether PyV and transferrin are present in the same endosomal compartment, particularly in such a crowded area of the cytoplasm. To circumvent this limitation, we used FRET, a method to detect protein colocalization at a 2- to 10-nm resolution. The range over which FRET between the donor (Cy3) and acceptor (Cy5) fluorescent molecule occurs is given by the spectral parameter R_0, i.e., the distance at which the FRET efficiency is 50%. R_0 for the Cy3-Cy5 system is 5 nm (4). Cells were bleached in the Cy5 channel by scanning a region of interest (ROI) using the 633-nm HeNe laser line at 100% intensity. We performed FRET in 15 different cells and bleached more then 60 different ROIs. Before and after the bleaching, Cy3 images were collected to assess changes in donor fluorescence. Figure 8A, panel a, shows the images of the donor (transferrin, Cy3) and the acceptor (VP1 PyV, Cy5) before and after photobleaching in the ROI marked in the figure. Fig. 8A, panel b, presents the intensity value in the ROIs marked on Fig. 8A, panel a.

As a control, we performed a similar calculation in the same number of nonbleached regions of the specimen to evaluate background FRET signals. We calculated the histogram distribution of FRET efficiency for the bleached and nonbleached regions. Distribution of FRET efficiency for bleached regions is positive-shifted from the pseudo-FRET efficiency observed in the nonbleached regions (histogram in Fig. 8A, panel c). The average FRET efficiency values between transferrin and PyV were 9.3 ± 6.9 for the bleached ROIs, which represent the true FRET, and an average value of 2.3 ± 3.2 for the nonbleached ROIs, which represent the background (or false) FRET.

We were further interested in whether the membrane compartments carrying both PyV and transferrin are recycling endosomes. Therefore, we repeated the experiments with Cy3-labeled Rab11 and measured the FRET efficiency of selected ROIs (Fig. 8B). Fig. 8B, panel b, represents intensity values in the ROIs marked on the images (Fig. 8B, panel a), and the FRET efficiency distribution is shown on the histogram (Fig. 8B, panel c). We calculated the FRET efficiency in 60 different ROIs from 14 different cells. An average value of 4.8 ± 2.8 for the bleached ROIs (representing the true FRET) has been assessed. An average value of 2.21 ± 3.6 for background FRET, or false FRET (from the nonbleached ROIs), has been obtained. We obtained very similar background FRET (false FRET) values for both transferrin and Rab11 under the same sample conditions (type of cells, virus, fluorescence donor, and acceptor) and the same acquisition conditions (objective and laser lines). Moreover, in both experiments, we obtained a positive-shifted distribution of FRET efficiency in respect to the nonbleached regions and average values of FRET efficiency higher than those of background FRET. The conclusion can be made that both Rab11 and transferrin exhibit a true FRET and that PyV and transferrin are in intimate contact in a Rab11-positive compartment.

DISCUSSION

Despite intensive studies on the early events of mouse polyomavirus infection, the mechanism of virus uptake and trafficking in the host cell still remains puzzling. Even closely related viruses such as SV40 and human JC virus differ in their modes of entry and subsequent trafficking. JC virus uses the

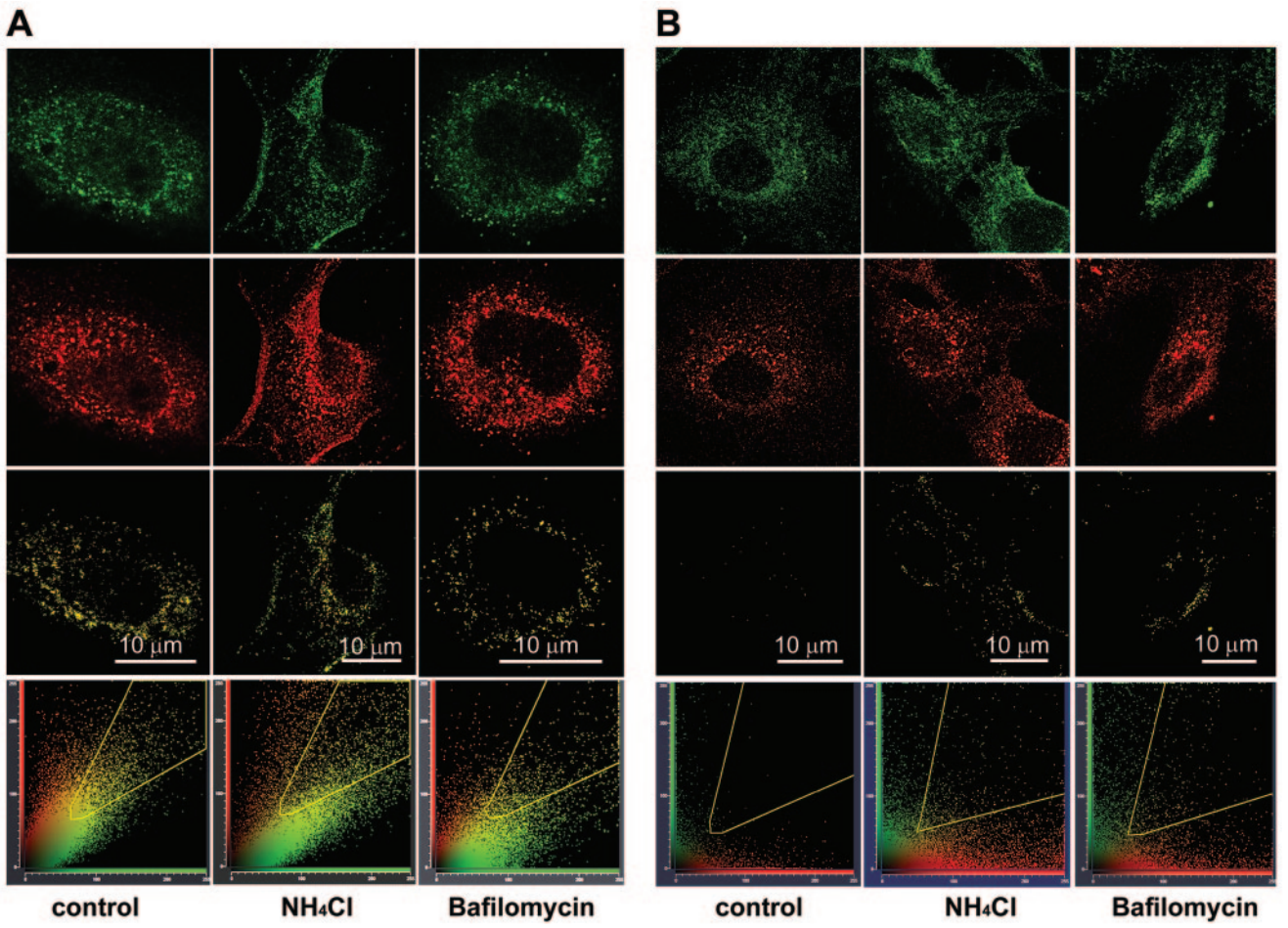

FIG. 7. Incoming PyV (VP1 signal; green) is trapped in early endosomes, when acidification is blocked by NH_4Cl or bafilomycin A1. (A) At early times postinfection (30 min), colocalization of VP1 with the EEA1 marker is strong in both control and drug-treated cells. (B) At later times postinfection (4 h p.i.), residual but significant colocalization of VP1 and EEA1 was detected only in drug-treated cells. VP1, green; EEA1, red. The third image (from the top) of each panel represents colocalization signals (yellow) corresponding to those selected by scatter plot in the fourth image.

classical endocytic pathway via clathrin-coated pits to enter early endosomes (30), while SV40 is internalized by caveolae (1). Also, another human polyomavirus, BK virus, is dependent on an intact caveolin-1 scaffolding domain to enter the host cell (11). The role of lipid raft microdomains in PyV entry is also unclear. Treatment of cells with cholesterol-depleting agents such as methyl-β-cyclodextrin, which disrupts detergent-resistant lipid rafts, revealed controversial results, most likely due to the different PyV strains and cell lines used (13, 15, 33). We have previously shown the presence of caveolin-1 on monopinocytic vesicles carrying PyV virions (33). Observations of interactions of PyV with caveolin-1 domains and compartments in living cells revealed that some PyV particles enter cells through caveolin-1-rich domains, while others bypass them, and at later times postinfection, the signal of PyV can be seen in large caveolin-1-rich compartments in the perinuclear space (Fig. 2; see movies at http://www.natur.cuni.cz/molbio/virology/suppl.html). Is caveolin-1 indeed necessary for PyV infection? Many toxins that are transported from the cell surface to the ER utilize ganglioside receptors similar to those of polyomaviruses (37). CTb exploits the same GM1 type of ganglioside as SV40 (16). The CTb enters cells via caveolae but can also be efficiently internalized in cells lacking caveolin-1 by a cholesterol-dependent process (26). We show here that in Jurkat cells that do not express caveolin, not only CTb but also SV40 (Fig. 3Bb) was efficiently endocytosed, and both antigens exhibited similar pericentriolar localization. The uptake of PyV occurred as well, but the virus signal remained spread within the cytoplasm. Nevertheless, no colocalization of clathrin with PyV was observed in Jurkat cells, and ultrastructural analysis proved that PyV virions were internalized in smooth, tightly fitting vesicles morphologically similar to those of caveolin-1-positive mouse fibroblast or epithelial cells (33). Moreover, expression of a dominant-negative mutant of caveolin-1 in NMuMG epithelial cells did not prevent their productive infection by PyV.

In mouse fibroblasts or in epithelial cells, virus-loaded monopinocytic vesicles were often shown to fuse with peripheral endosomes early after internalization (33). Therefore, we further examined the characteristics of these compartments. Colocalization of PyV with the early endosome antigen EEA1 has shown that the majority of the virus entered early endo-

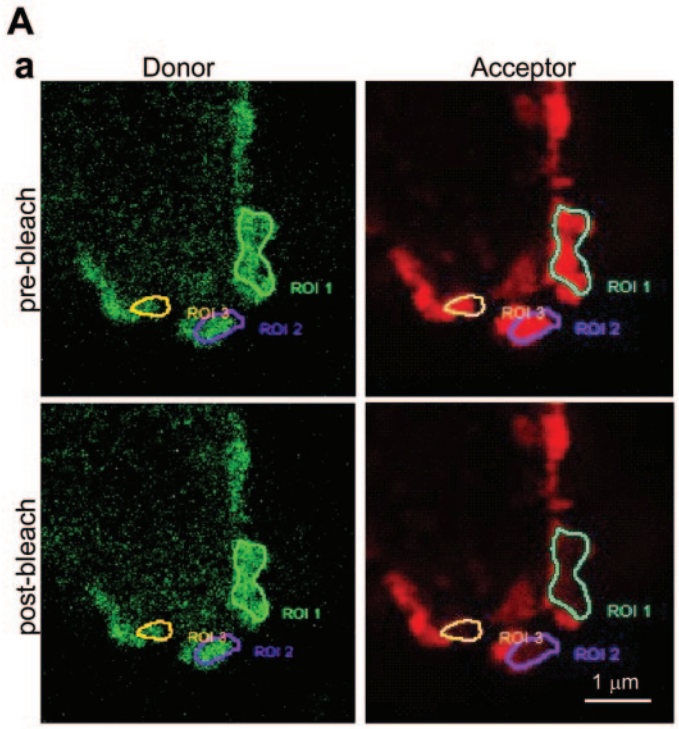

b

ROI	ROI_1	ROI_2	ROI_3
D pre	90.04	89.27	54.89
D post	103.75	103.17	59.73
A pre	125.13	121.48	90.29
A post	33.69	39.77	23.50
FRETeff (%)	13.22	13.47	8.11

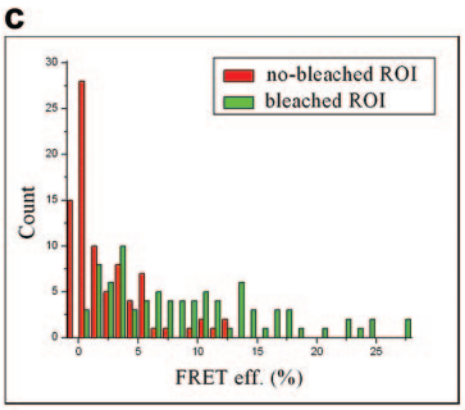

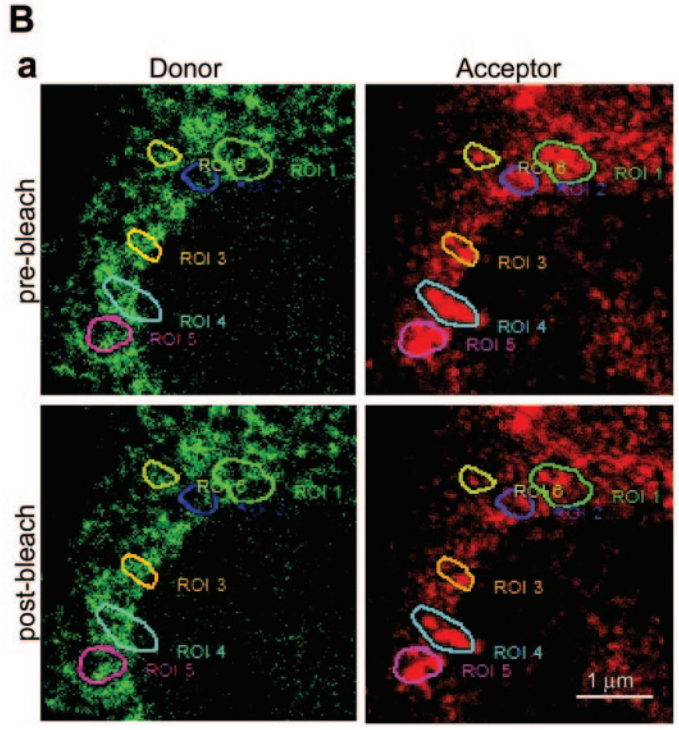

b

ROI	ROI_1	ROI_2	ROI_3	ROI_4	ROI_5	ROI_6
D pre	88.62	77.57	125.08	110.60	114.37	98.01
D post	102.13	83.09	127.96	116.35	124.61	105.40
A pre	203.17	191.66	177.42	198.17	211.05	142.80
A post	149.87	138.01	130.54	159.26	177.04	104.19
FRETeff (%)	13.22	6.63	2.25	4.94	8.22	7.01

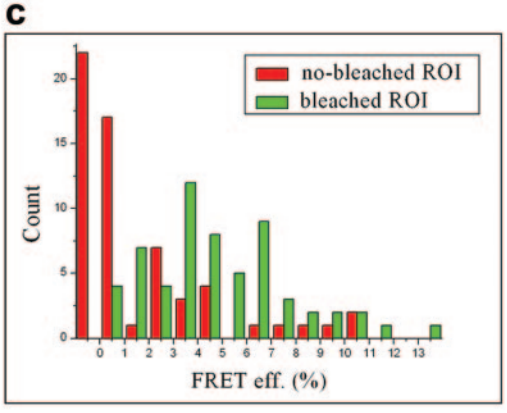

FIG. 8. PyV virions and transferrin appear in the same compartment. FRET between (A) VP1 (Cy5) and transferrin (Cy3) and between (B) VP1 (Cy5) and Rab11 GTPase (Cy3) reveals a tight association of the virus with transferrin and Rab11, both markers of recycling endosomes at the perinuclear area of infected cells. Mouse 3T6 fibroblasts were fixed at 3 h p.i. (a) Indirect immunofluorescence of the donor (transferrin [A] or Rab11 [B] stained by Cy3 and visualized in the green channel) and the acceptor (VP1 stained by Cy5 and visualized in the red channel). (b) FRET values measured in selected ROIs delimited in colors shown in panel a. A, acceptor; D, donor; pre, prior to bleaching; post, postbleaching. (c) Histogram of FRET efficiency (eff) distribution (green columns) calculated from 60 different ROIs of 14 different cells. As a control (red columns), a calculation of the same number of nonbleached regions of the specimen was performed to evaluate background FRET signals and measurement noises due to bleaching.

somes. The uptake of virions was slower than that of transferrin, and both cargos rarely met in early endosomes when added simultaneously to the cells. However, at later times postinfection (1.5 to 3 h p.i.), PyV VP1 colocalized with transferrin and Rab11 mostly in perinuclear areas, suggesting that recycling endosomes can be the compartments where they can encounter each other (20). Thus, PyV internalized in caveola-derived vesicles, or perhaps also in other raft-derived vesicles, later enters compartments of the classical clathrin-dependent pathway (e.g., early and/or recycling endosomes) and gets together with a cargo delivered there in a clathrin-dependent manner. Sharma et al. (34) previously demonstrated that glycosphingolipids could be internalized via caveola-related endocytosis and could then rapidly merge with the clathrin pathway in early endosomes. Glycosphingolipids can form distinct microdomains within the early endosomal membrane, which behave differently with respect to their subsequent intracellular trafficking and might play a role in cargo sorting (34).

We further examined the effect of the elevation of endosomal pH on PyV infection. Bafilomycin A1 disrupts the H^+ gradient that exists in vesicles of the vacuolar system (7, 39). We proved that, at least in mouse 3T6 fibroblasts and NMuMG epithelial cells, this agent prevents PyV productive infection. Moreover, exposition of these cells to NH_4Cl (which rapidly elevates endosomal pH) also inhibited infection by PyV when the cells were exposed to the drugs during the initial steps of infection. At later times postinfection, since the virus signal was detected in the perinuclear space, infection became pH insensitive. Remarkably, previous findings of other groups showed that neither SV40 (35, 38) nor PyV (13) infection was affected by NH_4Cl treatment. On the other hand, infection by human JC virus, but also BK virus (internalized by caveolae), was found to be sensitive to the elevation of endosomal pH (3, 11). Ashok and Atwood (3) previously found that JC virus infection is, in contrast to that of SV40, decreased by approximately 70% by NH_4Cl, while infection by both SV40 and JC virus can be completely inhibited by bafilomycin A1. The different sensitivities of cells to NH_4Cl treatment and the time of exposition could account for the discrepancy between our finding and previous (13) findings. Since under the conditions described previously by Ashok and Atwood (3), our cells died before they could have been analyzed, we shortened the time of NH_4Cl treatment by half.

Although both SV40 and cholera toxin bind the same ganglioside GM1 receptor, intoxication by CTb, in contrast to SV40 infection, depends on exposure to an acidic milieu (17). Recently, Pelkmans et al. (28) described a Rab5-dependent pathway in which caveolar vesicles are targeted to early endosomes, where they form distinct but transient membrane domains. When they monitored the SV40 and CTb cargo, the low pH of early endosomes selectively induced a conformational change of CTb (21) and its lateral diffusion into a surrounding membrane subdomain of the compartment, while SV40 remained trapped in the caveolin-positive subdomain from where it was subsequently sorted out into caveosomes. They also found that when caveolin-1 was down-regulated, virions of SV40 diffused into the lumen of endosomes, but that did not lead to infection. This is in agreement with the previous observations that the pathway through caveosomes and the ER is necessary for productive SV40 infection (29). We found out

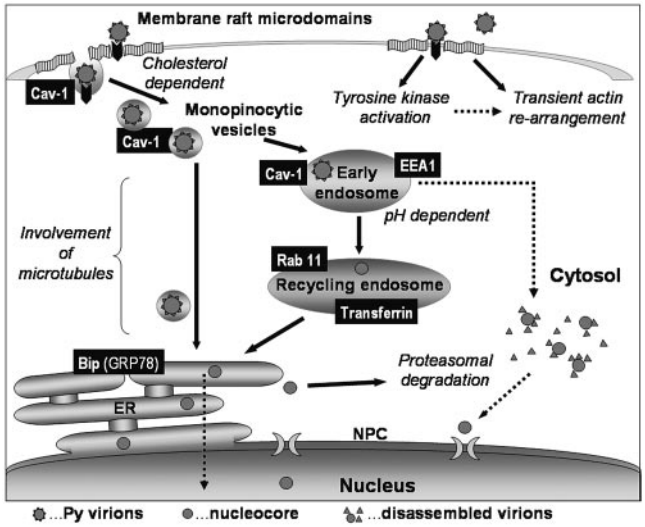

FIG. 9. Scheme of trafficking pathways used by PyV for the movement towards the cell nucleus. Virions are internalized through lipid raft domains into smooth, often caveolin-positive, monopinocytic vesicles. These vesicles then fuse with early endosomes, and endosomal acidic pH is (in contrast to SV40) necessary for efficient PyV trafficking. Virus uptake is accompanied with protein tyrosine kinase signaling (our unpublished observation) and with a transient reorganization of the actin network (33). Further movement of the virus is directed into the recycling endosomes, as we proved by FRET between PyV VP1 and transferrin or between PyV VP1 and Rab11 GTPase. Significant colocalization of VP1 with the BiP marker was observed previously (20) and suggests that PyV can be transported to the ER. However, in contrast to cholera toxin, or to SV40, the PyV route into the ER is independent of COPI vesicles (20). We also detected direct fusions of virus-carrying monopinocytic vesicles with the ER on ultrathin cell sections (33); therefore, both routes to the ER (the one from recycling endosomes and the direct one from monopinocytic vesicles) are considered alternative routes. The possibility that "successful" virions escape from early endosomes into the cytosol (as a result of conformation changes induced by acidic pH) still cannot be ruled out. The trafficking pathway leading to the ER via recycling endosomes would then represent a cell defense mechanism. We have shown previously (20) that only a few viral genomes reach the nucleus, while a substantial amount is directed to the ER-associated degradation pathway. It is conceivable that PyV misuses this pathway, like some bacterial toxins (10), counting upon an escape of several viral genomes into the nucleus prior to their degradation in the cytoplasm. Black arrows, experimentally proved routes; dotted arrows, possible alternative routes. NPC, nuclear pore complex.

that cells expressing a dominant-negative caveolin-1 mutant can be productively infected by PyV, and in cells with an elevated endosomal pH, the majority of PyV was retained in early endosomes, similar to the CTb that was found to be restricted in its mobility (28). The traffic of PyV is also similar to that of CTb (and differs from SV40) with respect to the dependence on Rab5 function.

Enveloped viruses make use of endosomal acidic pH for inducing the fusion of their envelopes with the vesicle membrane and for nucleocapsid escape to free cytosol. Some nonenveloped viruses, e.g., adenoviruses or human rhinovirus serotype 2, also exploit the acidic milieu of early endosomes to trigger conformational changes in their capsids followed by partial disassembly to evade the barrier of the endosomal membrane (23, 31).

It became obvious that the majority of PyV virions (or their

partially disassembled complexes) are further transported in membranous compartments to the perinuclear space. Time lapse microscopy (Fig. 2) showed that PyV was internalized in large caveolin-rich compartments located in the perinuclear space. We showed previously (20) that the signal of major capsid protein VP1 colocalized there with transferrin and Rab11 but also with BiP/GRP78, a marker of the ER. We suggest that similar to cholera or Shiga toxin, a vast proportion of PyV is carried from early endosomes, via recycling endosomes, to the ER. In contrast to bacterial toxins, PyV seems to bypass the Golgi compartment (our unpublished results). Recycling endosomes are mildly acidic compartments containing components of membrane rafts such as glycosylphosphatidylinositol-anchored proteins, sphingomyelin, cholesterol, and caveolin-1 (12). In this regard, they resemble caveosomes utilized by SV40. Moreover, in some cells, both caveosomes and recycling endosomes were found to share an overlapping distribution. Caveosomes immunolabeled with anti-caveolin-1 antibody merged with the transferrin receptor signal (present in recycling endosome membranes) in the perinuclear space near the MTOC of CHO cells. We suggest that caveosomes and recycling endosomes are intertwined rather than that they represent an identical membrane system (22). Nevertheless, positive FRET between VP1 and transferrin and between VP1 and Rab11 provides strong support for the presence of PyV VP1 and transferrin within the same compartment. Further research is required to define functional and biochemical differences between caveosomes and recycling endosomes and to reveal whether both compartments can communicate in a way similar to that of caveola-derived vesicles with early endosomes.

The most intricate question, from where and by what mechanism the PyV genome is delivered into the nucleus, remains unclear and is currently under vigorous investigation. A summary of results obtained by our studies of endocytic pathways exploited by mouse polyomavirus to deliver its genome into the cell nucleus is schematically drawn in Fig. 9.

ACKNOWLEDGMENTS

This work was generously supported by the Grant Agency of the Czech Republic (grant 204/03/0593), by the Centre of Functional Organization of Cells (LC545), by the Centre for New Antivirals and Antineoplastics (1M6138896301), by the programs of the Ministry of Education, Youth, and Sport of the Czech Republic, and by project no. AVOZ50520514.

We are grateful to all researchers (names are given in Materials and Methods) who provided Rab5, Eps15, and caveolin-A mutants or antibodies and to Š. Takáčová for assistance in preparation of the manuscript.

REFERENCES

1. **Anderson, H. A., Y. Chen, and L. C. Norkin.** 1996. Bound simian virus 40 translocates to caveolin-enriched membrane domains, and its entry is inhibited by drugs that selectively disrupt caveolae. Mol. Biol. Cell **7:**1825–1834.
2. **Anderson, H. A., Y. Chen, and L. C. Norkin.** 1998. MHC class I molecules are enriched in caveolae but do not enter with simian virus 40. J. Gen. Virol. **79:**1469–1477.
3. **Ashok, A., and W. J. Atwood.** 2003. Contrasting roles of endosomal pH and the cytoskeleton in infection of human glial cells by JC virus and simian virus 40. J. Virol. **77:**1347–1356.
4. **Bastiaens, P. I. H., and T. M. Jovin.** 1998. Fluorescence resonance energy transfer microscopy, p. 136–146. In J. E. Celis (ed.), Cell biology: a laboratory handbook, 2nd ed., vol. 3. Academic Press, New York, N.Y.
5. **Benmerah, A., M. Bayrou, N. Cerf-Bensussan, and A. Dautry-Varsat.** 1999. Inhibition of clathrin-coated pit assembly by an Eps15 mutant. J. Cell Sci. **112:**1303–1311.
6. **Benmarah, A., C. Lamaze, B. Begue, S. L. Schmid, A. Dautry-Varsat, and N. Cerf-Bensussan.** 1998. AP-2/Eps15 interaction is required for receptor-mediated endocytosis. J. Cell Biol. **140:**1055–1062.
7. **Bowman, E. J., A. Siebers, and K. Altendorf.** 1988. Bafilomycins: a class of inhibitors of membrane ATPases from microorganisms, animal cells, and plant cells. Proc. Natl. Acad. Sci. USA **85:**7972–7976.
8. **Breau, W. C., W. J. Atwood, and L. C. Norkin.** 1992. Class I major histocompatibility proteins are an essential component of the simian virus 40 receptor. J. Virol. **66:**2037–2045.
9. **Caruso, M., L. Belloni, O. Sthandier, P. Amati, and M.-I. Garcia.** 2003. $\alpha4\beta1$ integrin acts as a cell receptor for murine polyomavirus at the postattachment level. J. Virol. **77:**3913–3921.
10. **Deeks, E. D., J. P. Cook, P. J. Day, D. C. Smith, L. M. Roberts, and J. M. Lord.** 2002. The low lysine content of ricin A chain reduces the risk of proteolytic degradation after translocation from the endoplasmic reticulum to the cytosol. Biochemistry **41:**3405–3413.
11. **Eash, S., W. Querbes, and W. J. Atwood.** 2004. Infection of Vero cells by BK virus is dependent on caveolae. J. Virol. **78:**11583–11590.
12. **Gagescu, R., N. Demaurex, R. G. Parton, W. Hunziger, L. A. Huber, and J. Gruenberg.** 2000. The recycling endosome of Madin-Darby canine kidney cells is a mildly acidic compartment rich in raft components. Mol. Biol. Cell **11:**2775–2791.
13. **Gilbert, J. M., and T. L. Benjamin.** 2000. Early steps of polyomavirus entry into cells. J. Virol. **74:**8582–8588.
14. **Gilbert, J. M., J. Dahl, J. You, C. Vui, R. Holmes, W. Lencer, and T. L. Benjamin.** 2005. Ganglioside GD1a restores infectibility to mouse cells lacking functional receptors for polyomavirus. J. Virol. **79:**615–618.
15. **Gilbert, J. M., I. G. Goldberg, and T. L. Benjamin.** 2003. Cell penetration and trafficking of polyomavirus. J. Virol. **77:**2615–2622.
16. **Griffiths, S. L., R. A. Finkelstein, and D. R. Critchley.** 1986. Characterization of the receptor for cholera toxin and Escherichia coli heat-labile toxin in rabbit intestinal brush borders. Biochem. J. **238:**313–322.
17. **Janicot, M., F. Fouque, and B. Desbuquois.** 1991. Activation of rat liver adenylate cyclase by cholera toxin requires toxin internalization and processing in endosomes. J. Biol. Chem. **266:**12858–12865.
18. **Krauzewicz, N., J. Štokrová, C. Jenkins, M. Elliott, C. F. Higgins, and B. E. Griffin.** 2000. Virus-like gene transfer into cells mediated by polyoma virus pseudocapsids. Gene Ther. **7:**2122–2131.
19. **Li, G., and P. D. Stahl.** 1993. Structure-function relationship of the small GTPase rab5. J. Biol. Chem. **268:**24445–24480.
20. **Mannová, P., and J. Forstová.** 2003. Mouse polyomavirus utilizes recycling endosomes for a traffic pathway independent of COPI vesicle transport. J. Virol. **77:**1672–1681.
21. **McCann, J. A., J. A. Mertz, J. Czworkowski, and W. D. Pickin.** 1997. Conformational changes in cholera toxin B subunit-ganglioside GM1 complexes are elicited by environmental pH and evoke changes in membrane structure. Biochemistry **36:**9169–9178.
22. **Mundy, D. I., T. Machleidt, Y. S. Ying, R. G. Anderson, and G. S. Bloom.** 2002. Dual control of caveolar membrane traffic by microtubules and the actin cytoskeleton. J. Cell Sci. **115:**4327–4339.
23. **Nakano, M. Y., K. Boucke, M. Suomalainen, P. Stidwell, and U. G. Grebe.** 2000. The first step of adenovirus type 2 disassembly occurs at the cell surface, independently of endocytosis and escape to the cytosol. J. Virol. **74:**7085–7095.
24. **Nathke, I. S., J. Heuser, A. Lupas, J. Stock, C. W. Turck, and F. M. Brodsky.** 1992. Folding and trimerization of clathrin subunits at the triskelion hub. Cell **68:**899–910.
25. **Norkin, L. C., H. A. Anderson, W. A. Scott, and A. Oppenheim.** 2002. Caveolar endocytosis of simian virus 40 is followed by brefeldin A-sensitive transport to the endoplasmic reticulum, where the virus disassembles. J. Virol. **76:**5156–5166.
26. **Orlandi, P. A., and P. H. Fishman.** 1998. Filipin dependent inhibition of cholera toxin: evidence for toxin internalisation and activation through caveolae like domains. J. Cell Biol. **141:**905–915.
27. **Pasqualato, S., F. Senic-Matuglia, L. Renault, B. Goud, J. Salamero, and J. Cherfils.** 2004. The structural GDP/GTP cycle of Rab11 reveals a novel interface involved in the dynamics of recycling endosomes. J. Biol. Chem. **279:**11480–11488.
28. **Pelkmans, L., T. Burli, M. Zerial, and A. Helenius.** 2004. Caveolin-stabilized membrane domains as multifunctional transport and sorting devices in endocytic membrane traffic. Cell **118:**767–780.
29. **Pelkmans, L., J. Kartenbeck, and A. Helenius.** 2001. Caveolar endocytosis of simian virus 40 reveals a new two step vesicular transport pathway to the endoplasmic reticulum. Nat. Cell Biol. **3:**473–483.
30. **Pho, M. T., A. Ashok, and W. J. Atwood.** 2000. JC virus enters human glial cells by clathrin-dependent, receptor-mediated endocytosis. J. Virol. **74:**2288–2292.
31. **Prchla, E., C. Plank, E. Wagner, D. Blaas, and R. Fuchs.** 1995. Virus-mediated release of endosomal content in vitro: different behavior of adenovirus and rhinovirus serotype 2. J. Cell Biol. **131:**111–123.
32. **Richards, A. A., E. Stang, R. Pepperkok, and R. G. Parton.** 2002. Inhibitors of COP-mediated transport and cholera toxin action inhibit simian virus 40 infection. Mol. Biol. Cell **13:**1750–1764.
33. **Richterová, Z., D. Liebl, M. Horák, Z. Palková, J. Štokrová, P. Hozák, J.**

Korb, and J. Forstová. 2001. Caveolae are involved in the trafficking of mouse polyomavirus virions and artificial VP1 pseudocapsids toward cell nuclei. J. Virol. **75:**10880–10891.
34. **Sharma, D. K., A. Choudhury, R. D. Singh, C. L. Wheatley, D. L. Marks, and R. E. Paganos.** 2003. Glycosphingolipids internalized via caveolar-related endocytosis rapidly merge with the clathrin pathway in early endosomes and form microdomains for recycling. J. Biol. Chem. **278:**7564–7572.
35. **Shimura, H., Y. Umeno, and G. Kimura.** 1987. Effects of inhibitors of the cytoplasmic structures and functions on the early phase of infection of cultured cells with simian virus 40. Virology **158:**34–43.
36. **Trouet, D., D. Hermans, G. Droogmans, B. Nilus, and J. Eggermont.** 2001. Inhibition of volume-regulated anion channels by dominant-negative caveolin-1. Biochem. Biophys. Res. Commun. **284:**461–465.
37. **Tsai, B., J. M. Gilbert, S. Stehle, W. Lencer, T. L. Benjamin, and T. A. Rapoport.** 2003. Gangliosides are receptors for murine polyoma virus and SV40. EMBO J. **22:**4346–4355.
38. **Upcroft, P.** 1987. Simian virus 40 infection is not mediated by lysosomal activation. J. Gen. Virol. **68:**2477–2480.
39. **Yochimori, T., A. Yamamoto, Y. Moriyama, M. Futai, and Y. Tashiro.** 1991. Bafilomycin A1, a specific inhibitor of vacuolar type H^+ ATPase, inhibits acidification and protein degradation in lysosomes of cultured cells. J. Biol. Chem. **266:**17707–17712.

TITLE:

Dynamics of cytoplasmic trafficking of mouse polyomavirus revealed by time-lapse live imaging fluorescence confocal microscopy

Difato F.[1, 2] , Liebl D.[1], Zila V.[1], Klimova L.[1], Hornikova L.[1] and J. Forstová[1]

1. Faculty of Science, Charles University in Prague (Dept. of Genetics and Microbiology)
2. Institute of Physiology (Dept. of Biomathematics), Academy of Sciences, Prague

FOOTNOTE:

* Corresponding author's address: Dept. of Genetics and Microbiology, Faculty of Science, Charles University in Prague, Vinicna 5, 128 44 Prague 2, Czech Republic, tel: + 420 221 951 734, fax: + 420 221 951 729, e-mail: liebl@natur.cuni.cz. First two authors contributed equally.

RUNNING TITLE:

Dynamics of polyomavirus trafficking

KEY WORDS:

mouse polyomavirus, virus trafficking, transport velocity, actin comets, microtubule tracks, actin rings

ABBREVIATIONS:

mPyV - mouse polyomavirus, MTOC - microtubule organising centre, LatA - latrunculin A, CytoD - cytochalasin D, Noc - nocodazole, VLPs - virus-like particles, MTs - microtubules, EGFP - enhanced green fluorescent protein, EM - electron microscopy, MOI - multiplicity of infection, p.i. - post infection

ABSTRACT (200 words)

The endocytic transport of mouse polyomavirus (mPyV) is studied for prospective utilization of polyomaviral pseudocapsids in gene therapy and/or immunotherapy. We have used mPyV fluorophore-labelled virions as a trafficking cargo model and cells expressing GFP-tagged g-actin or α-tubulin to demonstrate the direct involvement of both cytoskeletal networks in virion cytoplasmic trafficking by time-lapse live imaging fluorescence confocal microscopy. Here, we show that at high multiplicity of infection, mPyV entry triggers reorganisation of actin stress fibre into actin ring structures that can enclose virion-loaded vesicles and slow down the rate of endocytosis as a possible result of cell defence mechanism. Disruption of actin by drug treatment enhanced virus uptake by the cell, but affected following steps of trafficking when actin polymerisation machinery is recruited by virion-loaded vesicles and used for their propulsion through the cytoplasm. Trafficking of virions along microtubular tracks revealed three modes of transport rates, reflecting characteristic dynamics of motor-driven transport with saltatory bi-directional movements and velocity peaks of 1.5 μm/sec. Trajectories of virion movements measured by single particle tracking appeared to be much more complex than previously recognised. They revealed events of pausing and switching direction during the long-range transport from the cell surface to the nuclear periphery.

INTRODUCTION

Intracellular trafficking of any cargo (lipid vesicles, multi-component protein assemblies, intracellular pathogens, or other macromolecular structures) in the cytoplasm is dependent on precisely regulated, time- and direction-specific machinery. Cytoplasmic concentration of macromolecules in a cell is very high and corresponds to protein density of approximately 20-30% (by volume). In such impenetrable cytoplasmic environment, free diffusion of complexes larger than 500 kDa has been shown to be practically ineffective [1]. Given the wide range of different sizes of proteins in the cytoplasm, macromolecular structures are often in close contact with each other [2], what further impedes their diffusion rate. Moreover, any movement in cytosol is obstructed by the dense cytoskeletal network, which implies that larger macromolecular assemblies, whether "naked" or enveloped in membrane sheets, cannot dispense with active, energy-consuming (and also temporarily and spatially regulated) transport device to reach specific sub-compartments of the cell. There is a growing list of evidences for utilization of cytoskeleton tracks and molecular motors in fast, long-range trafficking of many viruses [3, 4] or membrane organelles [5, 6].

Transport velocities of viral capsids in the cytoplasm are usually in the range of approximately 1 μm/sec. This value was found for HIV particles in a study of viral transport in live cells [7] and also for Herpesvirus HSV-1 and Adenovirus 2 (Ad-2) that also make use of the functional MT network to reach the nucleus and to start viral gene expression [8]. Adenovirus 2 is transported to MT minus-end by interaction with the dynein motor and oscillatory capsid movements consist of long-range minus end oriented trafficking paused by short-range movements to the MT plus end [3]. Interestingly, close related Adenovirus 5 does not recruit plus end motor for backward movement [9].

Recruiting an active transport mechanism is especially important for neurotrophic viruses, because the length of axons substantially limits the time needed by virions to traverse the distance from the gate of entry into the cell nucleus for replication, or by anterograde transport in opposite

orientation, for spreading in the tissue. Parvovirus capsids were shown to use MTs for fast axonal transport to the nucleus [10]. Assessment of trafficking rates for different viruses by MT-driven transport resulted in similar values, that point to utilisation of a common molecular device with a limited processiveness. The speed of HSV retrograde transport in neurons can reach 0.8 - 1.4 μm/sec [11] - similar to the values for anterograde egress [12]. Rabies virus moves at 0.6 - 1.2 μm/sec during entry [13] and 1.2 - 4.8 μm/sec during egress [14], while substantially smaller poliovirus is slightly faster, with the value of 2.0 μm/sec [15].

We found out earlier that in cells infected by mouse polyomavirus, actin stress fibres collapsed temporarily [16]. Also, SV40 which is known to be internalized through caveolae, induces transient disorganisation of actin stress fibres and recruits actin to polymerize on virus-containing vesicles [17]. For SV40 and mouse PyV, the mechanism of actin tail formation is unknown and is connected to trafficking of endocytic vesicles rather than induced by any viral protein. Hijacking of actin polymerization machinery has shown to be a useful strategy for bacterial or viral invasion. However, different mechanisms for pathogen propulsion in the cytoplasm using F-actin nucleation have evolved by *Listeria* [18], *Rickettsia* and *Shigella* [19] or by vaccinia virus [20, 21]. Not only bacterial pathogens mastered actin microfilament nucleation to facilitate intracellular movement and/or intercellular spreading. Also, membranous vesicles (e.g. endosomes, lysosomes, secretion vesicles) and other small organelles were found to be propelled by recruiting actin microfilament nucleation [22 - 25. Contrary to that, vesicular cargo transport from Golgi to endoplasmic reticulum (ER) is driven by the myosin motor using actin microfilaments as tracks instead of actin comets [26] and translocation and clustering of endosomes and lysosomes is dependent on functional MTs [27].

In this work, we have used mouse polyomavirus as a trafficking cargo model. The endocytic pathway of mouse polyomavirus is studied for potential utilization of polyomaviral virus-like particles (VLPs) in gene therapy and/or immunotherapy. There is evidence that intact microtubules are necessary for viral infectivity [28]. Partial co-localisation of VP1 capsid protein with caveolin 1,

EEA1 (early endosome antigen), GTPase Rab11 (marker of recycling endosomes) and with protein GRP78 (resident protein of endoplasmic reticulum) in early times post infection reflects the specific endocytic and trafficking pathway which virions can use for infectious genome delivery into the host cell nucleus [16, 29]. Nevertheless, the mechanism of virion transport and the cytoplasmatic compartment where the capsid disassembly and nucleocore release proceed is not known yet. This is the first study of polyoma virus trafficking in live cells focused on elucidation of the complex dynamics of virion cytoplasmic transport and active role of the cytoskeleton at early stages post infection revealed by time-lapse live imaging, single particle tracking and fluorescence confocal microscopy.

MATERIALS AND METHODS

GFP constructs and cell lines

Swiss albino mouse 3T6 fibroblast and normal murine mammary gland (NMuMG) epithelial cells were maintained in complete DMEM medium supplemented with 10% foetal calf serum (Sigma) and 2 mM glutamin. Plasmid pEGFP-human α-Tub vector (Clontech, cat. 6117-1) and pEGFP-human β-actin vector (Clontech, cat. 6116-1) were used to transfect cells by electroporation. Briefly, exponentially grown cells (one day after the passage) were trypsinized, homogenized cell suspension (1×10^7 cells) was pelleted and cells resuspended in 1 ml OPTIMEM-I medium (Gibco) with 10-20 μg DNA. Two hundred μl of suspension were electroporated using Gene Pulser Apparatus (BioRad) set on 960 μF, 1000 Ohms, 300 V with a pulse length 60-70 msec. Transfected cells were diluted 1:20 into fresh complete DMEM medium and grown for 48 h. Stable cell lines expressing GFP-tagged proteins were established by sub-cloning and maintaining upon G418 (Sigma) selection antibiotic in DMEM culture medium supplemented with 10% foetal calf serum (Gibco).

Virus

Mouse polyomavirus (A2 strain) was isolated from infected WME (whole mouse embryo) primary culture cells according to the standard protocol and purified to homogeneity by CsCl and sucrose gradient ultracentrifugation. Virions were labelled with the red fluorescent marker, Alexa-594, coupled with an amine-reactive probe (carboxylic acid succinimidyl ester, purchased from Molecular Probes) according to the labelling procedure: purified virus was dialyzed in 0.1 M carbonate buffer (pH 8.3) and 1 mg of the virus with 0.1 mg of the fluorescent reagent was incubated for 1 h at room temperature and then overnight in 4°C.

Separation of the conjugate from un-reacted labelling reagent was made by extensive dialysis and subsequent purification of the virus on 10-40 % sucrose gradient. The virus was aliquoted and stored at -20°C before use. The optimal degree of labelling (virus: fluorescent marker ratio) was assessed and improved not to affect virus natural infectiveness. Briefly, Alexa-594 pre-stained virus was used to infect cells and after fixation, co-immunolabelling with anti-VP1 antibody was performed, followed by green Alexa 488 secondary antibody. Co-localisation of red and green signals proved that all viral particles were conjugated with red Alexa-594 dye while the VP1 immuno-epitope remained available for anti-VP1 antibody binding.

Cytoskeletal drug inhibition assay and co-localisation by immunofluorescence

Cells were infected in the presence of nocodazole (1 and 10 μM), cytochalasin D (1 and 5 μM) and latrunculin A (0.5 and 2.5 μM) (all from Sigma), incubated until the time of fixation (15 and 40 or, 24 and 48 hrs p.i.) and immunostained by antibody against mouse polyomavirus LT antigen (expressed from 9 h p.i.). The efficiency of infection was calculated from the number of cells positive for LT antigen correlated to the control cells infected and incubated without a drug (100%). In parallel samples, drugs were washed out and cells were incubated for additional time prior to fixation and immunostaining to prove the reversibility of the inhibition effect. Microtubules and microfilaments were processed for immunofluorescence to reveal the current morphology of the

cytoskeleton at respective times of cell fixation with or without the drug. Briefly, cells were fixed in 3% paraformaldehyde in PBS, permeabilized in 0.5% Triton X-100 in PBS and immunostained with i) mouse anti-βtubulin primary antibody (Exbio) followed with anti-mouse Alexa-488 secondary antibody (Molecular Probes), or ii) with rhodamine-coupled phalloidin (Sigma). Coverslips were mounted onto 50% glycerol (with or without DAPI) and observed with an Olympus BX-60 fluorescence microscope.

VASP colocalization by immunofluorescence

At the indicated times postinfection (MOI of 102 to 103 virus particles per cell), cells grown on coverslips were washed three times with phosphate-buffered saline (PBS), fixed with 3% paraformaldehyde in PBS (30 min), and permeabilized with 0.5% Triton X-100 in PBS (10 min). After washing in PBS, cells were incubated (1 hour) with 0.25% bovine serum albumin and 0.25% porcine skin gelatin in PBS. Immunostaining with primary and secondary antibodies was carried out for 1 h and 30 min, respectively, with extensive washing with PBS after each incubation obtain a ratio between phosporylated and non phosphorylated VASP, following primary antibodies were used: rabbit polyclonal antibody to VASP and mouse monoclonal antibody to phosphorylated VASP (pVASP) (Alexis biochemicals: ALX-210-880 and ALX-804-240 respectively). The following secondary antibodies were used: chicken anti-rabbit conjugated with Alexa Fluor-594 for VASP; and donkey anti-mouse conjugated with Alexa Fluor-488 for pVASP (all purchased from Molecular Probes). For colocalization study with VP1, the same primary antibody mentioned above for pVASP followed by donkey anti-mouse conjugated with Alexa Fluor-594 as a secondary antibody and polyclonal rabbit anti-PyV VP1 (prepared in our laboratory) and goat anti-rabbit conjugated with Alexa Fluor-488 (from Molecular Probes) were used.

Virus tracking

For live microscopy, cells expressing EGFP markers (actin or tubulin) were grown on 40 mm glass coverslips in phenol red-free DMEM medium. The cell cycle was synchronised by

starving cultured cells in DMEM medium supplemented with 0.5% serum for 24 h before infection. Coverslips were mounted in an open metal chamber system maintained at 37°C and overlaid with fresh medium. To avoid rapid temperature changes and microtubule depolymerisation at 4°C, all procedures were performed at 37°C with pre-warmed media and solutions Virus was diluted with serum-free culture medium and added to cells at MOI = 100 - 1000 particles/cell. Unbound virus was gently washed away after 30 min and complete culture medium was added. Internalisation of the virus by the host cells and cytoplasmic transport was monitored at indicated times post infection by time-lapse live imaging using confocal microscopy. We used a Leica TCS SP2 AOBS confocal microscope operating with an Argon laser (458, 476, 488, 496, 514 nm; 10 mW) and HeNe (543, 594 nm; 1 mW). Cells were examined with 1.2 N.A. water immersion objective (60x). According to specific signal to noise ratio and GFP level of expression, we applied different sampling frequencies (ΔT = 1 - 6 sec). Sequential scanning between channels was used to separate fluorescence emission from different fluorochromes and to completely eliminate bleed through channels. Leica Confocal Software was used for live microscopy. Video sequences and images were processed by Image J (NIH, Bethesda, USA) and Adobe Photoshop 7.0 (Adobe Systems, San Jose CA, USA), respectively. Velocities and trajectories were calculated by Excel 2002 (Microsoft).

RESULTS and DISCUSSION

Disruption of microtubules impairs virus infectivity but depolymerisation of actin microfilaments has complex impact on virus genome delivery into the nucleus.

Further, we addressed the possible involvement of actin and/or microtubules in viral genome delivery into the nucleus by cytoskeletal drug assays using compounds selectively affecting cytoskeleton structure and dynamics (cytochalasin D, latrunculin A and nocodazole).

We found that inhibition of mPyV infection (more than 80%) in cells treated with nocodazole is reversible and can be fully restored by drug washout and by prolonged time of incubation before cell fixation and screening **(Fig. 1a)**. Our observation pointed to the retention of virions in the cytoplasm for a long time after infection while the MT network was collapsed. We concluded that in these restrictive conditions, virions are endocytosed in monopinocytic vesicles (MPC), but fail to be translocated forward - deeper into the cytoplasm, do not fuse with membranous organelles of the specific trafficking route and thus the virus retains its infectiveness. On the contrary, when MTs are intact, some virions deliver their DNA into the nucleus and the bulk of disassembled virus material becomes degraded in the cytoplasm (and partially eliminated out of the cell) up to 24 h p.i

When actin microfilament assembly and dynamics were destabilized, the number of infected cells decreased in a dose-dependent manner. However, when drugs were washed out (15 h p.i.) and microfilaments were left to recover their native organisation, the efficiency of infection in drug pre-treated cells increased two times in comparison to control non-treated cells **(Fig. 1b, c)**. Similar results were published for the RA (small plaque) strain of mPyV in BMK and 3T3 cells [30]. We showed here that actin microfilament rearrangement has a double role in mPyV virion entry and transport: apparently, two-dimensional cortical actin meshwork can play a role of sterical barrier for free movement of endocytosed vesicles into the cell interior and its disruption by drug treatment enhances virus uptake and substantially increases the amount of virions able to join the specific trafficking pathway. However, the following steps, leading to viral genome delivery into the nucleus, are dependent on functional actin cytoskeleton and its dynamic properties.

Actin tail-mediated virion propulsion in the cytoplasm

Cytoskeletal systems are interconnected by cross-linking proteins. Thus, drugs destroying actin microfilaments or microtubules can have non-specific effect even at low doses. Because co-localisation studies fail to show dynamics of virus-cytoskeleton interactions, we used time-lapse live imaging fluorescence confocal microscopy to reveal direct evidence for cytoskeleton-driven virus trafficking in host cells.

Cells expressing GFP-actin had standard morphology of fibroblasts and even lamellipodia, filopodia and membrane protrusions of intercellular contacts retained their natural dynamics (not shown). After infection of these cells with Alexa 594-prestained virus, we observed that moving virions (but not the static ones) were associated with EGFP-actin patches that were also detected separately from virus signal. These actin comet-like structures encompassed and propelled the virus cargo parallel to the cell surface membrane and they moved on and/or between actin stress fibres (**Fig. 2** and **Actin1-3 movies**). Our previous ultrastructural EM study has shown that at early times post virus internalisation, virions remain enveloped in tightly fitted monopinocytic vesicles that are often aligned to actin bundles [16]. Because we have never seen free viral particles in the cytosol (by electron microscopy), we conclude that our live imaging observations correspond to movements of virus-loaded or virus-free endosomes.

The observed patches of EGFP-actin resemble actin comet tails created by some bacterial pathogens or e.g. vaccinia virus [20, 21]

We hypothesize that virus-loaded vesicles are delivered under the cortical actin barrier, where they switch for MT tracks to reach the vicinity of the nucleus. Alternatively, switching between F-actin and MT tracks can occur continually during virion trafficking according to the type of recruited molecular motor. It is intriguing that employment of actin polymerisation machinery to the surface of late endosomes may also be used to facilitate process of finding fusion partner organelle [31] - the process, which is inevitable for the virus to follow a specific trafficking route.

Reorganisation of actin stress fibres into actin rings is triggered by virus uptake

Later post virus adsorption (90 min) at high MOI (10^4 virions/cell), we observed partial and temporal disorganisation of F-actin bundles. Interestingly, GFP-tagged actin was recruited into numerous ring-shaped basket-like structures, which organised themselves parallel to the cell surface, often engulfing labelled virions (**Fig. 3a-d**). Temporal disorganisation of actin stress fibres was described earlier on fixed, phalloidine-stained cells [16], but phalloidin, which binds only to F-actin at the junction between subunits [32], can only reveal polymerised F-actin bundles in fixed cells. In our live imaging experiments, we showed numerous actin rings per infected cell arranged to a pattern similar to desorganised actin in cells after prolonged treatment with cytochalasin D (**Fig. 1b**). These structures (clearly visible on tilted 3D reconstruction) appeared rather static and can reflect the cortical actin meshwork reorganised into actin ring-shaped assemblies around endocytic/exocytic vesicles sometimes filled with labelled PyV (in red) (**Fig 3c, d** and **Rings1-3 movies**). The average actin ring diameter measured by intensity line profile was 883 ± 172 nm.

Similar rings of bundled actin have been observed previously in quiescent starved 3T3 fibroblasts [33]. Similar to the plasma membrane, also internal organelles and vesicles possess their own peripheral matrix of cortical cytoskeleton [34]. This could also be applied for virus-loaded endosomes, where actin can serve as a scaffold for pinching off the membrane and further vesicle propelling through the dense microfilament network deeper into the cytoplasm. Alternatively, regarding a static behaviour of actin ring assemblies, we suggest, that they may be arranged as consequence of cell defence to slow-down endocytosis and uptake of foreign pathogen.

Besides single virion-containing vesicles, a substantial increase in the amount of the empty ones was observed beneath the plasmatic membrane on ultra-thin sections at early times post virus adsorption. An enormous load of vesicles is clearly visible in transmission light, accompanied by an increased actin fibres depolymerisation (**Fig. 4**). Whether this observation represents signal-induced enhancement in the rate of endocytosis triggered by virus binding, or intensive membrane recycling to equilibrate the membrane sheet loss during virus invasion, is not clear yet. However, cell membrane recycling turnover rates are very high. Stemman et al. [35] estimated that an average

fibroblast recovers 100% of its total surface area and 10-20% of its volume during two hours of endocytic activity. Therefore, we hypothesize that a massive virus uptake at high MOI consumes large area of membrane sheet, which fails to be recycled back at the same rate. As a result, the cell regulation machinery may promote a signal to pause endocytosis and thus also virus internalisation until the membrane loss recovery.

Virion trafficking on microtubular tracks

During virus tracking experiments in cells expressing GFP-tubulin, virions were transported along MT tracks into the cell interior, but surprisingly, also back to the cell periphery in bi-directional manner (**Fig. 5**). Virion trajectories and very complex dynamics of transport were clearly visible on **Tubulin1 movie**. Following the intensity and character of virion-coupled fluorescent signal, we revealed possible fusion events between two or more virion-containing vesicle compartments resulting in larger endosomal vesicles with several fluorophore-labelled virus particles inside (**Tubulin2 movie).**

We observed virion trafficking along MTs at the same times post infection as virion propulsion by actin patches (from 30 min to 1 h p.i.). It is possible that microtubules and microfilaments are involved simultaneously (including the presence of different types of specific molecular motors on virion-carrying vesicles) or, alternatively, after short-distance movement at the cell periphery (driven by actin polymerisation) vesicles can recruit a minus end microtubule-associated motor to reach the proximity of the nucleus (or MTOC). Similar mode of transport was described for influenza virions: the initial actin-driven motion of virus-loaded endosomes has been followed by unidirectional dynein-dependent transport to the perinuclear space [36]. We observed previously [29] that during infection with higher MOI, the majority of virions were diverted to a degradation pathway. According to the hypothesis of Sodeik [37], centrosome-directed transport on microtubules can also reflect a cell-defence mechanism against intracellular pathogens or protein

aggregates that are recognised as a foreign agens and sorted for degradation pathways into the lysosome, proteasome or autophagosome, which are all distributed around the MTOC.

Regarding bi-directionality and dynamics of long-distance movements of single mPyV particles on one microtubule, it is obvious that interaction with both, plus end-oriented kinesin and minus end-oriented dynein (or, unconventional kinesin, e.g. KIF4) can be involved. Moreover, virus particles were observed to change tracks from one MT to another one nearby, or microtubule structure change to assist virus particle walk (**see Fig. 5**).

HIV virus particles use MTs and dynein to reach the vicinity of the nucleus while moving back and forth between the cell periphery and perinuclear space [7]. Herpes simplex virus (HSV) was also reported to move bi-directionally [38] and to physically interact with both dynein [39] and kinesin [40] in host cells. Although disruption of MTs by nocodazole lowered substantially the number of infected cells, it did not abolish the infection by mPyV entirely. That is why the switching between MTs and F-actin tracks is anticipated as well for mPyV trafficking. These transitions might be facilitated by recently described interactions of myosin-V with kinesin [41] and dynein [42].

Complex trajectories and saltatory dynamics

Virus particle transport trajectories mapped by a single particle tracking revealed unexpected patterns **(Fig. 6a)**. Trajectories were not clearly oriented from the cell surface -towards the nucleus but, instead, possessed characteristics of Brownian motion with fast random switching in velocities and direction of movement.

The dynamics of virion transport was mostly saltatory - the fast forward movements were interrupted by short back-step movements or pausing in intervals (an average pause lasted 40 ± 6.5 sec). Our measurements of movement velocities fitted to approximately three main characteristic rates (graphs on **Fig. 6b, c, d):** i) slow movement (in a limited space) at rates up to 0.3 μm/sec, ii) faster movement of particles was observed with a peak around 0.6 μm/sec and iii) fast movement

with peaks reaching rates of 1.2 μm/sec - the speed typical for motor-driven transport on MT tracks [43].

Following single particle movements during the long-time scale, we counted the frequency of different velocity rates. The most prevalent was slow, diffusion-rate movement (< 0.2 μm/sec), which can be assigned to pausing of static virus-loaded vesicles on MT tracks before another motor is recruited (or activated). During this "stationary phase" we detected movement only at limited range (0.5 - 1 μm) where possible fusion or fission processes between distinct membrane compartments could occur. Contrary to that, fast, long-distance movements (up to 1.5 μm/sec) were very rare, with a distinct peak at 0.6 μm/sec (**Fig. 6g**).

In studies reported so far, short runs of transported cargo were the most frequent while longer ones became increasingly rare [38, 45, 46]. We observed runs interrupted by diffusive pausing very often. Our measurements of fast movements (≥ 0.6 μm/sec) revealed that the average length of a single continuous movement is 2.5 μm with a distinct peak at 1.5 μm (**Fig. 6e**) which corresponds to recruitment of a single motor molecule on transported vesicle, because the processivity of individual kinesin or dynein molecules limits movement distances to approximately 1.5 μm before the motor dissociates from the microtubule [47]. We observed that events of faster (> 0.6 μm/sec) long-range transport occurred exclusively for short time intervals and the time span of movements was characterised by two peaks at 1.5 and 5.7 sec (**Fig. 6f**). It seems evident that in case of PyV, the run length of the cargo-motor complex reflects an inherent motor processivity. However, *in vivo*, many runs are substantially shorter than would be expected from the processivity of motors *in vitro* [45].

The mechanism of the run length control is still not understood; nevertheless, it can be hypothesised that multiple motors (including those with the opposite polarity) can operate on the same virus-carrying vesicle and their activities are coordinated.

When we followed single-particle tracking at perinuclear space, we detected slow motion at speeds typical for diffusion (0.05 μm/sec) with occasional peaks of 0.25 μm/sec (**Fig. 7 and NuDiffusion movie**). Comparable diffusion rates were also reported for secretory granule vesicles (average diameter of 160 nm) during anterograde cytoplasmic transport from trans-Golgi network to the cell membrane [44].

Although the virus cargo was transported in both directions (often along the identical MT), the minus-end direction was prevalent during longer time span of trafficking, because at later times (up to 3 h p.i.), the virus fluorescent signal accumulated around the nucleus. We observed earlier, that not only the signal of PyV capsid proteins, but also viral genome DNA accumulates continually at the perinuclear space, and only a limited amount of genomes is delivered inside the nucleus for their expression [29]. With the increase of fluorescent signal around the nucleus later post infection (from 3 h p.i.), we observed bi-directional movement of the virus florescent signal along the outer nuclear membrane (at the space usually occupied by the membrane cisternae network of ER).

Conclusions

In conclusion, our data demonstrate a link between mPyV, F-actin rearrangement and MT network dynamics at early stages post infection. Recruitment of actin polymerisation machinery to virus-loaded vesicles can be misused by virus as a driving force for its movement. However, actin network also represents an active barrier for virus intracellular transport. Static ring-shaped actin assemblies around membranous vesicles, observed after virion internalisation at high doses, might be a part of cell defence, slowing-down endocytosis and uptake of foreign pathogen. Our measurements of virus trajectories and transport dynamics point to exploitation of microtubular tracks and associated molecular motors. It remains to be determined which class of motors are directly involved in mPyV intracellular trafficking and to dissect pathways used by virus to smuggle its genome into the nucleus to establish successful infection from those which misguide the virus to degradation as a result of anti-viral cell defence mechanism.

ACKNOWLEDGEMENT

This work was generously supported by the “Centre for New Antivirals and Antineoplastics” (1M6138896301), by the "Centre of Functional Organisation of Cells" (LC545) of the programmes of the Ministry of Education, Youth and Sport of the Czech Republic and by the Grant Agency of the Czech Republic (No. 204/03/0593). We are grateful to Jiřina Hanová for assistance with cytoskeleton drug assay, Jiří Janáček for help with tracking measurements.

REFERENCES

1. K. Luby-Phelps, Cytoarchitecture and physical properties of cytoplasm: volume, viscosity, diffusion, intracellular surface area, Int Rev Cytol. 192 (2000) 189-221.
2. J.Martin, F.U. Hartl, The effect of macromolecular crowding on chaperonin-mediated protein folding, Proc Natl Acad Sci U S A. 94 (1997) 1107-12.
3. M.Suomalainen, M.Y. Nakano, S. Keller, K. Boucke, R.P. Stidwill, U.F. Greber, Microtubule-dependent plus- and minus end-directed motilities are competing processes for nuclear targeting of adenovirus, J Cell Biol. 144 (1999) 657-72.
4. B. Sodeik, M.W. Ebersold, A.Helenius, Microtubule-mediated transport of incoming herpes simplex virus 1 capsids to the nucleus, J. Cell Biol.136 (1997) 1007-21.
5. M. Bomsel, R. Parton, S.A. Kuznetsov, T.A. Schroer, J. Gruenberg, Microtubule- and motor-dependent fusion in vitro between apical and basolateral endocytic vesicles from MDCK cells, Cell 62 (1990) 719-31.
6. G. Apodaca, L.A. Katz, K.E. Mostov, Receptor-mediated transcytosis of IgA in MDCK cells is via apical recycling endosomes, J. Cell Biol. 125 (1994) 67-86.
7. D. McDonald, M.A. Vodicka, G. Lucero, T.M. Svitkina, G.G. Borisy, M. Emerman, T.J. Hope, Visualization of the intracellular behavior of HIV in living cells, J. Cell Biol. 159 (2002) 441-52.

8. H. Mabit, M.Y. Nakano, U. Prank, B. Saam, K. Dohner, B. Sodeik, U.F. Greber, Intact microtubules support adenovirus and herpes simplex virus infections, J. Virol. 76 (2002) 9962-71.
9. P.L. Leopold, G. Kreitzer, N. Miyazawa, S. Rempel, KK. Pfister, E. Rodriguez-Boulan, R.G. Crystal, Dynein- and microtubule-mediated translocation of adenovirus serotype 5 occurs after endosomal lysis, Human Gene Ther. 11 (2000) 151-65.
10. K. Kaelin, S. Dezelee, M.J. Masse, Bras F, A. Flamand, The UL25 protein of pseudorabies virus associates with capsids and localizes to the nucleus and to microtubules, J. Virol. 74 (2000) 474-82.
11. E. Lycke, K. Kristensson, B. Svennerholm, A. Vahlne, R. Ziegler, Uptake and transport of herpes simplex virus in neurites of rat dorsal root ganglia cells in culture, J. Gen. Virol. 65(1984) 55-64.
12. P.T. Ohara, M.S. Chin, J.H. LaVail, The spread of herpes simplex virus type 1 from trigeminal neurons to the murine cornea: an immunoelectron microscopy study, J. Virol. 74 (2000) 4776-86.
13. H. Tsiang, P.E., Ceccaldi E. Lycke, Rabies virus infection and transport in human H sensory dorsal root ganglia neurons, J. Gen. Virol. 72 (1991) 1191-4.
14. H. Tsiang, E. Lycke, P.E. Ceccaldi, A. Ermine, X. Hirardot, The anterograde transport of rabies virus in rat sensory dorsal root ganglia neurons, J Gen Virol. 70 (1989) 2075-2085.
15. S.Ohka, W.X. Yang, E. Terada, K. Iwasaki, A. Nomoto, Retrograde transport of intact poliovirus through the axon via the fast transport system. Virology 250 (1998) 67-75.
16. Z. Richterova, D.Liebl, M.Horak, Z.Palkova, J.Stokrova, P.Hozak, J. Korb, J. Forstova, Caveolae are involved in the trafficking of mouse polyomavirus virions and artificial VP1 pseudocapsids toward cell nuclei, J Virol. 75 (2001) 10880-91.
17. L. Pelkmans, D. Puntener, A. Helenius, Local actin polymerization and dynamin recruitment in SV40-induced internalization of caveolae, Science 296 (2002) 535-9.
18. M.D. Welch, J.Rosenblatt, J.Skoble, D.A. Portnoy, T.J Mitchison, Interaction of human Arp2/3 complex and the Listeria monocytogenes ActA protein in actin filament nucleation, Science 281 (1998) 105-8.
19. E. Gouin, H. Gantelet, C. Egile, I. Lasa, H. Ohayon, V. Villiers, P. Gounon, P.J. Sansonetti, P. Cossart, A comparative study of the actin-based motilities of the pathogenic bacteria Listeria monocytogenes, Shigella flexneri and Rickettsia conorii, J. Cell Sci. 112 (1999) 1697-708.
20. N. Scaplehorn, A. Holmstrom, V. Moreau, F. Frischknecht, I. Reckmann, M.Way, Grb2 and Nck act cooperatively to promote actin-based motility of vaccinia virus, Curr. Biol. 12 (2002) 740-5.
21. F. Frischknecht, V. Moreau, S. Rottger, S. Gonfloni, I. Reckmann, G. Superti-Furga, M. Way, Actin-based motility of vaccinia virus mimics receptor tyrosine kinase signalling, Nature 401 (1999 926-9.
22. A.L. Rozelle, L.M. Machesky, M.Yamamoto, M,H. Driessens, R.H. Insall, M.G. Roth, K. Luby-Phelps, G. Marriott, A. Hall, H.L. Yin, Phosphatidylinositol 4,5-bisphosphate induces actin-based movement of raft-enriched vesicles through WASP-Arp2/3, Curr. Biol. 10 (2000) 311-20.
23. E. Lee, P. De Camilli, Dynamin at actin tails, Proc. Natl. Acad. Sci. U S A. 99 (2002) 161-6.

24. J.D. Orth, E.W. Krueger, H. Cao, M.A. McNiven, The large GTPase dynamin regulates actin comet formation and movement in living cells, Proc. Natl. Acad. Sci. U S A. 99 (2002) 167-72.

25. S. Benesch, S. Lommel, A. Steffen, T.E. Stradal, N. Scaplehorn, M. Way, J. Wehland, K. Rottner, Phosphatidylinositol 4,5-biphosphate (PIP2)-induced vesicle movement depends on N-WASP and involves Nck, WIP, and Grb2, J. Biol. Chem. 277 (2002) 37771-6.

26. J.M. Duran, F. Valderrama, S. Castel, J. Magdalena, M. Tomas, H. Hosoya, J. Renau-Piqueras, V. Malhotra, G. Egea, Myosin motors and not actin comets are mediators of the actin-based Golgi-to-endoplasmic reticulum protein transport, Mol. Biol. Cell 14 (2003) 445-59.

27. R. Matteoni, T.E. Kreis, Translocation and clustering of endosomes and lysosomes depends on microtubules, J. Cell Biol. 105 (1987) 1253-65.

28. J.Gilbert, T. Benjamin, Uptake Pathway of Polyomavirus via Ganglioside GD1a, J. Virol. 78 (2004) 12259-12267.

29. P. Mannova, J. Forstova, Mouse polyomavirus utilizes recycling endosomes for a traffic pathway independent of COPI vesicle transport, J. Virol. 77 (2003) 1672-81.

30. J.M. Gilbert, I.G. Goldberg, T.J. Benjamin, Cell Penetration and Trafficking of Polyomavirus, J. Virol. 77 (2003) 2615-2622.

31. R. Kjeken, M.Egeberg, A. Habermann, M. Kuehnel, P. Peyron, M. Floetenmeyer, P. Walther, A. Jahraus, H. Defacque, S.A. Kuznetsov, G. Griffiths, Fusion between phagosomes, early and late endosomes: a role for actin in fusion between late, but not early endocytic organelles, Mol. Biol. Cell 15 (2004) 345-58.

32. J.A. Barden, M. Miki, B.D. Hambly, C.G. Dos Remedios, Localization of the phalloidin and nucleotide-binding sites on actin, Eur. J Biochem. 162 (1987) 583-8.

33. L.M. Macheski, A. Hall, Role of actin polymerisation and adhesion to extracellular matrix in Rac- and Rho- induced cytoskeletal reorganisation, J. Cell Biol. 138 (1997) 913-926.

34. J. Lippincott-Schwartz, Cytoskeletal proteins and Golgi dynamics, Curr. Opin. Cell Biol. 10 (1998) 52-9.

35. R.M. Stemman, S.E. Brodie, Z.A. Colin, Membrane flow during pinocytosis. A stereologic analysis, J. Cell Biol. 68 (1976) 665-687.

36. M. Lakadamyali, M.J. Rust, H.P. Babcock, X. Zhuang, Visualizing infection of individual influenza viruses, Proc. Natl. Acad. Sci. U S A 100 (2003) 9280-9285.

37. B. Sodeik, Unchain my heart, baby let me go - The entry and intracellular transport of HIV, J. Cell Biol. 159 (2002) 393-5.

38. G.A. Smith, S.P. Gross, L.W. Enquist, Herpesviruses use bidirectional fast-axonal transport to spread in sensory neurons, Proc. Natl. Acad. Sci. U S A. 98 (2001) 3466-70.

39. K. Dohner, A. Wolfstein, U. Prank, C. Echeverri, D. Dujardin, R. Vallee, B. Sodeik, Function of dynein and dynactin in herpes simplex virus capsid transport, Mol. Biol. Cell 13 (2002) 2795-809.

40. R.J. Diefenbach, M. Miranda-Saksena, E. Diefenbach, D.J. Holland, R.A. Boadle, P.J. Armati, AL. Cunningham, Herpes simplex virus tegument protein US11 interacts with conventional kinesin heavy chain, J. Virol. 76 (2002) 3282-91.

41. J.D. Huang, S.T. Brady, B.W. Richards, D. Stenolen, J.H. Resau, N.G. Copeland, N.A. Jenkins, Direct interaction of microtubule- and actin-based transport motors, Nature 397 (1999) 267-270.

42. J. Fan, Q. Zhang, H. Tochio, M. Li, M. Zhang, Structural basis of diverse sequence-dependent target recognition by the 8 kDa dynein light chain, J. Mol. Biol. 306 (2001) 97-108.

43. J.F. Presley, C. Smith, K. Hirschberg, C. Miller, N.B. Cole, K.J. Zaal, J. Lippincott-Schwartz, Golgi membrane dynamics, Mol. Biol. Cell 9 (1998) 1617-26.

44. S. Felder, Z. Kam, Human neutrophil motility: time-dependent three-dimensional shape and granule diffusion, Cell Motil Cytoskeleton 28 (1994) 285-302.

45. S.P. Gross, M.A. Welte, S.M. Block, E.F. Wieschaus, Dynein-mediated cargo transport in vivo, A switch controls travel distance, J. Cell Biol. 148 (2000) 945-56.

46. S.P. Gross, M.A. Welte, S.M. Block, E.F. Wieschaus, Coordination of opposite-polarity microtubule motors. J. Cell Biol. 156 (2002) 715-724

47. S.M. Block, L.S. Goldstein, B.J. Schnapp, Bead movement by single kinesin molecules studied with optical tweezers, Nature 348 (1990) 348-52.

48. Loisel,T.P., Boujemaa,R., Pantaloni,D. & Carlier,M.F. Reconstitution of actin-based motility of Listeria and Shigella using pure proteins. *Nature* **401**, 613-616 (1999).

49. Carlier,M.F., Wiesner,S., Le Clainche,C. & Pantaloni,D. Actin-based motility as a self-organized system: mechanism and reconstitution in vitro. *Comptes Rendus Biologies* **326**, 161-170 (2003).

50. Cameron,L.A., Footer,M.J., van Oudenaarden,A. & Theriot,J.A. Motility of ActA protein-coated microspheres driven by actin polymerization. *Proceedings of the National Academy of Sciences of the United States of America* **96**, 4908-4913 (1999).

51. Pantaloni,D., Le Clainche,C. & Carlier,M.F. Cell biology - Mechanism of actin-based motility. *Science* **292**, 1502-1506 (2001).

52. Carlier,M.F.T., Loisel,T.P., Boujemaa,R. & Pantaloni,D. Reconstitution of actin-based motility of Listeria and Shigella using pure proteins. *Biophysical Journal* **78**, 240A (2000).

53. Pelkmans,L. & Helenius,A. Endocytosis via caveolae. *Traffic* **3**, 311-320 (2002).

54. Pelkmans,L., Puntener,D. & Helenius,A. Local actin polymerization and dynamin recruitment in SV40-induced internalization of caveolae. *Science* **296**, 535-539 (2002).

55. Rafelski,S.M. & Theriot,J.A. Bacterial shape and ActA distribution affect initiation of Listeria monocytogenes actin-based motility. *Biophysical Journal* **89**, 2146-2158 (2005).

56. Purich,D.L., Kang,F., Laine,R.O., Bubb,M.R. & Southwick,F.S. Mechanism of actin-based Listeria motility: Interaction of profilin with VASP's GPPPPP repeat sequences. *Molecular Biology of the Cell* **7**, 2194 (1996).

57. Laurent,V. *et al.* Role of proteins of the Ena/VASP family in actin-based motility of Listeria monocytogenes. *Journal of Cell Biology* **144**, 1245-1258 (1999).

58. Nakamura,K. *et al.* Transiently increased colocalization of vesicular glutamate transporters 1 and 2 at single axon terminals during postnatal development of mouse neocortex: a quantitative analysis with correlation coefficient. *Eur. J. Neurosci.* **28**, 1032-1046 (2008).

59. Richterova,Z. *et al.* Caveolae are involved in the trafficking of mouse polyomavirus virions and artificial VP1 pseudocapsids toward cell nuclei. *J. Virol.* **75**, 10880-10891 (2001).

FIGURES

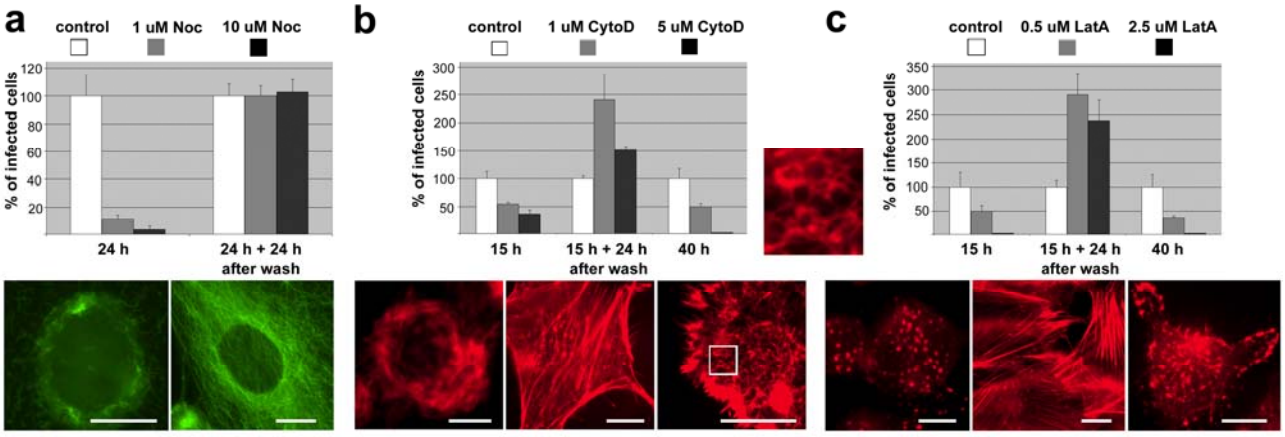

Fig. 1: Cytoskeletal drug assay. Cells infected in the presence of nocodazole (**a**), cytochalasin D (**b**) and latrunculin A (**c**) in two different concentrations, incubated until the time of fixation and immunostained against viral LT antigen. The efficiency of infection was calculated from the number of cells positive for LT antigen correlated to the control cells infected and incubated without a drug (100%). In parallel samples, the drug was washed out and cells were thereafter incubated for additional time prior to fixation and immunostaining to prove the reversibility of the inhibition effect. Immunofluorescent staining (lower panel) of microtubules (anti-βtubulin) and microfilaments (rhodamine-coupled phalloidin) shows the current morphology of the cytoskeleton at respective times of cell fixation with or without the drug (according to column graphs above). Bars = 5 μm

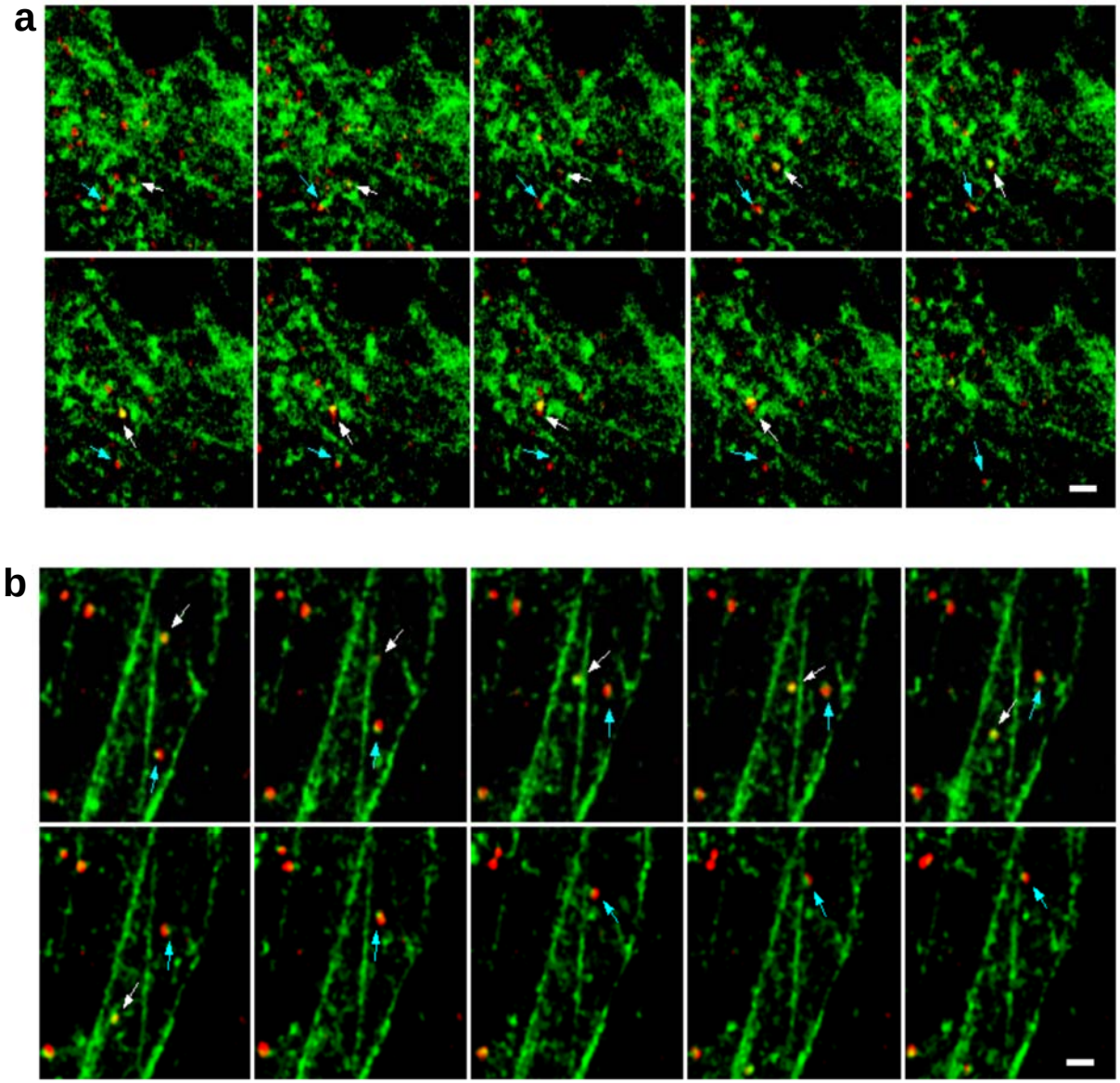

Fig. 2: Two examples of mouse 3T6 fibroblasts expressing GFP-actin infected with Alexa 594-prestained virus (MOI = 10^3 virus particles per cell) and scanned in an open, medium containing chamber with ΔT = 3 sec. Selected frames from two different cells are shown in detail (see Actin1-2 movies in supplementary material). Arrowheads point to virions propelled by the associated actin comet tail along F-actin bundles. Bars = 5 μm

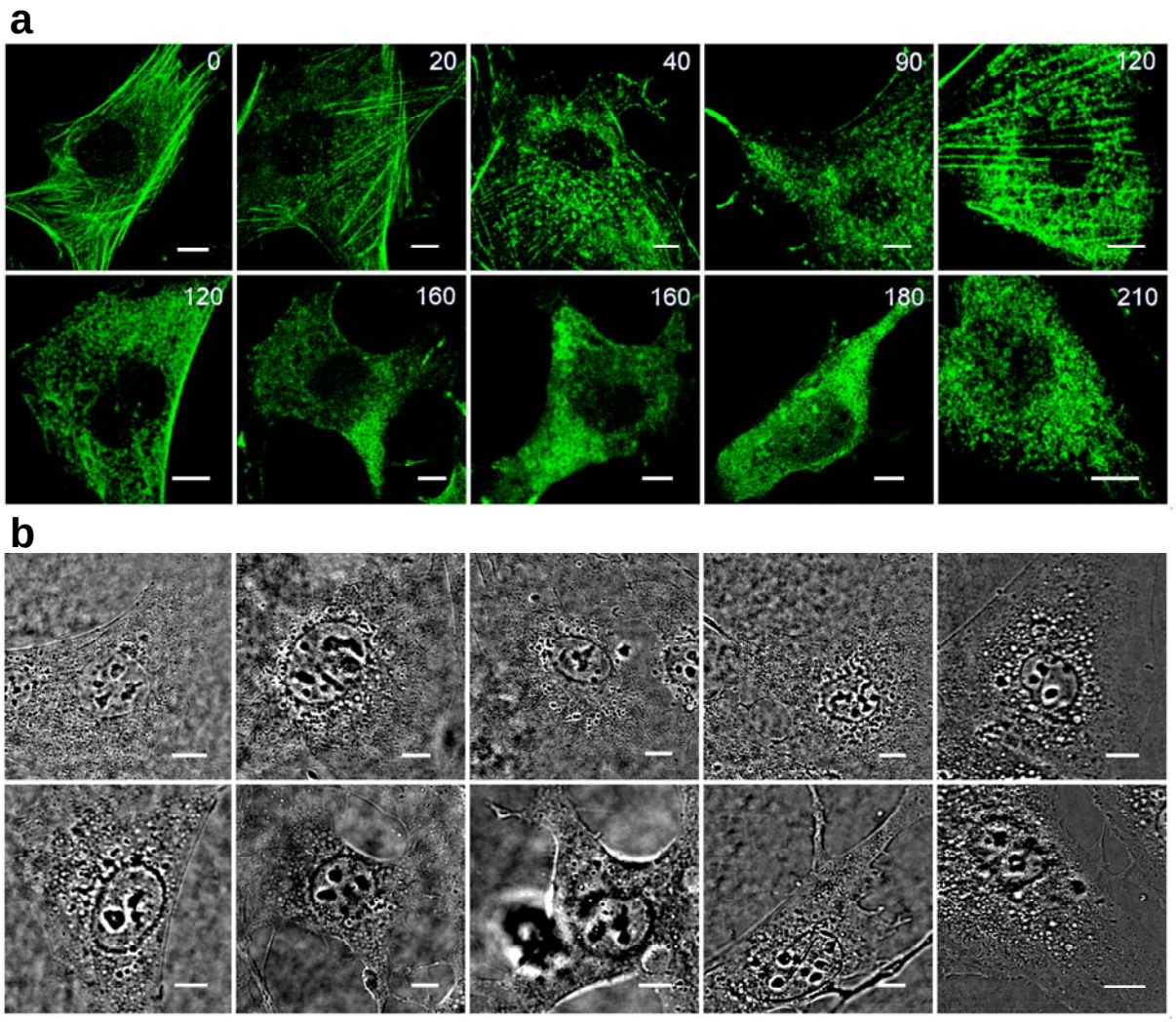

Fig. 3: Depolymerization of F-actin stress fibres and reorganisation into actin rings. Mouse 3T6 fibroblast cells expressing GFP-actin infected by Alexa-594 pre-stained PyV (red) at high MOI (10^4 virions per cell). Fluorescence image at different times post infection (**a**), and respective tramsition image (**b**)

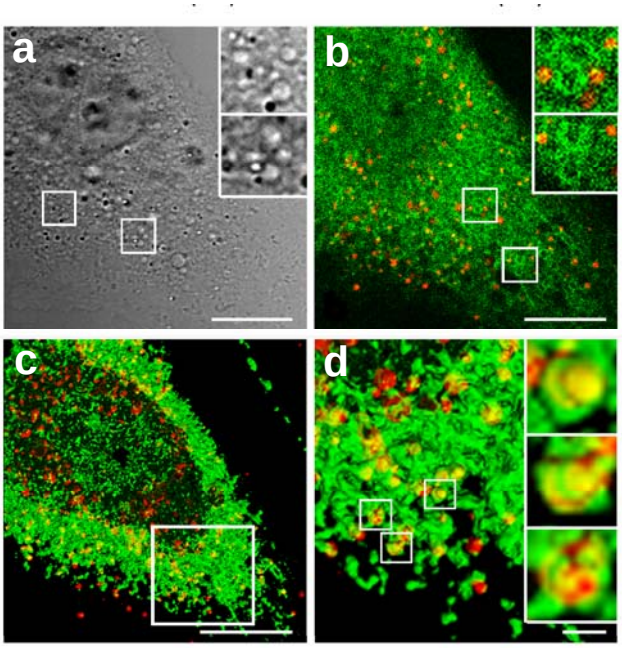

Fig. 4: Actin rings and Pyv colocalization.

Mouse 3T6 fibroblast cells expressing GFP-actin infected by Alexa-594 pre-stained PyV (red) at high MOI (10^4 virions per cell). Transmission light (**a**), one merged confocal section (**b**).

3D rendering image mounted from confocal sections (**c**) with a detailed view (**d**) where reorganisation of F-actin into the array of ring-shaped structures is clearly visible on enlarged inserts (see Rings1 movies in supplementary material).

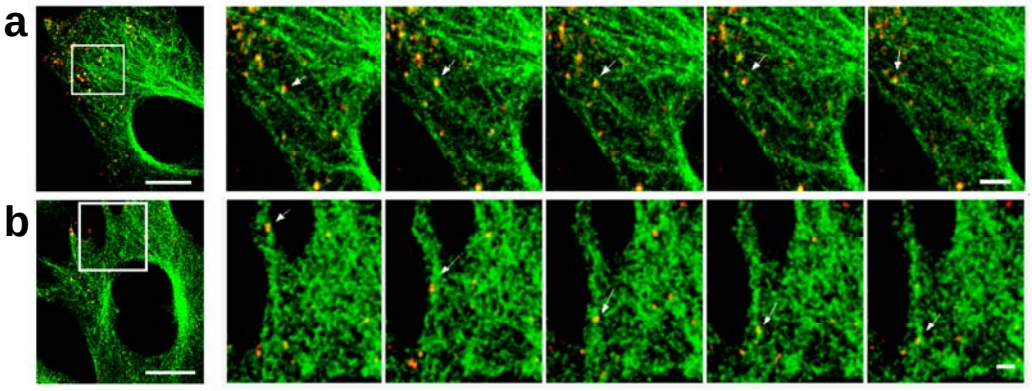

Fig. 5: Two example of mouse 3T6 fibroblasts expressing GFP-tubulin infected with Alexa-594-prestained virus (MOI = 10^3 virus particles per cell) and scanned in an open, medium containing chamber with ΔT = 6 sec. Virions are transported to both directions: to the cell periphery (upper

panel) and to the nuclear periphery (lower panel). Selected frames from two different cells are shown in detail (see Tubulin1 and Tubulin2 movies in supplementary material). Bars = 5 μm

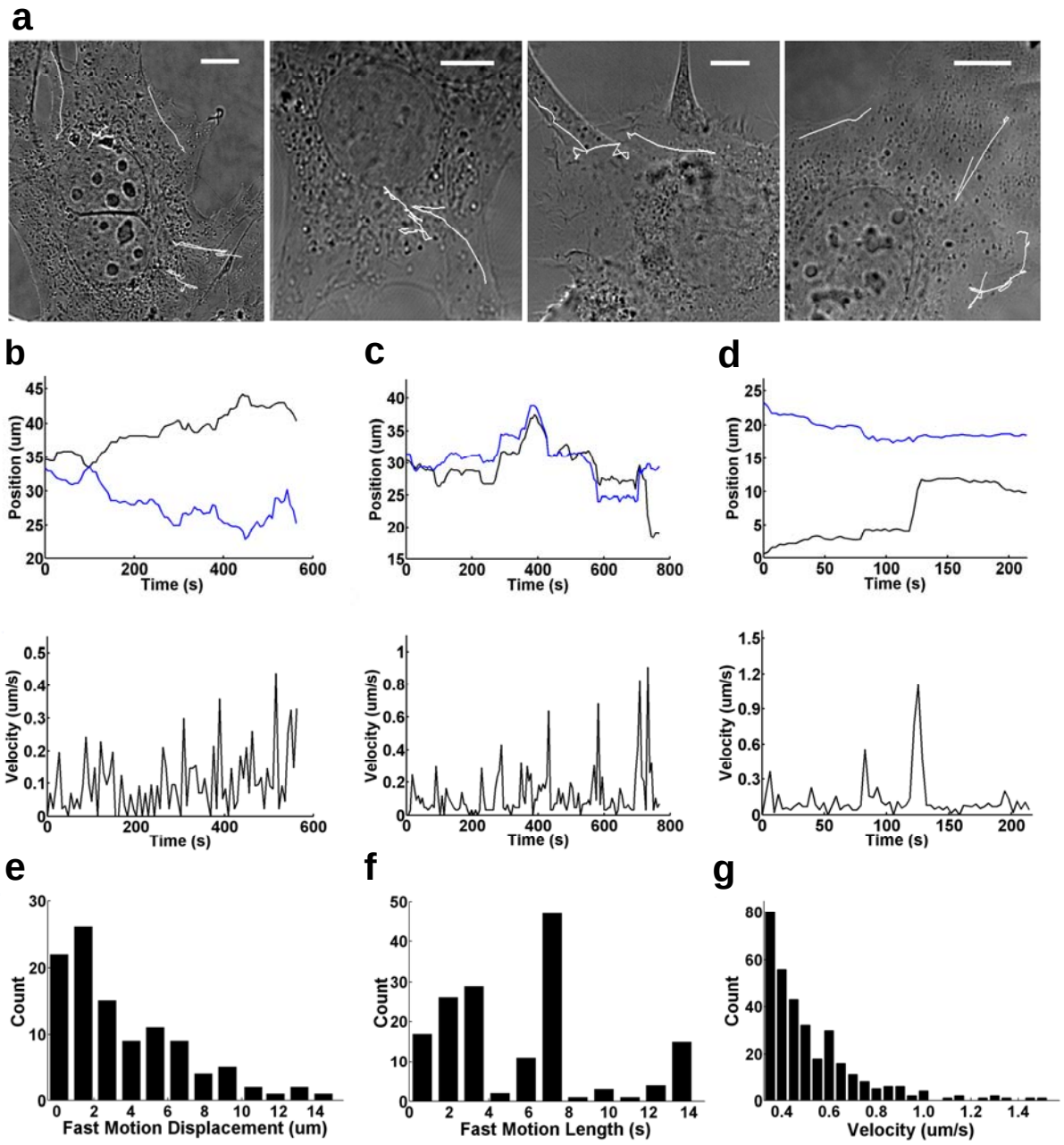

Fig. 6: Single particle tracking of fluorescently labelled virions in host cells. Complex trajectories marked in white tracking curves in four selected cells shown in transmission light (**a**). Three main types of virion transport velocities (**b-d**) with single particle position tracking on x-y coordinates (upper graphs) and course of movement velocities (lower graphs) measured in time intervals of 3

sec (mean velocity was averaged from each three following time steps). Dynamics of three independent single particle trackings are shown.

Histogram of fast movement distances (**e**), counted from 109 single fast movements and sampled into 0.5 µm step intervals, with a peak at 1.5 µm and the average distance of 2.5 µm. Time span frequency (**f**) of fast (≥ 0.6 µm/sec) movements with peaks at 1.5 and 5.7 sec. Frequency of virion transport velocity rates (**g**), counted from 200 different tracking experiments in 3T6 mouse fibroblast cells, with a distinct peak at 0.6 µm/sec (x-coordinate was cropped to cut off the high frequency of short-range movements at diffusion rates < 0.3 µm/sec).

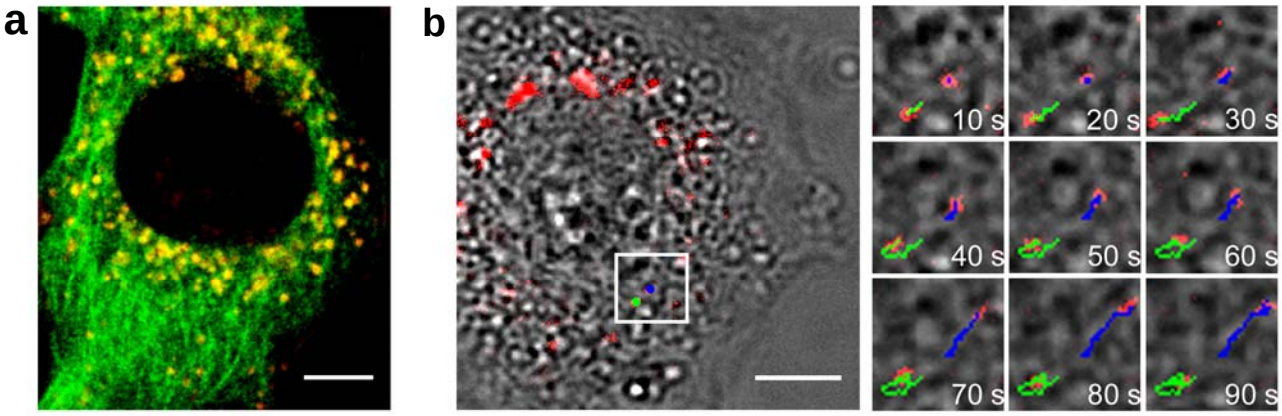

Fig. 7: Pyv colocalicalization at the perinuclear membrane (3 h p.i.). In green GFP tubulin, in red PyV marked with alexa 594 **(a).** Particle tracking of fluorescently labelled virions in a host cell later post infection. The cell is shown in transmission light merged with the red fluorophore-coupled virus signal **(b)**. Trajectories of two selected virions marked green and blue (on left). Time sequence frames detail (on right) (see Tracking1 movie in supplementary material).

1.4 FRAP technique

1. **Creatine kinase binds more firmly to the M-band of rabbit skeletal muscle myofibrils in the presence of its substrates.**
   J. Zurmanova, **F. Difato**, D. Malacova, J. Mejsnar, B. Stefl, I. Zahradnik**.** Mol Cell Biochem. 2007 Jun 20; 17578655

2.4.1. Aims and results

Aims:

- To localize the catalytic site of creatine kinase (CK) in myofibrils.
- To estimate the reaction rate between CK and M-line in myofibrils by FRAP technique.
- To compare reaction rate of CK in presence of different substrates.

Results:

- The ability of myofibrils to contract was proved by confocal microscopy visualization of the length of sarcomers. Relaxed myofibrils had a resting length of 2.1 ± 0.20 μm and after the contraction, in presence of 5 mM ATP and 7 mM $CaCl_2$, they shortened to the length of 1.6 ± 0.12 μm
- Location of binding of fluorophore conjugated CK (CK-IAF) in the M-band was confirmed by confocal microscopy. The resulting visualization of the M-band by confocal microscopy showed "discs" of CK-IAF molecules, associated with the M-bands and without penetration in the axial direction of the myofibrils.
- We defined a FRAP protocol where photobleaching was applied on the surrounding of the sample and not directly to the structure.
- FRAP method allowed us to evaluate the exchange rate of CK-IAF (substrates free) between the M-band in the myofibrils and the solution.
- The value of pH has a strong influence on the CK-IAF interaction with myofibrils. The amount of exchanged CK-IAF in the M-band under different pH condition was relatively expressed as ratio of fluorescence intensity in the M-band and its surroundings. In acid pH (pH 6.8–6.9), we did not observe any fluorescence signal in the M-band during the exchange experiment and therefore, the ratio equalled 1. In neutral pH, the exchange reaction occurs at the ratio 2.45 ± 0.15 and reaches its maximum value of 5.67 ± 1.26 in a basic environment of pH 7.10–7.15. We performed FRAP experiment in the pH range of 7.10–7.15.
- The exchange rate in the presence of substrates is more than 60 times slower. The experiments show how the conformation change of the CK molecule, evoked by substrates binding, affects the process of exchange between the M-band and surroundings.

2.4.2. Discussion

The more important characteristic of fluorescence microscopy is the possibility to apply live imaging. This permits to monitor the temporal dimension of a process and therefore to analyse its dynamics. FRAP and FLIP are dual techniques based on very similar protocol, where fast photobleaching of fluorescent molecules permits to resolve some aspects of the biological process in the temporal domain.
We applied a photobleaching protocol to study reaction kinetic of CK in the M line of a sarcomere. By fitting the fluorescence intensity curve, with a simple two exponential equation (taking into account the reaction exchange rate and the unwanted photobleaching occurring during fluorescence imaging) we compare the reaction kinetics of the molecule CK with the myofibrils under different experimental conditions. This was important to understand the interaction of the enzyme with structural proteins, which can play a role in the cellular control of the myofibril activity. Purified myofibrils preserved their physiological function, which was proved by their ability to contract. Therefore, we measured the reaction kinetics of the enzyme with the entire structure of muscle, in experimental conditions close to that in a living organism.
We developed FRAP protocol where photobleaching was applied on the surrounding of the sample and not directly on the structure. This enables us to measure directly fluorescence dynamics during

photobleaching, with no blind temporal window between bleaching and recording phase, and without drastic photodamage of the specimen. This is an important issue because a high intensity laser light can induce conformational changes in the molecule and imply changes of its functional behaviour.
With these measurements, we were also able to evidence that elution of CK from the myofibrils by low ionic-strength medium decreased the specific CK activity. The aim of elution was to obtain a simpler kinetic model and to eliminate the fixed portion of CK molecules on M-line that constitutes a background signal. FRAP experiments showed irreversible binding of CK-IAF in contrast to the ‘‘intact’’ myofibrils. Subsequently SDS-PAGE results showed a loss of other proteins from myofibrils besides CK. Therefore, by FRAP measurements it was possible to define less invasive preparation protocol of the myofibrils.
We could also notice the pH dependence of CK interaction with the M-line in the sarcomere: in a slightly acidic environment the bond of the native CK is so strong that it excludes the CK exchange between myofibrils and their surroundings, while in a slightly basic environment the exchange process reaches its maximum rate. This fact can be hypothetically explained by the physiological function of CK, as a pH and ATP buffer upon muscle contraction.
Furthermore, we observed as CK’s substrates change the affinity of CK molecule to the myofibrils.
Only by FRAP measurement, it was possible to distinguish bounded and unbounded portion of CK molecules to the M line in the sarcomere and to reveal a reaction exchange with the surroundings, which was not noticed in the preliminary measurements, where we defined the CK localization in the sarcomere by 3D reconstruction. In conclusion, also a qualitative analysis of FRAP data can give important information on the sample, which cannot be obtained by the spatial architecture of the structure.

2.4.3. Publications

Mol Cell Biochem (2007) 305:55–61
DOI 10.1007/s11010-007-9527-1

Creatine kinase binds more firmly to the M-band of rabbit skeletal muscle myofibrils in the presence of its substrates

Jitka Zurmanova · Francesco Difato · Daniela Malacova · Jiri Mejsnar · Bohumir Stefl · Ivan Zahradnik

Received: 5 March 2007 / Accepted: 23 May 2007 / Published online: 20 June 2007

Abstract Creatine kinase (CK) (E.C. 2.7.3.2) buffers cellular ATP concentration during fluctuating ATP turnover. Muscle cytosolic CK isoform interacts with various subcellular structures where it is functionally coupled with relevant ATPases. However, how this interaction affects its activity is not known. We have therefore studied the interaction of CK with myofibrils and the role of different conformational states of CK molecule induced by ATP, phosphocreatine, ADP and the ATP-creatine pair. Purified rabbit psoas myofibrils with CK specific activity of 0.4 ± 0.02 IU/mg were used. The exchange rates between the myofibrillar M-band and its surroundings were measured with fluorofore conjugated CK (IAF) by the Fluorescence Lost in Photobleaching (FLIP) method within a very narrow pH range 7.1–7.15. For CK-IAF without docked substrates, the time derivative of the initial loss of the fluorescent signal within the M-band equalled –3.26 at the fifth second and the decrease reached 82% by the 67th second. For CK-IAF with added substrates, the derivatives fell into the range of –0.95 to –1.30, with respective decreases from 16 to 46% at the 67th second. The results show that the substrates slowed down the exchange rate. This indicates that the strength of the bond between CK and the M-band of myofibrils increased.

Keywords Muscle · Creatine kinase · Myofibrillar—sarcoplasmic exchange

J. Zurmanova (✉) · F. Difato · D. Malacova · B. Stefl
Department of Physiology, Faculty of Science, Charles University in Prague, Prague 2 128 00, Czech Republic
e-mail: jizurman@natur.cuni.cz

J. Zurmanova · D. Malacova
Institute of Physiology, Academy of Sciences, Prague, Czech Republic

J. Mejsnar
Institute of General Biology and Genetics, 3rd Faculty of Medicine, Charles University, Prague, Czech Republic

I. Zahradnik
Institute of Molecular Physiology and Genetics Academy of Sciences, Bratislava, Slovak Republic

Introduction

The creatine kinase/phosphocreatine system plays an important role in muscle energetic metabolism. It is well compartmentalized and is a very efficient system of maintaining optimal ATP/ADP ratio during muscle contraction; for review see [1, 2]. The control of creatine kinase (CK) activity is realized by conformational changes of the CK molecule that are closely related to changes in the Gibbs free energy due to the concentrations of the substrates. However, the force field computation for three energetic states (the substrate-free CK molecule, the molecule conjugated with the MgATP complex and the pair MgATP-creatine) revealed an inactive "open", reactive "closed" and a non-reactive "intermediary" conformation, respectively [3]. The data have been confirmed experimentally by measuring anisotropies, lifetimes of the fluorescence by intrinsic tryptophans and the radii of CK molecule gyration determined by the respective rotational correlation times [4]. These results propose the existence of an essential cellular component of the CK activity control, consisting of CK interaction with a given subcellular structures (reviewed by Wallimann et al. [5]) and resulting in the conformational shift to the reactive "closed" form of the CK molecule.

The unique interaction with myofibrils involves two parts, namely the binding of the CK molecule to the myofibrillar M-band and the exchange of CK between the M-band and its cytosol surroundings, the both of which are still poorly understood. According to Stolz and Wallimann [6] the N-terminal region of MM-CK mediates its specific isoform interaction with sarcomeric M-bands. Two pairs of key amino acid residues at this region were determined on the dimeric MM-CK molecule. The first is represented by highly conserved lysine residues (K104, K115) which creates a strong binding site; the second (K8, K24) is a weak interacting site [7]. The specific bonding partners of MM-CK in the M-band were identified as myomesin and M-protein [8].

The labelled MM-CK binding with rather high affinity to the M-band during equilibration can be replaced rather rapidly by unlabelled enzyme from its surroundings [9]. In other words, from a thermodynamic point of view, the M-band – CK bond is at its physiological role in the stationary state, which is maintained by the exchange of CK between myofibrils and cytosol. The finding has two consequences. The first, under definite conditions, the exchange rate between myofibrils and their surroundings should indicate – in reciprocal proportion – the force that holds CK and M-band proteins together. The second, CK (with its docked substrates) has to be kinetically different from experimentally prepared CK (substrates free), in order to maintain the stationary state [10]. Furthermore, for the physiological role, the strength of the CK (with substrates) – M-band bond has to be stronger than the bond with the CK (substrates free) – M-band, indicated by their exchange rates. Thus the experimental question arises how the interaction of the CK with myofibril is influenced by a conformational state of CK molecule, evoked by its binding with substrates.

Results of the present study show the stronger bond of the CK (with substrates) during its specific interaction with myofibrils in the M-band. In the stationary state, its exchange rate with the surroundings in real time is slower than in comparison with the exchange rate of the CK (substrates free) and with the rates for non-specifically bound CK.

Materials and methods

Chemicals

Creatine kinase from rabbit muscle (CK) was obtained from Roche Diagnostic GmbH, as well as all enzymes and substrates for enzyme coupled assays. Fluorescent probes and conjugates were from Molecular Probes (USA), DC Protein assay and SDS-PAGE molecular weight standards from Bio-Rad Laboratories Inc.; all other chemicals were from Sigma-Aldrich.

Rabbit creatine kinase from skeletal muscle was conjugated with 5-iodoacetamidofluorescein (IAF) as described previously by Gregor et al. [11].

Solutions

(A) *no calcium isotonic solution* (mM): NaCl 121, fresh protease inhibitors –Phenylmethylsulphonylfluoride (PMSF) 0.1, NaN_3 3 and Ethylene glycol-bis(beta-aminoethyl ether)-N,N,N′,N′-tetraacetic acid (EGTA) 1; Ethylenediamine-tetraacetic acid (EDTA) 5, 1,4 Dithio-DL-threitol (DTT) 0.2; pH 7.0. B) *low-ionic-'strength medium* (mM): 3-morpholinopropanesulfonic acid (MOPS) 20, Manitol 11, EDTA 4, DTT 5; pH 7.1. C) *relaxing buffer* (mM): HEPES 20, $MgCl_2$ 1.2, EGTA 5, EDTA 1, DTT 2, PMSF 0.1, NaN_3 3, potassium propionate 100 and Di(Adenosin) Pentaphosphate (Ap_5A) - adenylate kinase inhibitor –0.2 at pH 7.1.

Isolation of myofibrils

The experiments were performed in accordance with local ethical committee guidelines (Czech Ministry of Agriculture, No. 1020/437/A/99).

Muscle tissue was obtained from a half-year-old male rabbit Chinchila weighing 2.8–3.2 kg. Seven rabbits were used for a whole study. The rabbits were killed by rapid cervical dislocation and bleed. Left and right psoas muscles were isolated and immediately immersed into no calcium isotonic solution A and placed at room temperature. The muscles were cut into small pieces and transferred to solution A free of NaCl containing 100 mM KCl and 50% glycerol [12]. After 60-min glycerol penetration into the pieces of muscle the samples could be stored at –20°C for up to 2 months. Isolation of myofibril was performed by homogenization at 4°C using solution A free of NaCl containing 100 mM KCl. Sample was twice homogenized by rotation homogenizer and centrifuged at 1000 g. After 20 min incubation of sediment on ice this homogenization/washing cycle was repeated five times using glass homogenizer with teflon plunger [12, 13]. The myofibrillar fraction was then incubated with 1% Triton X-100 (vol/vol) for 5 min on ice and centrifuged [14]. After that seven washing cycles were repeated. We made following modification: $MgCl_2$ (2.5 mM) was added into medium from the third washing cycle in order to prevent the degradation of actin filaments.

Two sorts of myofibrils were used for the FLIP experiment: "*intact*" and "*treated*".

In the case of "*intact*" myofibrils, the exchange rate of naturally bound CK in the M-band with external fluorescently labelled CK by 5-iodoacetamidfluorescein (CK-IAF)

was measured directly after isolation. In the second case, "*treated*" myofibrils were incubated in a low-ionic-strength medium B for 15 min which removed the native CK molecules from the M-band. Subsequent reconstitution of the native CK by the external CK-IAF was performed according to Ventura-Clapier et al. [15]. This is stated in the Exchange experiments chapter.

A protein profile, obtained by elution using low ionic strength medium, was detected by SDS-PAGE electrophoresis (acrylamide gel 5% for stacking and 12% running gel, 210V, 90 min, Mini Protean 3-Bio Rad). Stained by silver according to Blum et al. [16].

Lengths of sarcomers and fluorescence intensity were measured using the quantification mode of Leica Confocal Software (LCS Lite) and ImageJ software, respectively.

The protein concentration of myofibrils was determined by DC Protein Assay with bovine serum albumin as a standard.

Exchange experiments

The replacement of naturally bound CK in the M-band of sarcomere by external fluorescently labelled CK-IAF was performed according to Kraft et al. [9] as follows. Purified myofibrils, in a concentration of 8–12 mg protein/ml, were incubated in a total volume of 100 µl of relaxing solution C with 2.5 µl of CK-IAF (5 mg protein/ml) added on a cover glass at 20°C for 10 min. This experiment was carried out either with or without CK substrates, adding each one individually, and for ATP-creatine pair at resting physiological concentrations (5 mM ATP, 12 mM phosphocreatine, 8 mM creatine and 0.62 µM ADP) [17].

Substrates' presence in freshly purified myofibrils was tested, using enzymatic-coupled assays [18, 19].

Myofibrils stained by Phalloidin-Alexa 633 conjugate were used for determining the location of CK-IAF. Location of CK-IAF binding site in sarcomere was proved using confocal microscopy resolution on the level of A- and I-bands. However it is well known that CK binds in A-bands to M-lines, therefore we present interaction of CK in the M-band despite of lower resolution of confocal microscopy.

FLIP measurements and data evaluation

The exchange interactions have been studied mainly by confocal microscopy, using the Fluorescence Lost in Photobleaching (FLIP) method according to scheme (Fig. 1a). The myofibrils equilibrated with CK-IAF were surrounded by a bleached region. The loss in the fluorescent signal in the central region of interest is due to the fact that, before the CK-IAF molecules reach the M-band sites of interaction, they have to pass the bleaching region. Therefore we evaluated the exchange between the fluorescent and the bleached CK-IAF molecules in the central region as the loss in the fluorescent signal in time (Fig. 1b).

Fluorescence Lost in Photobleaching measurements were performed on a confocal microscope (Leica SP2 AOBS) with 63×/1.2 NA water-immersion objective operating with an Argon laser tuned to 488 nm (10 mW) to excite the IAF dye. Bleaching was performed in a closed band around the myofibril with a 488 nm line operating at 25% laser power. Fluorescence loss was monitored at a low laser intensity (at 5% laser power) in 1.686 s intervals for 40 frames with a total acquisition time of 67 s. The exchange of CK-IAF between the myofibrils and its surroundings was measured in a stationary state by evaluating the loss of the fluorescent signal in myofibrils.

Myofibrils labelled under the same condition on actin filaments by Phalloidin-FITC conjugate were used for the bleaching control.

Fluorescence Lost in Photobleaching measurements were carried out in different substrate conditions, and repeated 6–20 times to aid the statistical evaluation. Data of

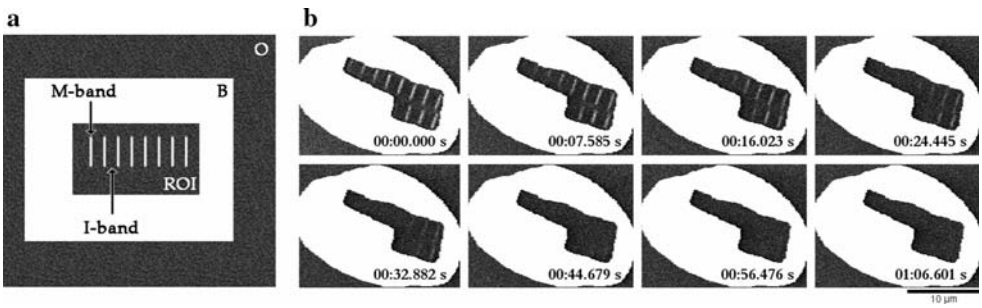

Fig. 1 (**a**) FLIP measurement organization. CK-IAF molecules bound into M-bands of the myofibril were surrounded by a continuously bleached region (B). The loss in the fluorescent signal in the central region of interest (ROI) including the M-bands is due to the fact that, before the CK-IAF molecules from outer surroundings of myofibril (O) reach the M-band sites of interaction, they have to pass the bleaching region (B). (**b**) The loss in the fluorescent signal in time sequence corresponds to the exchange rate between the fluorescent and bleached CK-IAF molecules in the M-bands during the FLIP measurement

fluorescent intensity decay obtained from M-bands for each group were averaged and normalized to 100% at the start of FLIP measurement. The experimental data of fluorescence decay were fitted to two-exponential curves. All the exchange rates presented in Figs. 4 and 5 are characterized for mutual comparison by two values: the derivative at the fifth second, and the percentage decrease of the fluorescence at the end of the experiment (67 s). The absolute value of the derivative, as well as the decrease, is proportional to the respective exchange rate.

The intensities of the signals are expressed as means ± S.E.M., n equals number of myofibrillar preparations. Differences amongst groups were compared by analysis of variance (ANOVA) after confirmation of the normal distribution of a variable (χ^2-test). In a case in which the normal distribution was not confirmed, a non-parametric Kruskal–Wallis test was used instead. Compairson was performed in five time intervals: 5, 10, 20, 40 and 60 s after the start of the FLIP measurement. The differences are accepted for $P < 0.05$ (using the Bonferroni multiplex comparison method).

Results

Characterization of myofibrils

Myofibrils were standardized for exchange rate measurements in the following three steps.

First, in order to study the effects of substrates for muscle creatine kinase (CK) interaction in the M-band, their absence was verified after the isolation procedure. The enzyme assays confirmed the absence of ATP, ADP, phosphocreatine and creatine in both preparations of myofibrils (see Methods). Second, the ability of myofibrils to contract was proved by the length of sarcomers. Relaxed myofibrils had a resting length of 2.1 ± 0.20 μm and after the contraction in presence of 5 mM ATP and 7 mM $CaCl_2$ they shortened to the length of 1.6 ± 0.12 μm. Third, creatine kinase specific activity was determined for "*intact*" and "*treated*" myofibrils as 0.4 ± 0.02 IU/mg protein and 0.01 ± 0.008 IU/mg protein, respectively.

The SDS-PAGE protein profile (Fig. 2) shows that the treatment of myofibrils with a low-ionic-strength medium lead to elution of not only the CK (43 kD), but also eluted proteins with a higher molecular weight of approximately 120, 80 and 70 kD and at a lower molecular weight of 43 kD (Fig. 2). The elution of proteins significantly changed the behaviour of myofibrils in the exchange experiments. The FLIP measurements revealed irreversible binding of CK-IAF (substrates free) in contrast to the "*intact*" myofibrils. "*Treated*" myofibrils were excluded from further exchange measurements.

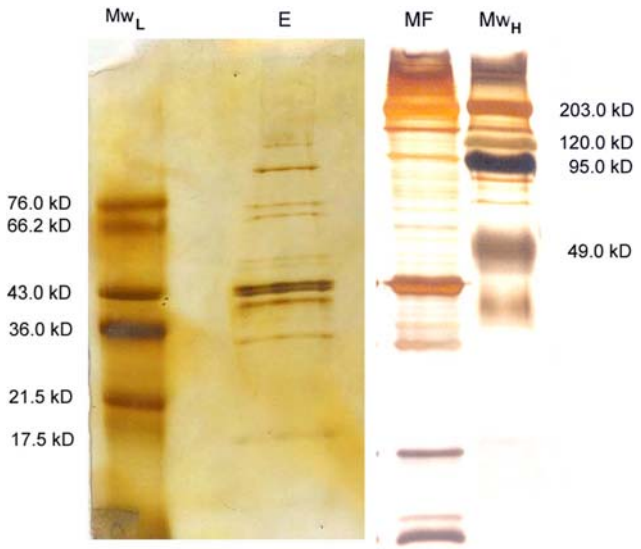

Fig. 2 Protein profiles of "*intact*" myofibrils (MF) and supernatant eluted from myofibrils using low-ionic-strength medium (E). (Mw_L) low molecular weight marker, (Mw_H) high molecular weight marker

Myofibrillar CK-IAF binding

Location of CK-IAF binding in the M-band was confirmed by confocal microscopy. Staining actin filaments within the I-bands, in red, and labelling CK-IAF, in green, within myofibrils (Fig. 3a) showed alternating green and red stripes, confirming the place of bound CK-IAF between two I-bands.

Unspecific surface adhesion of CK-IAF molecules and their axial distribution within the lumen of myofibrils (which could affect the measurements of the exchange rate) were excluded by xyz projection with subsequent 3D reconstruction from the data. The resulting visualization of the M-band by confocal microscopy showed "discs" of CK-IAF molecules, associated in the M-bands and without penetration in the axial direction (Fig. 3b). This result allowed us to study the real time exchange of CK-IAF molecules in the M-band by the FLIP method just in the two-coordinate planar system x-y with respect to time.

FLIP measurements evaluation

Results presented in Fig. 4 show weak but specific interaction of substrate free CK-IAF within the M-band which differs from the control. Phalloidin FITC conjugate tightly bound in the I-band was used as a control for CK-IAF bleaching in the M-band and its percentage fluorescence decrease reached 40% at the 67th second of the FLIP and the derivative at the fifth second (see Methods) equalled –0.96. These two characterizing values are compared with fluorescence decays of CK-IAF (substrates free) molecules in the M-band, the I-band and close surroundings. The

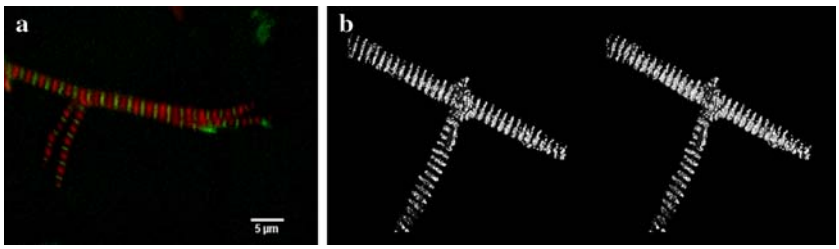

Fig. 3 Location of CK-IAF in the M-band of myofibrils visualized by confocal microscopy. (**a**) Staining of actin filaments within the I-bands by Phalloidin-Alexa 633 and CK-IAF marked in green. (**b**) 3D reconstruction of CK-IAF associated in the M-band of myofibrils, without its penetration in the axial direction

CK-IAF (substrates free) fluorescence decay in the M-band is characterized by the derivative –3.08, and the 80% decrease and it is significantly different ($P < 0.05$) from Phalloidin-FITC bleaching control values. The fluorescence intensities in the I-band and close surroundings are very low and identical.

CK-IAF (with substrates) molecules demonstrate very slow fluorescence decay during the experiment, presented in Fig. 5. The decay is not significantly different from the bleaching control, nevertheless it is different ($P < 0.05$) from the signal of CK-IAF (substrates free) molecules. The distinctive two values derivative/decrease for CK-IAF associated with the respective substrates are: ATP: –1.30/16%, phosphocreatine: –1.10/46%, ATP-creatine pair: –0.95/33%. The respective data for ADP (values are not shown in Fig. 5) equal 0.98/25%. There are not any significant differences amongst the substrates variants. The derivatives in this way fall within the range of –0.95 to –1.30 with the respective decreases ranging from 16 to 46%.

The decay of fluorescence signal of CK-IAF (substrates free) was repeatedly measured as a control to group of CK-IAF (with substrates) (Fig. 5) and reached –3.26/82%. Both sets of measurement of CK-IAF (substrates free) (Figs. 4 and 5) do not significantly differ ($P < 0.05$).

pH dependence of CK-IAF interaction in the M-band

The value of pH has a strong influence on the CK-IAF interaction with the myofibrils and the amount of exchanged CK-IAF in the M-band under different pH condition can be relatively expressed as ratio of fluorescence intensity in the M-band and its surroundings. Values of the ratio were measured as follows. In acid pH (pH 6.8–6.9) we did not observe any fluorescence signal in the M-band

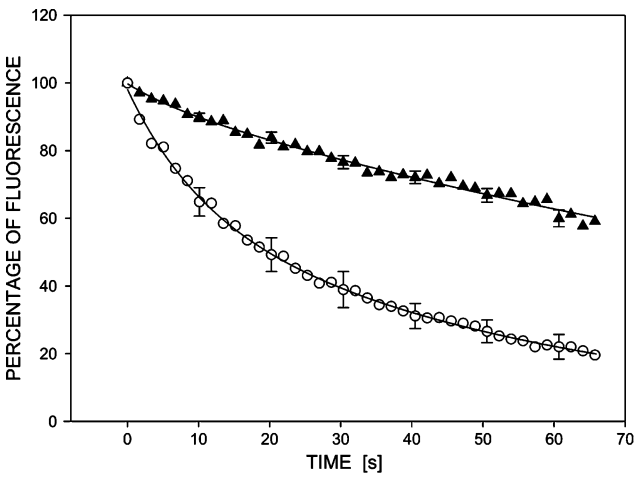

Fig. 4 Fluorescent intensities decrease from two compartments, which represent the respective rates of labelled molecules movement, evaluated in time by FLIP. The values expressed as means ± S.E.M. ($n = 6$, number of myofibrillar preparations) represent: Phalloidin-FITC conjugate tightly bound in the I-band as bleaching control value (▲), CK-IAF (substrates free) associated in the M-band (○). The exchange rate of CK-IAF (substrates free) molecules is significantly different from the bleaching control ($P < 0.05$)

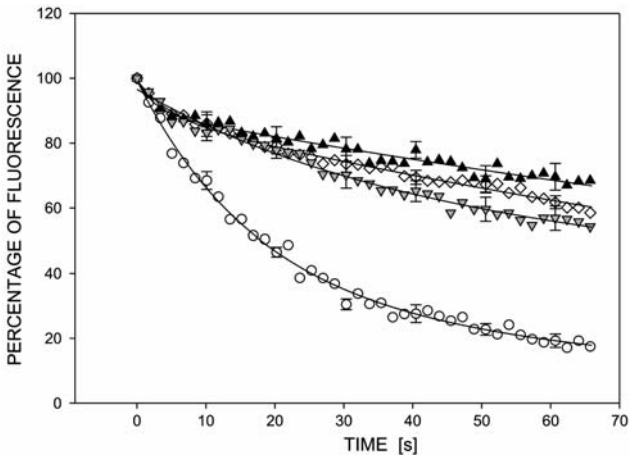

Fig. 5 Fluorescent intensities decrease from the M-bands of myofibrils incubated with CK substrates, which represent the respective rate of labelled CK-IAF molecules movement, evaluated in time by FLIP. The values expressed as means ± S.E.M. ($n = 6$, number of myofibrillar preparations) represent: CK-IAF - (ATP-Creatine pair) (▲), CK-IAF-ATP (◇), CK-IAF-Phosphocreatine (▽) and CK-IAF (substrates free) (○). The exchange rate CK-IAF (substrates free) differ significantly from all the variants of CK-IAF (with substrates) ($P < 0.05$)

during the exchange experiment and therefore the ratio equalled 1. In neutral pH, the exchange reaction occurs at the ratio 2.45 ± 0.15 and reaches its maximum 5.67 ± 1.26 in a basic environment of pH 7.10–7.15. Within this pH range all the following FLIP experiments were performed. The fluorescent signal in the M-band was weak or absent at pH ≥ 7.2 and the ratio fell to 1.21 ± 0.02.

Discussion

It is a problem of general interest whether the interaction of enzymes with structural proteins related to their intracellular compartmentalization plays, in general, a role in the cellular control of their activity. The essential physiological component (proposed in the Introduction of this article) which controls muscle CK activity turns the attention towards the nature of the interaction of CK with myofibrils.

Myofibrils can be considered as the simplest structure that still preserves a cellular function (contraction). It simultaneously enables access to the molecular level of CK-myofibrillar interaction which could affect the enzyme activity. For such an interaction the following are decisive: an exchange of CK between the respective cellular compartments, and the bond that holds CK and M-band-proteins together. Both of which are within the scope of this article.

Myofibrils as an experimental object

Purified myofibrils preserve its physiological function, which is proved by its ability to contract, and CK activity (0.4 ± 0.02 IU/mg) corresponds to Ventura-Clapier et al. [15] and agrees with our previous findings [13].

Elution of CK from the myofibril ("*treated*" myofibrils) by low-ionic-strength medium was effective and decreased the specific CK activity by up to 0.01 ± 0.008 IU/mg protein. The aim of elution was to obtain a simpler kinetic model. However, the FLIP experiment showed that reconstituted CK-IAF bound in the M-band is fixed. And on the base of analyses of eluted proteins, the "*treated*" myofibrils were excluded from FLIP measurements. These SDS-PAGE results showed a loss of other proteins from myofibrils besides that of CK (43 kD) (see Fig. 2). Namely actin (upper 43 kD band) together with CK (lower 43 kD band) was proved by mass spectroscopy (data not shown). Some other higher molecular weight (Mw) proteins about 70, 80 and 120 kD were detected by SDS-PAGE. At lower Mw two main bands about 30 and 20 kD appeared. 30 kD protein could be DRAL/FHL-2, which mediates targeting of CK with titin [20, 21]. Figure 2 shows that a low-ionic-strength medium could harm the structure of sarcomers in the case of smaller proteins. This way could uncover some unspecific interaction for CK in the M-band. These results could also show that the smaller proteins are indispensable for natural interaction of CK in the M-band as well as its main binding partners like myomesin (185 kD) and M-protein (165 kD) [8].

pH dependence of CK-IAF interaction in A bands of myofibrils

Results show a strong pH dependence of the CK interaction with myofibrils in the M-band. In a slightly acidic environment the bond of the native CK is so strong that it excludes the CK exchange between myofibrils and their surroundings. These findings correspond to a recent observation of a strong pH effect on the binding strength between CK and myomesin [8]. This fact can be hypothetically explained by the physiological function of CK, as a pH buffer [22] and ATP buffer, within the range of intracellular pH changes that occur upon muscle contraction [23]. Also energy channelling between creatine kinase and myosin ATPase, reaching its maximum at pH 6.95 [13], could help to explain the importance of a strong CK bond in the M-band during acidification. The exchange process reaches its maximum rate in a slightly basic environment (7.10–7.17), which is in accordance with previous data [15] that show the reconstitution of CK bound in the M-band at pH 7.1. A weaker interaction of CK could be also explained by its isoelectric points at a slightly basic pH [24, 25]. On the other hand Kraft et al. [9] used neutral pH for the exchange of CK molecules at skinned fibres. At this pH we observed only partial and slow exchange of CK-IAF molecules in the M-band.

The role of CK substrates

Results presented in Fig. 3a, b justify the FLIP method employed in the two-coordinate planar system. Resulting data (Figs. 4 and 5) allow us to evaluate the exchange of CK, or reciprocally, to estimate the force of the bond. Under a slightly basic (pH 7.10–7.17) condition the exchange and equilibration between CK-IAF (substrates free) and the natively bound CK in the M-band is very fast (in seconds) (Fig. 4). The exchange rate in the presence of substrates is more than 60 times slower (in minutes) during equilibration. The FLIP experiments show, how the conformation change of the CK molecule, evoked by substrates binding, affects the process of exchange between the M-band and surroundings. This result indicates a stronger bond due to the presence of substrates. The ATP induced autophosphorylation of muscle CK [26] and nucleotidylation [27] can also influence the interaction with myofibrils, as well as the conformational change due to other substrates' binding [28, 3, 4].

We present at this article that the substrates slowed down the exchange rate of the CK molecule within a narrow pH range. This indicates that the strength of the bond between CK and the M-band is increased. Based on these results, we conclude that the structural strong interaction of M-CK with the M-band demands a presence of its substrates.

Acknowledgements Authors would like to thank Dr. Marta Novotova and Dr.Tomas Soukup for critical reading and valuable comments during preparation of the manuscript. This study was supported by Myores No 511978 and GACR 304/05/0327grants and by the Research project AV0Z 50110509.

References

1. Saks VA, Ventura-Clapier R, Aliev MK (1996) Metabolic control and metabolic capacity: two aspects of creatine kinase functioning in the cell. Biochim Biophys Acta 1274:81–88
2. Ventura-Clapier R, Veksler J, Hoerter JA (1994) Myofibrillar creatine kinase and cardiac contraction. Mol Cell Biochem 133/134:125–144
3. Mejsnar JA, Sopko B, Gregor M (2002) Myofibrillar creatine kinase activity inferred from a 3D model. Physiol Res 51(1):35–41
4. Mejsnar JA, Herman P, Malacova D et al (2005) The substrate-dependent three conformations of muscle creatine kinase. Physiol Res 54:33P
5. Wallimann T, Wyss M, Brdiczka D et al (1992) Intracellular compartmentation, structure and function of creatine kinase isoenzymes in tissues with high and fluctuating energy demands: the 'phosphocreatine circuit' for cellular energy homeostasis. Biochem J 281(1):21–40
6. Stolz MT, Wallimann T (1998) Myofibrillar interaction of cytosolic creatine kinase (CK) isoenzymes: allocation of N-terminal binding epitope in MM-CK and BB-CK. J Cell Sci 111(9):1207–1216
7. Hornemann T, Stolz M, Wallimann T (2000) Isoenzyme-specific interaction of muscle-type creatine kinase with the sarcomeric M-band is mediated by NH(2)-terminal lysine charge-clamps. J Cell Biol 149(6):1225–1234
8. Hornemann T, Kempa S, Himmel M et al (2003) Muscle-type creatine kinase interacts with central domains of the M-band proteins myomesin and M-protein. J Mol Biol 332(4):877–887
9. Kraft T, Messerli M, Rothen-Rutishauser B et al (1995) Equilibration and exchange of fluorescently labeled molecules in skinned skeletal muscle fibers visualized by confocal microscopy. Biophys J 69(4):1246–1258
10. Prigogine I (1967) Introduction to thermodynamics of irreversible processes. Interscience Publishers, New York, London, Sydney, pp 83–85
11. Gregor M, Kubala M, Amler E et al (2003) Frequency-domain lifetime fluorometry of double-labeled creatine kinase. Physiol Res 52(5):579–585
12. Wallimann T, Schlosser T, Eppenberger HM (1984) Function of M-band-bound creatine kinase as intramyofibrillar ATP regenerator at the receiving end of the phosphorylcreatine shuttle in muscle. J Biol Chem 259(8):5238–5246
13. Gregor M, Janovska A, Stefl B et al (2003) Substrate channelling in a creatine kinase system of rat skeletal muscle under various pH conditions. Exp Physiol 88(1):1–6
14. Solaro RJ, Pang DC, Briggs FN (1971) The purification of cardiac myofibrils with Triton X-100. Biochim Biophys Acta 245:259–262
15. Ventura-Clapier R, Saks VA, Vassort G et al (1987) Reversible MM-creatine kinase binding to cardiac myofibrils. Am J Physiol Cell Physiol 253:C444–C455
16. Blum M, Beier H, Gross MJ (1987) Improved silver staining of plan proteins, RNA and DNA in polyacrylamide gels. Electrophoresis 8(2):93–99
17. Stefl B, Mejsnar JA, Janovska A (1999) Energy metabolism of rat skeletal muscle modulated by the rate of perfusion flow. Exp Physiol 84:651–663
18. Gerhardt W (1983) Phosphotransferases: creatine kinase. In: Bergmeyer HU (ed) Methods of Enzymatic Analysis, vol. III. 3rd edn, Verlag Chemie, Weinheim, pp 508–518
19. Wahlefeld AW, Siedel J (1985) Metabolites 3: lipids, amino acid related compounds: creatinine and creatine. In: Bergmeyer HU (ed) Methods of enzymatic analysis, vol. VIII. 3rd edn, Verlag Chemie, Weinheim, pp 488–507
20. Lange S, Auerbach D, McLoughlin P et al (2002) Subcellular targeting of metabolic enzymes to titin in heart muscle may be mediated by DRAL/FHL-2. J Cell Sci 115(24):4925–4936
21. Lange S, Agarkova D, Perriard JC et al (2005) The sarcomeric M-band during development and disease. J Muscle Res Cell Motil 26(6–8):375–379
22. Adams GR, Foley JM, Meyer RA (1990) Muscle buffer capacity estimated from pH changes during rest-to-work transitions. J Appl Physiol 69:968–972
23. Chase PB, Kushmerick MJ (1988) Effect of pH on contraction of rabbit fast and slow skeletal muscle fibers. Biophys J 53:935–946
24. Malacova D, Zurmanova J, Mejsnar J (2004) Three isoelectric points of the creatine kinase M-subunit, purified from myofibrils. Physiol Res 53:22P
25. Wright-Weber B, Held BC, Brown A et al (2006) Immunological and physical comparison of monomeric and dimeric phosphagen kinases: some evolutionary implications. Biochim Biophys Acta 1760(3):364–371
26. Stolz M, Hornemann T, Schlattner U et al (2002) Mutation of conserved active-site threonine residues in creatine kinase affects autophosphorylation and enzyme kinetics. Biochem J 363:785–792
27. Satyajit SM, Boyd D, Haley E (1999) ATP Nucleotidylation of creatine kinase. Biochemistry 38:8492–8500
28. Lahiri SD, Wang PF, Babbitt PC et al (2002) The 2.1 Å structure of Torpedo californica creatine kinase complexed with the ADP-Mg^{2+}-NO_3-creatine transition-state analogue complex. Biochemistry 41(47):13861–13867

2.5 Cell Motility and Optical Tweezers

1. **Properties of the force exerted by filopodia and lamellipodia and the involvement of cytoskeletal components.**
   D. Cojoc***,** **F. Difato*,** E. Ferrari***,** R. B. Shahapure***,** J. Laishram**,** M. Righi**,** E. M. Di Fabrizio**,** V. Torre**.** *** These authors equally contributed.** PLoS ONE. 2007 ;2 (10):e1072 17957254

2. **Force generation in lamellipodia is a probabilistic process with fast growth and retraction events.**
   R. B. Shahapure, **F. Difato**, A. Laio, D. Cojoc, E. Ferrari, J. Laishram, , G. Bisson & V. Torre **(**Submited to PNAS**)**

2.5.1. Aims and results

Aims:

- To develop an experimental setup that permit to measure force developed by living cells.
- To obtain a quantitative characterization of the force exerted by lamellipodia and filopodia during neuronal differentiation.
- To visualize polymerization steps during cell differentiation.
- To apply drug assay to clarify the role of cytoskeleton components during motion.
- To measure with high temporal resolution and sensitivity the force-velocity (Fv) relationship of lamellipodia, to discriminate between mathematical models of cell motility.

Results:

- We developed a model to measure the force exerted by a living cell during motion with sub piconewton sensitivity and ms temporal resolution
- We found that single filopodium exerts a force not exceeding 3 piconewton. The measured force of approximately 1 piconewton could be developed within 30 ms. Collisions between filopodia and beads rarely lasted more than 30 s.
- Filopodia appeared to decrease the duration of the collision when encountering a stiffer obstacle.
- Lamellipodia exerted a force up to 20 piconewton and possibly more.
- We observed lamellipodium increasing the exerted force in well resolved steps of approximately 0,2 piconewton, corresponding to displacements of approximately 18 nm.
- We characterize the force field generated by lamellipodia by trapping multiple beads in front of a lamellipodium. The forces simultaneously exerted at three locations separated by 3 mm by a lamellipodium were sometimes in opposite directions, and often, the direction of the force exerted at one location reversed within 10 s.
- Treatment of growing cones with the selective myosin light chain kinase (MLCK) inhibitor, ML-7 or with the microtubule depolymerising agent, nocodazole, drastically reduced the motion and force exerted by lamellipodia, while filopodia continued to move and exert forces up to 3 piconewton.
- Growing cones treated with the actin depolymerising agent, latrunculin A, did not exert any detectable force.
- At a low temporal resolution, the force can increase with an almost constant velocity and the Fv relationships are flat. At a higher temporal resolution, the velocity oscillates and transient periods of negative velocities are observed.

2.5.2. Discussion

Neuronal cells possess ability to create a complex and dense network of contacts between many cells, to produce computational capacity of stimuli coming from the environment. During neuronal differentiation, neurites are guided towards their final target by filopodia and lamellopodia. Such structures sense chemical properties of the surrounding and exert forces on the environment to test its mechanical characteristics. Optical tweezers represents a non invasive force measurement method which can be utilized to measure and analyze the force operated by cells in exploratory motion and therefore to understand how cell operate mechanic transduction.
With optical microscopy, it is possible to follow the motion of the cell, but force measurements permit to quantify how many molecular motors are involved in a movement and therefore to quantify how much the molecular machinery of the cell is recruited in such action. This means that

thanks to force measurement, we are able to distinguish random motion from well organized shift of the cell.
Therefore, we built a photonic force setup to measure the force exerted by a living cell during differentiation. We observed that filopodia, which explore the environment by rapidly moving in all directions, modulate its activity, changing the duration of the collision with the bead, in response to different stiffness of the load. This could represent sensing of the obstacle force.
Lamellipodia, which follow the pathway analyzed from filopodia, showed a more complex behavior in response to the obstacle: sometimes, they entirely retract, other times they move around it to progress forward or they remove the obstacle by lifting it and giving it back. Lamellipodia have more differentiated structure and are thought to exert a force with variable directions in space, while filopodia have a defined structure, and the force they exert is well localized in space. Therefore, we applied multi-tweezers measurement on lamellipodia to understand their overall organization and to measure complex force exerted during growth cone motion. Such kind of measurements can be used to understand the response of the cells to molecular cues, or to understand the molecules involved in different steps of motor planning. Further, we observed that in absence of actin polymerization, growth cones cannot exert any force, and microtubule polymerization is necessary for development of forces exceeding 3 piconewton. Therefore, actin filaments and microtubules cooperate and interact in a complex way to generate a wide range of forces. The motion of filopodia and lamellipodia seems to follow well defined patterns: the stiffness of an obstacle is first probed from a filopodia and eventually, lamellipodia could remove the obstacle or change direction. Moreover, quantification of the force exerted by growth cone shows that neurons act on the environment, exerting forces varying 1 to 2 orders of magnitude, which can represent mechanical computation capability.
The nanometer and millisecond resolution of our setup allows us to observe polymerization steps in the force trace and to obtain an experimental force-velocity curve which can be compared with the theoretical ones. This permits to discern between different mathematical models of cell motility.
On a finer time scale, random occurrence of fast growths and sub-second retractions were observed. These results suggest that force generation in lamellipodia is an inherent probabilistic process and does not follow a deterministic mechanism. In order to characterize this probabilistic dynamics, we determine average Fv relationships. When force and velocity are averaged over 3-5 s, the exerted force can increase maintaining a constant velocity and the Fv relationships are flat. This experimental result can be explained by autocatalytic models of force generation: when the underlying system of actin filaments and controlling proteins has the time to self-reorganize, velocity becomes independent of applied force.
In conclusion, we develop a model to observe cell locomotion at different time scales, from millisecond to second resolution; and at spatial scale, from diffraction limited to nanometer resolution. This permits to study cell locomotion during differentiation:

- In the high resolution bandwidth, it will be possible to understand the molecular mechanism underlying the cell movement
- In the long time scale, it will be possible to understand cell reaction to mechanical and chemical stimuli from the environment. This can be possible due to the optical manipulation tool which permits to arbitrary localize the stimuli in the cell culture.

2.5.3. Publications:

OPEN ACCESS Freely available online

PLoS one

Properties of the Force Exerted by Filopodia and Lamellipodia and the Involvement of Cytoskeletal Components

Dan Cojoc[1,4❦]*, Francesco Difato[2❦], Enrico Ferrari[1❦], Rajesh B. Shahapure[2❦], Jummi Laishram[2], Massimo Righi[2], Enzo M. Di Fabrizio[1,3], Vincent Torre[2,5]*

1 Consiglio Nazionale delle Ricerche (CNR)-Istituto Nazionale per la Fisica della Materia (INFM), Laboratorio Nazionale Tecnologie Avanzate E Nanoscienza (TASC), Area Science Park Basovizza, Trieste, Italy, **2** International School for Advanced Studies (SISSA-ISAS), Trieste, Italy, **3** Università Magna Graecia di Catanzaro, Campus Germaneto, Catanzaro, Italy, **4** Centro per la Biomedicina Molecolare (CBM), LANADA Laboratory, Trieste, Italy, **5** Italian Institute of Technology, International School for Advanced Studies (ISAS) Unit, Italy

During neuronal differentiation, lamellipodia and filopodia explore the environment in search for the correct path to the axon's final destination. Although the motion of lamellipodia and filopodia has been characterized to an extent, little is known about the force they exert. In this study, we used optical tweezers to measure the force exerted by filopodia and lamellipodia with a millisecond temporal resolution. We found that a single filopodium exerts a force not exceeding 3 pN, whereas lamellipodia can exert a force up to 20 pN. Using metabolic inhibitors, we showed that no force is produced in the absence of actin polymerization and that development of forces larger than 3 pN requires microtubule polymerization. These results show that actin polymerization is necessary for force production and demonstrate that not only do neurons process information, but they also act on their environment exerting forces varying from tenths pN to tens of pN.

Citation: Cojoc D, Difato F, Ferrari E, Shahapure RB, Laishram J, et al (2007) Properties of the Force Exerted by Filopodia and Lamellipodia and the Involvement of Cytoskeletal Components. PLoS ONE 2(10): e1072. doi:10.1371/journal.pone.0001072

INTRODUCTION

During morphogenesis, neuronal precursor cells migrate from the zone where they are born to their final destination, which, in some cases, is at a distance of several millimeters[1,2]. After reaching their destination, neurons must establish appropriate synaptic connections by sending out from their soma projections called neurites. The motion of neurites is guided by growth cones located at their tips[3,4]. Growth cones contain a variety of chemical and mechanical receptors and sophisticated biochemical machinery that couples these receptors to the cytoskeleton[5–7]. Extruding from the tip of the growth cone are highly motile structures called filopodia and lamellipodia that are used to explore and probe the environment[3,6]. All these complex events, which are at the basis of neuronal development and differentiation, involve cell motility requiring a precise control of cellular and molecular motors. The motion of these structures has been analyzed and characterized to some extent by time-lapse microscopy[8–12].However, little is known about how neurons use these structures to sense the mechanical properties of their environment and about what range of forces these structures exert during their exploratory motion.

Analysis of the forces exerted by neurons has been limited to theoretical considerations; experimental analysis has been limited to samples of isolated filaments[13–17]or migrating cells[18,19]. Measured forces range from 1 or 2 pN in isolated actin filaments and microtubules to 1 nN in migrating keratocytes. Quantitative characterization of the force exerted by lamellipodia and filopodia during neuronal differentiation could help to elucidate how neurons sense the environment and process mechanical information. Precise description of the mechanical and dynamic events that occur during neuronal differentiation and migration would provide new insights regarding the molecular events controlling these biological functions. In addition, it would offer a more precise way for evaluating the role of molecular motors in cell motility under physiological conditions and in neurodegenerative disease.

In this study, we used optical tweezers[20–22] to measure the force exerted by filopodia and lamellipodia during neuronal differentiation. Unlike other force measurement methods, optical tweezers are non-invasive and provide direct high temporal resolution for position detection ($<$10 nm) and force measurement ($<$1 pN), highly relevant in biological systems[21]. We found that a single filopodium exerts a force not exceeding 3 pN. In contrast, lamellipodia exert forces of 20 pN or more lasting less than 1 s to approximately 30 s. Treatment of growth cones with the selective myosin light chain kinase (MLCK) inhibitor ML-7[23] or the microtubule depolymerizing agent nocodazole[24] drastically reduced the motion and force exerted by lamellipodia, while filopodia continued to move and exert forces up to 3 pN. Growth cones treated with the actin depolymerizing agent latrunculin A[24] did not exert any detectable force. These findings suggest that no force can be produced in the absence of actin polymerization and that development of forces larger than 3 pN requires microtubule polymerization. This study shows that not only do neurons process information, but also they act on the environment, exerting forces varying 1 to 2 orders of magnitude.

Academic Editor: Lin Mei, Medical College of Georgia, United States of America

Received July 6, 2007; **Accepted** October 4, 2007; **Published** October 24, 2007

Funding: This work was partially supported by the EU grants NEURO and BINASP, by a FIRB grant from the Italian Government and by the GRAND grant from CIPE/FVG.

Competing Interests: The authors have declared that no competing interests exist.

* **To whom correspondence should be addressed.** E-mail: cojoc@tasc.infm.it (DC); torre@sissa.it (VT)

❦ These authors contributed equally to this work.

RESULTS

During neuronal differentiation and development, the growth cone of each neurite extends its filopodia and lamellipodia to explore the chemical nature of the environment and to probe the rigidity and composition of the extracellular matrix[23]. Under these circumstances, cell motility is strictly linked to the generation of forces. Therefore, we used optical tweezers[20–22] to measure the force exerted by the growth cones of differentiating neurons.

Force exerted by growth cones of differentiating neurons

Neurons from dorsal root ganglia (DRG) were isolated from P10-P12 rats and plated on poly-L-lysine-coated glass coverslips and positioned on the stage of an inverted microscope that was used for imaging and measurement of forces (see Methods). After incubation for 24 to 48 h, neurites could be seen emerging from the DRG soma. Their motion was analyzed with time-lapse differential interference contrast microscopy (Movie S1). Filopodia and lamellipodia moved rapidly, exploring the three-dimensional space in all directions, with velocities of up to 1.2 μm s-1 and reaching heights up to 1–3 μm.

Silica beads 1 μm in diameter were functionalized with amino groups to reduce sticking and trapped with 1064-nm infrared optical tweezers (laser power between 8 and 44 mW) close to the growth cones of the differentiating neurites (Fig. 1a and Movie S2). We verified that 50 mW laser power reaching the specimen plane and focused on the growth cone did not affect its motion for at least 1 h. Often we observed both lateral and axial displacement of the trapped bead by a growth cone. In several experiments, the growth cone moved the bead as much as 2–3 microns from its equilibrium position inside the trap (Fig. 1b). After the collision, the bead did not remain attached to the growth cone and could return to its original position in the trap (Fig. 1c). We measured the lateral force exerted by the growth cone Fneu = (Fx, Fy) by following the bead position with a quadrant photo diode (QPD)[22] and video tracking[25] (see Methods). When the bead was far from the growth cone, QPD recordings of Fx and Fy were

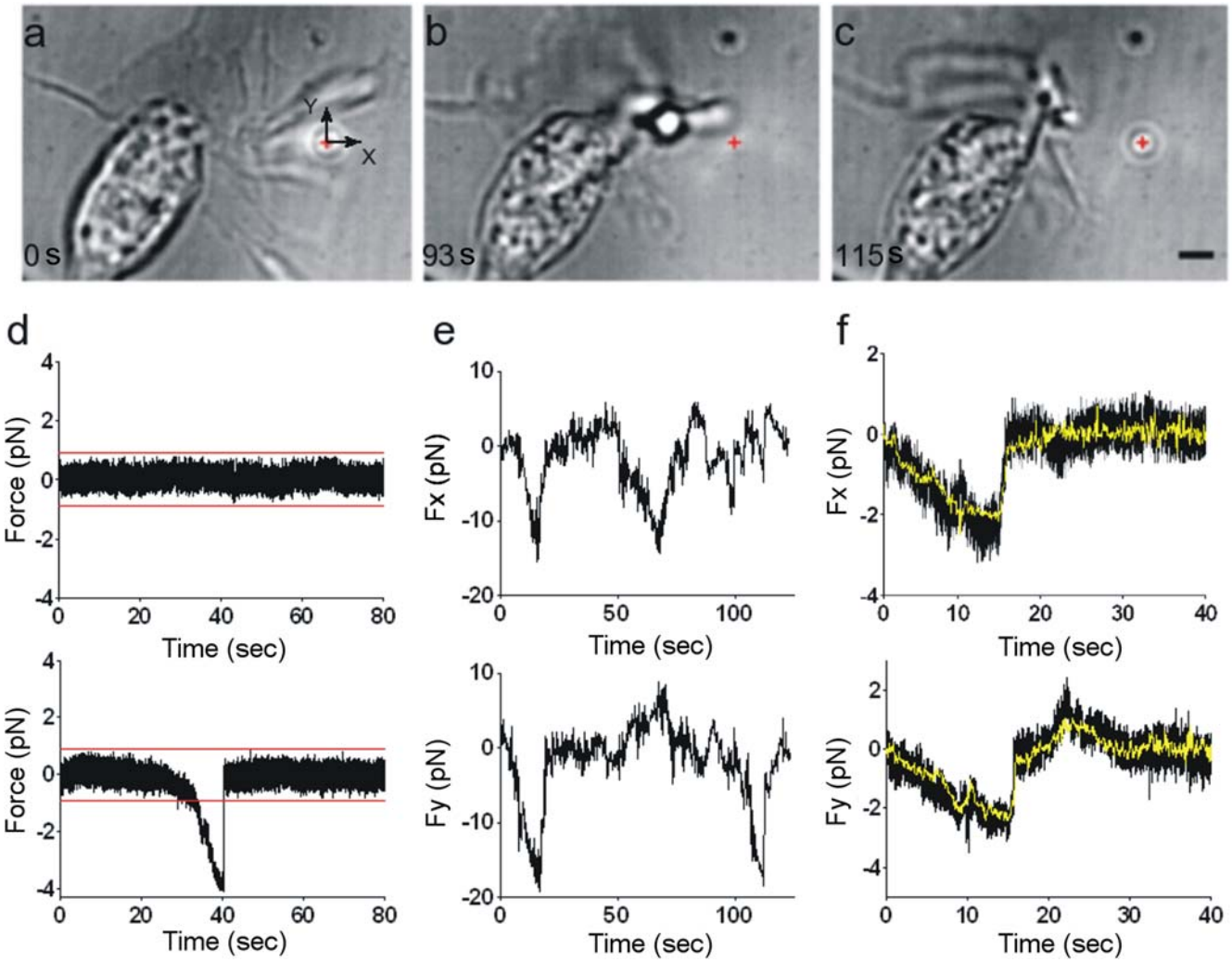

Figure 1. Collisions between a growth cone and a trapped bead. **(a–c)** A growth cone displacing a bead from the optical trap. The red cross indicates the bead's equilibrium position inside the optical trap. Scale bar, 2 μm. **(d)** Example of a force component obtained with QPD when the bead was distant from the growth cone (upper trace) and when the bead was in contact with the growth cone (lower trace). Red lines are drawn 5 σ from the 0 mark. σ, s.d. of force fluctuations. When the QPD trace crossed the red lines for at least 100 ms and a lamellipodium or filopodium was seen hitting the bead, a reliable collision was detected. **(e)** Example of F_x and F_y during repetitive collisions between a moving lamellipodium and a trapped bead. Trap stiffness was 0.05 pN nm^{-1}. **(f)** Comparison of F_x and F_y determined with a QPD (black traces) and video tracking (yellow traces).
doi:10.1371/journal.pone.0001072.g001

quiet, with a s.d. σ of approximately 0.18 pN (Fig. 1d, upper trace), but when the bead was moved close to the growth cone, collisions producing a force greater than 5 σ were observed (Fig. 1d, lower trace). On several occasions, Fx and Fy increased within 1–10 s, reaching values of 20 pN (Fig. 1e), and when the growth cone stopped pushing, the bead rapidly returned to its equilibrium position, often in less than 1 ms.

The presence of floating debris and wandering filopodia near the bead could affect the light pattern impinging on the QPD. Therefore, a collision was considered reliable when the bead displacement obtained with the QPD and video tracking were in agreement (black and yellow traces, respectively, in Fig. 1f) and the presence of a colliding filopodium or lamellipodium was verified by visual inspection of the movie. We analyzed collisions between growth cones and trapped beads in more than 200 experiments. Each experiment lasted 2 min, and in many experiments there were several collisions that could be used for statistical analysis (see Methods). These collisions produced maximal forces ranging from less than 1 pN to at least 20 pN, with a maximal rate of increase of 10 pN s-1. They lasted for less than 1 s to approximately 60 s. Typically, larger forces were observed during longer lasting collisions. As these forces extended over a wide range of intensities and durations, we took the further step of characterizing the force developed by each major component of growth cones, filopodia and lamellipodia.

Force exerted by filopodia

Filopodia have an elongated and well defined shape with diameters varying from 100 to 500 nm and an average length of approximately 15 μm[26]. Filopodia can exert force during both exploratory motion and growth. During their exploratory motion often filopodia pivot and push beads aside, possibly as a consequence of shearing movements of the lamellipodial actin network where the filopodial shaft emerges. We refer to the first case as lateral collisions and to the latter case, where the filopodium pushes the bead, as protrusion. An isolated filopodium, after wandering around the bead (Fig. 2a), sometimes collided with it (Fig. 2b and Movie S3), exerting a maximal force of up to 1 pN (Fig. 2c). The force measured during lateral collisions depends on the exact geometry of the collision: a moving filopodium can strike a trapped bead at its center or just lightly touch its surface. Results from 42 experiments show that filopodia never exerted a force larger than 2 pN (Fig. 2g), which is a reliable upper boundary for the maximal force exerted during a lateral collision. Some lateral collisions lasted less than 1 s, but on several occasions we observed filopodia pushing beads for 15 s.

The force exerted by a filopodium is generated by its elastic properties[19] and a variety of molecular processes[27], including polymerization of actin filaments[28,29], which generates a protrusion force counterbalanced by the membrane resistance force[30–32], leading to a net force Ftip. To measure forces produced during protrusion, beads were trapped in front of filopodia tips (Fig. 2d). In 33 experiments, we observed protruding filopodia displacing beads, often repeatedly (Fig. 2e and Movie S4; see also Figure S1 and Movie S5). The measured force was approximately 1 pN, and it developed within 30 ms (Fig. 2f). Ftip did not exceed 3 pN (Fig. 2h). These collisions rarely lasted more than 30 s.

When a filopodium collides with an encountered obstacle, it senses the object's chemical properties and also probes its mechanical resistance and size. Therefore, we investigated whether the force exerted by filopodia varies with the stiffness of the optical trap. We conducted several experiments in which we increased the trap stiffness from 0.006 pN nm-1 to 0.01 pN nm-1 and analyzed the collisions that occurred between the same growth cone and trapped beads. Under the two conditions of trap stiffness, collisions produced forces similar in magnitude (Fig. 3a, b), but collisions with beads trapped with a higher stiffness appeared to be shorter in duration. Data from 18 experiments show a similar distribution of measured forces under the two conditions but more frequent longer lasting collisions with the lower trap stiffness (Fig. 3c, d).

As shown in Figure 3, filopodia appeared to modulate their mechanical response by decreasing the duration of the collision when encountering a stiffer obstacle. Thus, they appear to be able to communicate the mechanical properties of the environment to the internal biochemical machinery that powers the cytoskeleton.

Force exerted by lamellipodia

We often observed that a lamellipodium repeatedly pushes a trapped bead (Fig. 4a,b and Movie S6), exerting a force of 3–4 pN (Fig. 4c). Lamellipodia could displace beads from the trap when the maximum trapping force was 20 pN. In 6 experiments, we observed lamellipodium increasing the exerted force in well resolved steps of approximately 0.2 pN, corresponding to displacements of approximately 18 nm (Fig. 4d). These steps have properties very similar to those observed during microtubule assembly, where discrete jumps of approximately 20–30 nm are observed[16]. In 65 experiments, lamellipodia exerted a force ranging from less than 1 pN to at least 20 pN, with a variable duration (Fig. 4e, f).

An isolated filopodium is complex from a molecular point of view, but it has a defined structure, and the force it exerts is well localized in space. In contrast, lamellipodia have a more differentiated structure and are thought to exert a force with variable direction in space. Therefore, we attempted to characterize the force field generated by lamellipodia by trapping multiple beads in front of a lamellipodium. Traps were separated by 3–6 μm and located on the same plane. In several experiments, 3 beads were displaced simultaneously by the lamellipodium (Fig. 5a), and we determined their trajectory with video imaging. The direction of forces at the three locations changed during the experiment and could span a large fraction of the free space surrounding the moving lamellipodium (Fig. 5b).

The force simultaneously exerted at the two locations separated by 3 μm was sometimes in opposite directions, and often the direction of force exerted at one location reversed within 10 s. This confirms that the force field generated by a lamellipodium is complex and dynamic over a short time scale.

Effects of metabolic inhibitors on force exertion

In order to identify the molecular mechanisms of force production, we analyzed the effect of metabolic inhibitors at concentrations known to be effective[23,24]. Within 5 min after addition of 50 nM latrunculin A, an inhibitor of actin polymerization[24], the exploratory motion of growth cones was drastically reduced; under this condition, the force exerted by filopodia and lamellipodia did not exceed 3 or 4 pN, and collisions were shorter (black symbols in Fig. 6d). When the concentration of latrunculin A was increased to 100 nM, moving filopodia collapsed (Fig. 6a–c), and no detectable motion or force was observed in filopodia or lamellipodia (red symbols in Fig. 6d). In contrast, addition of 50 nM nocodazole, an inhibitor of microtubule polymerization[24], had a more specific effect. It reduced the motion of lamellipodia but not of filopodia, which continued to move (Fig. 6e–g), exerting a force of up to 3 pN (Fig. 6e). Upon addition of 4 μM of the myosin II inhibitor ML-7[23], a fast retraction of moving filopodia was observed (Fig. 6i–j), but within 2–5 min new filopodia emerged from the growth cone (Fig. 6k), which exerted a force in the pN range (Fig. 6l).

These results suggest the existence of two distinct but coupled molecular motors within growth cones. Actin polymerization

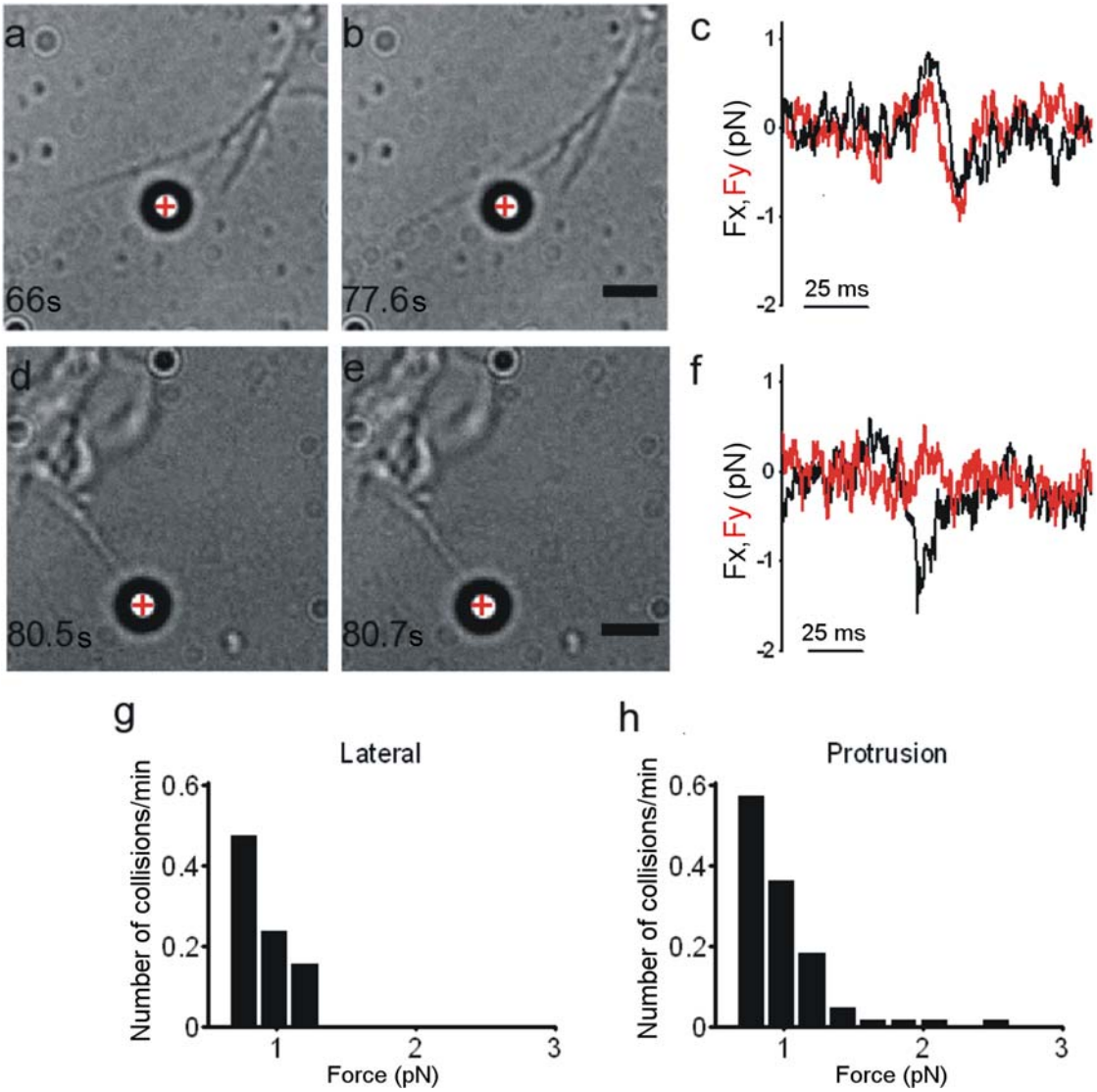

Figure 2. Force exerted by Filopodia. (a–b) Lateral collision between a filopodium and a trapped bead. Trap stiffness was 0.008 pN nm^{-1}. The red cross indicates the bead's equilibrium position inside the optical trap. **(c)** F_x and F_y from the QPD during the lateral collision shown in (a–b). **(d–e)** Collision between a protruding filopodium and a trapped bead. **(f)** F_x and F_y from the QPD during the filopodial protrusion shown in (d–e). Trap stiffness was 0.008 pN nm^{-1}. **(g–h)** Histograms of forces measured during lateral collisions and protrusions. Data were collected from 75 experiments, each lasting 2 min. Scale bar, 2 μm.
doi:10.1371/journal.pone.0001072.g002

seems necessary for the development of any significant motion and force in filopodia and lamellipodia. Microtubule polymerization is not essential for filopodia motion or for the generation of weak forces, but it is necessary for lamellipodia motion and generation of forces larger than 3 pN.

DISCUSSION

A typical growth cone can be divided into two regions: the central region and the peripheral region. The latter consists of filopodia and a lamellipodia[33–36]; the motion of these structures is a major component of neuronal differentiation. This is the first report of a quantitative determination with a millisecond temporal resolution of the force exerted by filopodia and lamellipodia in differentiating neurons. The force developed over time, with a maximal rate of increase of 10 pN s-1. Thin filopodia, during a protrusion or lateral collision (Fig. 2), exerted a force not exceeding 3 pN. In contrast, lamellipodia exerted a force of up to 20 pN and possibly more, which could increase in discrete steps of approximately 0.2 pN (Fig. 4d). These steps had properties very similar to those observed during the assembly of isolated microtubules[16]. The measured forces were smaller than forces involved in cellular traction force or measured in migrating keratocytes[15,18]. Measured forces here reported, may not fully represent the ability that lamellipodia have because, at least in some cases, only a fraction of the forces exerted is picked up by the beads and therefore the value of 20 pN here reported for lamellipodia is the maximal force that was measured. Indeed we expect lamellipodia to exert larger forces, possibly up to hundreds of pN, as in migrating epithelial cells[37]. The diameter of filopodia tips is approximately 100 nm, i.e. 10 times smaller than the diameter of the used beads, therefore the maximal force measured for filopodia is expected to be a reliable estimate of the force exerted by these structures.

Force measurements with optical tweezers require test beads to be in the harmonic potential well of the trapping optical force and

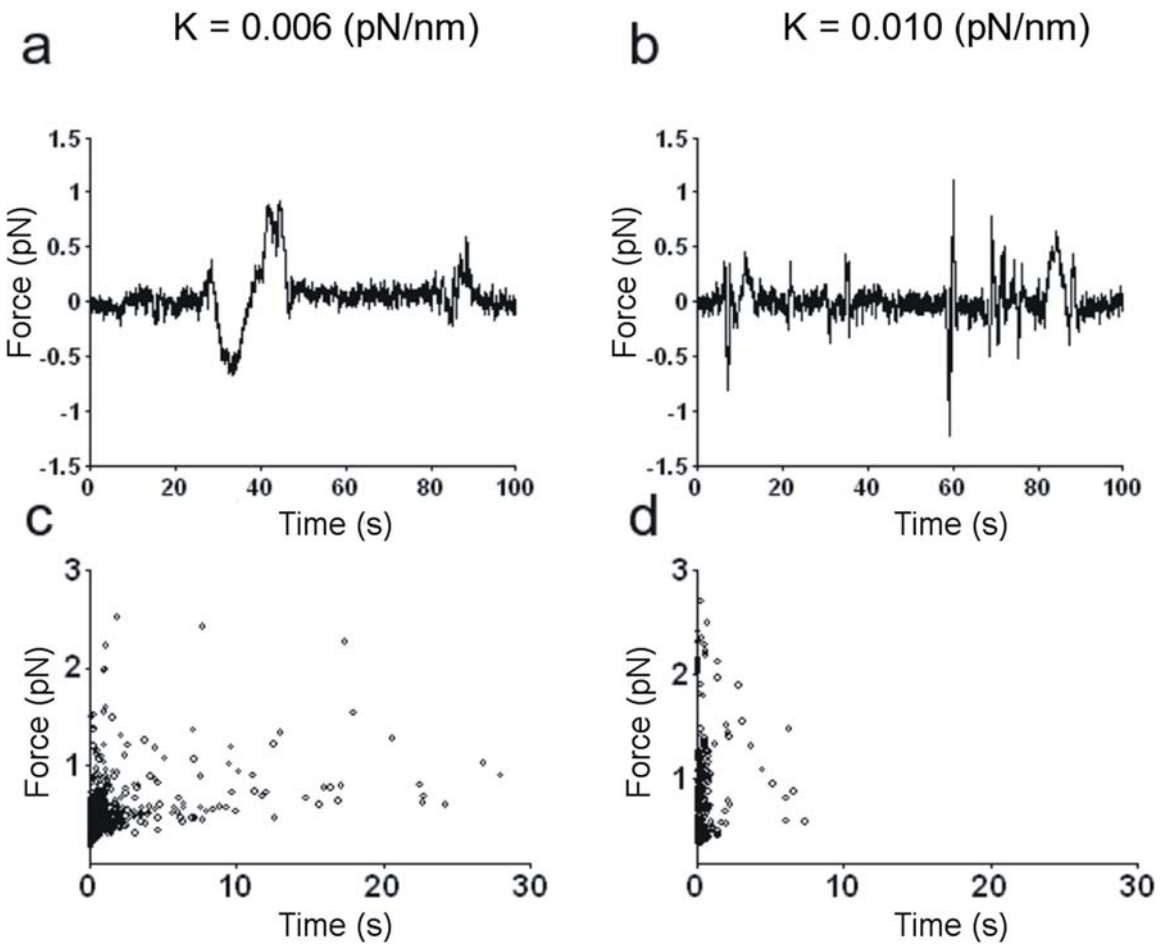

Figure 3. Effect of trap stiffness on force exerted. (a–b) F_x from the QPD during collisions between the same filopodium and the same bead trapped with a stiffness of 0.006 and 0.010 pN nm^{-1}. Traces were filtered at 50 Hz and sub-sampled. **(c–d)** Scatter plot of force duration for collisions between filopodia and beads trapped with a stiffness of 0.006 and 0.010 pN nm^{-1}. Data collected from 15 experiments at each stiffness.
doi:10.1371/journal.pone.0001072.g003

to be displaced from its equilibrium position inside the well only by the force to be measured. When adhesion forces between the bead and the growth cone and/or between the bead and the substrate become dominant, the stiffness of the optical trap is profoundly modified and it is impossible to obtain an accurate force measurement. Therefore, it is necessary to place the bead at 1 micron or so from the substrate where neurons are growing. As exploring filopodia and lamellipodia lift up from the substrate, forces can be reliably measured under these conditions.

Filopodia are composed of bundles of actin filaments and occasional microtubules [5,24]. We observed that the force exerted by a protruding filopodium is in the pN range, not exceeding 3 pN. Its amplitude is of the same order as that measured during polymerization of actin filaments[14,17] and microtubules[16]. This similarity implies that the protrusion force generated by polymerization is minimally counterbalanced by the membrane surrounding actin bundles and microtubules, indicating that the membrane at the filopodia tips has a low stiffness[38,39].

Simple mechanical considerations show that the force exerted by a wandering filopodium during a lateral collision (Fig. 2a–c) can be accounted for by the elastic force expected from its flexural rigidity[19,40] and its bending or buckling. No additional contribution from other force-generating mechanisms is required. The exact mechanisms causing filopodia to bend and/or buckle are not understood. Thermal fluctuations certainly provide a constant driving force, but a variety of other motor proteins[19,29,29] present in the growth cone could intervene, although their relative contribution is still unknown. Indeed, inhibition of myosin II and microtubule polymerization blocked lamellipodia motion and drastically reduced the force produced by growth cones (Fig. 6), while filopodia continued to move and were able to exert forces in the pN range. In contrast, with blockade of actin polymerization, filopodia and lamellipodia produced no measurable forces. Thus, in the absence of actin polymerization, growth cones cannot exert any force, and microtubule polymerization is necessary for development of forces exceeding 3 pN. Therefore, actin filaments and microtubules cooperate and interact in a complex way so as to generate a wide range of forces.

The motion of filopodia and lamellipodia seems to follow stereotyped patterns wherein the stiffness of an obstacle is first probed. Often, an isolated filopodium changed its direction of growth after colliding with a trapped bead. In contrast, lamellipodia could remove an obstacle, often by growing underneath it and lifting it. Exploring filopodia exerted forces in the pN range, whereas migrating cells exert forces in the nN range[18]. A migrating neuron must be able to displace large obstacles; hence, it uses large forces. Filopodia gently explore their environment using only weak forces, and lamellipodia can exert a larger force opening the way for the growth cone. Thus, not only do neurons process information but they are also able to mechanically modify their environment by selecting forces varying from less than 1 pN to 1 nN[18]. Indeed,

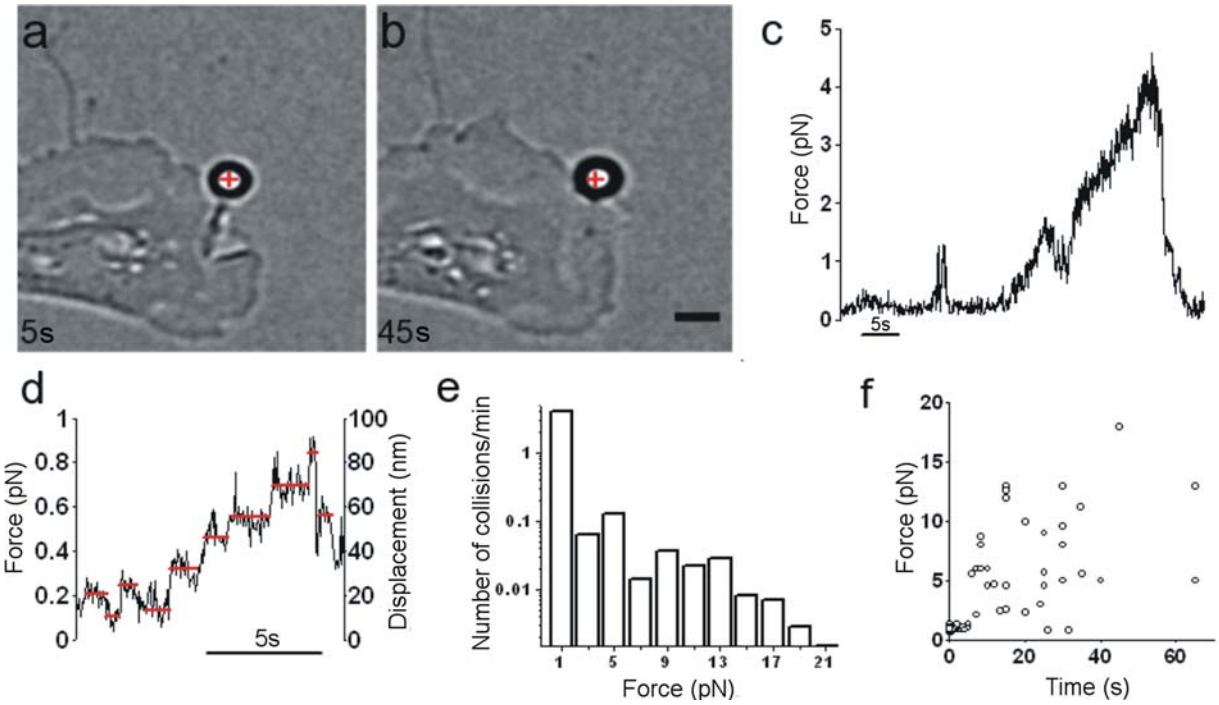

Figure 4. Force exerted by lamellipodia. (a–b) A lamellipodium growing and pushing a trapped bead. The red cross indicates the equilibrium position inside the optical trap. Scale bar, 2 μm. **(c)** F_{neu} in the x,y plane obtained from a QPD recording. Trap stiffness was 0.009 pN nm^{-1}. **(d)** The force exerted by a lamellipodium showing step-like jumps. Red lines, drawn by eye, indicate presumed discrete levels. The QPD recording was sub-sampled and filtered at 50 Hz. After low-pass filtering, the value of σ was reduced to 0.05 pN. Trap stiffness was 0.01 pN nm^{-1}. **(e)** Histogram of forces measured during collisions between lamellipodia and trapped beads. Data reflect 65 experiments, each lasting 2 min. **(f)** Scatter plot of force duration for the collisions shown in (e).
doi:10.1371/journal.pone.0001072.g004

differentiating neurons sense the mechanical and chemical properties of barriers in front of their neurites and appear to have smart molecular motor planning, which guides and modifies the ultimate direction taken by neurites in the developing nervous system. Notably, these capabilities are in sharp contrast with metal and/or silicon components used for commercial information processing, which lack motility and motor planning.

MATERIALS AND METHODS

Rats (P10−12) were anesthetized with CO2 and sacrificed by decapitation in accordance with the Italian Animal Welfare Act. DRGs were incubated with trypsin (0.5 mg/ml), collagenase (1 mg/ml), and DNase (0.1 mg/ml) in 5 ml Neurobasal medium in a shaking bath (37°C, 35–40 min). They were mechanically dissociated, centrifuged at 300 rpm, resuspended in culture medium, and plated on poly-L-lysine-coated (0.5 ug/ml) coverslips. Cells were incubated for 24 to 48 h, and nerve growth factor (50 ng/ml; Alomone, Israel) was added before measurements were obtained.

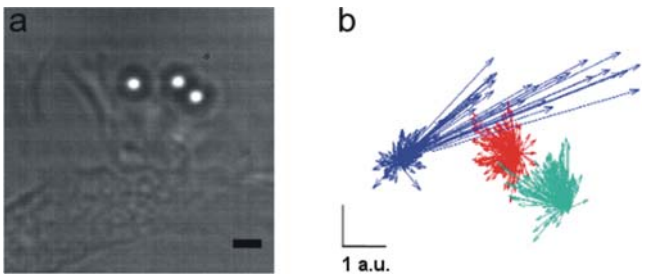

Figure 5. Force field exerted by lamellipodia. (a) A lamellipodium colliding with three trapped beads. **(b)** Direction and amplitude (in arbitrary units, a.u.) of forces exerted on the three beads. Superposition of bead displacements was obtained by video tracking at 5 Hz from a 4-min recording. Scale bar, 2 μm.
doi:10.1371/journal.pone.0001072.g005

The optical tweezers setup was built as previously described.[41] The dish containing the differentiating neurons and the beads (PSI-1.0NH2; G.Kisker GbR, Steinfurt, Germany) was placed on a microscope stage, which could be moved by a 3-axis piezoelectric nanocube (17 MAX 301; Melles Griot Inc., USA). The temperature of the dish was maintained at 37°C using a Peltier device. Bead position was determined in the x,y plane with an accuracy of 10 nm, using back focal plane (BFP) detection which relies on the interference between forward scattered light from the bead and unscattered light[22,42]. The BFP of the condenser was imaged onto a QPD, and the light was converted to differential outputs digitized at 4 kHz and low-pass filtered at 2 kHz. The bead displacement d = (dx,dy) from the equilibrium position inside the optical trap was also determined by video tracking using correlation methods with sub-pixel resolution. The lateral trap stiffness κx,y = (kx,ky) and the detector sensitivity were calibrated using the power spectrum method[22], with voltage signals filtered and digitized at 5 and 20 kHz, respectively. For multiple trapping experiments, computer-generated diffractive optical elements were projected onto the liquid crystal display of the phase-programmable modulator (PPM X8267-11; Hamamatsu Photonics, Japan)[41,43] in order to generate multiple spots in the specimen with a Gaussian intensity profile. For experiments where a single Gaussian beam was required, the PPM was switched off. In multiple trapping experiments, only the direction of the force was determined but not its amplitude.

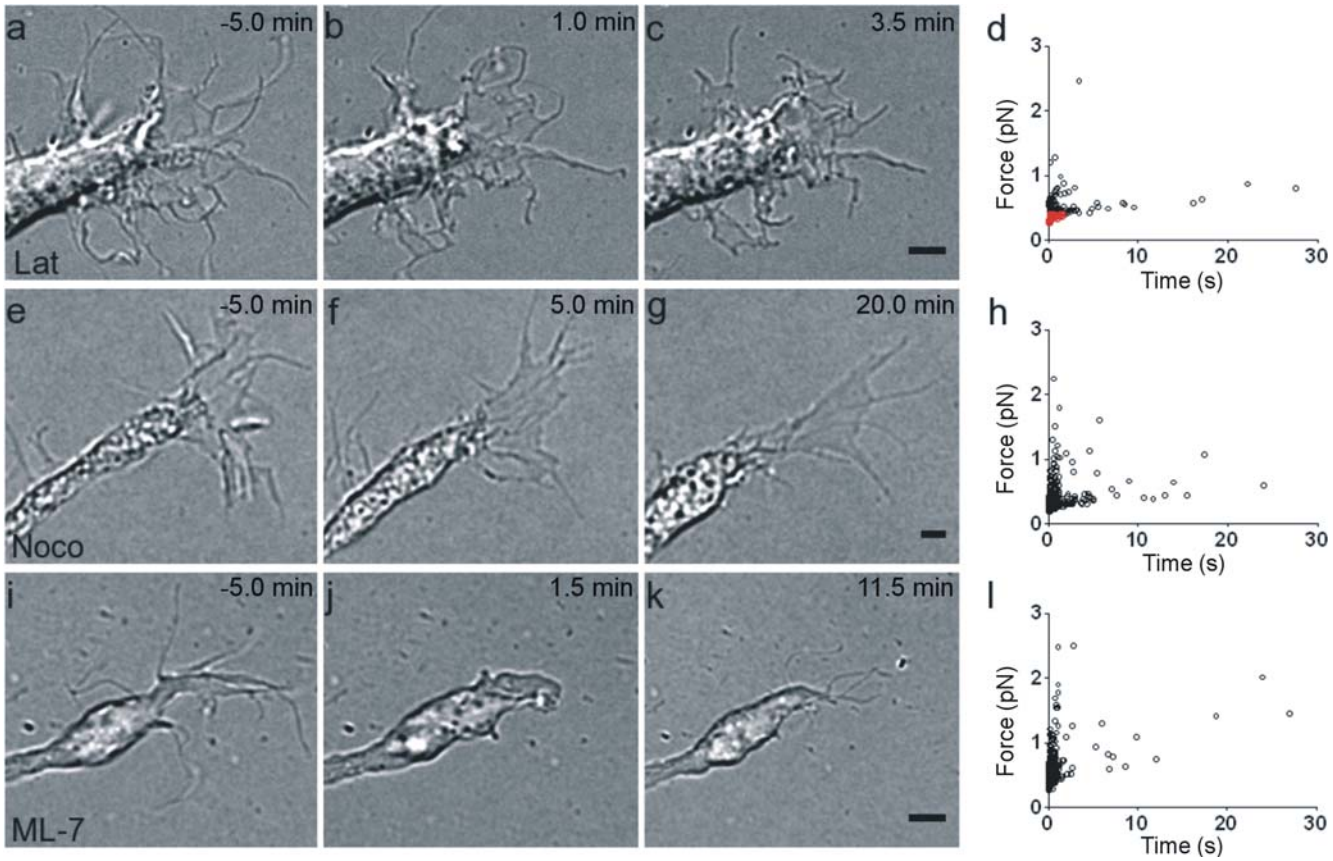

Figure 6. Effect of inhibitors on force exertion. A growth cone before **(a)** and after **(b–c)** application of 100 nM latrunculin A. No motion was observed after 3.5 min of exposure. **(d)** Scatterplot of force duration for collisions after application of 50 nM (black symbols) and 100 nM (red symbols) latrunculin A. A growth cone is shown before **(e)** and after **(f–g)** application of 50 nM nocodazole. The growth cone retracted, but filopodia continued to move for at least 30 min after drug exposure. **(h)** Scatterplot of force duration for collisions after application of 50 nM nocodazole. A growth cone is shown before **(i)** and after **(j–k)** application of 4 μM ML-7. Filopodia quickly retracted but then regrew and moved for at least 20 min after drug application. **(l)** Scatterplot of force duration for collisions after application of 4 μM ML-7. Scale bars, 2 μm. Drugs were added at time 0.
doi:10.1371/journal.pone.0001072.g006

For statistical analysis, QPD traces were low-pass filtered at 50 Hz. Collisions selected for statistical analysis had to satisfy three criteria: 1) maximal amplitude larger than 5σ, 2) duration longer than 100 ms, and 3) presence of a colliding filopodium or lamellipodium in contact with a bead verified by visual inspection of the movie. The collision duration was calculated as the interval between two consecutive crossings of 5σ. The force exerted by the neurite Fneu was calculated as -Ftrap. When the displacement of the bead from its equilibrium position inside the trap was less than 400 nm, Ftrap = (Fx, Fy) was calculated as Fx = dxkx and Fy = dyky[22]. When the bead was also moved along the vertical axis, the lateral displacement measured with the QPD was compared with data obtained from video tracking; the data were discarded if lateral displacements measured with the two methods differed by more than 50%. The axial force along the z axis was not measured.

SUPPORTING INFORMATION

Figure S1 (a–b) Another example of a collision between a protruding filopodium and a trapped bead . The filopodium grows and hits the trapped bead. Trap stiffness was 0.006 pN/nm. c: Fy from the QPD during the protrusion lateral of a–b. Scale bar, 2 μm. Numbers in the lower right corner indicate time in seconds.
Found at: doi:10.1371/journal.pone.0001072.s001 (3.29 MB TIF)

Movie S1 Movie of the motion of a growth cone imaged with time-lapse differential interference contrast (DIC) microscopy on the surface of the coverslip where the growth cone is located and at three focal planes 1, 2 and 3 μm above the coverslip. The four planes were scanned every 5 seconds. Filopodia are often seen in focus at 2 and 3 μm from the coverslip. (Acquisition rate: 5Hz; Scale bar, 2 μm). Numbers in the upper right corner indicate time in seconds.
Found at: doi:10.1371/journal.pone.0001072.s002 (1.97 MB MOV)

Movie S2 Movie of the collision between the growth cone and a trapped bead shown in Fig.1a–c. The trap stiffness was 0.02 pN/nm. The time of image acquisition is indicated in the corresponding frame (Acquisition rate: 5Hz; Scale bar, 2 μm). Numbers in the upper right corner indicate time in seconds.
Found at: doi:10.1371/journal.pone.0001072.s003 (4.95 MB MOV)

Movie S3 Movie of the lateral collision between the filopodium and a trapped bead shown in Fig.2a–b. The trap stiffness was 0.006 pN/nm. (Acquisition rate: 20Hz; Scale bar, 2 μm). Numbers in the upper right corner indicate time in seconds.
Found at: doi:10.1371/journal.pone.0001072.s004 (4.07 MB MOV)

Movie S4 Movie of the collision between the protruding filopodium and a trapped bead shown in Fig.2d–e. The trap stiffness was 0.006 pN/nm. (Acquisition rate: 20Hz; Scale bar, 2 μm). Numbers in the upper right corner indicate time in seconds.
Found at: doi:10.1371/journal.pone.0001072.s005 (4.45 MB MOV)

Movie S5 Movie of the collision between the protruding filopodium and a trapped bead shown in Supplementary Figure 1a–b. The trap stiffness was 0.006 pN/nm. (Acquisition rate: 20Hz; Scale bar, 2 μm). Numbers in upper right corner indicate time in seconds.
Found at: doi:10.1371/journal.pone.0001072.s006 (3.60 MB MOV)

Movie S6 Movie of the collision between the lamellipodium and a trapped bead shown in Fig.4a–b. The trap stiffness was 0.02 pN/nm. (Acquisition rate 20Hz; Scale bar, 2 μm). Numbers in upper right corner indicate time in seconds.
Found at: doi:10.1371/journal.pone.0001072.s007 (3.20 MB MOV)

ACKNOWLEDGMENTS

We thank Walter Vanzella (Glance Vision Technologies) for computational support.

Author Contributions

Conceived and designed the experiments: VT DC ED. Performed the experiments: EF FD RS. Analyzed the data: DC EF FD RS JL. Contributed reagents/materials/analysis tools: RS JL MR. Wrote the paper: VT DC ED.

REFERENCES

1. Solecki DJ, Govek EE, Hatten ME (2006) mPar6 alpha controls neuronal migration. J Neurosci 26: 10624–10625.
2. Ghashghaei HT, Lai C, Anton ES (2007) Neuronal migration in the adult brain: are we there yet? Nat Rev Neurosci 8: 141–151.
3. Goodman CS (1996) Mechanisms and molecules that control growth cone guidance. Annu Rev Neurosci 19: 341–377.
4. Bray D, Thomas C, Shaw G (1978) Growth cone formation in cultures of sensory neurons. Proc Natl Acad Sci U S A 75: 5226–5229.
5. Gordon-Weeks PR (2004) Microtubules and growth cone function. J Neurobiol 58: 70–83.
6. Song H, Poo M (2001) The cell biology of neuronal navigation. Nat Cell Biol 3: E81–E88.
7. Gallo G, Letourneau PC (2000) Neurotrophins and the dynamic regulation of the neuronal cytoskeleton. J Neurobiol 44: 159–173.
8. Aletta JM, Greene LA (1988) Growth cone configuration and advance: a time-lapse study using video-enhanced differential interference contrast microscopy. J Neurosci 8: 1425–1435.
9. Gomez TM, Letourneau PC (1994) Filopodia initiate choices made by sensory neuron growth cones at laminin/fibronectin borders in vitro. J Neurosci 14: 5959–5972.
10. Baker MW, Macagno ER (2007) In vivo imaging of growth cone and filopodial dynamics: evidence for contact-mediated retraction of filopodia leading to the tiling of sibling processes. J Comp Neurol 500: 850–862.
11. Galbraith CG, Yamada KM, Galbraith JA (2007) Polymerizing actin fibers position integrins primed to probe for adhesion sites. Science 315: 992–995.
12. Mongiu AK, Weitzke EL, Chaga OY, Borisy GG (2007) Kinetic-structural analysis of neuronal growth cone veil motility. J Cell Sci 120: 1113–1125.
13. Janson ME, de Dood ME, Dogterom M (2003) Dynamic instability of microtubules is regulated by force. J Cell Biol 161: 1029–1034.
14. Kovar DR, Pollard TD (2004) Insertional assembly of actin filament barbed ends in association with formins produces piconewton forces. Proc Natl Acad Sci U S A 101: 14725–14730.
15. Marcy Y, Prost J, Carlier MF, Sykes C (2004) Forces generated during actin-based propulsion: a direct measurement by micromanipulation. Proc Natl Acad Sci U S A 101: 5992–5997.
16. Kerssemakers JW, Munteanu EL, Laan L, Noetzel TL, Janson ME, et al. (2006) Assembly dynamics of microtubules at molecular resolution. Nature 442: 709–712.
17. Footer MJ, Kerssemakers JW, Theriot JA, Dogterom M (2007) Direct measurement of force generation by actin filament polymerization using an optical trap. Proc Natl Acad Sci U S A 104: 2181–2186.
18. Prass M, Jacobson K, Mogilner A, Radmacher M (2006) Direct measurement of the lamellipodial protrusive force in a migrating cell. J Cell Biol 174: 767–772.
19. Howard J (2001) Mechanics of Motor Proteins and the Cytoskeleton. Sunderland, MA: Sinauer Associates, Inc.
20. Ashkin A (1997) Optical trapping and manipulation of neutral particles using lasers. Proc Natl Acad Sci U S A 94: 4853–4860.
21. Bustamante C, Macosko JC, Wuite GJ (2000) Grabbing the cat by the tail: manipulating molecules one by one. Nat Rev Mol Cell Biol 1: 130–136.
22. Neuman KC, Block SM (2004) Optical trapping. Rev Sci Instrum 75: 2787–2809.
23. Giannone G, Dubin-Thaler BJ, Dobereiner HG, Kieffer N, Bresnick AR, et al. (2004) Periodic lamellipodial contractions correlate with rearward actin waves. Cell 116: 431–443.
24. Dent EW, Kalil K (2001) Axon branching requires interactions between dynamic microtubules and actin filaments. J Neurosci 21: 9757–9769.
25. Pralle A, Prummer M, Florin EL, Stelzer EH, Horber JK (1999) Three-dimensional high-resolution particle tracking for optical tweezers by forward scattered light. Microsc Res Tech 44: 378–386.
26. Bovolenta P, Mason C (1987) Growth cone morphology varies with position in the developing mouse visual pathway from retina to first targets. J Neurosci 7: 1447–1460.
27. Myers KA, He Y, Hasaka TP, Baas PW (2006) Microtubule transport in the axon: Re-thinking a potential role for the actin cytoskeleton. Neuroscientist 12: 107–118.
28. Mogilner A, Oster G (1996) Cell motility driven by actin polymerization. Biophys J 71: 3030–3045.
29. Mogilner A (2006) On the edge: modeling protrusion. Curr Opin Cell Biol 18: 32–39.
30. Raucher D, Sheetz MP (2000) Cell spreading and lamellipodial extension rate is regulated by membrane tension. J Cell Biol 148: 127–136.
31. Mogilner A, Rubinstein B (2005) The physics of filopodial protrusion. Biophys J 89: 782–795.
32. Atilgan E, Wirtz D, Sun SX (2006) Mechanics and dynamics of actin-driven thin membrane protrusions. Biophys J 90: 65–76.
33. Guan KL, Rao Y (2003) Signalling mechanisms mediating neuronal responses to guidance cues. Nat Rev Neurosci 4: 941–956.
34. Pollard TD, Blanchoin L, Mullins RD (2000) Molecular mechanisms controlling actin filament dynamics in nonmuscle cells. Annu Rev Biophys Biomol Struct 29: 545–576.
35. Grunwald IC, Klein R (2002) Axon guidance: receptor complexes and signaling mechanisms. Curr Opin Neurobiol 12: 250–259.
36. Huber AB, Kolodkin AL, Ginty DD, Cloutier JF (2003) Signaling at the growth cone: ligand-receptor complexes and the control of axon growth and guidance. Annu Rev Neurosci 26: 509–563.
37. du Roure O, Saez A, Buguin A, Austin RH, Chavrier P, et al. (2005) Force mapping in epithelial cell migration. Proc Natl Acad Sci U S A 102: 2390–2395.
38. Dai J, Sheetz MP (1995) Mechanical properties of neuronal growth cone membranes studied by tether formation with laser optical tweezers. Biophys J 68: 988–996.
39. Liu AP, Fletcher DA (2006) Actin polymerization serves as a membrane domain switch in model lipid bilayers. Biophys J 91: 4064–4070.
40. Gittes F, Mickey B, Nettleton J, Howard J (1993) Flexural rigidity of microtubules and actin filaments measured from thermal fluctuations in shape. J Cell Biol 120: 923–934.
41. Cojoc D, Emiliani V, Ferrari E, Malureanu R, Cabrini S, et al. (2004) Multiple Optical Trapping by Means of Diffractive Optical Elements. Jpn J Appl Phys 43: 3910–3915.
42. FGittes, Schmidt C (1998) Interference model for back-focal-plane displacement detection in optical tweezers. Opt Lett 23: 7–9.
43. Dufresne ER, Spalding GC, Dearing MT, Sheets SA (2001) Computer-Generated Holographic Optical Tweezer Arrays. Review of Scientific Instruments 72: 1810–1816.

Force generation in lamellipodia is a probabilistic process with fast growth and retraction events

Shahapure R. B.[1], Difato F.[1,2], Laio, A.[1], Cojoc D.[3], Ferrari E. [3], Laishram, J.[1], Bisson G.[1]& Torre V.[1,2]

[1]International School for Advanced Studies (SISSA-ISAS), Trieste, Italy. [2]Italian Institute of Technology, ISAS Unit, Italy.[3]CNR-INFM Laboratorio Nazionale TASC, 34012 Trieste, Italy

Running head: Force Development in biological system

Character count: 18,826

Abbreviations: Force (F) and velocity (v) (normal font) indicate either the modulus or a component of the respective vectors while **F** and **v** (bold font) indicate vectors.

Correspondence to Vincent Torre: torre@sissa.it

Abstract

Polymerization of actin filaments is the primary source of motility in lamellipodia (Pollard, T., and G. Borisy. 2003. *Cell*. 112: 453 - 465) controlled by a variety of regulatory proteins (Pak,C.W., K.C.Flynn, and J.R.Bamburg. 2008. *Nature Reviews Neuroscience* 9:136-147). Underlying molecular mechanisms are only partially understood and a precise determination of dynamical properties of force generation is necessary. Using optical tweezers we have measured with high temporal resolution and sensitivity the force-velocity (Fv) relationship and the work done on the external environment by lamellipodia of dorsal root ganglia (DRG) neurons. The measured maximal force and power per unit area are 20 pN μm^{-2} and 10^{-16} Joule s^{-1} μm^{-2} respectively. When force and velocity are averaged over 3-5 s, the exerted force can increase maintaining a constant velocity and the Fv relationships are flat. On a finer time scale, random occurrence of fast growths and sub-second retractions become predominant.

Introduction

The addition of actin polymers to actin filaments in close contact with the membrane pushes the cellular membrane forward and represents the elementary mechanism of force generation (Howard, 2001;Raucher and Sheetz, 2000). The overall dynamics regulating and controlling the formation of an actin network is not yet clear and several models and theoretical predictions have been produced requiring an experimental validation, such as a precise determination of the Fv relationships (Mogilner, 2006;Parekh et al., 2005;Marcy et al., 2004;Prass et al., 2006), where F and v can be either a component or the modulus of $\mathbf{v}$ and $\mathbf{F}$, where $\mathbf{v} = (v_x,v_y,v_z)$ is the velocity of lamellipodium leading edge and $\mathbf{F} = (F_x,F_y,F_z)$ is the force exerted by the lamellipodium. Fluctuations of contacts between the tip of actin filaments and the surrounding membrane is an essential feature in Brownian ratchet models (Peskin et al., 1993) leading to Fv relationships in which velocity decreases exponentially with increasing force. In these models, the velocity v drops quickly by increasing the opposing load, equal to the force F but with an opposite versus. In autocatalytic models (Carlsson, 2001;Mogilner, 2006) when an obstacle is encountered the actin network and controlling proteins give origin to new branches of actin filaments, so that the velocity v remains constant for increasing values of F.

Results and Discussion

DRG neurons isolated from P10-P12 rats were plated on poly-L-lysine-coated glass coverslips, positioned on the stage of an inverted microscope used for imaging and measuring forces (see Methods). After 1 or 2 days of incubation, neurites emerged from the DRG soma and their motion was analysed. Filopodia and lamellipodia moved rapidly exploring the three dimensional (3D) space in all directions. Silica beads of 1 μm in diameter, functionalised with amino groups to reduce sticking to the coverslip, were trapped with a 1064 nm infrared (IR) optical tweezers positioned close to the growth cones of differentiating neurites (Fig.1a). When lamellipodia or filopodia collided with the bead, the bead was displaced, sometimes by some hundreds nm (Fig.1b). The displacement of the bead $\mathbf{x}$ = (x,y,z) from the equilibrium position inside the optical trap was measured with a high temporal resolution using a Quadrant Photo Diode (QPD) and by determining the trap stiffness $\boldsymbol{k} = (k_x,k_y,k_z)$, $\mathbf{F}$ was obtained as $(-x\ k_x, -y\ k_y, -z\ k_z)$ (Kress et al., 2005;Neuman and Block, 2004).

At a low temporal resolution the force can increase with an almost constant velocity and the Fv relationships are flat.

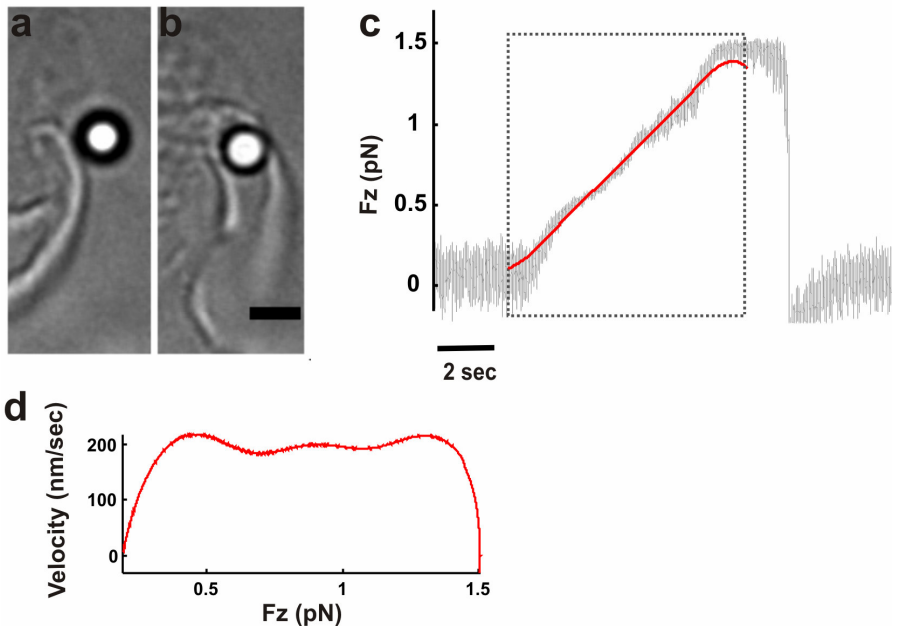

Figure 1 (a-b) *Lamellipodium colliding with a bead trapped with an infrared laser. During the collision the bead is lifted up by about 200 nm. Scale bar, 2 µm.* ***(c)*** *F_z (grey trace) used for computing the Fv relationship. The dotted box indicates the section of force measurement used to compute the Fv relationship after Gaussian filtering at 0.2 Hz (red trace).* ***(d)*** *Fv relationship obtained from the red trace in (c).*

When the bead was far from the neuron, the recordings of the components of **F** were quiet (red trace in inset fig.2a), but when lamellipodia pushed the bead, forces up to 20 pN were observed (blue trace in inset fig.2a)(Cojoc et al., 2007). In some experiments, the lamellipodium lifted up the bead by 200-400 nm (Fig.1a and b) exerting forces of 1.5-10 pN . When the bead displacement was low pass filtered with a cut-off at 0.2 Hz (red trace in Fig.1c) corresponding to a temporal smoothing over a time window of 3-5 seconds, and velocity v_z was computed by numerical differentiation, the Fv relationships shown in Fig.1d was obtained. The Fv relationships - following an initial rise - are almost

flat, indicating that the lamellipodium can increase the exerted force while the velocity of its leading edge remains almost constant. Almost identical results were obtained when Fv relationships were computed from the modulus of **F** and not from a single component (F_z.) as in fig.1d. Autocatalytic models of force generation predict that when the underlying system of actin filaments and controlling proteins has the time to self-reorganize, v becomes independent of F.

At a higher temporal resolution the velocity oscillates and transient periods of negative velocities are observed

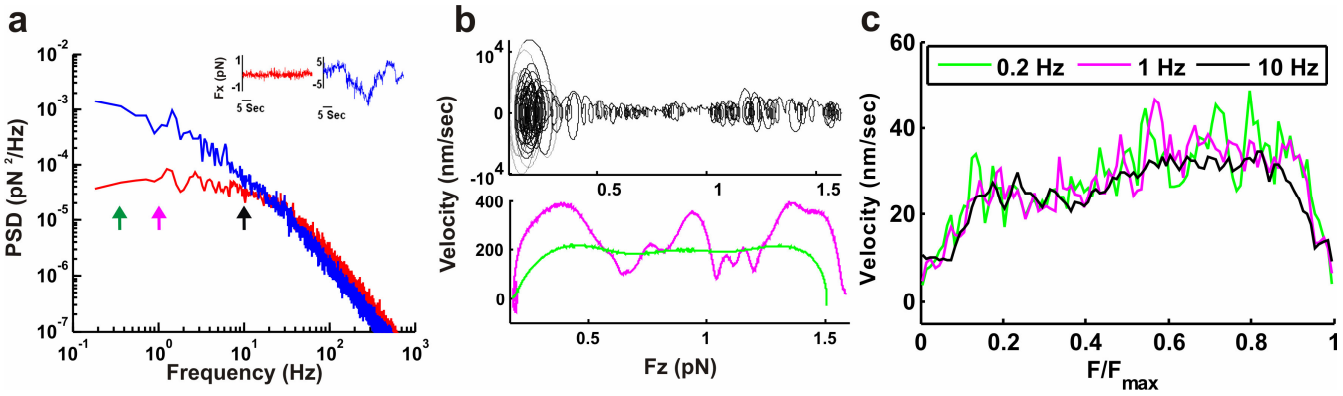

Figure.2 (a) *The power spectrum density of forces measured far from the lamellipodium (red trace) and during collisions between the bead and a moving lamellipodia (blue trace).Green, pink and, black arrows indicate 0.2, 1 and 10 Hz respectively.* ***(b)*** *Fv relationships obtained after smoothing at 10Hz (black trace in upper panel), 1 Hz (pink trace in the lower panel), and 0.2Hz (green trace in the lower panel).* ***(c)*** *Average $\langle Fv \rangle_x$ relationships from data filtered up to a bandwidth of X Hz. $\langle Fv \rangle_{0.2}$, (green trace), $\langle Fv \rangle_1$ (pink trace), and $\langle Fv \rangle_{10}$ (black trace).*

The almost flat Fv relationships (see Fig.1d) were obtained when the position of the lamellipodium leading edge **x** and the exerted force **F** were averaged over a time window of 3-5 seconds. Averaging a temporal series over a time window of 3-5 seconds corresponds to smoothing the data with a low pass filter with a bandwidth up to 0.2 Hz. Therefore, we decided to investigate the bandwidth of biological

events underlying force generation. We computed and compared the power spectrum density $PSD_{noise}(f)$ of forces measured far from the lamellipodium (red trace in Fig.2a) - originating from Brownian fluctuations and instrumental noise - and the $PSD_{collisions}$ (f) of forces during collisions between the bead and the lamellipodium (blue trace in Fig.2a). $PSD_{noise}(f)$ and $PSD_{collisions}(f)$ are very similar and almost indistinguishable (Fig.2a) for f > 30 Hz, but at frequencies below 1 Hz the energy of biological collisions is at least 30 times larger than that caused by Brownian collisions with water molecules. Therefore, we computed Fv relationships after smoothing at 0.2 (green trace in lower panel of Fig.2b), 1 (pink trace in lower panel of Fig.2b) and 10 Hz (black trace in upper panel of Fig.2b). When data were smoothed at 1 and 10 Hz the velocity oscillated widely around an almost constant value of 200 nm sec^{-1} reaching occasional peak values up to 1-10 μm sec^{-1}, and at this bandwidth, Fv relationships exhibit fast oscillations around an almost constant value of v.

We determined Fv relationships from 95 experiments during which lamellipodia exerted forces from 1 or 2 pN up to 20 pN. The almost flat Fv relationships illustrated in Fig.1d were obtained in 7 (out of 95) experiments. In the majority of the experiments (87/95) the shape of measured Fv relationships was different - at some extent - for each experiment. In some experiments (14/95) repetitive collisions were measured from the same lamellipodium and also in these cases the maximal force and the shape of Fv relationships measured at different times varied. These results suggest that force generation in lamellipodia is an inherent probabilistic process and does not follow a deterministic mechanism. In order to characterize this probabilistic dynamics we attempted to determine average Fv relationships <Fv>. The individual 95 Fv relationships where normalized to the same maximal stall force F_{max} and we computed their average value <Fv> by averaging the measured velocity for a given value of F/F_{max}. F_{max} was defined as the maximal force beyond which the lamellipodium leading edge does not advance and the velocity is consistently negative for at least 10 s. We computed average $<Fv>_x$

relationships (Fig.2c) from data filtered at different bandwidths of X Hz. $\langle Fv \rangle_{0.2}$ (green trace), $\langle Fv \rangle_{1}$ (pink trace), and $\langle Fv \rangle_{10}$ (black trace) exhibited the same overall behavior, with the velocity increasing together with the force, up to about 30 nm/s and remaining approximately stable up to F_{max}.

In several force recordings, transient periods in which the bead reverted its motion were observed (Fig.3a). In these cases, computed Fv relationships had knots (Fig.3b) and two values of F were associated to the same velocity v. As the numerical computation of derivatives from noisy data is ill-conditioned (Bertero et al., 1988) we asked whether these knots were originated by the specific method used to compute the velocity from the displacement. Therefore, we compared two alternative methods to obtain the velocity from the displacement, such as Gaussian filtering and Linear regression. In Gaussian filtering the velocity is obtained from the displacement by its convolution with the derivative of a Gaussian function with a given cut-off frequency, while in the Linear regression method (see Methods) the velocity is obtained from the displacement and a linear interpolation of the data on a window containing W data points. In these two methods the time scale is given by the cut-off frequency of the Gaussian function and by the number of points W in the window respectively. As shown in Fig.3b (compare black and red trace) Fv relationships computed by the two methods had the same number of knots. The number of knots, however, increased when the bandwidth of Gaussian filtering increased from 0.2 to 1 Hz (red and black traces in Fig.3c respectively).

As numerical differentiation is very sensitive to noise and it amplifies its high frequency components, we investigated at what extent knots, i.e. periods with a negative velocity, are caused by Brownian fluctuations. We computed Fv relationships from force measurements obtained far from the lamellipodia. The obtained velocity was Gaussian distributed around 0, with a standard deviation σ_v increasing with the bandwidth of Gaussian filtering, depending also on the trap stiffness (see Fig.3d).

Periods with a negative velocity - less than $-3\sigma_v$ - cannot be ascribed to Brownian fluctuations and all negative velocities exceeding $-3\sigma_v$ lines (red and black dotted lines in Fig.3b and c) are caused by interactions with the lamellipodium. As shown in Fig.3c, the $-3\sigma_v$ line is crossed several times and more often at larger bandwidths.

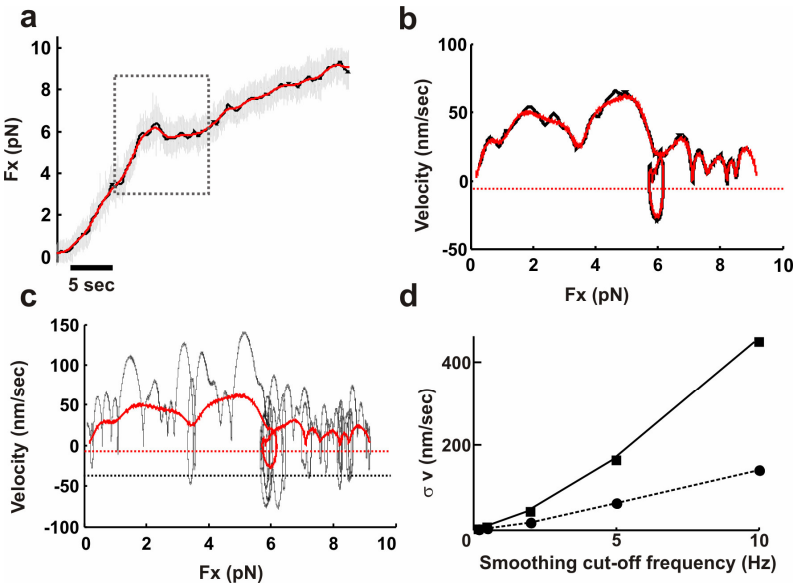

Figure 3 ***(a)*** *Force measurement used to compute the Fv relationships (grey trace) and after Gaussian filtering at 0.2 and 1 Hz (red and black traces). Dotted box indicates the section of the recording used to compute Fv relationships in (b) and (c).* ***(b)*** *Red and black Fv relationships were computed with Gaussian filtering and Linear regression respectively. Dotted red line represents* $-3\sigma_v$ *at the 0.2 Hz bandwidth.* ***(c)*** *Fv relationships computed with Gaussian filtering at 0.2 and 1 Hz (red and black traces respectively). Dotted red and black lines represent* $-3\sigma_v$ *at the 0.2 and 1Hz bandwidths respectively.* ***(d)*** *Relationship between standard deviation of velocity distribution as a function of smoothing and for two trap stiffness 0.005 pN/nm (squares) and 0.045 pN/nm (dots).*

Having established the existence of periods during which lamellipodia leading edge have negative velocities, we asked whether these periods occurred at random times or occurred more frequently near the maximal stall force F_{max}. We computed the probability distribution of the occurrence of negative

velocities as a function of the ratio F/F_{max} , i.e. the probability distribution of velocities being less than $-3\sigma_v$ at fixed forces F/F_{max} is $p(v < -3\sigma_v | F/F_{max})$. This probability distribution was estimated from the 95 experimentally determined Fv relationships. The value of $p(v < -3\sigma_v | F/F_{max})$ varied between 0.05 and 0.1 (Fig.4a) and was nearly identical when it was derived from Fv relationships computed at 0.2, 1 and 10 Hz bandwidth. This result indicates that retractions of lamellipodium leading edge are not triggered by a strong load but their occurrence is random.

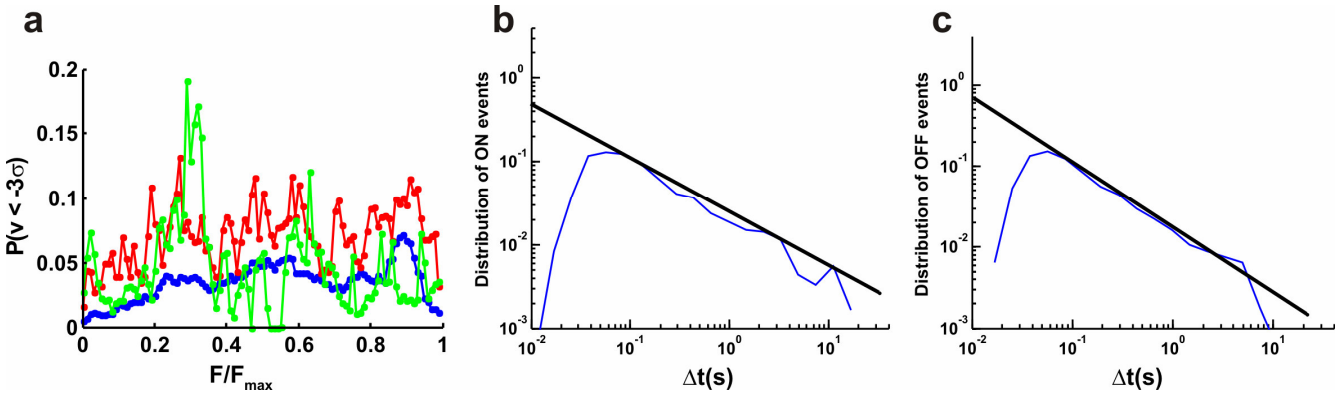

Figure 4 (a) *Probability distribution $p(v<-3\ \sigma_v | F/F_{max})$ of velocities being less than $-3\sigma_v$ at fixed forces (F/F_{max}).(Average Fv relationships from 95 experiments obtained by the data filtered with a Gaussian filter with a cut-off frequency at 0.2 (green), 1 (red) and, 10 (blue) normalized to F_{max}.).* ***(b-c)*** *Distribution of ON and OFF events, respectively. Black straight lines have a slope of -0.6 and -0.78 in (c) and (d) respectively.*

Statistical properties of Fv relationships were characterized by measuring the distribution of intervals (Δt) with a positive (Fig.4b) and a negative velocity (Fig.4c) representing the ON and OFF events of the lamellipodium leading edge. Detected ON and OFF events were seen using a bandwidth of 0.2 Hz, to allow the underlying dynamical system to reorganize itself properly. The distributions of the ON and OFF events obtained at the a bandwidth of 0.2 Hz do not have an exponential behaviour but

exhibit a power law distribution of the type $\Delta t^{-1.2}$ (see straight lines in Fig.4b and Fig.4c) over almost two log units, suggestive of a growth characterized by avalanches (Jensen, 1998).

Lamellipodia dissipate power up to 10^{-16} joule s^{-1} μm^{-2} during force production

Having determined the Fv relationships and estimated the maximal exerted pressure, we asked how much mechanical work and power lamellipodia exert on encountered obstacles such as beads. During collisions, often lamellipodia displace beads in a complex way and F_x, F_y, F_z change almost independently, reaching their maximum amplitude at different times (Fig.5a). In these cases, the bead motion is not a simple upward axial motion as in Fig.1, but the bead moves along a trajectory that often changes its direction (see black trace in Fig.5d). We determined the three components of **F** and **v**. When the lamellipodia exerted a significant force, **F** and **v** had approximately the same versus and direction, only occasionally they had an opposite versus (see red and blue arrows in Fig.5d). The work done per second (power) by the lamellipodium is the scalar product **F**$\circ$**v**. As shown in Fig.2, the amplitude of the instantaneous velocity depends on the bandwidth used for filtering the data; during the collision described in Fig.5a, **F**$\circ$**v** reached values up to 4 10^{-18} Joule s^{-1}, when **v** was computed at a bandwidth of 0.2 Hz but up to 10^{-16} Joule s^{-1} at a bandwidth up to 10 Hz.(Fig.5b) The instantaneous maximal power exerted by a lamellipodium was 10^{-16} Joule s^{-1} and was observed only transiently for approximately 100 msec.

The analysis of the angle ϕ between **F** and **v** provides useful information to understand the mechanics of collisions between beads and lamellipodia: when ϕ is close to 0 the lamellipodium pushes the bead and develops a positive work, and when ϕ is close to π the lamellipodium retracts. When the angle ϕ is close to $\pi/2$ lamellipodia do not perform any work. No work is performed primarily in two occasions: firstly, when the lamellipodium exerts a very small force on the bead. In this case the bead

dynamics is primarily determined by Brownian collisions with water molecules and under these conditions **F** is almost orthogonal to **v** and the lamellipodium does not develop any significant work. Secondly, if the modulus of **F** and **v** are large, but the bead slides over the lamellipodium, **F** becomes orthogonal to **v** and no work will be generated. The angle ϕ was determined as $\phi = \text{Arccos}(\mathbf{F} \circ \mathbf{v} / |\mathbf{F}|\,|\mathbf{v}|)$ (Fig.5c). During collisions, when the modulus of **F** was larger than 2 pN, ϕ was, for most of the time, close to either 0 or to π (Fig.5f), indicating that **F** and **v** are usually parallel or antiparallel with an opposite versus. Occasionally ϕ had values close to $\pi/2$, indicating that **F** and **v** were orthogonal and no work was performed on the bead. In contrast, when the modulus of **F** is smaller than 2 pN (Fig. 5e) the value of ϕ is most of the time close to $\pi/2$. A sudden change of the bead motion like the one shown in Fig. 5d could be caused either by a momentary sliding of the bead over the lamellipodium or by a transient retraction of the lamellipodium leading edge. These two mechanisms can be easily distinguished by looking at the work: if the bead slides over the lamellipodium no work will be done and ϕ will be close to $\pi/2$. Instead, if the lamellipodium transiently retracts the work done by the lamellipodium will be negative and ϕ will be close to π. With this procedure we verified that periods with negative velocities analyzed in Fig.3 and Fig.4 were associated to values of ϕ close to π and therefore were not caused by an occasional sliding of the bead but by transient retractions of the lamellipodial leading edge.

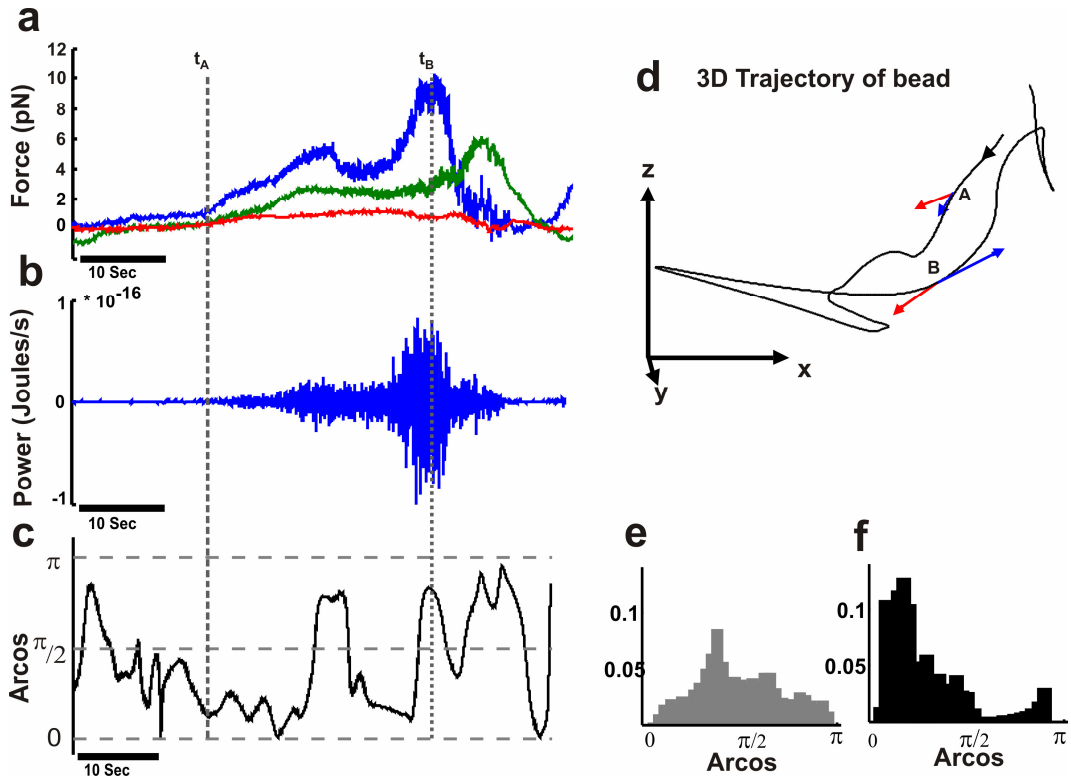

Figure.5 ***(a)*** *Three components of the force F_x (blue), F_y (green) and F_z (red) exerted by a lamellipodium during a collision with a trapped bead smoothed at 10 Hz.* ***(b)*** *Instantaneous power* $\mathbf{F}\cdot\mathbf{v}$ *(blue trace)acting on the bead.* ***(c)*** *Time evolution of Arcos* ($\mathbf{F}\cdot\mathbf{v} / |\mathbf{F}||\mathbf{v}|$) *during the collision.* ***(d)*** *The trajectory of the bead in the 3D space during the collision. The black arrow indicates the direction of the trajectory. Red and blue arrowson A and B indicate the instantaneous* $\mathbf{F}$ *and* $\mathbf{v}$ *respectively at the two times t_A and t_B indicated by the vertical dashed and dotted lines in panels (a-c). When* $\mathbf{F}$ *and* $\mathbf{v}$ *are parallel Arcos* ($\mathbf{F}\cdot\mathbf{v} / |\mathbf{F}||\mathbf{v}|$) *is close to 0 and when* $\mathbf{F}$ *and* $\mathbf{v}$ *are antiparallel Arcos* ($\mathbf{F}\cdot\mathbf{v} / |\mathbf{F}||\mathbf{v}|$) *is close to* π. ***(e)*** *Histogram of the Arcos when* $|\mathbf{F}|$ *was smaller than 2 pN.* ***(f)*** *Histogram of the Arcos when* $|\mathbf{F}|$ *was larger than 2 pN.*

In this work several basic properties of force generation in lamellipodia (Weiner et al., 2007;Pak et al., 2008;Lacayo et al., 2007) have been obtained from a precise measurement performed with optical tweezers. The maximal force exerted by lamellipodia on a 1 μm diameter bead was approximately 20 pN (Cojoc et al., 2007), indicating that the maximal pressure exerted by DRG lamellipodia is 20 pN

μm^{-2}. In some experimental observations of force generation, the system of actin-based filaments and controlling proteins self-organizes rather efficiently and within 3-5 s is able to exert on the leading edge an increasing force maintaining a constant velocity (Fig.1). In the great majority of experiments force generation was characterized by large fluctuations of the velocity. The Fv relationships averaged over several experiments show that F can increase, while v remains approximately constant, quickly dropping to zero when F_{max} is reached, in agreement with the autocatalytic model of force generation. The maximum power exerted by lamellipodia was about 10^{-16} J s^{-1} μm^{-2}. The hydrolysis of one molecule of ATP provides energy of about 10^{-19} J (Bray, 1992) and, if this energy is converted into work with an efficiency of about 20 % , the hydrolysis of about 10^4 molecules of ATP per μm^2 is necessary to produce the measured power. The number of actin filaments in keratocyte and fibroblast lamelipodia has been estimated to be of the order of 100 per μm^2 (Prass et al., 2006;Abraham et al., 1999). Therefore the number of elementary motors per μm^2 is likely to be of the order of 100, where each elementary motor consumes approximately 100 ATP per second.

Force generation in lamellipodia is probabilistic in nature and average <Fv> relationships (Fig.2c) exhibit a flat shape, during which the mean velocity remains constant while the force can increase, as expected from autocatalytic models. In individual experiments, the velocity does not remain constant but oscillates and can become negative, producing knots in Fv relationships. These knots indicate that the same force can be exerted with a positive and negative velocity, characteristic feature of system exhibiting hysteresis (Parekh et al., 2005). The time duration of periods with a negative velocity has a power law distribution reminiscent of self-organized systems near criticality (Jensen, 1998). During these events, the force exerted on the bead by the lamellopodium acts in the opposite direction of its velocity, indicating that the bead is not simply sliding on the membrane, but that the actin filaments

network is retracting, possibly due to local catastrophe or organized depolymerization controlled by cofilin and other severing proteins (Pak et al., 2008). Therefore force generation is not a smooth process but it is characterized by a random alternation of fast growths and retractions of lamellipodium leading edge.

What could be the mechanism responsible for the frequent occurrence of negative velocity events? This complex dynamics could be produced by a collective behavior of producing waves (Weiner et al., 2007) and large-scale shape changes (Lacayo et al., 2007). Proteins controlling the network of actin filaments, such as cofilin, could randomly sever a large branch of actin filaments leading to a local catastrophe causing a transient retraction of the lamellipodium leading edge. Growth and retraction in conditions of marginal stability allow fast reactions and could provide lamellipodia the flexibility necessary for its physiological functions.

Methods

Rats (P10−12) were anaesthetised with CO_2 and sacrificed by decapitation in accordance with the Italian Animal Welfare Act. DRGs were incubated with trypsin (0.5 mg/ml), collagenase (1 mg/ml), and DNase (0.1 mg/ml) in 5 ml Neurobasal medium in a shaking bath (37°C, 35-40 minutes). DRGs were mechanically dissociated, centrifuged at 300 rpm, resuspended in culture medium and plated on poly-L-lysine-coated (0.5 ug/ml) coverslips.

The optical tweezers setup was built as described in (Cojoc et al., 2007). The dish containing the differentiating neurons and the beads (PSI-1.0NH2, G.Kisker GbR, Steinfurt Germany) was placed on the microscope stage which could be moved by a 3 axis piezoelectric nanocube (17 MAX 301, Melles Griot Inc., USA). The temperature of the dish was kept at 37°C by a Peltier device. Bead position $\mathbf{x}$ = (x,y,z) was determined in the (x, y) plane with an accuracy of 10 nm using back focal plane (BFP) detection, which relies on the interference between the forward scattered light from the bead and the unscattered light (Gittes and Schmidt, 1998;Neuman and Block, 2004). The BFP of the condenser was imaged onto a QPD and the light was converted to differential outputs digitized at 20 kHz and low pass filtered at 5 kHz. Bead z position was determined using the Gouy phase shift effect (Neuman and Block, 2004).

The velocity was obtained by numerical differentiation of the position (x(n),y(n),z(n)) n=1,…N. Numerical differentiation was computed either by convolution of the position with the derivative of a Gaussian filter $\frac{1}{\sigma\sqrt{2\pi}}\exp\left[-t^2/(2\sigma^2)\right]$ (Gaussian filtering) and by Linear regression. In the Linear regression method the velocity v is calculated by a linear least square fit of the equation $x(n)= a + v_x(n)(i - n)\Delta t$ with i = -W……W where Δt is the sampling interval. The two parameters a and $v_x(n)$ are determined by minimizing the cost function:

$$[v_x, a] = \arg\min_{[v,a]} \left[\sum_{i=n-W}^{n+W} \left(a + v_x (i-n)\Delta t - y(i) \right)^2 \right]$$

Acknowledgement We thank Walter Vanzella (Glance Vision Technologies s.r.l.) for computational support.

References

Abraham, V.C., V.Krishnamurthi, D.L.Taylor, and F.Lanni. 1999. The actin-based nanomachine at the leading edge of migrating cells. *Biophysical Journal* 77:1721-1732.

Bertero, M., T.A.Poggio, and V.Torre. 1988. Ill-Posed Problems in Early Vision. *Proceedings of the Ieee* 76:869-889.

Bray, D. 1992. Cell Movements. Garland Publishing, New York.

Carlsson, A.E. 2001. Growth of branched actin networks against obstacles. *Biophysical Journal* 81:1907-1923.

Cojoc, D., F.Difato, E.Ferrari, R.B.Shahapure, J.Laishram, M.Righi, E.M.Di Fabrizio, and V.Torre. 2007. Properties of the force exerted by filopodia and lamellipodia and the involvement of cytoskeletal components. *PLoS. ONE.* 2:e1072.

Gittes, F. and C.F.Schmidt. 1998. Interference model for back-focal-plane displacement detection in optical tweezers. *Optics Letters* 23:7-9.

Howard, J. 2001. Mechanics of Motor Proteins and the Cytoskeleton. Sinauer Associates, Inc, Sunderland, MA.

Jensen, H.J. 1998. Self-Organized Criticality.Cambridge Lecture Notes in Physics. Cambridge University Press.

Kress, H., E.H.K.Stelzer, G.Griffiths, and A.Rohrbach. 2005. Control of relative radiation pressure in optical traps: Application to phagocytic membrane binding studies. *Physical Review e* 71.

Lacayo, C.I., Z.Pincus, M.M.VanDuijn, C.A.Wilson, D.A.Fletcher, F.B.Gertler, A.Mogilner, and J.A.Theriot. 2007. Emergence of large-scale cell morphology and movement from local actin filament growth dynamics. *Plos Biology* 5:2035-2052.

Marcy, Y., J.Prost, M.F.Carlier, and C.Sykes. 2004. Forces generated during actin-based propulsion: A direct measurement by micromanipulation. *Proceedings of the National Academy of Sciences of the United States of America* 101:5992-5997.

Mogilner, A. 2006. On the edge: modeling protrusion. *Current Opinion in Cell Biology* 18:32-39.

Neuman, K.C. and S.M.Block. 2004. Optical trapping. *Review of Scientific Instruments* 75:2787-2809.

Pak, C.W., K.C.Flynn, and J.R.Bamburg. 2008. Actin-binding proteins take the reins in growth cones. *Nature Reviews Neuroscience* 9:136-147.

Parekh, S.H., O.Chaudhuri, J.A.Theriot, and D.A.Fletcher. 2005. Loading history determines the velocity of actin-network growth. *Nature Cell Biology* 7:1219-1223.

Peskin, C.S., G.M.Odell, and G.F.Oster. 1993. Cellular Motions and Thermal Fluctuations - the Brownian Ratchet. *Biophysical Journal* 65:316-324.

Pollard, T.D. and G.G.Borisy. 2003. Cellular motility driven by assembly and disassembly of actin filaments. *Cell* 112:453-465.

Prass, M., K.Jacobson, A.Mogilner, and M.Radmacher. 2006. Direct measurement of the lamellipodial protrusive force in a migrating cell. *Journal of Cell Biology* 174:767-772.

Raucher, D. and M.P.Sheetz. 2000. Cell spreading and lamellipodial extension rate is regulated by membrane tension. *Journal of Cell Biology* 148:127-136.

Weiner, O.D., W.A.Marganski, L.F.Wu, S.J.Altschuler, and M.W.Kirschner. 2007. An actin-based wave generator organizes cell motility. *Plos Biology* 5:2053-2063.

3. General conclusions

The interest in optical microscopy is constanly growing, mainly because of its unique features in examining biological systems in four dimensions (x-y-z-t)[1]. The work presented here was focused on biological applications of optical microscopy by exploring and improving the spatial and temporal resolution performances and by futher developing optical tools for manipulating biological samples.

First, I studied the resolution performances of the system in the three dimensional space and I contributed in improving the experimental spatial resolution of microscope by applying deconvolution. In this respect, theoretical modelling can characterize the image formation process of the microscope, but only experimental measurement of the PSF can quantify the limitations of the real system. Indeed, experimental PSF presents shape assymetry due to spherical aberrations introduced by optical elements, while theoretical PSF is symmetric and account only for the resolution limits of an ideal imaging system. The disadvantage of experimental PSF is that could be corrupted by noise, otherwise deconvolution with the theoretical PSF offer only a qualitative improvement of the image, because the introduced artefacts cannot be quantified. Deconvolution of the acquired data with experimental PSF permited to better quantify the 3D morphological properties of the sample and remove noise from the image as shown in my experimental results.

Successively, I've focused on the the time resolution of optical microscopy. , the available resolution permits following the evolution of biological processes which cannot be understood through structural organization of the living organism. For example, by live imaging we followed the infectious pathway of Polyomavirus and we were able to observe the active role of actin polymerization in virion transport, while immunofluorescence assays indicated cortical actin as a merely steric barrier during first steps of infections. Additionally, I've explored the potentialities of FRAP technique to study reaction kinetics in living sample[51].

With the four dimensions of space and time and available resolution with optical microsopy, other measurable variables can be analyzed. The wavelength λ dimention enables for example multi labeling and discrimination of different entities in the sample. Spectral properties of fluorochromes such as the lifetime of the excited state, give information on the environmental condition of the molecule. Changes in the intracellular environment, related to the cell metabolism, could influence the structure of the fluorescent molecules and its optical properties. Therefore, cell states and physiology of living sample could be studied at molecular level. This is the so called lifetime dimension. Futhermore, the Second Harmonic Generation, occuring when an intense laser beam passes through a polarizable material with non-centrosymmetric molecular organization, gives another possible dimension for optical microscopy measurements[206].

This unique multidimensionality of data acquired by innovative optical microscopy methods has to face the limited spatial resolution in comparison with other kind of imaging methods. An important effort was dedicated in the last decade to improve the resolution of optical microscopy by developing alternative methodologies. For example fluorescent techniques like FRET represent a distance ruler at nanometer resolution which could be used to break the resolution limit in combination with scanning probe microscopy techniques[67].

Improvements in resolution are also achieved with new optical configurations. Total Internal Reflection Fluorescence Microscopy can follow processes in an illuminated thin layer (on the order of 100 nm) of the sample near the coverslip interface[207]. Structured light excitation permit to expand the spatial frequency bandwidth of the optical system. The interference of light shift the Fourier transform of the sample image in the bandwidth of the microscope and it allow to acquires a larger frequency range than the support of the system[28,208]. Techniques as photo-activated localization microscopy (PALM) and stochastic optical reconstruction microscopy (STORM) apply a fitting between the PSF of the system and the point like features of the image to obtain the centre of mass of the labelled molecule at 20nm resolution[209]. Stimulated emission depletion (STED) exploits the optical properties of dyes to obtain nanometre resolution. Stimulated emission of photons from molecules inside a ring shaped region permits to observe the fluorescence from the centre hole. The dimension of such hole can be modulated through laser intensity for stimulated emission, and can

reach nanometre dimension[13,14,210]. This technique in combination with another ones called 4pi, (which utilize interference of two counter propagating short pulse infrared laser beams) reaches 100 nm resolution in the z axis and 10 nm resolution in x,y[211].
The classical optical resolution of microscopes is well suited for biology studies on tissues: two photon microscopy improved the deep penetration of optical systems while SPIM (Selective Plane Illumination Microscopy) technique permits to obtain 3D imaging of entire organisms[212]. With the evolution of new optical systems, the optical resolution go well beyond the diffraction limit and opens the perspective to follow biological process of living samples at molecular resolution.
The last aspects treated in my work were optical tweezers tools, given the high potentialities of their use for biological studies. Optical Tweezers open the field of single molecule manipulation and its biophysical caracterization[70,100]. Calibrated optical tweezers, the so called photonic force microscope, add another controlled[101,103] or measurable[102] variable to optical microscopy: the force. In this work, we used optical tweezers to measure force exerted by cellular structure, and to study the molecular system involved in cell motility. Such measurements give the possibility to analyze quantitatively motor planning of the cell in response to different stimuli and study its mechanotrasduction process.
With perspective of advancing from microscopy to nanoscopy, I think that usual artificial microsphere manipulation and visualization as presented in my studies will be replaced in the near future by bio-particles[213]. In the experimental result with Polyoma-virus, I developed an experimental protocol to study endocytic routes and cytoskeleton organization during intracellular trafficking. Better understanding of virus infection is necessary to define possible application of virus like particle as bio-probe but this can evolve sinergically with their employment and characterization as nano-devices[213]. Optical tweezers were already used to manipulate single virion[70]; mPyV empty caspid can be used as a trafficking cargo model, to measure PSF inside cells, as probe to perform intracellular force measurements, to apply intracellular stresses, or target specific molecule in cellular compartments[214] through their optical manipulation[70,183,192].
A complementary system to light manipulation tools that is fast evolving is laser dissection. By laser scissors it was possible to cut living biological samples with subcellular resolution: the cytoskeleton organization could be disturbed while leaving the cells unaffected in any other respect[215,216]. Optical tweezers and laser dissection tools were also used to control the location and timing of optical uncaging in chemical stimulation experiments[217], or for optoporating the cell membrane[218]. These opportunities encourage the use of optical tools in probing and quantifying biophysical cellular parameters as alternative descriptive markers, and open the new field of nanosurgery[216].

4. List of abbreviations

- ADF: actin depolymerising factor
- AFM: atomic force microscopy
- ATP: adenosine-5'-triphosphate
- CK: creatine kinase
- CK-IAF: fluorophore conjugated CK
- ECM: extracellular matrix
- EEA1: early endosome antigen
- EGFP: enhanced GFP
- FRAP: fluorescence recovery after photobleaching
- FRET: fluorescence resonant energy transfer
- FLIP: fluorescence loss in photobleaching
- FWHM: full width at half maximum
- Fv: force-velocity
- GFP: green fluorescent protein
- G proteins: GTP-binding protein
- GTP: guanosine-5'-triphosphate
- IFRAP: inverse-FRAP
- MLCK: myosin light chain kinase
- MOI: multiplicities of infection
- mPyV: mouse polyomavirus
- NA: numerical aperture
- PAGFP: photo-activable GFP
- PALM: photo-activated localization microscopy
- PSF: point spread function
- STED: stimulated emission depletion
- STORM: stochastic optical reconstruction microscopy
- SPIM: Selective Plane Illumination Microscopy
- SV40: Simian virus 40
- TPE: two photon excitation
- WASP: Wiskott-Aldrich syndrome
- VASP: vasodilatator-stimulated phosphoprotein
- VP1: viral protein 1

5. References

1. Diaspro,A. *et al.* Multi-photon excitation microscopy. *Biomed. Eng Online.* **5**, 36 (2006).

2. Lippincott-Schwartz,J. & Patterson,G.H. Development and use of fluorescent protein markers in living cells. *Science* **300**, 87-91 (2003).

3. Patterson,G.H. & Lippincott-Schwartz,J. A photoactivatable GFP for selective photolabeling of proteins and cells. *Science* **297**, 1873-1877 (2002).

4. Lippincott-Schwartz,J., Snapp,E. & Kenworthy,A. Studying protein dynamics in living cells. *Nat. Rev. Mol. Cell Biol.* **2**, 444-456 (2001).

5. Putman,E. Entering the small, small world of nanotechnology. *Biomed. Instrum. Technol.* **36**, 375-381 (2002).

6. Hansma,H.G., Sinsheimer,R.L., Li,M.Q. & Hansma,P.K. Atomic force microscopy of single- and double-stranded DNA. *Nucleic Acids Res.* **20**, 3585-3590 (1992).

7. Bustamante,C., Bryant,Z. & Smith,S.B. Ten years of tension: single-molecule DNA mechanics. *Nature* **421**, 423-427 (2003).

8. Neuman,K.C., Chadd,E.H., Liou,G.F., Bergman,K. & Block,S.M. Characterization of photodamage to Escherichia coli in optical traps. *Biophysical Journal* **77**, 2856-2863 (1999).

9. Neuman,K.C. & Block,S.M. Optical trapping. *Review of Scientific Instruments* **75**, 2787-2809 (2004).

10. Coirault,C., Pourny,J.C., Lambert,F. & Lecarpentier,Y. [Optical tweezers in biology and medicine]. *Med. Sci. (Paris)* **19**, 364-367 (2003).

11. Meller,A. *et al.* Localized dynamic light scattering: a new approach to dynamic measurements in optical microscopy. *Biophys. J.* **74**, 1541-1548 (1998).

12. S.J.Flint, L.W Enquist, R.M.Krug, V.R.Racaniello & A.M.Skalka. Principle of Virology. Molecular Biology, Pathogenesis, and Control. (2000).

13. Willig,K.I. *et al.* Nanoscale resolution in GFP-based microscopy. *Nat. Methods* **3**, 721-723 (2006).

14. Willig,K.I., Harke,B., Medda,R. & Hell,S.W. STED microscopy with continuous wave beams. *Nat. Methods* **4**, 915-918 (2007).

15. Ward,B.M. Visualization and characterization of the intracellular movement of vaccinia virus intracellular mature virions. *J. Virol.* **79**, 4755-4763 (2005).

16. Ward,B.M. Pox, dyes, and videotape: making movies of GFP-labeled vaccinia virus. *Methods Mol. Biol.* **269**, 205-218 (2004).

17. Naghavi,M.H. & Goff,S.P. Retroviral proteins that interact with the host cell cytoskeleton. *Curr. Opin. Immunol.* **19**, 402-407 (2007).

18. Munter,S. *et al.* Actin polymerisation at the cytoplasmic face of eukaryotic nuclei. *BMC. Cell Biol.* **7**, 23 (2006).

19. Munter,S., Way,M. & Frischknecht,F. Signaling during pathogen infection. *Sci. STKE.* **2006**, re5 (2006).

20. Kaksonen,M., Toret,C.P. & Drubin,D.G. Harnessing actin dynamics for clathrin-mediated endocytosis. *Nat. Rev. Mol. Cell Biol.* **7**, 404-414 (2006).

21. Wilson T. & Sheppard C.J.R. Theory and Practice of Scanning. Optical Microscopy. (1984).

22. Sheppard,C.J.R. & Cogswell,C.J. 3-Dimensional Image-Formation in Confocal Microscopy. *Journal of Microscopy-Oxford* **159**, 179-194 (1990).

23. Lukosz,W. & Warga,M.E. Thd11 - A New Theorem on Ultimate Limit of Performance of Optical Systems. *Journal of the Optical Society of America* **56**, 548-& (1966).

24. Minsky M. Microscopy apparatus. *United State Patent* (1961).

25. Alberto Diaspro. Confocal and Two-Photon Microscopy: Foundations, Applications and Advances. (2002).

26. Petran,M., HADRAVSK.M, Egger,M.D. & Galambos,R. Tandem-Scanning Reflected-Light Microscope. *Journal of the Optical Society of America* **58**, 661-& (1968).

27. Egner,A., Andresen,V. & Hell,S.W. Comparison of the axial resolution of practical Nipkow-disk confocal fluorescence microscopy with that of multifocal multiphoton microscopy: theory and experiment. *Journal of Microscopy-Oxford* **206**, 24-32 (2002).

28. Neil,M.A.A., Juskaitis,R. & Wilson,T. Method of obtaining optical sectioning by using structured light in a conventional microscope. *Optics Letters* **22**, 1905-1907 (1997).

29. Neil,M.A.A., Wilson,T. & Juskaitis,R. A light efficient optically sectioning microscope. *Journal of Microscopy-Oxford* **189**, 114-117 (1998).

30. Goppert Mayer M. Elementary processes with two-quantum transitions. *Ann. d. Physik* **9**, 273-295 (1931).

31. Brakenhoff,G.J., Muller,M. & Ghauharali,R.I. Analysis of efficiency of two-photon versus single-photon absorption for fluorescence generation in biological objects. *Journal of Microscopy-Oxford* **183**, 140-144 (1996).

32. Diaspro,A. *et al.* Two-photon microscopy and spectroscopy based on a compact confocal scanning head. *Journal of Biomedical Optics* **6**, 300-310 (2001).

33. Nakamura,O. Fundamental of two-photon microscopy. *Microscopy Research and Technique* **47**, 165-171 (1999).

34. So,P.T., Dong,C.Y., Masters,B.R. & Berland,K.M. Two-photon excitation fluorescence microscopy. *Annu. Rev. Biomed. Eng* **2**, 399-429 (2000).

35. Denk,W., Strickler,J.H. & Webb,W.W. 2-Photon Laser Scanning Fluorescence Microscopy. *Science* **248**, 73-76 (1990).

36. Hell,S., Reiner,G., Cremer,C. & Stelzer,E.H.K. Aberrations in Confocal Fluorescence Microscopy Induced by Mismatches in Refractive-Index. *Journal of Microscopy-Oxford* **169**, 391-405 (1993).

37. Born M. & Wolf E. Principles of Optics: Electromagnetic Theory of Propagation, Interference and Diffraction of Light. (2002).

38. Gu,M. & Sheppard,C.J.R. Comparison of 3-Dimensional Imaging Properties Between 2-Photon and Single-Photon Fluorescence Microscopy. *Journal of Microscopy-Oxford* **177**, 128-137 (1995).

39. Stelzer,E.H.K. *et al.* Nonlinear Absorption Extends Confocal Fluorescence Microscopy Into the Ultra-Violet Regime and Confines the Illumination Volume. *Optics Communications* **104**, 223-228 (1994).

40. Diaspro,A., Annunziata,S., Raimondo,M. & Robello,M. Three-dimensional optical behaviour of a confocal microscope with single illumination and detection pinhole through imaging of subresolution beads. *Microscopy Research and Technique* **45**, 130-131 (1999).

41. Carlsson,K. The Influence of Specimen Refractive-Index, Detector Signal Integration, and Nonuniform Scan Speed on the Imaging Properties in Confocal Microscopy. *Journal of Microscopy-Oxford* **163**, 167-178 (1991).

42. Pawley,J.B. Handbook of Biological Confocal Microscopy. (1990).

43. vanKempen,G.M.P., vanVliet,L.J., Verveer,P.J. & Vandervoort,H.T.M. A quantitative comparison of image restoration methods for confocal microscopy. *Journal of Microscopy-Oxford* **185**, 354-365 (1997).

44. Bertero,A. & Boccacci,P. Super-resolution in computational imaging. *Micron* **34**, 265-273 (2003).

45. Bertero,M. & Demol,C. Stability Problems in Inverse Diffraction. *Ieee Transactions on Antennas and Propagation* **29**, 368-372 (1981).

46. Bertero,M., Boccacci,P., Brianzi,P. & Pike,E.R. Inverse Problems in Confocal Scanning Microscopy. *Advances in Electronics and Electron Physics* 225-239 (1987).

47. Bertero M. & Boccaccio P. Introduction to Inverse Problems in Imaging. (1998).

48. Tikhonov,A.N. Solution of Incorrectly Formulated Problems and Regularization Method. *Doklady Akademii Nauk Sssr* **151**, 501-& (1963).

49. Bertero,M. Regularization Methods for Linear Inverse Problems. *Lecture Notes in Mathematics* **1225**, 52-112 (1986).

50. Periasamy,A., Skoglund,P., Noakes,C. & Keller,R. An evaluation of two-photon excitation versus confocal and digital deconvolution fluorescence microscopy imaging in Xenopus morphogenesis. *Microscopy Research and Technique* **47**, 172-181 (1999).

51. McNally,J.G. Quantitative FRAP in analysis of molecular binding dynamics in vivo. *Methods Cell Biol.* **85**, 329-351 (2008).

52. Misteli,T., Gunjan,A., Hock,R., Bustin,M. & Brown,D.T. Dynamic binding of histone H1 to chromatin in living cells. *Nature* **408**, 877-881 (2000).

53. Phair,R.D. & Misteli,T. High mobility of proteins in the mammalian cell nucleus. *Nature* **404**, 604-609 (2000).

54. Dundr,M., McNally,J.G., Cohen,J. & Misteli,T. Quantitation of GFP-fusion proteins in single living cells. *J. Struct. Biol.* **140**, 92-99 (2002).

55. Schneider,M., Barozzi,S., Testa,I., Faretta,M. & Diaspro,A. Two-photon activation and excitation properties of PA-GFP in the 720-920-nm region. *Biophys. J.* **89**, 1346-1352 (2005).

56. Joseph R.Lakowicz. Principles of Fluorescence Spectroscopy. (2007).

57. dos Remedios,C.G., Miki,M. & Barden,J.A. Fluorescence resonance energy transfer measurements of distances in actin and myosin. A critical evaluation. *J. Muscle Res. Cell Motil.* **8**, 97-117 (1987).

58. Day,R.N., Periasamy,A. & Schaufele,F. Fluorescence resonance energy transfer microscopy of localized protein interactions in the living cell nucleus. *Methods* **25**, 4-18 (2001).

59. Periasamy,A. Imaging the dynamic events: FRET microscopy. *Biophysical Journal* **80**, 161A (2001).

60. Bastiaens,P.I. & Squire,A. Fluorescence lifetime imaging microscopy: spatial resolution of biochemical processes in the cell. *Trends Cell Biol.* **9**, 48-52 (1999).

61. Elangovan,M., Day,R.N. & Periasamy,A. Dynamic imaging using fluorescence resonance energy transfer. *Biotechniques* **32**, 1260-1265 (2002).

62. Elangovan,M., Day,R.N. & Periasamy,A. Nanosecond fluorescence resonance energy transfer-fluorescence lifetime imaging microscopy to localize the protein interactions in a single living cell. *J. Microsc.* **205**, 3-14 (2002).

63. Periasamy,A., Elangovan,M., Elliott,E. & Brautigan,D.L. Fluorescence lifetime imaging (FLIM) of green fluorescent fusion proteins in living cells. *Methods Mol. Biol.* **183**, 89-100 (2002).

64. Bastiaens,P.I. & Jovin,T.M. Microspectroscopic imaging tracks the intracellular processing of a signal transduction protein: fluorescent-labeled protein kinase C beta I. *Proc. Natl. Acad. Sci. U. S. A* **93**, 8407-8412 (1996).

65. Elangovan,M. & Periasamy,A. Spectral bleed through and photo bleaching correction in FRET microscopy. *Biophysical Journal* **80**, 161A (2001).

66. Karpova,T.S. *et al.* Fluorescence resonance energy transfer from cyan to yellow fluorescent protein detected by acceptor photobleaching using confocal microscopy and a single laser. *Journal of Microscopy-Oxford* **209**, 56-70 (2003).

67. Vickery,S.A. & Dunn,R.C. Combining AFM and FRET for high resolution fluorescence microscopy. *J. Microsc.* **202**, 408-412 (2001).

68. Ashkin,A. Acceleration and Trapping of Particles by Radiation Pressure. *Physical Review Letters* **24**, 156-& (1970).

69. Ashkin,A. & Dziedzic,J.M. Optical Levitation by Radiation Pressure. *Applied Physics Letters* **19**, 283-& (1971).

70. Ashkin,A. & Dziedzic,J.M. Optical Trapping and Manipulation of Viruses and Bacteria. *Science* **235**, 1517-1520 (1987).

71. Ashkin,A., Dziedzic,J.M. & Yamane,T. Optical Trapping and Manipulation of Single Cells Using Infrared-Laser Beams. *Nature* **330**, 769-771 (1987).

72. Ashkin,A., Dziedzic,J.M., Bjorkholm,J.E. & Chu,S. Observation of A Single-Beam Gradient Force Optical Trap for Dielectric Particles. *Optics Letters* **11**, 288-290 (1986).

73. E.Ferrari. Optical Manipulation And Force Spectroscopy At The Cellular And Molecular Level By Means Of Laser Tweezers. (Ph.D Thesis). 2007.

Ref Type: Thesis/Dissertation

74. Liu,Y., Sonek,G.J., Berns,M.W., Konig,K. & Tromberg,B.J. 2-Photon Fluorescence Excitation in Continuous-Wave Infrared Optical Tweezers. *Optics Letters* **20**, 2246-2248 (1995).

75. Lee,W.M., Reece,P.J., Marchington,R.F., Metzger,N.K. & Dholakia,K. Construction and calibration of an optical trap on a fluorescence optical microscope. *Nat. Protoc.* **2**, 3226-3238 (2007).

76. Visscher,K., Brakenhoff,G.J. & Krol,J.J. Micromanipulation by "multiple" optical traps created by a single fast scanning trap integrated with the bilateral confocal scanning laser microscope. *Cytometry* **14**, 105-114 (1993).

77. Dholakia,K., Reece,P. & Gu,M. Optical micromanipulation. *Chem. Soc. Rev.* **37**, 42-55 (2008).

78. V.Garbin. Optical tweezers for the study of microbubble dynamics in ultrasound. (Ph.D Thesis). 2007.

Ref Type: Generic

79. Carnegie,D.J., Stevenson,D.J., Mazilu,M., Gunn-Moore,F. & Dholakia,K. Guided neuronal growth using optical line traps. *Opt. Express* **16**, 10507-10517 (2008).

80. Schonbrun,E. & Crozier,K.B. Spring constant modulation in a zone plate tweezer using linear polarization. *Opt. Lett.* **33**, 2017-2019 (2008).

81. Kurt D.Wulff *et al.* Aberration correction in holographic optical tweezers. *Optics Express* **14**, 4169-4174 (2006).

82. Ericsson,M., Hanstorp,D., Hagberg,P., Enger,J. & Nystrom,T. Sorting out bacterial viability with optical tweezers. *Journal of Bacteriology* **182**, 5551-5555 (2000).

83. Sacconi,L., Tolic-Norrelykke,I.M., Antolini,R. & Pavone,F.S. Combined intracellular three-dimensional imaging and selective nanosurgery by a nonlinear microscope. *J. Biomed. Opt.* **10**, 14002 (2005).

84. Liang,H. *et al.* Directed Movement of Chromosome Arms and Fragments in Mitotic Newt Lung-Cells Using Optical Scissors and Optical Tweezers. *Experimental Cell Research* **213**, 308-312 (1994).

85. Visscher,K. & Brakenhoff,G.J. Single Beam Optical Trapping Integrated in A Confocal Microscope for Biological Applications. *Cytometry* **12**, 486-491 (1991).

86. Block,S.M., Blair,D.F. & Berg,H.C. Compliance of Bacterial Flagella Measured with Optical Tweezers. *Nature* **338**, 514-518 (1989).

87. Molloy,J.E. & Padgett,M.J. Lights, action: optical tweezers. *Contemporary Physics* **43**, 241-258 (2002).

88. Berg-Sorensen,K., Peterman,E.J.G., Weber,T., Schmidt,C.F. & Flyvbjerg,H. Power spectrum analysis for optical tweezers. II: Laser wavelength dependence of parasitic filtering, and how to achieve high bandwidth. *Review of Scientific Instruments* **77**, (2006).

89. Berg-Sorensen,K. & Flyvbjerg,H. Power spectrum analysis for optical tweezers. *Review of Scientific Instruments* **75**, 594-612 (2004).

90. Schaffer,E., Norrelykke,S.F. & Howard,J. Surface forces and drag coefficients of microspheres near a plane surface measured with optical tweezers. *Langmuir* **23**, 3654-3665 (2007).

91. Gittes,F. & Schmidt,C.F. Interference model for back-focal-plane displacement detection in optical tweezers. *Opt. Lett.* **23**, 7-9 (1998).

92. Denk,W. & Webb,W.W. Optical Measurement of Picometer Displacements of Transparent Microscopic Objects. *Applied Optics* **29**, 2382-2391 (1990).

93. Peterman,E.J., Gittes,F. & Schmidt,C.F. Laser-induced heating in optical traps. *Biophys. J.* **84**, 1308-1316 (2003).

94. Christian Tischer *et al.* Three-dimensional thermal noise imaging. *Applied Physics Letters* **79**, (1 A.D.).

95. Rohrbach,A., Kress,H. & Stelzer,E.H. Three-dimensional tracking of small spheres in focused laser beams: influence of the detection angular aperture. *Opt. Lett.* **28**, 411-413 (2003).

96. Rohrbach,A. & Stelzer,E.H. Trapping forces, force constants, and potential depths for dielectric spheres in the presence of spherical aberrations. *Appl. Opt.* **41**, 2494-2507 (2002).

97. Lukic,B. *et al.* Direct observation of nondiffusive motion of a Brownian particle. *Phys. Rev. Lett.* **95**, 160601 (2005).

98. Lukic,B. *et al.* Motion of a colloidal particle in an optical trap. *Phys. Rev. E. Stat. Nonlin. Soft. Matter Phys.* **76**, 011112 (2007).

99. Rohrbach,A. Switching and measuring a force of 25 femtoNewtons with an optical trap. Optics Express 13(24). 28-11-2005.
Ref Type: Generic

100. Bustamante,C., Macosko,J.C. & Wuite,G.J.L. Grabbing the cat by the tail: Manipulating molecules one by one. *Nature Reviews Molecular Cell Biology* **1**, 130-136 (2000).

101. Dai,J. & Sheetz,M.P. Mechanical properties of neuronal growth cone membranes studied by tether formation with laser optical tweezers. *Biophys. J.* **68**, 988-996 (1995).

102. Dai,J. & Sheetz,M.P. Regulation of endocytosis, exocytosis, and shape by membrane tension. *Cold Spring Harb. Symp. Quant. Biol.* **60**, 567-571 (1995).

103. Apodaca,G. Modulation of membrane traffic by mechanical stimuli. *Am. J. Physiol Renal Physiol* **282**, F179-F190 (2002).

104. Pralle,A., Prummer,M., Florin,E.L., Stelzer,E.H. & Horber,J.K. Three-dimensional high-resolution particle tracking for optical tweezers by forward scattered light. *Microsc. Res. Tech.* **44**, 378-386 (1999).

105. Oddershede,L., Dreyer,J.K., Grego,S., Brown,S. & Berg-Sorensen,K. The motion of a single molecule, the lambda-receptor, in the bacterial outer membrane. *Biophys. J.* **83**, 3152-3161 (2002).

106. Sacconi,L., Tolic-Norrelykke,I.M., Stringari,C., Antolini,R. & Pavone,F.S. Optical micromanipulations inside yeast cells. *Appl. Opt.* **44**, 2001-2007 (2005).

107. D.E.Ingber. Tensegrity I. Cell structure and hierarchical systems biology. *Journal of Cell Science* **116**, 1157-1173 (2008).

108. Yu-Li Wang & Dennis E.Discher. Cell Mechanics. (2007).

109. Cai,Y. *et al.* Nonmuscle myosin IIA-dependent force inhibits cell spreading and drives F-actin flow. *Biophys. J.* **91**, 3907-3920 (2006).

110. Giannone,G., Jiang,G., Sutton,D.H., Critchley,D.R. & Sheetz,M.P. Talin1 is critical for force-dependent reinforcement of initial integrin-cytoskeleton bonds but not tyrosine kinase activation. *J. Cell Biol.* **163**, 409-419 (2003).

111. Galbraith,C.G., Yamada,K.M. & Galbraith,J.A. Polymerizing actin fibers position integrins primed to probe for adhesion sites. *Science* **315**, 992-995 (2007).

112. Adams,J.C. *et al.* Cell-matrix adhesions differentially regulate fascin phosphorylation. *Molecular Biology of the Cell* **10**, 4177-4190 (1999).

113. Palazzo,A.F., Eng,C.H., Schlaepfer,D.D., Marcantonio,E.E. & Gundersen,G.G. Localized stabilization of microtubules by integrin- and FAK-facilitated Rho signaling. *Science* **303**, 836-839 (2004).

114. Giannone,G. & Sheetz,M.P. Substrate rigidity and force define form through tyrosine phosphatase and kinase pathways. *Trends in Cell Biology* **16**, 213-223 (2006).

115. Giannone,G. *et al.* Lamellipodial actin mechanically links myosin activity with adhesion-site formation. *Cell* **128**, 561-575 (2007).

116. Giannone,G. *et al.* Periodic lamellipodial contractions correlate with rearward actin waves. *Cell* **116**, 431-443 (2004).

117. Carlsson,A.E. Growth of branched actin networks against obstacles. *Biophysical Journal* **81**, 1907-1923 (2001).

118. Carlsson,A.E. & Katz,J.I. Growth dynamics of branched actin networks. *Biophysical Journal* **80**, 496A (2001).

119. Etienne-Manneville,S. Actin and microtubules in cell motility: Which one is in control? *Traffic* **5**, 470-477 (2004).

120. Loisel,T.P., Boujemaa,R., Pantaloni,D. & Carlier,M.F. Reconstitution of actin-based motility of Listeria and Shigella using pure proteins. *Nature* **401**, 613-616 (1999).

121. Mogilner,A. & Oster,G. The physics of lamellipodial protrusion. *European Biophysics Journal with Biophysics Letters* **25**, 47-53 (1996).

122. Mogilner,A. & Rubinstein,B. The physics of filopodial protrusion. *Biophysical Journal* **89**, 782-795 (2005).

123. Carlier,M.F., Le Clainche,C., Wiesner,S. & Pantaloni,D. Actin-based motility: from molecules to movement. *Bioessays* **25**, 336-345 (2003).

124. Pantaloni,D., Le Clainche,C. & Carlier,M.F. Mechanism of actin-based motility (vol 292, pg 1502, 2001). *Science* **292**, 2012 (2001).

125. Pantaloni,D., Le Clainche,C. & Carlier,M.F. Cell biology - Mechanism of actin-based motility. *Science* **292**, 1502-1506 (2001).

126. Fletcher,D.A. & Theriot,J.A. An introduction to cell motility for the physical scientist. *Phys. Biol.* **1**, T1-10 (2004).

127. Gov,N.S. & Gopinathan,A. Dynamics of membranes driven by actin polymerization. *Biophysical Journal* **90**, 454-469 (2006).

128. Davenport,R.W., Dou,P., Rehder,V. & Kater,S.B. A Sensory Role for Neuronal Growth Cone Filopodia. *Nature* **361**, 721-724 (1993).

129. Hochmuth,R.M., Shao,J.Y., Dai,J.W. & Sheetz,M.P. Deformation and flow of membrane into tethers extracted from neuronal growth cones. *Biophysical Journal* **70**, 358-369 (1996).

130. Liu,A.P. & Fletcher,D.A. Actin polymerization serves as a membrane domain switch in model lipid bilayers. *Biophysical Journal* **91**, 4064-4070 (2006).

131. Sheetz,M.P. & Dai,J. Modulation of membrane dynamics and cell motility by membrane tension. *Trends Cell Biol.* **6**, 85-89 (1996).

132. Sheetz,M.P. Cellular plasma membrane domains. *Mol. Membr. Biol.* **12**, 89-91 (1995).

133. Raucher,D. & Sheetz,M.P. Characteristics of a membrane reservoir buffering membrane tension. *Biophysical Journal* **77**, 1992-2002 (1999).

134. Raucher,D. & Sheetz,M.P. Membrane expansion increases endocytosis rate during mitosis. *Journal of Cell Biology* **144**, 497-506 (1999).

135. Raucher,D. & Sheetz,M.P. Cell spreading and lamellipodial extension rate is regulated by membrane tension. *Journal of Cell Biology* **148**, 127-136 (2000).

136. Dai,J. & Sheetz,M.P. Cell membrane mechanics. *Methods Cell Biol.* **55**, 157-171 (1998).

137. Mogilner,A. & Oster,G. Cell motility driven by actin polymerization. *Biophysical Journal* **71**, 3030-3045 (1996).

138. Rodriguez,O.C. *et al.* Conserved microtubule-actin interactions in cell movement and morphogenesis. *Nature Cell Biology* **5**, 599-609 (2003).

139. Felgner,H., Frank,R. & Schliwa,M. Flexural rigidity of microtubules measured with the use of optical tweezers. *Journal of Cell Science* **109**, 509-516 (1996).

140. Alberts Et Al. & James D.Watson. Molecular Biology of the Cell. (2002).

141. Pantaloni,D., Boujemaa,R., Didry,D., Gounon,P. & Carlier,M.F. The Arp2/3 complex branches filament barbed ends: functional antagonism with capping proteins. *Nature Cell Biology* **2**, 385-391 (2000).

142. Schaus,T.E., Taylor,E.W. & Borisy,G.G. Self-organization of actin filament orientation in the dendritic-nucleation/array-treadmilling model. *Proceedings of the National Academy of Sciences of the United States of America* **104**, 7086-7091 (2007).

143. Pollard,T.D. & Borisy,G.G. Cellular motility driven by assembly and disassembly of actin filaments. *Cell* **112**, 453-465 (2003).

144. Chhabra,E.S. & Higgs,H.N. The many faces of actin: Matching assembly factors with cellular structures. *Nature Cell Biology* **9**, 1110-1121 (2007).

145. Steffen,A. *et al.* Filopodia formation in the absence of functional WAVE- and Arp2/3-complexes. *Molecular Biology of the Cell* **17**, 2581-2591 (2006).

146. Faix,J. & Rottner,K. The making of filopodia. *Current Opinion in Cell Biology* **18**, 18-25 (2006).

147. Vignjevic,D., Kojima,S., Svitkina,T. & Borisy,G.G. Role of fascin in filopodial protrusion. *Journal of Cell Biology* **174**, 863-875 (2006).

148. Dogterom,M. & Yurke,B. Measurement of the force-velocity relation for single growing microtubules. *Biophysical Journal* **74**, A244 (1998).

149. Dogterom,M. & Yurke,B. Measurement of the force-velocity relation for growing microtubules. *Science* **278**, 856-860 (1997).

150. Footer,M.J., Kerssemakers,J.W.J., Theriot,J.A. & Dogterom,M. Direct measurement of force generation by actin filament polymerization using an optical trap. *Proceedings of the National Academy of Sciences of the United States of America* **104**, 2181-2186 (2007).

151. Janson,M.E. & Dogterom,M. Scaling of microtubule force-velocity curves obtained at different tubulin concentrations. *Physical Review Letters* **92**, (2004).

152. Kikumoto,M., Kurachi,M., Tosa,V. & Tashiro,H. Flexural rigidity of individual Microtubules measured by a buckling force with optical traps. *Biophysical Journal* **90**, 1687-1696 (2006).

153. Kovar,D.R. & Pollard,T.D. Insertional assembly of actin filament barbed ends in association with formins produces piconewton forces. *Proceedings of the National Academy of Sciences of the United States of America* **101**, 14725-14730 (2004).

154. Mogilner,A. On the edge: modeling protrusion. *Current Opinion in Cell Biology* **18**, 32-39 (2006).

155. Mogilner,A. & Oster,G. Polymer motors: Pushing out the front and pulling up the back. *Current Biology* **13**, R721-R733 (2003).

156. Svitkina,T.M. & Borisy,G.G. Arp2/3 complex and actin depolymerizing factor/cofilin in dendritic organization and treadmilling of actin filament array in lamellipodia. *J. Cell Biol.* **145**, 1009-1026 (1999).

157. Hill,T.L. & Kirschner,M.W. Bioenergetics and kinetics of microtubule and actin filament assembly-disassembly. *Int. Rev. Cytol.* **78**, 1-125 (1982).

158. Mogilner,A. & Oster,G. Force generation by actin polymerization II: The elastic ratchet and tethered filaments. *Biophysical Journal* **84**, 1591-1605 (2003).

159. Peskin,C.S., Odell,G.M. & Oster,G.F. Cellular Motions and Thermal Fluctuations - the Brownian Ratchet. *Biophysical Journal* **65**, 316-324 (1993).

160. Oster,G.F. On the crawling of cells. *J. Embryol. Exp. Morphol.* **83 Suppl**, 329-364 (1984).

161. Parekh,S.H., Chaudhuri,O., Theriot,J.A. & Fletcher,D.A. Loading history determines the velocity of actin-network growth. *Nat. Cell Biol.* **7**, 1219-1223 (2005).

162. Schafer,D.A., Jennings,P.B. & Cooper,J.A. Dynamics of capping protein and actin assembly in vitro: Uncapping barbed ends by polyphosphoinositides. *Journal of Cell Biology* **135**, 169-179 (1996).

163. Schafer,D.A. & Cooper,J.A. Control of actin assembly at filament ends. *Annual Review of Cell and Developmental Biology* **11**, 497-518 (1995).

164. Upadhyaya,A. & van Oudenaarden,A. Biomimetic systems for studying actin-based motility. *Current Biology* **13**, R734-R744 (2003).

165. Upadhyaya,A., Chabot,J.R., Andreeva,A., Samadani,A. & van Oudenaarden,A. Probing polymerization forces by using actin-propelled lipid vesicles. *Proceedings of the National Academy of Sciences of the United States of America* **100**, 4521-4526 (2003).

166. Upadhyaya,A., Chabot,J.R., Andreeva,A. & van Oudenaarden,A. Probing the forces generated by actin polymerization: ActA coated lipid vesicles as force transducers. *Molecular Biology of the Cell* **13**, 11A (2002).

167. Marcy,Y., Prost,J., Carlier,M.F. & Sykes,C. Forces generated during actin-based propulsion: A direct measurement by micromanipulation. *Proceedings of the National Academy of Sciences of the United States of America* **101**, 5992-5997 (2004).

168. Hu,K., Ji,L., Applegate,K.T., Danuser,G. & Waterman-Stirer,C.M. Differential transmission of actin motion within focal adhesions. *Science* **315**, 111-115 (2007).

169. Riveline,D. *et al.* Focal contact as mechanosensor: Directional growth in response to local strain. *Molecular Biology of the Cell* **10**, 341A (1999).

170. Riveline,D. *et al.* Focal contacts as mechanosensors: Externally applied local mechanical force induces growth of focal contacts by an mDia1-dependent and ROCK-independent mechanism. *Journal of Cell Biology* **153**, 1175-1185 (2001).

171. Palazzo,A.F. & Gundersen,G.G. Microtubule-actin cross-talk at focal adhesions. *Sci. STKE.* **2002**, E31 (2002).

172. Radtke,K., Dohner,K. & Sodeik,B. Viral interactions with the cytoskeleton: a hitchhiker's guide to the cell. *Cellular Microbiology* **8**, 387-400 (2006).

173. Stidwill,R.P. & Greber,U.F. Intracellular virus trafficking reveals physiological characteristics of the cytoskeleton. *News in Physiological Sciences* **15**, 67-71 (2000).

174. Mabit,H. *et al.* Intact microtubules support adenovirus and herpes simplex virus infections. *J. Virol.* **76**, 9962-9971 (2002).

175. Burke,E., Dupuy,L., Wall,C. & Barik,S. Role of cellular actin in the gene expression and morphogenesis of human respiratory syncytial virus. *Virology* **252**, 137-148 (1998).

176. Lehmann,M.J., Sherer,N.M., Marks,C.B., Pypaert,M. & Mothes,W. Actin- and myosin-driven movement of viruses along filopodia precedes their entry into cells. *J. Cell Biol.* **170**, 317-325 (2005).

177. Apodaca,G. Endocytic traffic in polarized epithelial cells: Role of the actin and microtubule cytoskeleton. *Traffic* **2**, 149-159 (2001).

178. Giner,D. *et al.* Real-time dynamics of the F-actin cytoskeleton during secretion from chromaffin cells. *Journal of Cell Science* **118**, 2871-2880 (2005).

179. Pelkmans,L., Puntener,D. & Helenius,A. Local actin polymerization and dynamin recruitment in SV40-induced internalization of caveolae. *Science* **296**, 535-539 (2002).

180. Sanjuan,N., Porras,A. & Otero,J. Microtubule-dependent intracellular transport of murine polyomavirus. *Virology* **313**, 105-116 (2003).

181. Mannova,P. & Forstova,J. Mouse polyomavirus utilizes recycling endosomes for a traffic pathway independent of COPI vesicle transport. *J. Virol.* **77**, 1672-1681 (2003).

182. Kallewaard,N.L., Boxena,A.L. & Crowe,J.E. Cooperativity of actin and microtubule elements during replication of respiratory syncytial virus. *Virology* **331**, 73-81 (2005).

183. Sanderson,C.M., Way,M. & Smith,G.L. Virus-induced cell motility. *Journal of Virology* **72**, 1235-1243 (1998).

184. Favoreel,H.W., Van Minnebruggen,G., Adriaensen,D. & Nauwynck,H.J. Cytoskeletal rearrangements and cell extensions induced by the US3 kinase of an alphaherpesvirus are associated with enhanced spread. *Proc. Natl. Acad. Sci. U. S. A* **102**, 8990-8995 (2005).

185. Sherer,N.M. *et al.* Retroviruses can establish filopodial bridges for efficient cell-to-cell transmission. *Nat. Cell Biol.* **9**, 310-315 (2007).

186. Gouin,E., Welch,M.D. & Cossart,P. Actin-based motility of intracellular pathogens. *Current Opinion in Microbiology* **8**, 35-45 (2005).

187. Kuo,S.C. & McGrath,J.L. Steps and fluctuations of listeria monocytogenes during actin-based motility. *Molecular Biology of the Cell* **11**, 427A (2000).

188. McGrath,J.L. *et al.* The force-velocity relationship for the actin-based motility of Listeria monocytogenes. *Current Biology* **13**, 329-332 (2003).

189. Shaevitz,J.W. & Fletcher,D.A. Direct confirmation of the Brownian ratchet mechanism of actin-based Motility. *Biophysical Journal* 32A (2007).

190. Carlier,M.F., Wiesner,S., Le Clainche,C. & Pantaloni,D. Actin-based motility as a self-organized system: mechanism and reconstitution in vitro. *Comptes Rendus Biologies* **326**, 161-170 (2003).

191. Carlier,M.F.T., Loisel,T.P., Boujemaa,R. & Pantaloni,D. Reconstitution of actin-based motility of Listeria and Shigella using pure proteins. *Biophysical Journal* **78**, 240A (2000).

192. Cameron,L.A., Footer,M.J., van Oudenaarden,A. & Theriot,J.A. Motility of ActA protein-coated microspheres driven by actin polymerization. *Proceedings of the National Academy of Sciences of the United States of America* **96**, 4908-4913 (1999).

193. Cameron,L.A., Svitkina,T.M., Vignjevic,D., Theriot,J.A. & Borisy,G.G. Dendritic organization of actin comet tails. *Current Biology* **11**, 130-135 (2001).

194. Theriot,J.A. Actin Polymerization and the Propulsion of Intracellular Parasites. *Faseb Journal* **8**, A1429 (1994).

195. Theriot,J.A. Actin Polymerization and the Propulsion of Listeria-Monocytogenes. *Biophysical Journal* **66**, A352 (1994).

196. Gerbal,F. *et al.* Measurement of the elasticity of the actin tail of Listeria monocytogenes. *European Biophysics Journal with Biophysics Letters* **29**, 134-140 (2000).

197. Carlier,M.F.T., Boujemaa,R., Wiesner,S., Loisel,T.P. & Pantaloni,D. Mechanism of actin-based motility. *Molecular Biology of the Cell* **11**, 1A (2000).

198. Laurent,V. *et al.* Role of proteins of the Ena/VASP family in actin-based motility of Listeria monocytogenes. *Journal of Cell Biology* **144**, 1245-1258 (1999).

199. Wiesner,S. *et al.* A biomimetic motility assay provides insight into the mechanism of actin-based motility. *Journal of Cell Biology* **160**, 387-398 (2003).

200. Noireaux,V. *et al.* Growing an actin gel on spherical surfaces. *Biophysical Journal* **78**, 1643-1654 (2000).

201. Gerbal,F., Chaikin,P., Rabin,Y. & Prost,J. An elastic analysis of Listeria monocytogenes propulsion. *Biophysical Journal* **79**, 2259-2275 (2000).

202. Giardini,P.A., Fletcher,D.A. & Theriot,J.A. Compression forces generated by actin comet tails on lipid vesicles. *Proc. Natl. Acad. Sci. U. S A* **100**, 6493-6498 (2003).

203. Giardini,P.A., Lu,Y., Xia,Y. & Theriot,J.A. Polystyrene bacteria: Actin-based movement of artificial ellipsoidal particles. *Molecular Biology of the Cell* **13**, 176A (2002).

204. Giardini,P.A., Fletcher,D.A. & Theriot,J.A. Nanonewton squeezing forces generated by actin comet tails. *Molecular Biology of the Cell* **13**, 279A (2002).

205. Theriot,J.A. & Fung,D.C. Listeria monocytogenes-based assays for actin assembly factors. *Methods Enzymol.* **298**, 114-122 (1998).

206. Gauderon,R., Lukins,P.B. & Sheppard,C.J. Three-dimensional second-harmonic generation imaging with femtosecond laser pulses. *Opt. Lett.* **23**, 1209-1211 (1998).

207. Wang,M.D. & Axelrod,D. Time-lapse total internal reflection fluorescence video of acetylcholine receptor cluster formation on myotubes. *Dev. Dyn.* **201**, 29-40 (1994).

208. Gustafsson,M.G. *et al.* Three-dimensional resolution doubling in wide-field fluorescence microscopy by structured illumination. *Biophys. J.* **94**, 4957-4970 (2008).

209. Betzig,E. *et al.* Imaging intracellular fluorescent proteins at nanometer resolution. *Science* **313**, 1642-1645 (2006).

210. Hell,S.W. Far-field optical nanoscopy. *Science* **316**, 1153-1158 (2007).

211. Egner,A., Verrier,S., Goroshkov,A., Soling,H.D. & Hell,S.W. 4Pi-microscopy of the Golgi apparatus in live mammalian cells. *J. Struct. Biol.* **147**, 70-76 (2004).

212. Huisken,J., Swoger,J., Del Bene,F., Wittbrodt,J. & Stelzer,E.H. Optical sectioning deep inside live embryos by selective plane illumination microscopy. *Science* **305**, 1007-1009 (2004).

213. Vriezema,D.M. *et al.* Self-assembled nanoreactors. *Chemical Reviews* **105**, 1445-1489 (2005).

214. Boura,E. *et al.* Polyomavirus EGFP-pseudocapsids: analysis of model particles for introduction of proteins and peptides into mammalian cells. *FEBS Lett.* **579**, 6549-6558 (2005).

215. Colombelli,J., Reynaud,E.G. & Stelzer,E.H. Investigating relaxation processes in cells and developing organisms: from cell ablation to cytoskeleton nanosurgery. *Methods Cell Biol.* **82**, 267-291 (2007).

216. Colombelli,J., Pepperkok,R., Stelzer,E.H. & Reynaud,E.G. [Laser nanosurgery in cell biology]. *Med. Sci. (Paris)* **22**, 651-658 (2006).

217. Stracke,F., Rieman,I. & Konig,K. Optical nanoinjection of macromolecules into vital cells. *J. Photochem. Photobiol. B* **81**, 136-142 (2005).

218. Schneckenburger,H., Hendinger,A., Sailer,R., Strauss,W.S. & Schmitt,M. Laser-assisted optoporation of single cells. *J. Biomed. Opt.* **7**, 410-416 (2002).